Production, labeling and in vivo studies with the theranostic positron-emitting radiometals ^{44}Sc, $^{55/58m/58g}$Co, $^{61/64}$Cu, ^{86}Y and ^{69}Ge

by

Hector Francisco Valdovinos

A dissertation submitted in partial fulfillment
of the requirements for the degree of

Doctor of Philosophy

(Medical Physics)

at the

UNIVERSITY OF WISCONSIN – MADISON

2017

Date of final oral examination: 1/5/2017

The dissertation is approved by the following members of the Final Oral Committee:
Robert J Nickles, Emeritus Professor, Medical Physics
Weibo Cai, Associate Professor, Radiology
Bradley T Christian, Professor, Medical Physics
Onofre T DeJesus, Professor, Medical Physics
Bryan Bednarz, Associate Professor, Medical Physics
Jonathan W Engle, Associate Professor, Medical Physics

ABSTRACT

As a result of the recent advances in targeted radionuclide therapy (TRT), the demand for the cyclotron-produced positron-emitting radiometals ^{64}Cu, ^{61}Cu, ^{86}Y and ^{44}Sc has been gradually increasing in the last two decades, partly due to the diagnostic complement for treatment planning that they provide to their therapeutic analogues ^{67}Cu, ^{90}Y and ^{47}Sc. The positron emitters labeled to a targeting vector directed to a molecular signature of disease not just allow for noninvasive diagnosis via positron emission tomography (PET), but also for the prediction, via internal dosimetry calculations, of how effective the targeted agent labeled with the therapeutic analogue would be in a treatment scenario. Another explanation for the increase in demand for these PET radiometals is their gradual transition beyond the small animal preclinical environment into clinical applications, where more strict requirements in the quality of the radiolabel may be delaying their full incorporation into this setting. Hence, novel production methods that are more amenable to automation, more reproducible in terms of radiochemical separation yields and effective specific activities are necessary to satisfy this growing market.

In this dissertation, novel radiochemical separation methods for these radiometals that satisfy such requirements are presented, including a detailed characterization of the separated radionuclide in terms of radionuclidic purity, radionuclidic identity, reactivity to conventional chelators, trace metal purity and spatial resolution in a small animal PET scanner.

This dissertation also presents novel targetry and radiochemical separation methods for the production of other less conventional radiometals that constitute "theranostic" (therapeutic and diagnostic) pairs, namely the Auger electron emitters ^{58m}Co and ^{71}Ge and their positron emitting complements ^{55}Co and ^{69}Ge. These separated radiometals, except ^{71}Ge, are also fully characterized upon radiochemical separation.

The theranostic potential of each one of the radiometals that is covered in this thesis is demonstrated first by collecting biodistribution and pharmacokinetic data from PET imaging of tumor-bearing mice intravenously injected with radiolabeled agents, followed by internal dosimetry calculations using the Medical Internal Radiation Dose (MIRD) formalism, focusing on the therapeutic and radiotoxic implications caused by the radiolabeled agent when the radiometal is substituted with a therapeutic analogue. Special attention is given to the radionuclides with intrinsic theranostic properties in themselves: ^{64}Cu and the parent-daughter pair $^{58m/58g}$Co.

The radiolabeled agents that are employed include the radiometal by itself, that is, weakly bound to a simple ligand in solution (all radiometals in this thesis), strongly bound to a chelator-conjugated tumor-targeting antibody

called TRC105 (^{55}Co, ^{58m}Co, ^{58g}Co, ^{64}Cu and ^{86}Y) or incorporated into the structure of a super paramagnetic iron oxide nanoparticle (^{69}Ge).

In order to fully exploit the therapeutic potential of ^{58m}Co and ^{64}Cu for TRT, large amounts of activities and frequent doses of these radionuclides would have to be administered into a patient to compensate for their relatively short half life for TRT standards. Hence, large batches of activities and a frequent supply would have to become available to the scientific community that will be running the TRT studies and clinical trials. The novel production methods presented in Chapters 3 and 4 address these needs in an economically sustainable fashion, allowing for almost quantitative recycling of the respective iron and nickel isotopically-enriched target materials within 24 hours after a production run. Chapter 3 also presents a TRT study to demonstrate the theranostic potential of $^{58m/58g}$Co. In this study, ^{58m}Co labeled to TRC015, was injected into a group of tumor-bearing mice. PET images of the treated animals using the signal from the daugher ^{58g}Co were obtained to non-invasively visualize and, more importantly, quantitate the antibody targeting to the tumor post-therapy and to demonstrate how the quantification from PET can be used to evaluate the treatment efficacy.

ACKNOWLEDGEMENTS

Graduate school has been a long ride for me, with many ups and downs. It started very positively, with a fellowship from the Science and Medicine Graduate Research Scholars (SciMed GRS) program, which enabled me to move to Madison and become fully economically independent from my parents. I would like to express all my gratitude to this program.

In order of appearance in my graduate school experience, first I would like to thank Jon Engle for his mentorship, his advise and his teachings on how to use the tools and machines in the machine shop. Thank you for your help when I applied for a fellowship and for your suggestions when I was about to publish my first article. Thank you Todd Barnhart for teaching me about the cyclotron and the chemistry modules and for encouraging me to publish, to patent and to follow new ideas for research. Thanks Gary Frank for your help in the machine shop.

I am very thankful to my advisor Jerry Nickles for believing in me. I really appreciate that you sent me to every single conference even if I did not have anything to present at the beginning of my training. This was truly a big part of my preparation because it enabled me to interact with colleagues, to learn other ideas and other methods and to connect our research with industry. This is how I met Jim and Ann Lamb and Jerry Rasmussen from Cyclomedical, who taught me about management of cyclotron and radiopharmacy facilities. Thank you friends from Cyclomedical for sharing your knowledge with me. Thanks for your inspiration my dear friend Greg Severin. I was very lucky to share projects with you and to benefit from all the experience that you as a posdoc brought into our research group. I thank you for allowing me to collaborate in the scandium-44 project. That was how I broadened my perspective of our field and understood its significance and reach. Thanks for your discussions and for trying to speak Spanish with me to make me fill like I was with family.

I am very grateful with Katy Gagnon, who inspired me to be more productive and to enjoy work. Thanks for your suggestions on how to improve the way I present in public. Jonathan Siikanen was key in accelerating the development of my methods for radionuclide productions. Thanks to you a finally made progress on the automation business. Special thanks go to Reinier Hernandez who was willing to teach me basic concepts in chemistry, how to do bioconjugations and to share his novel ideas on how to use solid phase extraction resins. I am extremely grateful for your input in my first publication. Thanks to all the members and ex-members of the Cai research group, especially to Hao Hong, Yin Zhang, Shreya Goel, Chen Feng, Sixiang Shi, Chris England and Rubel Chakravarty. Right when I was feeling that my research was going nowhere, Rubel came along to find an important application of

the germanium-69 that I was producing, which resulted in an inspiring publication. Also thank you for your discussions on generators and on new radiolabeling strategies for scandium.

Thanks to Paul Ellison for your discussions on chemistry and radiochemistry and for teaching me how to use the high purity germanium detector and how to analyze the data that I collected with it. I really appreciate that you built the stand for the detector, which I used in practically all of my measurements.

Thanks to Justin Jeffery for his support in the Small Animal Imaging Facility.

Thanks to Professor Weibo Cai. I am particularly grateful for the Molecular Imaging course that you taught, which was very inspiring and informative to me. I also would like to thank you for you constructive comments on my presentations.

Special thanks to my dissertation committee members Jerry Nickles, Weibo Cai, Brad Christian, Onofre DeJesus, Bryan Bednarz, Jon Engle and Jim Holden.

Thanks to all my new friends in Madison that encouraged me to finish this dissertation, especially Paulina Reina, Carlos Ramirez, Ali Paulson, Adela Cedillo, Reinier Hernandez (again), Ever Flores, Carlos Ruiz and Arnoldo Lopez.

My family has been the main motivation for keeping up with this endeavor. My father Hector Valdovinos Gutierrez has been and will be my main inspiration for success. I will always remember your definition of discipline: “to do what you have to do even if you do not have the will to do it”, which motivated me to keep going and to keep working until the end. I dedicate all my work, all my pain, all my joy, all of these years away from you, everything to you. Thank you for your encouragement and love mother, Celia Uribe Diaz. Thank you for understanding me for taking this long journey of academic development. Thanks to my brothers Emmanuel and Alan for taking care of my parents while I was away from home. That allowed me to focus on this “project”, as my parents used to call it. You were an inspiration because I knew I had to set a good example on you. Thanks to all my Uribe family members in Guadalajara for your support.

Thanks to my family in California: my grandmother Elodia Gutierrez and all of my uncles, aunts and cousins. I am particularly grateful to “el compa” Chava and my padrino “Pancho” for checking on me and keeping me up to date with the family issues. Besides my dad, I would also like to dedicate this dissertation to my grandfather Francisco Valdovinos. You taught me that being modest is the best virtue that anyone can have. Even with a Ph.D. degree I will try to keep honoring this teaching.

TABLE OF CONTENTS

LIST OF TABLES

LIST OF FIGURES

Chapter 1 Introduction

Molecular imaging with positron emission tomography (PET) is routinely used in the diagnosis of diseases related to oncology, immunology, cardiology and neurology. The most widely used radionuclide is ^{18}F ($t_{1/2}$ = 110 min, 96.7% β^+, $E_{\beta+max}$ = 633 keV) due to its favorable decay properties, established and automated fluorination chemistry and wide availability from the proton bombardment on isotopically enriched ^{18}O water using small biomedical cyclotrons scattered across the country. F-18 is suitable for labeling small organic molecules, but has some disadvantages in labeling biomolecule vectors such as peptides, proteins or nanoparticles, mainly due to the large difference between its physical half-life and the biological half-life of the vector. Radiometals are more suitable for these kinds of targeting constructs particularly when they are conjugated to bifunctional chelators (BFC), which can coordinate these metals, keeping them bound to the targeting moiety. Positron-emitting radiometals that are increasingly receiving more attention for these applications are ^{68}Ga ($t_{1/2}$ = 68 min, 89.1% β^+, $E_{\beta+max}$ = 1899 keV) and ^{64}Cu ($t_{1/2}$ = 12.7 h; 17.4% β^+, $E_{\beta+max}$ = 653 keV; 39.0% β^-, $E_{\beta-max}$ = 579 keV), both of them are Period 4 metals having their valence electrons occupying the *3-d* sub-shell as cations when coordinated to ligands such as BFC. However, there are many other Period 4 and 5 positron-emitting radiometals, ranging from scandium to yttrium, which hold great potential for PET imaging applications.

Furthermore, many radiometals, namely titanium, copper and gallium, administered in buffered solutions, weakly bound to ligands such as chloride, acetate, citrate or oxalate, without labeling any targeting vector, have shown uptakes comparable to targeted agents in tumor and inflammation models [1-11]. This has increased interest in the application of these weakly bound or "free" radiometals in molecular imaging of disease. These results mandate for the exploration of the biodistribution in tumor models of other non-conventional radiometals such as manganese, cobalt, zinc, germanium and yttrium. Results from these experiments will also provide information on the organ destination of de-chelated radiometals from unstable complexes employed as targeted agents.

Moreover, different from the conventional radionuclides employed in PET, many positron-emitting radiometals have an isotope pair that emits either beta or low energy Auger and conversion electrons for targeted radiotherapy to cancer tumors. The existence of these so-called theranostic pairs expands the utility of positron-emitters from diagnosis of tumor lesions to effective tools for treatment planning via internal dosimetry. Fortunately, there are some radiometals that have theranostic properties by themselves, that is, that emit therapeutic beta particles or low energy electrons as well as positrons for PET imaging. Among these, ^{64}Cu stands out and this is reflected by the

continuous increase in number of publications in which it is employed as a tracer and, more recently, as a therapeutic [8-18].

The Cyclotron Research Group at the University of Wisconsin-Madison Medical Physics Department, with its CTI RDS 112 and GE PETtrace cyclotrons, is one of the few centers in the country that maintains a weekly supply of ^{64}Cu, in an economically self-sustaining manner, to more than 30 research institutions in the country. This demonstrates our expertise in target design and radiochemistry, and also the great potential of biomedical cyclotrons for the production of other radiometals, which could attain a similar mainstream status as ^{64}Cu, depending on their applications but also on a constant supply at a reasonable price.

The objective of this dissertation is to develop novel, economic and automated production methods of the radiometals ^{44}Sc, $^{55/58m/58g}$Co, ^{69}Ge, $^{61/64}$Cu and ^{86}Y, and to use each one of them in the following studies:

- **i.** Quantification of spatial resolution in a Siemens Inveon PET/CT for small animals using Derenzo phantoms.
- **ii.** Biodistribution via PET of weakly bound or "free" radiometals in mice implanted with tumors of murine breast cancer (4T1) or glioma (U87MG) cell lines.
- **iii.** Chelation to commercially available bifunctional chelators with a specific activity that is sufficient for practical and economic labeling of chelator-conjugated peptides or antibodies.
    a. The murine antibody TRC105 was labeled and administered to tumor-bearing mice to demonstrate the efficient and economic labeling of the radiometal and its stability *in vivo*.
    b. Biodistribution data in the form of time-activity curves from these studies was fit into mono-exponential functions to obtain biological half-lives and for dosimetry calculations of both the positron-emitter radiometal and the beta or low energy electron emitter analog to demonstrate the theranostic potential of the produced radionuclides.
    c. In case of low specific activity or no chelation, a chelator-free labeling protocol for nanoparticles was developed. The nanoparticle that was employed was super paramagnetic iron oxide (SPION), which is used as a contrast agent in MRI and in lymph node imaging applications.
- **iv.** In the case of the theranostic set ^{55}Co, ^{58m}Co and ^{58g}Co labeled to TRC105, a therapy study was performed in order to demonstrate: 1) the treatment planning possibilities pre-therapy with the positrion-emitter ^{55}Co;

2) the therapeutic potential of the Auger electron emitter ^{58m}Co; and 3) the potential to verify the targeting of ^{58m}Co post-therapy by PET imaging of its positron-emitter daughter ^{58g}Co.

Table 1.1 below shows the theranostic sets of radiometals with the nuclear decay properties that are relevant for PET imaging and for targeted therapy. The radionuclides that will be the focus of this dissertation are the ones that are available from biomedical cyclotrons like the ones that we have in our laboratory. A chapter will be dedicated to each radiometal.

Table 1.1 **N**uclear decay properties and availability from a small cyclotron of theranostic radiometals

PET nuclide	$t_{1/2}$	**Average energy of main β^+ [keV]**	**% all β^+**	**Accessible from biomedical cyclotron?**	**Therapeutic analog**	$t_{1/2}$	**Average E of β^- or conversion electrons [keV]**	**%**	**Accessible in large yields from biomedical cyclotron?**
^{44}Sc	3.97 h	632	94	YES	^{47}Sc	3.35 d	143	68	NO
							204	32	
^{55}Co	17.53 h	649	76	YES	^{58m}Co	9.10 h	17	73	YES
^{58g}Co	70.86 d	201	15	YES			24	24	
							25	3	
^{64}Cu	12.70 h	278	18	YES	^{64}Cu is theranostic		191	38	YES
^{61}Cu	3.33 h	524	51	YES	^{67}Cu	2.58 d	121	57	NO
							154	22	
							189	20	
^{69}Ge	1.63 d	522	21	YES	^{71}Ge	11.4 d	Only Auger electrons < 10 keV	164	YES
^{86}Y	14.74 h	535	32	YES	^{90}Y	2.67 d	934	100	NO

Chapter 2 Scandium-44

2.1 Introduction

Due to its favorable nuclear properties, shown in Figure 2.1, and amenable chemistry, ^{44}Sc ($t_{1/2}$ = 3.927 h; 94.3% β^+, E_{max} = 1474 keV) has been recently recognized as a radiometal holding great potential for PET applications. In spite of this, only a handful of small molecules have been radiolabeled with ^{44}Sc, and even less have been tested in a preclinical setting [19-24]. This is a result of the non-optimal current production and separation methods, which have limited the broad availability of this isotope. Currently, ^{44}Sc can be produced from a ^{44}Ti/^{44}Sc generator [25] and from biomedical cyclotrons via the ^{44}Ca(p,n)^{44}Sc route [23, 26-29]. However, several issues plague these methodologies. For instance, the difficult production of the parent isotope (^{44}Ti) together with the required extensive post-elution purification of the ^{44}Sc eluate, limit the applicability of generator-based ^{44}Sc [30]. On the other hand, cyclotron production provides a more efficient method to produce significantly larger activities of ^{44}Sc. Nevertheless, a simple yet efficient separation method to isolate ^{44}Sc from the irradiated calcium target remains nonexistent. In this study, we describe a novel separation method to obtain ^{44}Sc from irradiated natural calcium targets using extraction chromatography.

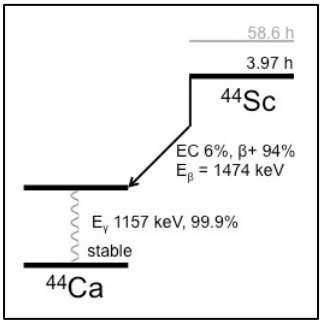

Figure 2.1 Simplified decay scheme of ^{44}Sc.

Furthermore, besides using ^{44}Sc as a label for PET imaging when bound to a chelator conjugated to a targeting vector, we verified its biodistribution in tumor-bearing mice when administered as scandium citrate based on evidence that this form of scandium is prone to ligand exchange with transferrin *in vivo* [31-33] and to challenge the binding of ^{67}Ga-citrate to plasma proteins *in vivo* [34-36]. This is important because it has been shown that after administration of weakly bound radiometals such as ^{67}Ga and ^{45}Ti, these nuclides are bound by transferrin *in vivo*, which in turn results in significant accumulation in tissue affected by cancer, infection or inflammation [1-7]. This discovery has turned ^{67}Ga- and ^{68}Ga-citrate into a useful tracer of malignancy in the clinical setting [37, 38].

Tri-n-butylphosphate (TBP), shown in Figure 2.2(a), is one of the most common organophosphorus extractants, for which extensive data on distribution coefficients of most metals is available [39]. Based on this data the separation of Sc(III) from bulk calcium can be effectively achieved in a TBP-HCl extraction system, since Sc(III) and Ca(II) have more than 1000-fold difference in distribution coefficients when the concentration of the acid is ≥ 9 M. Hence, given the striking structural similarities between TBP and dipentyl pentylphosphonate (DP[PP]), shown in Figure 2.2(b), we hypothesized that separation of radioactive scandium from calcium could be achieved using UTEVA, a commercially available resin functionalized with DP[PP].

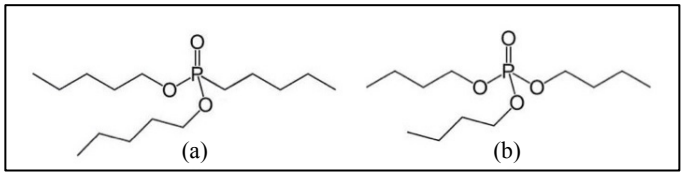

Figure 2.2 (a) Dipentyl pentylphosphonate (DP[PP]), the active extractant in the UTEVA resin and (b) Tri-n-butylphosphate (TBP)

Herein, we report the successful production and facile UTEVA-based separation of ^{44}Sc from proton irradiated natural calcium targets with excellent yield and effective specific activity towards the chelators DOTA (tetraazacyclododecane-1,4,7,10-tetraacetic acid) and DTPA (diethylenetriamine-pentaacetic acid). Additionally, we determined the distribution coefficients of Sc(III) and Ca(II) between UTEVA and HCl to confirm the optimal conditions for their separation. We compare our improved method to those from the following references [23, 27-29], which are based on the difference in binding affinity of scandium and calcium to the chelating resin Chelex 100, the difference in their distribution coefficients in the extraction resin N,N,N',N'-tetra-n-octyldiglycolamide (DGA), their difference in solubility, and their difference in distribution coefficients in a hydroxamate-functionalized resin, respectively.

Moreover, we assessed the biodistribution of ^{44}Sc-citrate in tumor-bearing mice implanted with murine breast cancer (4T1) and human glioblastoma cells (U87MG) via PET imaging and with this data we estimated the absorbed doses to normal organs and to the tumor, as well as the whole body effective dose caused by ^{44}Sc from proton-irradiated natural calcium and a hypothetical administration of a therapeutic dose of ^{47}Sc-citrate.

Sc-47, whose simplified decay scheme is shown in Figure 2.3, is an excellent radionuclide for targeted therapy due to: 1) its 3.35 day half-life that allows for an integration of thousands of cumulated decays in the target lesion if clearance from it is negligible (cumulated decays per administered activity $\sim \int_0^\infty e^{-\ln(2)/t_{1/2}} dt \sim t_{1/2}/\ln(2) = 4.2\times10^5$ Bq·s/Bq); and 2) its main decay emissions composed of two β^- particles with average energies of 143 and

204 keV and intensities of 68.4% and 31.6%, respectively; as well as a low-energy 156 keV gamma emission with 68.3% intensity [40]. The absorbed dose from the β^- particles is highly localized due to their short mean range in water of 0.3 and 0.5 mm, respectively [41]; and the low energy gamma emission is potentially useful for *in vivo* imaging with single photon emission computed tomography (SPECT), as it is comparable to that of the so-called "workhorse of nuclear medicine" ^{99m}Tc of 140 keV.

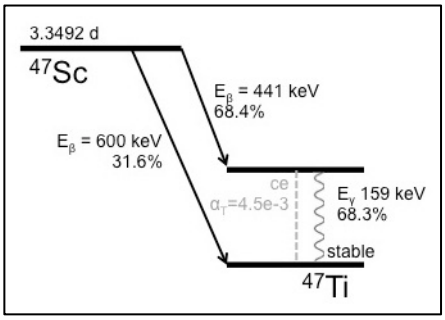

Figure 2.3 Simplified decay scheme of ^{47}Sc.

Finally, we believe that the implementation of our simple purification method promise to greatly simplify the cyclotron production of radioactive scandium using metallic calcium targets and allow for its automation and application in preclinical and perhaps even clinical studies.

2.2 Materials and Methods

Optima grade HCl comes from Aristar Ultra, VWR, West Chester, PA. Natural calcium (^{nat}Ca, 99.99%) in dendritic chunks comes from Sigma Aldrich, St. Louis MO. UTEVA (100-150 μm) resin comes from Eichrom, Lisle IL. The cyclic chelating ligand1,4,7,10-tetraazacyclododecane-1,4,7,10-tetraacetic acid (DOTA) was purchased from Macrocyclics, Dallas TX. The acyclic chelating ligand diethylenetriamine pentaacetic acid (DTPA) was purchased from Acros Organics (Geel, Belgium). Sodium acetate (NaOAc) was purchased from Fisher Scientific, Pittsburg PA. Both chelating ligands and NaOAc were dissolved in 18 MΩ·cm^{-1} water and mixed with Chelex 100 from Sigma Aldrich for trace metal purification. Scandium foil (99.9%) was purchased from Alfa Aesar, Ward Hill MA. A 50 ppm multi-element standard for calibration and Agilent's 4200 Microwave Plasma Atomic Emission Spectroscopy (MP-AES) system comes from Agilent Technologies, Santa Clara CA.

2.2.1 *Cyclotron targetry and irradiations*

The target system is very similar to that described by Severin, et al [28]. Briefly, 312 ± 19 mg (n = 11) of ^{nat}Ca were pressed with a hydraulic press at > 400 kg/cm^2 into an annular ring of 1.26 cm^2, 2.2 mm deep made of aluminum. A 0.56 mm thick silver disk in direct contact with the pressed calcium separated it from water-jet cooling

applied on the backside. Irradiations were performed on the UW-Madison PETtrace cyclotron using 16 MeV protons for 1 hour with an average current of 25 μA. A 25 μm molybdenum foil was placed over the irradiated face of the target to protect the cyclotron from sublimed calcium.

2.2.2 *Target yields, separation yields and radionuclidic contaminants*

^{44}Sc activities for separation yield quantification were measured with a Capintec CRC-Dual PET (Capintec, Ramsey NJ) dose calibrator using the calibration setting 938 suggested by the manufacturer. However, the actual activity from ^{44}Sc and other radionuclidic impurities was measured from the gamma intensities of 50 μL samples placed at distances with known efficiency calibration from a 60 cm^3 high purity germanium (HPGe) detector (Canberra C1519) (FWHM = 2.7 keV @ 1333 keV). Gamma-ray spectrum analysis software package, Maestro-32 MCA Emulator (Ortec, Oak Ridge TN), was used to collect and analyze the gamma-ray spectra. The gamma lines used to determine yields are listed in Table 2.1. The dead time was always kept below 10% and the acquisition time was set so that the statistical uncertainty from the number of counts per peak was kept below 1%, except for the 373 keV peak from ^{43}Sc, for which the statistical uncertainty was 3%. From the accurate activity value of ^{44}Sc it was confirmed that the Capintec measurement was within 10% of the HPGe result, thus this reading was used for the quantification of the separation yields.

Table 2.1 Gamma emissions from the scandium radioisotopes used for yield quantification

Nuclide	Gamma energies [keV]	Branching ratio
^{43}Sc	373	0.23
^{44}Sc	1157	0.999
^{44m}Sc	271	0.867
^{47}Sc	159	0.683
^{48}Sc	983.5	1.00

Theoretical activity yields at saturation for ^{43}Sc, ^{44}Sc and ^{44m}Sc at EoB were calculated using the cross-section data from Levkovskij [42]. However, this cross-section data was reduced by 20%, due to incorrect assessment of the excitation functions of the monitor reactions in the original publication [43]. The stopping power of protons in calcium was obtained from the SRIM (Stopping and Range of Ions in Matter) software [44].

After separation, the activity from a sample of the separated stock was logged into a spreadsheet every 10 seconds for 9 hours by connecting the dose calibrator (Capintec CRC-Dual PET) to a custom made LabVIEW program. This data was fit to a mono-exponential function and a decay half-life was quantified and compared to the accepted value for ^{44}Sc, 3.97 h [45].

2.2.3 *Radiochemical separation*

The ~300 mg calcium target was pushed out of the target holder cavity into a 50 mL centrifuge tube, to which 5 to 15 mL of concentrated HCl were added to dissolve the target and maintain the H^+ concentration > 9 M. This solution was then manually transferred to one of the three syringes that act as reservoirs connected to an automated module similar to the one described by Siikanen et al [46], which contains programmable dual pinch valves that control the access to the reservoirs. The module also includes two radiation detectors made in-house by encapsulating PIN photodiodes (HTV S9269, Hamamatsu Photonics, Japan) coupled with a CsI scintillator crystal. One detector monitors the activity in the syringe with the target solution and the other one the activity in the chromatography column. Before the activity was transferred onto the module, new syringes were connected and then filled with several milliliter of DI water to flush the tubing and remove metal impurities left from previous separations. Then, one of the reservoirs was filled with 5 mL of 10 M HCl for the washing step and another one with 400 μL of deionized water for the ^{44}Sc release step. A peristaltic pump with a flow rate of 1.1 mL/min sent the solution to a 5 mm diameter column cartridge (SPE 1.5 mL reservoir, Grace Davison Discovery Sciences, Deerfield IL) filled with 52 ± 2 mg of UTEVA resin. This packed resin is previously equilibrated with 1 mL of 10 M HCl manually. We selected ~50 mg as the amount of resin for practical reasons such as establishing an appropriate resin bed in the column that permitted maximum contact with the mobile phase. Additionally, when we reduced the amount of resin by half (~25 mg, Table 5, row a) a significant drop on the trapping efficiency from 83% to 52% was observed, possibly due to an inefficient equilibration between the mobile and stationary phases in the column. The trap and release sequence was as follows:

1. Load the target solution at varying HCl concentrations (9.1, 10.5, 11 M) to trap ^{44}Sc
2. Wash the column with 5 mL of 10 M HCl
3. Elute ^{44}Sc in successive fractions of 200 μL deionized water. The two most concentrated fractions, usually fractions 2 and 3, were mixed and used as the ^{44}Sc stock solution for labeling of DOTA and DTPA and for the formulation of ^{44}Sc-citrate for assessment of biodistribution in tumor-bearing mice. This stock solution had an acid concentration [H^+] of approximately 1 M.

Figure 2.4 shows a schematic of the automated module with the numbered arrows indicating the sequence of steps used in the separation.

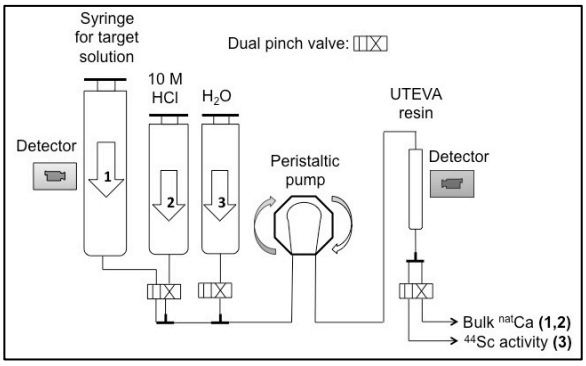

Figure 2.4 Scheme of the separation process overlaid in a schematic of the automated module

Trace metal analysis was performed on samples from three separation runs dissolving the target in 10 mL of concentrated HCl for a final solution concentration of ~10.5 M HCl. Table 2.2 describes the samples that were analyzed using Agilent's 4200 MP-AES system.

Table 2.2 Samples analyzed by MP-AES

	Volume [µL]	**Sample description**
i)	50	Target dissolution in 10 mL
ii)	50	Eluate after trapping Sc
iii)	50	Eluate from 5 mL 10 M HCl wash
iv)	400	First eluted fraction with isolated Sc
v)	200	Second eluted fraction with isolated Sc

2.2.4 *Determination of K_d values of Sc^{3+} and Ca^{2+} in UTEVA and HCl solution at various concentrations*

K_d values for Sc^{3+} and Ca^{2+} in UTEVA were determined in batch experiments using different concentrations of HCl similar to the method described by Filosofov et al [25]. ^{44}Sc dissolved in ~1 M HCl from one of the separations was used as a tracer of Sc^{3+}. 26.2 mg of 99.99% ^{nat}Ca were dissolved in 6 M HCl, dried down and re-dissolved in 0.05 M HCl in order to have a concentration of 1 mg / 20 µL. Aliquots were prepared in Eppendorf 1.5 mL vials with 100 mg of UTEVA resin. To all solutions 1 mL of HCl was added, then 20 µL of the ^{44}Sc tracer solution (12.1 MBq), followed by 20 µL of the ^{nat}Ca solution (1.0 mg). Each of the vials was shaken at room temperature for 4 hour in a shaker set at 500 rpm. 400 µL of the supernatant was taken from every vial and radioactivity A' was measured on the Capintec. The mass of calcium m' in this fraction was assayed using the MP-AES system. The dimensionless K_d value was calculated by the following equation:

$$K_d = \frac{^{44}\text{Sc Activity per gram of resin}}{^{44}\text{Sc Activity per mL of liquid}} = \frac{\left[A - \frac{A'}{0.4\ mL}(1.04\ mL)\right] \cdot \frac{1}{0.1\ g}}{\left[\frac{A'}{0.4\ mL}(1.04\ mL)\right] \cdot \frac{1}{1.04\ mL}} = \frac{4A - 10.4A'}{A'} \qquad \text{Equation 2.1}$$

A being the activity of the whole vial and A' being the activity of a 400 µL sample of the solution after the extraction, both decay-corrected to the time when the vials were removed from the shaker. In the case of calcium, K_d was calculated from the analogous equation:

$$K_d = \frac{\text{Ca mass per gram of resin}}{\text{Ca mass per mL of liquid}} = \frac{\left[1.0\text{ mg} - \frac{m'}{0.4\text{ mL}}(1.04\text{ mL})\right]\cdot\frac{1}{0.1\text{ g}}}{\left[\frac{m'}{0.4\text{ mL}}(1.04\text{ mL})\right]\cdot\frac{1}{1.04\text{ mL}}} = \frac{4 - 10.4m'}{m'} \qquad \text{Equation 2.2}$$

2.2.5 *Reactivity with DOTA and DTPA*

The reactivity or effective specific activity (ESA) of a separated radiometal towards a chelating ligand is an indirect method for quantifying the amount of competing non-radioactive metal impurities in a solution. The reactivity of the separated ^{44}Sc was assayed using the macrocycle 1,4,7,10-tetraazacyclododecane-1,4,7,10-tetraacetic acid (DOTA) as well as the acyclic chelating ligand diethylene triamine pentaacetic acid (DTPA) following the method described by Severin et al [28]. First, a stock solution is made by mixing 100 µL (> 74 MBq) of the ^{44}Sc eluate with 1 mL of deionized water and 1 mL of 0.25 M sodium acetate (NaOAc). Fractions of 100 µL (~3.7 MBq) from this buffered solution are distributed into two sets of ten 1.5 mL Eppendorf vials, each containing 100 µL of an aqueous solution of DOTA or DTPA with a known mass of chelator that ranges from zero to 10 µg. All reaction vials had a pH of 4.5. The DOTA solutions were incubated at 85-95°C for 1 hour and the DTPA solutions at room temperature for 30 min. Samples from each vial were then spotted onto aluminum backed silica gel ITLC plates (EMD Chemicals, Gibbstown NJ) for Thin Layer Chromatography (TLC), using 1:1 MeOH:10%NH_4OAc as the mobile phase. The activity distribution on the plates was assessed by autoradiography with a Cyclone Phosphor-Plate imaging system (Perkin Elmer).

2.2.6 *Image quality of ^{44}Sc*

A miniature Derenzo phantom [47] was used to evaluate the spatial resolution of ^{44}Sc PET images using an Inveon microPET/CT rodent model scanner (Siemens Medical Solutions USA). The phantom was printed with a 3D printer (Viper Si2 stereolithography machine, 3D Systems, Rock Hill, SC, USA) with holes of diameters 0.8, 1.0, 1.25, 1.5, 2.0 and 2.5 mm separated by 2 times their diameter [48]. These rods were filled with an aqueous solution of 40 MBq and data was collected for < 30 min until one billion coincident counts were acquired by the software. The raw data was collected in a histogram and reconstructed using the two-dimensional filtered back projection algorithm (FBP2D), without attenuation correction, using a matrix size of 512 × 512 pixels. Image quality was

evaluated by visual inspection of transaxial slices in the middle of the phantom and by profile analysis in the region in which optimal resolution was observed.

2.2.7 *Biodistribution and pharmacokinetics of ^{44}Sc-citrate and $^{44}ScCl_3$ in PBS in tumor-bearing mice*

In order to accurately quantify the ^{44}Sc activity concentrations in regions of interest (ROI) of the PET images, a quantification calibration was performed as indicated in the Inveon microPET/CT scanner manual. Briefly, a cylinder phantom with 1.4 cm length and 6.0 cm diameter was filled with 40.0 MBq of ^{44}Sc diluted in 0.1 M HCl solution, placed inside the field of view of the scanner parallel to the axis of the bore and then scanned until 1 billion coincident counts were acquired by the software. The data was reconstructed using the three-dimensional ordered subset expectation maximization OSEM3D algorithm and then 10 circular ROIs with a single slice thickness were drawn inside the cylinder image at equally spaced distances along the axis. Three samples of 1 mL were taken from the phantom and the average ^{44}Sc activity concentration, decay-corrected to the start time of the PET scan acquisition, was quantified using the same efficiency calibrated HPGe detector mentioned in section 2.2.2. A calibration factor for ^{44}Sc was created and saved by the software after the average count density from the 10 ROIs was converted to Bq/cm^3 from the measured activity.

Murine breast cancer tumors were established in two groups of three four- to five-week-old female Balb/c mice purchased from Harlan Sprague-Dawley Inc. by subcutaneous injection of approximately 2×10^6 murine mammary carcinoma 4T1 cells, suspended in 100 μL of 1:1 mixture of RPMI 1640 and Matrigel (BD Biosciences), into the front flank of three mice. Tumor sizes were monitored and mice were used for the imaging experiments when the axis of the quasi-ellipsoid tumors reached lengths of 6 - 9 and 5 - 8 mm, 10 days after inoculation. The total body mass of the mice at this time was 18.0 ± 1.0 g. Human glioblastoma (U87MG) cells were used for tumor inoculation when they reached ~80% confluence. U87MG tumors were established in four- to five-week-old female athymic nude mice by subcutaneously injecting 5×10^6 cells, suspended in 100 μL of 1:1 mixture of DMEM medium and matrigel, into the right upper flank of the mice. The tumor sizes were monitored every alternate day, and *in vivo* experiments were carried out when the diameter of the tumors reached 6 – 8 mm (typically, 3 weeks after inoculation). The total body mass of these mice at this time was 23.2 ± 1.9 g.

The ^{44}Sc-citrate stock solution for injection was prepared by diluting 20 μL of the separated ^{44}Sc stock solution with 600 μL of 10 mM sodium citrate ($Na_3C_6H_5O_7\bullet2H_2O$ or Na_3Cit) (Fisher Scientific) with the pH adjusted to ~7 by adding 10 μL of 1 M Na_2CO_3. A dose of 12.5 ± 0.4 MBq of ^{44}Sc-citrate in 200 μL was administered to each

mouse of the 4T1 group and static PET scans were performed at 0.5, 4 and 8 hours post-injection (p.i.). A dose of 24.7 ± 2.3 MBq ^{44}Sc-citrate was injected to each mouse of the U87MG group and scans were carried out at 0.5, 2, 4, 8 and 20 h p.i. Similarly, 100 µL from the separated stock with $^{44}ScCl_3$ solution was diluted with 500 µL of phosphate buffered saline (PBS) and 50 µL of 1 M Na_2CO_3 in order to reach neutral pH. Fractions of 200 µL from this solution with 22.4 ± 0.6 MBq were injected into another group of 4T1 tumor bearing-mice and scans were completed at 0.5, 4, 8 and 23 h p.i.. This latter agent will be referred to as $^{44}ScCl_3$ in PBS to emphasize that the formulation contains ~9 mM phosphate anions, which could complex with Sc^{3+} to form a neutral complex, perhaps a colloid.

The PET acquisitions were set to collect at least 40 million coincident counts per mouse, which implicated scanning times of 5 - 15 min. Static images were reconstructed using the OSEM3D algorithm and then analyzed with the Inveon Research Workplace software. Volumes of interest (VOI) were drawn on the whole volume of the delineable organs: heart, liver and spleen, as well as the whole tumor volume. Muscle uptake was quantified by drawing two ellipsoidal VOIs, each of 100 – 200 mm^3, flanking the urinary bladder in regions with low activity uptake where the adductor and biceps femoris muscles are located. The uptake data from each of the VOIs is decay-corrected to time of injection and expressed as percentage injected dose per gram (%ID/g). Whole body VOIs of each mouse were drawn and the whole body %ID was obtained by multiplication of the %ID/g by the volume of the VOI, assuming that 1 cm^3 = 1 g, which is a good approximation for most physiologic tissue. The %ID of each delineable organ and tumor was calculated in the same manner.

The %ID versus time plots, also known as time-activity curves, of the whole body and the heart were each fit into a mono-exponential decay function in order to calculate the whole body biological half-life and circulation half-life of ^{44}Sc-citrate. The time-activity curves of the delineable and remaining organs were used for internal dosimetry estimations as explained in section 2.2.8.

2.2.8 *Internal dosimetry of ^{44}Sc-citrate and the therapeutic analog ^{47}Sc-citrate in humans*

The internal dosimetry of ^{44}Sc- and ^{47}Sc-citrate was estimated for a standard adult male of 73.7 kg as defined by Cristy and Eckerman [49] using the OLINDA/EXM software [50], which is now approved by the Food and Drug Administration (FDA) for internal dosimetry calculations in clinical trials of radiopharmaceuticals [51]. The organ %ID/g data from small animals was extrapolated to %ID per organ in human using the mass method by Kirschne [52], which is summarized by the following formula:

$$\left[\left(\frac{\%\text{ID}}{g_{organ}}\right)_{animal} \times \left(kg_{total\ body\ weight}\right)_{animal}\right] \times \left(\frac{g_{organ}}{kg_{total\ body\ weight}}\right)_{human} = (\%\text{ID})_{human\ organ}$$

Equation 2.3

The %ID versus time data set for the delineable and remaining organs were input into the EXM portion of the OLINDA/EXM software, which is designed to fit this data into exponential functions to then integrate them, taking the radionuclide's physical decay into account, in order to obtain a cumulative amount of disintegrations or decays ($\widetilde{A}_i$) per source organ *i*. The software automatically feeds this factor into several equations like Equation 2.4 below, defined by the committee on Medical Internal Radiation Dose (MIRD) [53], to calculate the absorbed dose to each of the target organs *j* ($\widetilde{D}_j$) in the anthropomorphic standard adult male phantom designed by Cristy and Eckerman [49].

$$D_j = \frac{\tilde{A}_i}{m_j} C \sum_k n_k E_k \phi_k$$

Equation 2.4

D_j is the absorbed dose in a target organ *j* in Gy units; $\widetilde{A}_i$ is the cumulated activity (sum of all nuclear transitions that occurred) in a source organ *i* in units of MBq-s; n_k is the number of radiations with energy E_k emitted per nuclear transition; E_k is expressed in MeV units; ϕ_k is the absorbed fraction (fraction of radiation energy absorbed in the target organ), which are intrinsic in the OLINDA software and were derived using Monte Carlo simulation of radiation transport in models of the body and its internal structures (organs, tissue, et cetera), in our case the athropomorphic adult male phantom designed by Cristy and Eckerman [49]; *k* represents each of the different emissions emitted by the nuclide, either gamma rays, beta particles, conversion electrons or Auger electrons; m_j is the mass of target organ in kg; and *C* is a constant that equals 1.602×10^{-7} Gy-kg/MBq-s-MeV.

It is important to point out that the mono-exponential fit to the time-activity data set of each organ does not take into account the uptake phase of the radiotracer, and therefore we are assuming that there is an initial maximum uptake at time zero. This implies that the integration from time zero to the time of the first scan overestimates the actual number of cumulative decays since the time of maximum uptake was not determined. Nevertheless, the overestimation is very small since the 30 min p.i. scan time is several times smaller than the biological half-life of the radiotracer as it will be shown in section 2.3.7.

Besides the absorbed dose to each organ D_j, OLINDA also computes the Effective Dose (ED) by adding the products of the individual absorbed doses to each organ times a corresponding stochastic risk weighting factor, as defined in Publication 60 of the International Commission on Radiation Protection (ICRP) [54]. The ED is important

because it allows non-uniform internal doses to be expressed as an equivalent whole body dose that is related to overall radiation risk.

Since cyclotron-produced ^{44}Sc from natural calcium targets is not >99% radionuclidically pure, the effective dose from the other radioactive scandium impurities needs to be taken into account in order to demonstrate the feasibility of clinical translation of this kind of ^{44}Sc. This is easily achieved by simply replacing the type of scandium radionuclide (^{43}Sc, ^{44m}Sc, ^{47}Sc and ^{48}Sc) in the original OLINDA file, without modification to the original ^{44}Sc-citrate pharmacokinetic data.

However, the effective dose concept is not appropriate for therapy cases in which acute effects from radiation are prevalent due to the fact that highly ionizing and non-penetrating radiation are being employed, namely beta, alpha and low-energy electron emissions; and also due to the administration of excessively high amounts of radioactivity in the case of beta and low-energy electron emitters. Therefore, in the case of radionuclide therapy, a more appropriate dosimetric measure is the absorbed dose to each target organ, which we have computed for the case of a standard adult male by employing the ^{44}Sc-citrate pharmacokinetic data and replacing the scandium nuclide by ^{47}Sc.

2.2.9 *Tumor and normal organ dosimetry of ^{44}Sc-citrate and the therapeutic analog ^{47}Sc-citrate in mice*

The absorbed dose delivered to the 4T1 and U87MG tumors by accumulated ^{44}Sc-citrate and by a hypothetical administration of therapeutic ^{47}Sc-citrate was estimated using the dose-to-sphere model included in the OLINDA software. This model assumes a homogeneous distribution of the radiotracer inside a sphere volume and combines the decay data from the radionuclide with the absorbed fractions for spheres developed by Stabin and Konijnenberg [55]. In this case, the only input required by OLINDA is the total cumulative decays or disintegrations inside the tumor (which we will assume to be spherical) per administered activity in units of Bq-h/Bq. This value is obtained by trapezoidal integration of the non-decay-corrected time-activity curve of the tumor up to the last time point that was measured (8 hours p.i.) and then by integration from this time point up to infinity assuming that there is only physical decay of the radiotracer. These integrations were performed in an Excel Spreadsheet for ^{44}Sc and ^{47}Sc.

Since the OLINDA version that we posses does not include absorbed fractions (ϕ_k) from small animal phantoms, in order to estimate the absorbed dose to the normal organs of a mouse after a hypothetical administration of therapeutic ^{47}Sc-citrate, we employed the absorbed fractions (AF or ϕ_k) for different source-to-target organ configurations in a 27 g transgenic mouse that were calculated and published by Stabin et al. [56]. The AFs reported

in this publication were calculated by simulating mono-energetic photons and electrons inside a voxel-based, not mathematically modeled, transgenic mouse using a Monte Carlo particle transport code. The AFs for the three main emissions of ^{47}Sc (two β^- particles of average energies of 143 and 204 keV and a γ emission of 159 keV) were interpolated from the published AF values at energies of 100 and 200 keV for both photons and electrons.

Following the MIRD schema [53] for internal dosimetry, the AF values are then input into the equation for the *S*-value:

$$S(r_T \leftarrow r_S) = \frac{\sum_i n_i E_i AF(r_T \leftarrow r_S)}{m} \qquad \text{Equation 2.5}$$

where n_i, E_i, $AF(r_T \leftarrow r_s)$ and m are the number of nuclear transitions per nuclear decay, the energy per radiation, the absorbed fraction at a target organ (r_T) from emissions coming from a source organ (r_s) and the mass of the target organ, respectively. The organ masses of the 27 g transgenic mouse used for the AF calculations are also reported in the same publication [56]. The mean absorbed dose to a target organ is then calculated by substituting the *S*-values in the following equation:

$$D(r_T, T_D) = \sum_{r_S} \int_0^\infty \tilde{A}(r_S, t) S(r_T \leftarrow r_S) dt \qquad \text{Equation 2.6}$$

where $\tilde{A}(r_s,t)$ is the cumulative activity or total number of decays in source organ r_s over a dose integration period up to infinity. As it was explained in section 2.2.8, $\tilde{A}$ in each of the source organs can be obtained by fitting to exponential functions and then integrating the time-activity curves of each organ, taking the radionuclide's physical decay into account, using the EXM portion of the OLINDA/EXM software.

2.3 Results and discussion

2.3.1 *Cyclotron targetry and irradiations*

The metallic calcium target is able to withstand a current of 25 μA without any noticeable effect in its integrity. The 25 μm molybdenum foil degrader drops the 16 MeV proton beam from the PETtrace cyclotron down to 15.56 ± 0.04 MeV according to a SRIM simulation [44]. The exit energy after passing through 2.2 mm of calcium is 3.4 ± 0.4 MeV also according to a SRIM simulation. This constitutes a thick target since 4.5 MeV is the threshold energy for the ^{44}Ca(p,n)^{44g}Sc reaction.

2.3.2 *Target yields, separation yields and radionuclidic contaminants*

Table 2.3 lists the experimental activity yields at end of bombardment (EoB) of the scandium isotopes produced after our irradiation setting of 15.56 MeV protons, at 25 μA for one hour. These experimental yields are in

agreement with the yields calculated from the excitation functions published in [42] after a correction of 20% [57] and the yields reported by Severin et al [28].

Table 2.3 Radioactive scandium reaction products after proton bombardment of calcium at 15.56 MeV

Target	**% abundance**	**Product**	$t_{1/2}$	**Instantaneous measured yield [MBq/μAh]**	**Predicted yield using corrected data in [42] [MBq/μAh]**	**% of predicted yield**	**% of yield measured by Severin et al. [28] at 16 MeV**
^{40}Ca	96.941	-	-	-	-	-	
^{42}Ca	0.647	-	-	-	-	-	
^{43}Ca	0.135	^{43}Sc[b]	3.89 h	0.9 ± 0.2	1.3	68%	90%
^{44}Ca	2.086	**^{44g}Sc**	**3.93 h**	**31.5 ± 4.0**	**45.4**	**70%**	**84%**
		^{44m}Sc	58.6 h	0.18 ± 0.02	0.24	76%	88%
^{46}Ca	0.004	^{46}Sc	83.8 h	*unobserved*			
^{48}Ca	0.187	^{48}Sc	43.7 h	0.25 ± 0.04	-	-	75%
		^{47}Sc	80.4 h	0.010 ± 0.002	-	-	129%

[b] The ^{43}Sc produced from ^{44}Ca(p,2n) is not distinguished from ^{43}Ca(p,n), with an energy threshold of 14.5 MeV, in this study.

From our irradiation setting it is reasonable to expect about 0.79 ± 0.08 GBq of ^{44}Sc in the target. The percentage impurities at EoB and 9 hours after EoB are presented in Table 2.4.

Table 2.4 Radionuclidic purity of the separated scandium at EoB and 9 hours after EoB (n = 8)

Scandium isotope	**% of total activity at EoB**	**kBq ^{4x}Sc / MBq ^{44}Sc at EoB**	**% of total activity 1 h after EoB**	**% of total activity 9 h after EoB**
^{44g}Sc	**95.7 ± 0.3**	-	**95.4**	**90.6**[c]
^{44m}Sc	0.6 ± 0.1	6 ± 1	0.7	2.3
^{43}Sc	2.6 ± 0.3	27 ± 3	2.6	2.3
^{47}Sc	0.40 ± 0.05	4.0 ± 0.5	0.4	1.7
^{48}Sc	0.8 ± 0.1	8 ± 1	0.9	3.0

[c] Bateman's equilibrium equation between ^{44m}Sc and ^{44}Sc was included in the computation of this value.

Figure 2.5 shows the gamma spectra and a decay logging from a sample of the separated stock of ^{44}Sc. The exponential fit to the logged activity reading from the dose calibrator indicates that the half-life of the separated product is 4.27 ± 0.12 h, or 7.6 ± 2.9% greater than the accepted value for ^{44}Sc: 3.97 h [45]. This discrepancy is due to the presence of impurities with longer half-lives: ^{44m}Sc, ^{48}Sc and ^{47}Sc.

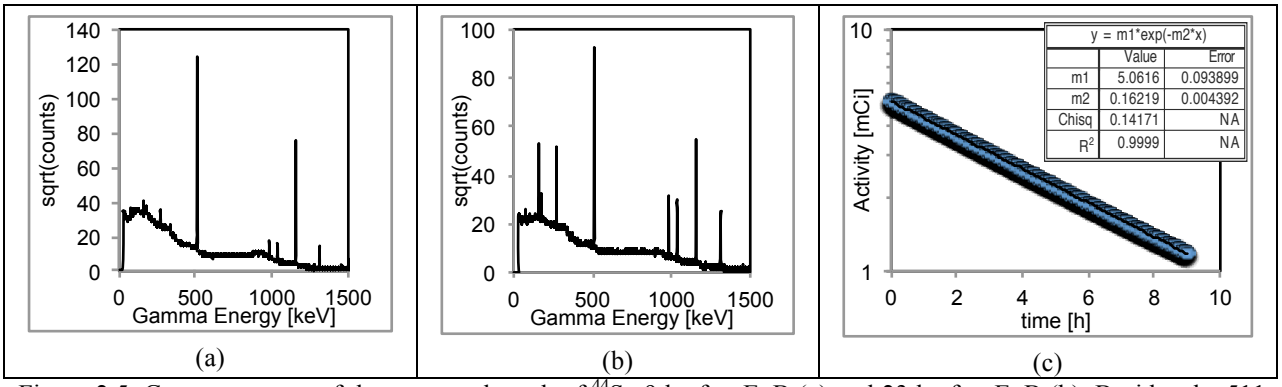

Figure 2.5. Gamma spectra of the separated stock of ^{44}Sc 9 h after EoB (a) and 23 h after EoB (b). Besides the 511 keV gamma from positron annihilation, the most prominent gamma peak in (a) at 1157 keV corresponds to ^{44}Sc. The impurities become more visible in (b) with the gamma peaks at 159 and 271 keV that correspond to ^{47}Sc and ^{44m}Sc, respectively; and the ones at 984, 1038 and 1312 keV from ^{48}Sc. (c) shows the data from logging the activity of a sample from the separated stock every 10 seconds for 9 hours and an exponential fit to the data which indicates that the half-life of the radioactivity in the sample is 4.27 ± 0.12 h, or 7.6 ± 2.9% greater than the value from accepted nuclear data: 3.97 h.

The radioactivity of the product is > 95% ^{44}Sc at EoB and the radionuclidic purity will remain above 90% up to 9 hours after EoB. This level of purity is tolerable for preclinical PET studies and perhaps even human studies if dosimetry estimations with a particular ^{44}Sc-labeled radiopharmaceutical demonstrate tolerable doses from the longer lived impurities ^{44m}Sc, ^{47}Sc and ^{48}Sc. If this is the case, we believe that ^{44}Sc from irradiated natural calcium targets is suitable for clinical applications. Natural calcium targets are in metallic form with a thermal conductivity of 200 W/m-K, which is comparable to aluminum, 235 W/m-K. Calcium is inexpensive and readily available so thick targets for higher yields are economically feasible and target recycling is unnecessary. However, if a higher radionuclidic purity is needed (> 99%, with the co-produced ^{44m}Sc representing the remaining 1%), then isotopically enriched ^{44}Ca targets are mandatory. To our knowledge, five groups have reported the use of these targets [23, 27, 58-60], all of them employing encapsulated enriched calcium carbonate, $^{44}CaCO_3$.

2.3.3 *Radiochemical separation*

The activity measured with the Capintec dose calibrator set at the calibration number 938 suggested by the manufacturer for ^{44}Sc was < 10% higher than the ^{44}Sc activity measured with the HPGe detector. Thus, this reading was used for the determination of separation yields. Loading the target at a H^+ concentration of ~10.5 M, 80 ± 4% (n = 7) of the original activity (decay corrected) was recovered in 400 µL of deionized water. The ^{44}Sc from this separation setting offered the highest separation yield with a high reactivity with DOTA, as will be shown in section 2.3.5, and is highlighted in bold in Table 2.5. Table 2.5 contains these and other results, together with the parameters involved in the separation. All activities are decay corrected to EoB.

Table 2.5 Results from separation experiments

	n	Calcium mass [mg]	mL of conc. HCl added for dissolution	Molarity of dissolution[c] [mol/L]	UTEVA mass [mg]	% of activity trapped in UTEVA	% of total activity eluted in 1st fraction (400 µL)	% of total activity eluted in 2nd fraction (200 µL)
a)	1	295.7	5	~ 9.1	24.5	52	43	2.5
b)	3	313 ± 14	5 - 5.5	~ 9.1	52 ± 1	83 ± 5	68 ± 4	4.7 ± 1.6
c)	7	317 ± 22	10	**~ 10.5**	52 ± 3	89 ± 3	**80 ± 4**	5.1 ± 1.3
d)	6	304 ± 8	15	~ 11.1	52 ± 1	92 ± 2	82 ± 2	5.6 ± 2.7

[c] The molarity is estimated by subtracting the amount of moles of hydrogen released as H_2 gas from the amount of moles of H^+ ions in solution, and then diving this by the total volume of the dissolution. The amount of H_2 that is released is estimated from the reaction equation $Ca + 2HCl \rightarrow CaCl_2 + H_2$

As it was pointed out in Section 2.2.3, ~50 mg of resin was selected for the optimization experiments since we observed a significant drop in the trapping efficiency, from 83% to 52%, when we reduced the amount of resin by half (~25 mg, Table 2.5, row a) when loading the target solution in a HCl concentration of ~9.1 M. Combining the results in Tables 2.5 and 2.7 we can see that there is a trade off between the separation efficiency and the reactivity of the radioactive scandium. Loading the target solution onto the resin at a concentration of 10.5 M HCl results in the optimum with both high separation yield and reactivity. The final product from this separation method was further characterized by analyzing it with MP-AES for trace metal contaminants and by titration with the acyclic ligand DTPA.

The results from the MP-AES analysis indicated that that the most significant metal impurities in decreasing order of concentration are: calcium (2.1 mM), iron (93 µM), zinc (72 µM), nickel (29 µM), aluminum (6.4 µM) and manganese (2.0 µM). These results are summarized in Table 2.6. The concentrations highlighted in bold correspond to the 400 µL fraction of ^{44}Sc employed in the radiolabeling experiments.

Table 2.6 Results from MP-AES analysis on the samples described in Table 2.2.

	Sample	i)	ii)	iii)	iv)	v)
Ca	[ppm]	33707	*overrange*	1242 ± 7	63.2 ± 0.2	50.8 ± 0.5
	[mM]	841	*overrange*	31.0 ± 0.2	**1.58 ± 0.01**	1.27 ± 0.01
	Mass in total volume [mg]	310.1	*overrange*	6.209 ± 0.035	0.0253 ± 0.0001	0.0102 ± 0.0001
	Separation factor				1.2×10^4	
Zn	[ppm]	7.5 ± 1.6	23.9 ± 4.2[d]	19.6 ± 6.5	6.5 ± 0.4	9.0 ± 1.1
	[µM]	115 ± 25	365 ± 64	299 ± 99	**100 ± 6**	137 ± 17
	Mass in total volume [µg]	69.2 ± 15.0	219 ± 38.5	97.8 ± 32.4	2.6 ± 0.2	1.8 ± 0.2
	Separation factor				27	
Fe	[ppm]	4.8 ± 1.4	< 1	< 1	3.1 ± 0.1	< 0.3
	[µM]	86 ± 24	< 18	< 18	**55 ± 2**	< 5
	Mass in total volume [µg]	44.4 ± 12.5	< 5	< 5	1.2 ± 0.1	< 0.05
	Separation factor				36	
Ni	[ppm]	3.0 ± 0.8	4.2 ± 1.5[d]	1.9 ± 1.2	0.7 ± 0.1	1.5 ± 0.2
	[µM]	52 ± 13	72 ± 26	32 ± 20	**12 ± 1**	26 ± 3
	Mass in total volume [µg]	27.9 ± 7.1	39.1 ± 14.2	9.3 ± 6.0	0.28 ± 0.02	0.31 ± 0.04
	Separation factor				98	
Al	[ppb]	< 500	< 500	689 ± 494	195 ± 5	592 ± 105
	[µM]	< 19	< 37	26 ± 18	**7.2 ± 0.2**	22 ± 4
	Mass in total volume [µg]	< 5	< 10	3.4 ± 2.5	0.08 ± 0.01	0.12 ± 0.02
	Separation factor				59	
Mn	[ppm]	1.2 ± 0.1	2.1 ± 0.1[d]	1.7 ± 0.2	0.21 ± 0.02	0.47 ± 0.04
	[µM]	22 ± 1	38 ± 2	32 ± 3	**3.8 ± 0.3**	8 ± 1
	Mass in total volume [µg]	11.1 ± 0.5	19.1 ± 1.0	8.7 ± 0.9	0.08 ± 0.01	0.09 ± 0.01
	Separation factor				1.3×10^2	

[d] The increase in Zn, Ni and Mn content in the eluate after loading the Sc may come from the UTEVA resin or the tubing in the separation module.

The stability constants (log K_{ML}) between metals and ligands, such as DOTA and DTPA, provide a convenient gauge of the ligand's relative affinity for a specific metal [61]. The main contaminants in the final product are calcium, iron, zinc and nickel, the three latter ones being important competitors for DOTA chelation based on the magnitude of their thermodynamic stability constants when bound to this chelator: 29.4, 20.8 and 20.0, respectively [62, 63], which are comparable to that of Sc(III), 22.5 [64]. The main impurity calcium, on the other hand, is not a strong competitor for DOTA chelation, since its log K_{ML} value is 17.2 [62]. A typical production run of 25 µA-h generates 637 MBq of ^{44}Sc in 400 µL, which corresponds to an activity concentration of 1593 GBq/L. Dividing this by the sum of the concentrations, in µmol/L, of the main metallic impurities that behave chemically similar to Sc^{3+} ions in aqueous solution (Zn^{2+}, Fe^{2+}, Fe^{3+}, Ni^{2+}, Al^{3+} and Mn^{2+}) results in an effective specific activity of 8.2 GBq/µmol, which as we will see in section 2.3.5, has the same order of magnitude of the reactivity between scandium and DOTA, 18.1 ± 6.7 GBq/µmol.

2.3.4 *Determination of K_d values of Sc^{3+} in UTEVA and HCl solution at various concentrations*

Figure 2.6 shows the distribution coefficients expressed as the logarithm of K_d between resin and acid for scandium and calcium in HCl concentrations ranging from 0 to 12.1 mol/L. Clearly, this plot confirms the

hypothesis that the UTEVA resin and TBP have similar extraction properties with respect to calcium and scandium in hydrochloric acid medium.

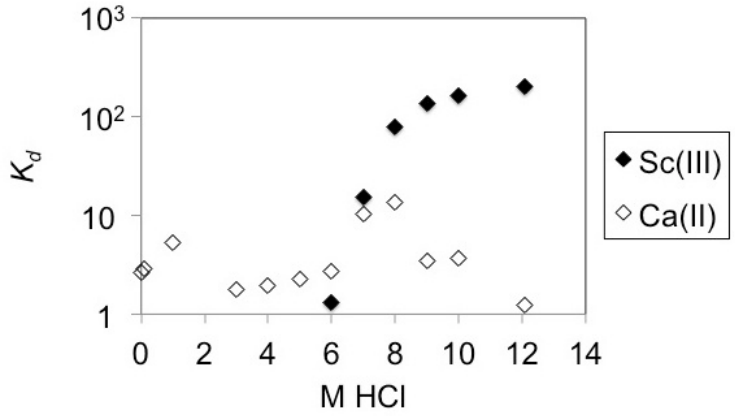

Figure 2.6 Distribution coefficients of Sc^{3+} and Ca^{2+} in UTEVA resin at different HCl concentrations.

Furthermore, the separation was possible in a "trap-and-release" fashion employing 50 mg of UTEVA packed in a 5 mm diameter column with the solution flowing at 1.1 mL/min thanks to the > 10-fold difference in the distribution coefficients between calcium and scandium at a HCl concentration > 9 M.

2.3.5 *Reactivity with DOTA and DTPA*

Thin layer chromatography of the DOTA and DTPA titrations showed retention factors of 0.4 and 0.7, respectively, consistent with the production of the Sc complex since these peaks were not present in the control vial with no chelator. These peaks increased in activity concentration as a greater mass of chelating ligand was added to the reaction vial. Plotting the percentage of chelated ^{44}Sc against mass of chelator, a sigmoid curve is obtained from which the reactivity or effective specific activity is calculated by dividing the activity in each vial over the amount of mass with which 50% of the radioactive scandium is chelated, and then multiplying this value times two. Figure 2.7 shows the autoradiography of typical plates used for TLC and how the distribution of activity is plotted against mass of chelator.

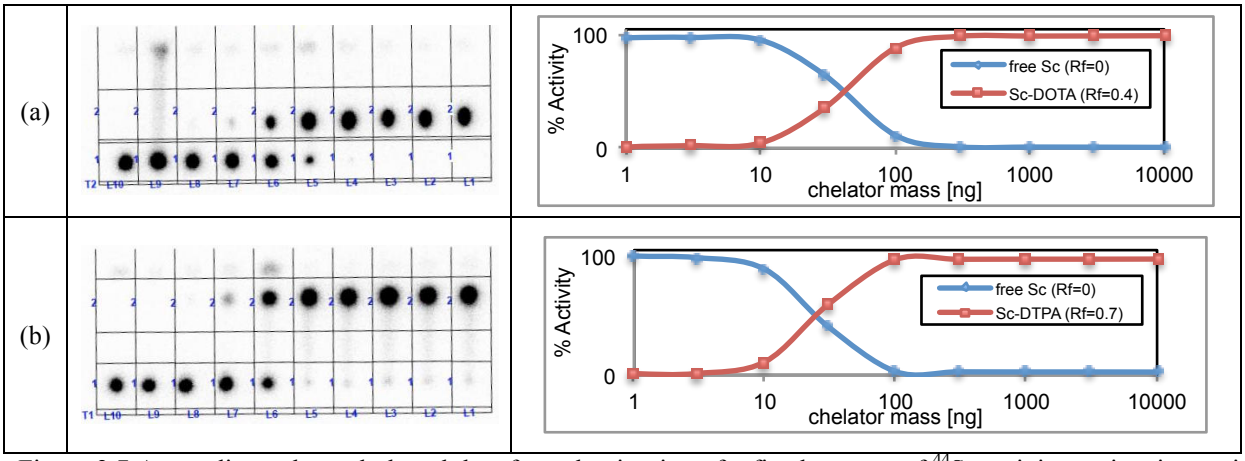

Figure 2.7 Autoradiography and plotted data from the titration of a fixed amount of ^{44}Sc activity against increasing amounts of DOTA (a) and DTPA (b).

When the solution is loaded onto the UTEVA column at a concentration of ~10.5 M, the reactivity was 18.1 ± 6.7 GBq/µmol, which was enough for radiolabeling with > 90% yield the DOTA conjugated cyclic arginine-glycine-aspartate (RGD) dimer E[c(RGDyK)]$_2$ as well as the DTPA derivative cyclohexyl-diethylene-triamine-pentaacetic acid ligand (CHX-A"-DTPA) conjugated to a Cetuximab antibody fragment, at the nmol or µg scale per 37 MBq of activity [22, 24]. The rest of the results are presented in Table 2.7.

Table 2.7 Results of the reactivity experiments from the separation runs explained in Table 2.5.

	Reactivity of 1st fraction with DOTA [GBq/µmol]	**Reactivity of 1st fraction with DTPA [GBq/µmol]**
a)	15.2	-
b)	18.5 ± 3.5	-
c)	**18.1 ± 6.7**	**55 ± 42**
d)	3.8 ± 0.7	-

The Sc-DOTA reactivity is about 3 and 5 times less than that reported in [28, 65], 54 and 100 GBq/µmol, respectively. Nevertheless, it has the same order of magnitude as the one inferred from the pioneer work in [30], 7.0 GBq/µmol, in which the peptide DOTATOC was successfully labeled to ^{44}Sc from a ^{44}Ti generator with > 98% yield.

The Sc-DTPA reactivity is more than two times higher than with DOTA, which renders this ligand or its derivatives as potential labels of targeted agents, such as the FDA-approved ^{90}Y-Ibritumomab tiuxetan, tiuxetan being the DTPA derivative 1B4M-DTPA [66]. We believe that an explanation for the greater reactivity of our separated ^{44}Sc towards DTPA compared to DOTA is due to the much lower thermodynamic stability constant of Ca-DTPA compared to Ca-DOTA, 10.7 and 17.2, respectively. Hence, the remaining bulk calcium in our isolated product, with ~2.1 mM concentration, offers less competition for DTPA occupation by the ^{44}Sc isotopes.

Huclier-Markai, et al. [64] measured the *in vitro* stability of Sc^{3+} complexes with DOTA, DTPA, NOTA, TETA and EDTA in the presence of hydroxyapatite and rat serum and discovered that the most stable one was Sc-DOTA, followed by Sc-DTPA. However, the same kind of stability has not been determined for scandium complexed with modified versions of DTPA. For instance CHX-A"-DTPA was proven to have a greater *in vivo* stability than DTPA when labeled with ^{90}Y [66].

2.3.6 *Image quality*

The image quality of ^{44}Sc was assessed by visual inspection of the reconstructed microPET images from a Derenzo phantom. As seen in Figure 2.8(a), clear resolution was observed down to a rod diameter of 1.5 mm. Figure 2.8(b) shows the gray intensity profile from a 2.10 mm (10 pixels) wide region of interest that covers the bottom row of 1.5 mm diameter rods on the image. Each peak was fitted with a gaussian curve revealing a full width at half maximum (FWHM) of 4.7 ± 1.3 mm. The average peak to valley ratio in this profile was 1.14 ± 0.11. These measurements will be compared to those from Derenzo phantoms filled with the other radionuclides that will be covered in this dissertation in Appendix A.

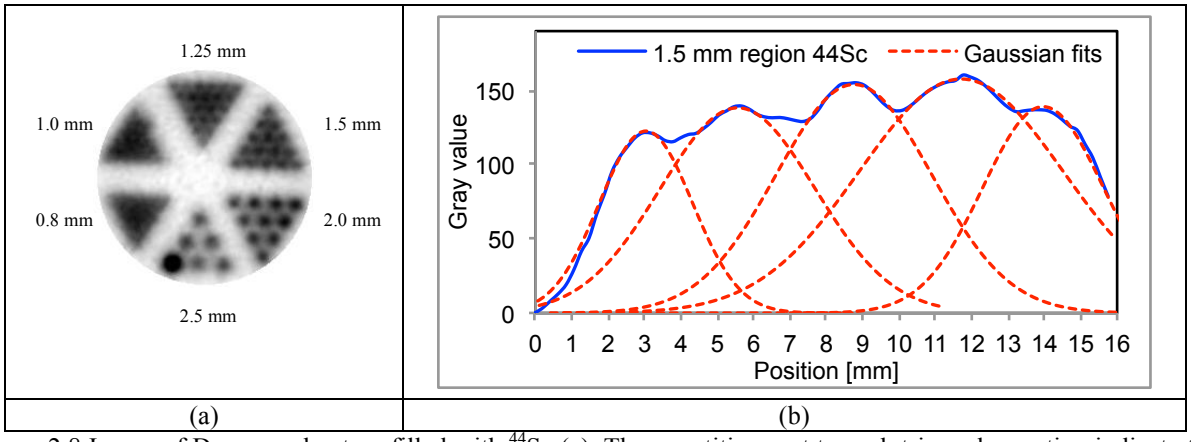

Figure 2.8 Image of Derenzo phantom filled with ^{44}Sc (a). The quantities next to each triangular section indicate the diameter of each of the rods, which are separated from center to center by twice the diameter distance. As the figure shows, rods up to 1.5 mm can be easily resolved in PET images of ^{44}Sc. Profile distribution of ^{44}Sc from the 1.5-mm rods (b).

The relatively low spatial resolution is the result of the high maximum energy of 1474 keV of the main positron emitted by ^{44}Sc [45], which has a mean and maximum range in water of 2.46 and 7.36 mm, respectively [67].

2.3.7 *Biodistribution and pharmacokinetics of ^{44}Sc-citrate and $^{44}ScCl_3$ in PBS in tumor-bearing mice*

PET scans were performed at 0.5, 4 and 8 hours post-injection (p.i.) of ^{44}Sc-citrate and $^{44}ScCl_3$ in PBS in groups of three 4T1 tumor-bearing mice. The U87MG tumor-bearing group was scanned at 0.5, 2, 4, 8 and 20 h p.i Figure 2.9 shows the coronal and sagittal maximum intensity projection (MIP) images of one of the mouse from each

group. In both tumor models, circulation of ^{44}Sc-citrate in the blood is prominent within the first 30 minutes after injection as seen by the high intensity in signal in the heart, abdominal aorta and carotid arteries. Tumor uptake becomes evident at 4 h p.i.. Quantification of the VOIs covering the whole urinary bladder of each of the 4T1 tumor-bearing mouse reveals that 7.6 ± 0.8 %ID (obtained from 22.6 ± 1.1 %ID/g × 0.336 ± 0.043 cm^3) is about to be excreted within the first 30 min after injection. In stark contrast to ^{44}Sc-citrate, $^{44}ScCl_3$ in PBS shows no systemic circulation at all, with 100% of the activity accumulating in the liver without any indication of excretion over time.

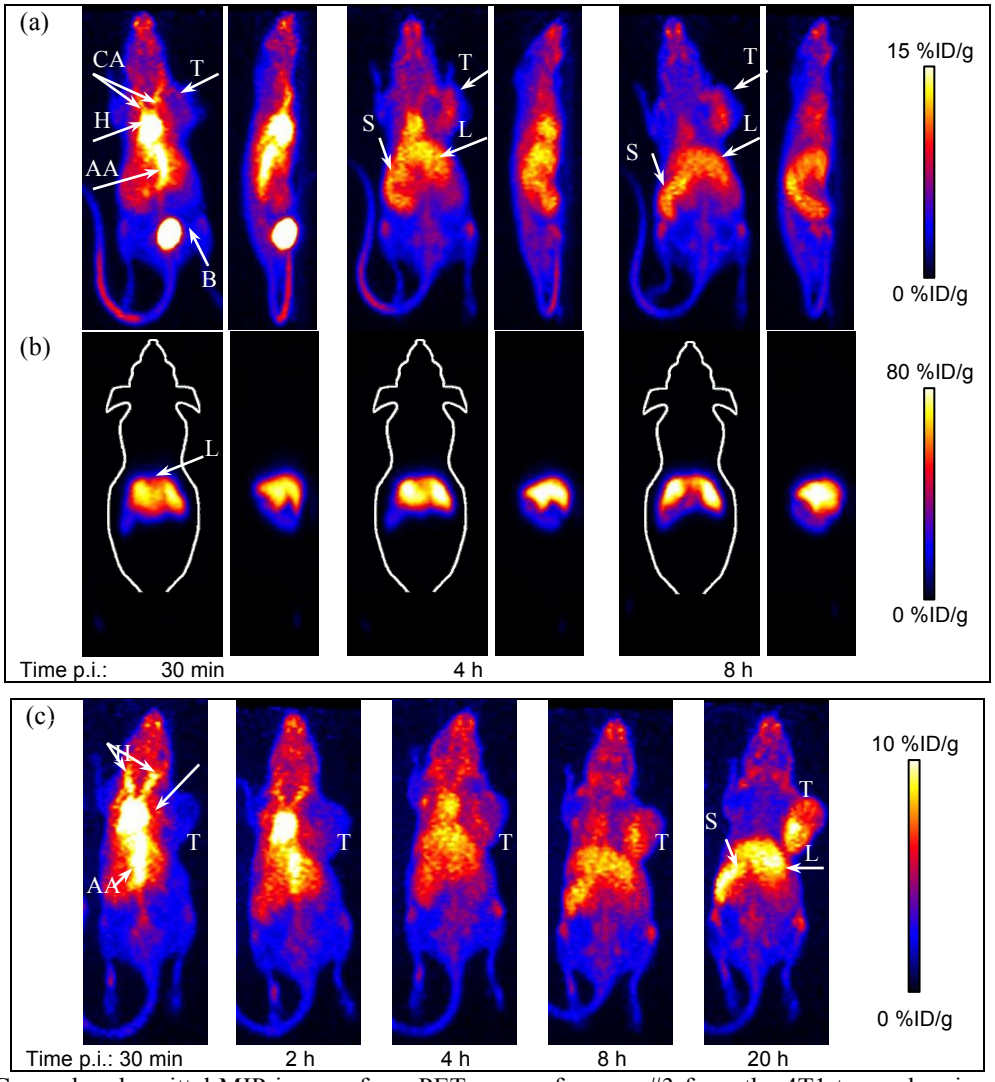

Figure 2.9 Coronal and sagittal MIP images from PET scans of mouse #3 from the 4T1 tumor-bearing group at 30 min, 4 h and 8 h injected with ^{44}Sc-citrate (a) or with ^{44}Sc-PBS (b). MIP images of mouse #2 from the U87MG tumor-bearing group at 30 min, 2, 4, 8 and 20 h p.i of ^{44}Sc-citrate. The ^{44}Sc uptake level is color coded by the %ID/g bar shown on the right of each set of images. The PET scans for the other two mice in each group show the same trend in biodistribution of each ^{44}Sc-labeled agent. CA: carotid arteries; H: heart; AA: abdominal aorta; T: tumor; B: bladder; S: spleen; L: liver.

Figure 2.10 shows the biodistribution over time and the time-activity curves in terms of %ID/g and %ID, respectively, from quantifications of VOIs covering the whole body, tumor, adductor and biceps femoris muscles and the delineable organs: heart, liver and spleen. The %ID plot also shows exponential fits to the whole body and heart uptake from which biological and circulation half-lives were quantified as 33.0 h and 6.4 h, respectively, in the 4T1 tumor-bearing mice; and 238 h and 16.6 h, respectively in U87MG tumor-bearing mice. From the biodistribution chart it can be seen that the tumor contrast in terms of tumor-to-muscle ratio is always > 1 and that it increases over time up to a value of 2.9 ± 0.3 at 8 h p.i. However, the tumor-to-liver contrast is < 1 throughout the study, which means that ^{44}Sc-citrate is not a good tracer for liver metastasis.

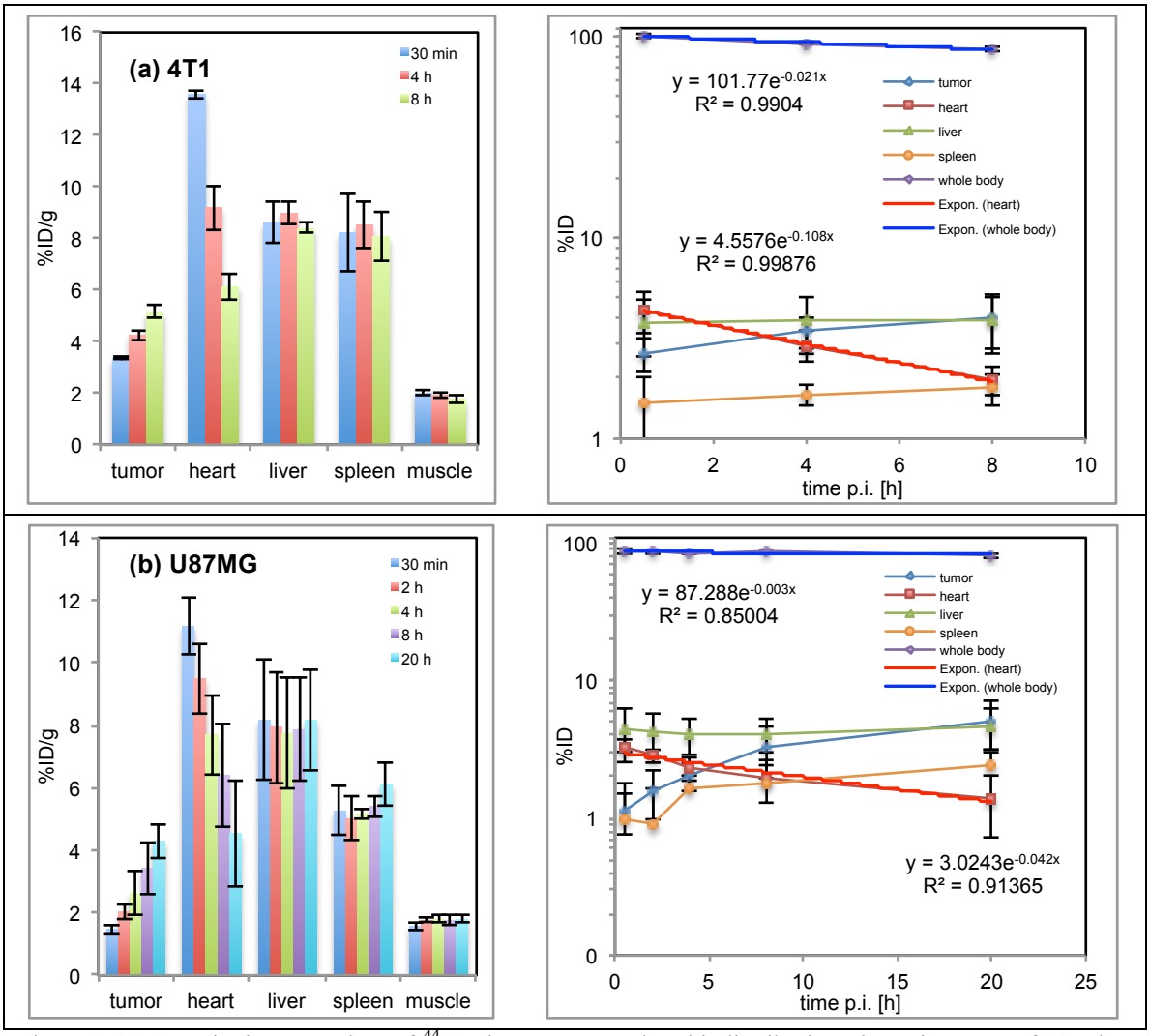

Figure 2.10 Quantitative PET data of ^{44}Sc-citrate presented as biodistribution charts in terms of %ID/g and time-activity curves in terms of %ID in mice bearing 4T1 tumors (a) and U87MG tumors (b). All data is decay-corrected to time of injection. Error bars represent standard deviation from quantifications in three mice.

The reason the administered ^{44}Sc-citrate has a relatively long circulation half-life of ≥ 6.4 h in both tumor model mice has to do with the fact that Sc^{3+} is trans-chelated to serum transferrin *in vivo* as it was shown by Ford-Hutchinson and Perkins [31]. In their work, they demonstrate that 25%, 75% and 95% of administered scandium citrate is bound to transferrin 10 min, 1 h and 24 h, respectively, after i.v. injection into rabbits. Perhaps the amount of ^{44}Sc that shows in the bladder of the 4T1 group and that is about to be excreted in the 30 min scan corresponds to the fraction of ^{44}Sc that did not label to transferrin. From quantification of the images, this bladder content accounts to 7.6 ± 0.8 %ID. Therefore, the actual tracer that we are looking at in the PET images is ^{44}Sc-transferrin. This same phenomenon of trans-chelation to transferrin of a weakly-bound radiometal has been observed after administration of ^{45}Ti-citrate into tumor-bearing mice by Vavere and Welch [7] and after injection of ^{67}Ga-citrate into rabbits by Vallabhajosula et al [1]. The implication of this is that ^{44}Sc-citrate turned into ^{44}Sc-transferrin *in vivo* serves as a tracer for malignancies such as cancer, inflammation and infection. Transferrin is an 80 kDa glycoprotein that serves for iron transport in blood into cells that express the transferrin receptor. When transferrin is loaded with two Fe^{3+} ions it binds strongly to its receptor, whereupon it is internalized by cells, the iron is released, and the protein is re-circulated [68]. In humans, about 30% of transferrin in circulation is saturated with iron [69] and therefore there is potential capacity for binding to other metal ions that are i.v. administered such the weakly-bound ^{44}Sc employed in our study. All cells in the body express the transferrin receptor but cancer cells have a very high level of expression since they require extra amounts of iron to grow [70, 71]. Proliferating cells require iron especially for ribonucleotide reductase production, which is essential for DNA synthesis and for Fe proteins such as hemoglobin [68]. Indeed, we observed increasing uptake of ^{44}Sc in the 4T1 tumors of 3.4 ± 0.1, 4.3 ± 0.2 and 5.1 ± 0.3 %ID/g at 0.5, 4 and 8 h p.i., respectively (Figure 2.10(a)); as well as in the U87MG tumors of 1.5 ± 0.2, 2.0 ± 0.2, 2.6 ± 0.7, 3.4 ± 0.9 and 4.3 ± 0.6 %ID/g at 0.5, 2, 4, 8 and 20 h p.i., respectively (Figure 2.10(b)). This same trend was observed in terms of %ID with uptakes in the 4T1 tumors of 2.7 ± 0.5, 3.4 ± 0.6 and 4.0 ± 1.2 %ID; and in the U87MG tumors of 1.1 ± 0.4, 1.6 ± 0.6, 2.0 ± 0.5, 3.3 ± 1.4 and 5.1 ± 1.9 %ID at the same time points.

A comparison of the biodistribution of ^{44}Sc-citrate to two ^{44}Sc-labeled targeted agents: ^{44}Sc-DOTA-$(cRGD)_2$ [22] and ^{44}Sc-DTPA-CHX-A"-Cetuximab(Fab) [24], all targeting the same tumor model U87MG, demonstrates the favorable pharmacokinetic properties of the former tracer. First, ^{44}Sc-citrate shows a gradually increasing uptake in the tumor even at the latest time point that was imaged at 20 h p.i., whereas ^{44}Sc-DOTA-$(cRGD)_2$ shows a gradually decreasing uptake in the tumor starting at 3.93 ± 1.19 %ID/g at 30 min p.i., dropping down to 3.00 ± 1.25 %ID/g at

4 h p.i [22]. In this regard, ^{44}Sc-DTPA-CHX-A"-Cetuximab(Fab) shows more favorable tumor targeting properties on a U87MG xenograft with 7.1 ± 0.6 and 12.7 ± 0.7 %ID/g at 0.5 and 4 h p.i., respectively [24], which is about a factor a five larger than those of ^{44}Sc-citrate at the same time points. In terms of normal organ uptake, ^{44}Sc-citrate shows almost negligible uptake in the kidneys, whereas the two targeted agents show prominent accumulation in this organ that reached a peak of 32.7 ± 2.8 %ID/g at 2 h p.i., which was maintained at 31.3 ±1.5 %ID/g at 4 h p.i. for ^{44}Sc-DTPA-CHX-A"-Cetuximab(Fab); and a peak of 3.53 ± 1.36 %ID/g at 30 min p.i. for ^{44}Sc-DOTA-(cRGD)$_2$. The uptake in the liver of ^{44}Sc-citrate was about five times higher than that of ^{44}Sc-DOTA-(cRGD)$_2$ but significantly lower than that of ^{44}Sc-DTPA-CHX-A"-Cetuximab(Fab), which showed %ID/g of 15.9 ± 1.4 and 13.8 ± 1.6 at 30 min and 4 h p.i., respectively.

Another implication of the observed tumor targeting is that scandium citrate can be employed as a cancer therapeutic if the radioactive scandium is substituted by the beta emitter ^{47}Sc ($t_{1/2}$ = 3.35 d, 68.4% β_1, $E_{\beta 1\ max}$ = 441 keV; 31.6% β_2, $E_{\beta 2\ max}$ = 600 keV; 68.3% γ, E_γ = 159 keV) [40]. In the following two sections on internal dosimetry the therapeutic potential of ^{47}Sc-citrate will be evaluated.

2.3.8 *Internal dosimetry of ^{44}Sc-citrate and the therapeutic analog ^{47}Sc-citrate in humans*

Only the biodistribution data from U87MG tumor-bearing mice was employed for the estimation of human dosimetry, since more time points post-injection in this tumor model were analyzed. Table 2.8 shows the %ID uptake values of ^{44}Sc-citrate extrapolated to a 73.7 kg standard adult male as defined by Cristy and Eckerman [49], using the mass extrapolation method by Kirschner [52], with the whole body mass per mouse set to the average value of 23 g in this study.

Table 2.8 Extrapolation to %ID uptake of ^{44}Sc-citrate in standard adult male organs from studies in mice.

Organ	Organ mass in human male adult [g] [49]	Conversion factor %ID/g in mouse to %ID in human	%ID				
			0.5 h	2 h	4 h	8 h	20 h
Heart contents	840	0.265	3.0	2.5	2.0	1.7	1.2
Liver	1910	0.596	4.9	4.7	4.6	4.7	4.9
Spleen	183	0.057	0.3	0.3	0.3	0.3	0.4
Remaining organs	Balance	Balance	79.8	78.7	78.3	79.5	75.8

After setting these %ID uptake values in the EXM portion of the OLINDA software and fitting them to mono-exponential functions, the software automatically calculated the cumulative number of decays in each source organ and then the absorbed dose in every target organ considered by the software as well as the total body effective dose. The effective dose was estimated as 52.4 μSv/MBq of ^{44}Sc-citrate injected. However, these estimates only take into account the dose from ^{44}Sc as if it was 100% radionuclidically pure, which is not the case for the cyclotron-produced

^{44}Sc employed in this work. After substituting ^{44}Sc by other scandium radionuclides, maintaining the original biodistribution, the effective dose from impurities was estimated as 29.6, 54.4, 125 and 549 µSv/MBq for ^{43}Sc, ^{44m}Sc, ^{47}Sc and ^{48}Sc, respectively. However, these quantities have to be multiplied by the percentage of impurity per unit of administered activity of ^{44}Sc. For instance, in a worst-case scenario, if the tracer is injected 9 hours after EoB, the effective dose contribution from each impurity would have to be multiplied by the percentage impurity shown in the last column in Table 2.4. In this case the actual effective dose contribution from each impurity per MBq of ^{44}Sc would be 0.7, 1.3, 2.1, and 16.5 µSv, for ^{43}Sc, ^{44m}Sc, ^{47}Sc and ^{48}Sc, respectively. Therefore the total effective dose from cyclotron-produced ^{44}Sc-citrate injected 9 hours after EoB is 72.9 µSv/MBq ^{44}Sc. The same kind of correction was applied for the absorbed dose per target organ and the results are shown in Figure 2.11(a) for 100% ^{44}Sc-citrate and cyclotron-produced ^{44}Sc-citrate administered 1 and 9 hours after EoB. Figure 2.11(b) shows the contribution to the absorbed dose to each target organ of ^{44}Sc and each scandium impurity if the tracer is injected 9 hours after EoB. Table 2.9 summarizes the contribution to the total effective dose from the measured amount of radioactive impurities present in the cyclotron-produced ^{44}Sc obtained from this work.

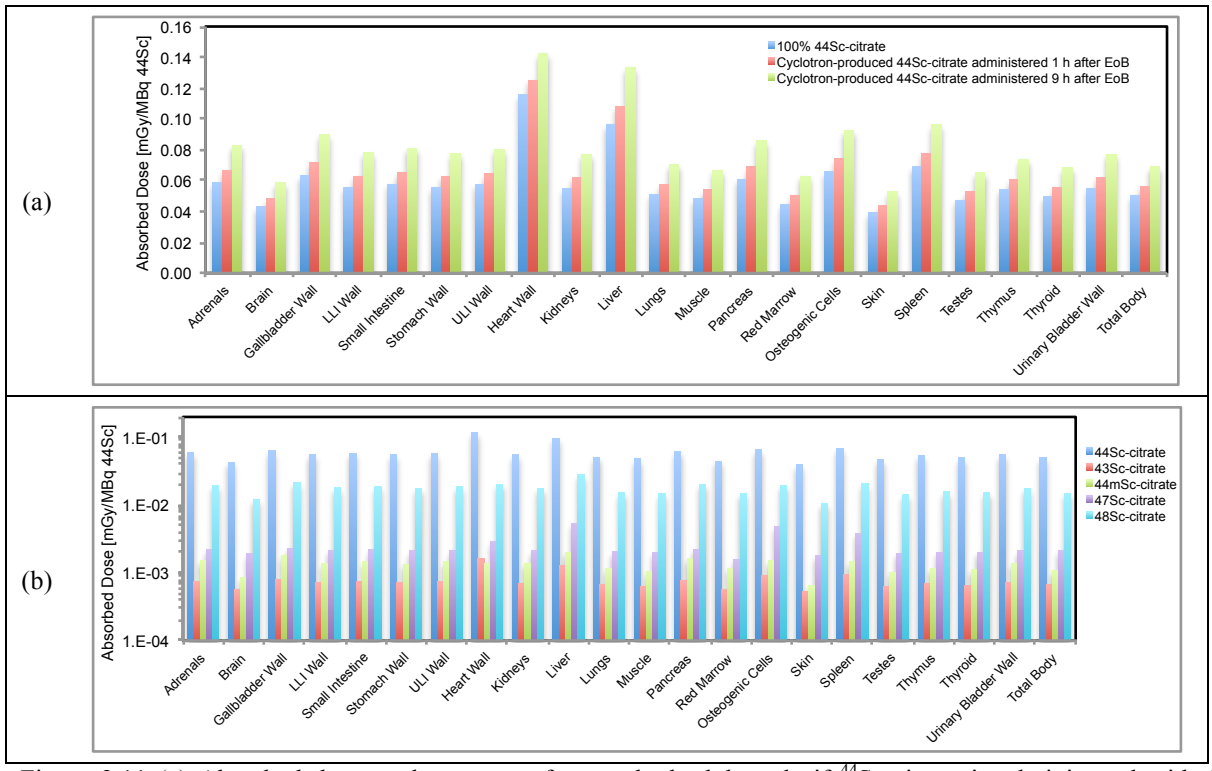

Figure 2.11 (a) Absorbed dose to the organs of a standard adult male if ^{44}Sc-citrate is administered with 100% radionuclidic purity or if it is cyclotron-produced from ^{nat}Ca as described in previous sections and administered 1 h and 9 h after EoB. (b) Absorbed dose contribution from each radioactive scandium impurity if the cyclotron-produced ^{44}Sc-citrate is administered 9 h after EoB.

Table 2.9 Effective dose from each impurity in cyclotron-produced ^{44}Sc-citrate

	Effective dose contribution [μSv/MBq ^{44}Sc]			
Nuclide	1 h after EoB (%)		9 h after EoB (%)	
^{44}Sc	52.4	(88.8%)	52.4	(71.9%)
^{44m}Sc	0.4	(0.6%)	1.3	(1.7%)
^{43}Sc	0.8	(1.3%)	0.7	(0.9%)
^{47}Sc	0.5	(0.8%)	2.1	(2.9%)
^{48}Sc	4.9	(8.4%)	16.5	(22.6%)

The critical tissues are the heart wall, liver and spleen with absorbed doses of 0.14, 0.13 and 0.10 mGy/MBq of ^{44}Sc-citrate, respectively, administered 9 hours after EoB. Sc-48 will be the main concern for clinical translation of cyclotron-produced ^{44}Sc from natural calcium targets. It causes the largest contribution to the effective dose due to its relatively long physical half-life of 43.7 h and due to the emission of three prominent and penetrating gammas with energies of 983, 1037 and 1312 keV and intensities of 100, 98 and 100%, respectively [72], which will inevitably deposit energy throughout every organ of the injected subject as seen in Figure 2.11(b). However, since it only represents 3.0% of the administered ^{44}Sc activity (if injected nine hours after EoB), as seen in Table 2.4, its contribution to the total effective dose is only 22.6% of the total. This is very impressive, considering that ^{46}Sc-citrate remained accumulated in the liver and spleen with negligible biological clearance throughout our study as seen in Figures 9 and 10, and hence it irradiated the whole body from these two source organs until it completely disappeared by nuclear decay with a physical half-life of 43.7 h.

Based on the only clinical application of 100% pure ^{44}Sc from a ^{44}Ti generator reported in the literature [73, 74], mere 37 MBq of ^{44}Sc-DOTATOC were enough to visualize somatostatin-receptor-positive liver metastasis in patients even at a late PET scan 18 p.i. If such small amount of activity in the form of ^{44}Sc-citrate were to be administered into a patient, we can expect a very low effective dose of 2.7 mSv and an absorbed dose to the critical organs: heart wall, liver and spleen, of 5.3, 4.9 and 3.6 mGy, respectively, deposited by the >90% pure cyclotron-produced ^{44}Sc obtained in this work. Therefore, up to 357 MBq of this kind of ^{44}Sc-citrate could be administered into a male patient within a year, considering that the FDA regulations have set a maximum annual dose to any organ or ED of 50 mGy or mSv, respectively, for adult research subjects [75]. Similar internal dosimetry analysis would have to be performed to determine if > 90% pure cyclotron-produced ^{44}Sc is suitable for clinical applications as a label for tracers such as ^{44}Sc-DOTATOC.

As a comparison, the widely used tracers ^{68}Ga-DOTATATE and ^{68}Ga-HBED-CC-PSMA deposit effective doses of 25.7 μSv/MBq [76] and 15.8 μSv/MBq [77], respectively; and since a minimum of 150 MBq are typically injected into a patient, the total effective doses are >3.9 and >2.4 mSv, respectively, which are of the same order of

magnitude as the 2.7 mSv ED caused by 37 MBq of >90% pure cyclotron-produced ^{44}Sc-citrate. If imaging is to be performed up to several hours after injection, it is reasonable to administer much less activity of ^{44}Sc compared to ^{68}Ga due to their more than three-fold difference in half-lives.

The internal dosimetry estimation from ^{44}Sc-citrate justifies the clinical application of this economical supply of ^{44}Sc as an alternative to the expensive options that involve high investments and recycling efforts on expensive isotopically-enriched targets [23, 27, 58-60], extremely long irradiations in >25 MeV proton accelerator facilities to create the long lived ^{44}Ti generator via ^{45}Sc(p,2n) [25] or even expensive alpha cyclotrons to produce the positron emitter ^{43}Sc via ^{nat}Ca(α,n) [78, 79].

Since there is significant tumor uptake of ^{44}Sc-citrate in mice, we can explore the possibility of using the therapeutic analog ^{47}Sc-citrate for targeted radionuclide therapy, although the "targeted" adjective may not be strictly applicable since there is no targeting vector in this hypothetical agent. As it was mentioned in section 2.2.8, in the case of radionuclide therapy with ^{47}Sc-citrate, the effective dose concept is not appropriate for therapy cases in which deterministic effects from radiation are prevalent. Thus, a more appropriate dosimetric measure is the absorbed dose to each target organ, which we have computed for the case of a standard adult male by employing the ^{44}Sc-citrate pharmacokinetic data and replacing the scandium nuclide by ^{47}Sc. Figure 2.12 shows these results.

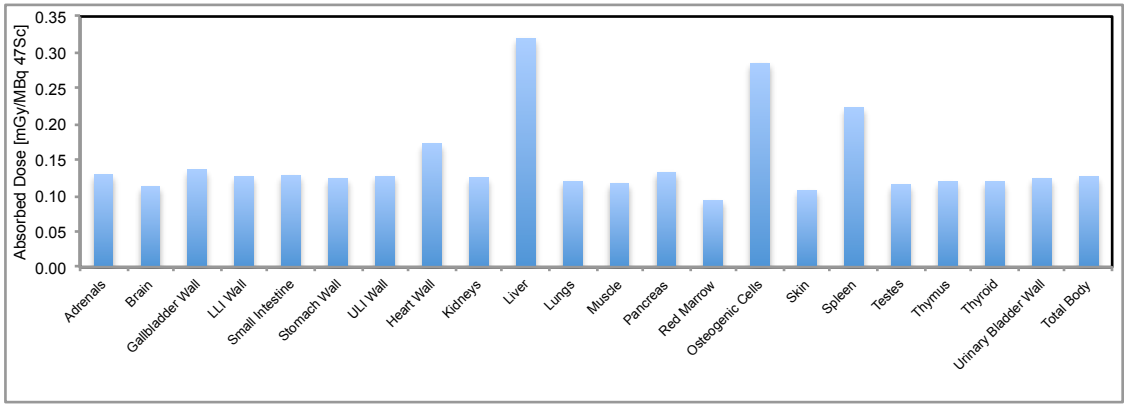

Figure 2.12 Absorbed dose to the organs of a standard adult male after administration of ^{47}Sc-citrate.

Clearly, the critical organ is the liver, which receives an absorbed dose of 0.32 mGy/MBq ^{47}Sc. Since the maximum amount of absorbed dose that can be tolerated by this organ is 40 Gy, this means that a maximum amount of 125 GBq of ^{47}Sc-citrate can be safely administered into a patient in order to stay below the toxicity level for this organ.

The necessary amount of ^{47}Sc-citrate that has to be administered in order to control a tumor in a patient depends on the tumor uptake and on the size of the tumor. Therefore, this kind of estimation is beyond the scope of this work. However, from the tumor uptake data in the mice employed in this work we can estimate the absorbed dose to the implanted tumors for both the diagnostic and therapeutic analog agents and then predict what is the necessary amount of ^{47}Sc-citrate that would result in tumor regression in our small animal models as a proof of principle of the therapeutic efficacy of ^{47}Sc-citrate.

2.3.9 *Tumor and normal organ dosimetry of ^{44}Sc-citrate and the therapeutic analog ^{47}Sc-citrate in mice*

The absorbed dose delivered to the 4T1 or U87MG tumors in mice by ^{44}Sc-citrate and by a hypothetical administration of therapeutic ^{47}Sc-citrate was estimated using the dose-to-sphere model of OLINDA, which only requires the total cumulative decays or disintegrations inside the tumor per administered activity in units of MBq-h/MBq. This value was obtained by trapezoidal integration of the non-decay-corrected time-activity curve of the tumor up to the last time point that was measured (8 and 20 hours p.i. for the 4T1 and U87MG xenografts, respectively) and then by integration from this time point up to infinity assuming: 1) that the uptake phase in the tumor is over, 2) that there is no biological clearance and 3) that there is only physical decay of the radiotracer. The formula for this latter integration is as follows:

$$\int_T^\infty \%ID_{\text{non-decay corrected}}(t=T)e^{-\frac{\ln(2)}{t_{1/2}}t}dt = \int_T^\infty \%ID(t=T)e^{-\frac{\ln(2)}{t_{1/2}}T}e^{-\frac{\ln(2)}{t_{1/2}}t}dt = \frac{\%ID(t=T)\cdot t_{1/2}}{\ln(2)}e^{\frac{-2\ln(2)}{t_{1/2}}\cdot T}$$

Equation 2.7

in which *T,* is the last time point of the PET scans. Thus, after substitution for the physical half-lives, the integrals for the 4T1 model are 0.35×%ID(t = 8 h) and 101.0×%ID(t = 8 h) for ^{44}Sc and ^{47}Sc, respectively; and for the U87MG model the integrals are 0.005×%ID(t = 20 h) and 82.1×%ID(t = 20 h) for ^{44}Sc and ^{47}Sc, respectively.

Figure 2.13(a) show the tumor uptake over time of ^{44}Sc-citrate obtained from VOI analysis of the PET images in units of %ID decay-corrected to the time of injection. Figures 2.13(b) and (c) show this same data after consideration of decay of ^{44}Sc and ^{47}Sc, respectively; including the continuation of the time-activity curve after the last measured time point, assuming that only physical decay occurs up to infinity.

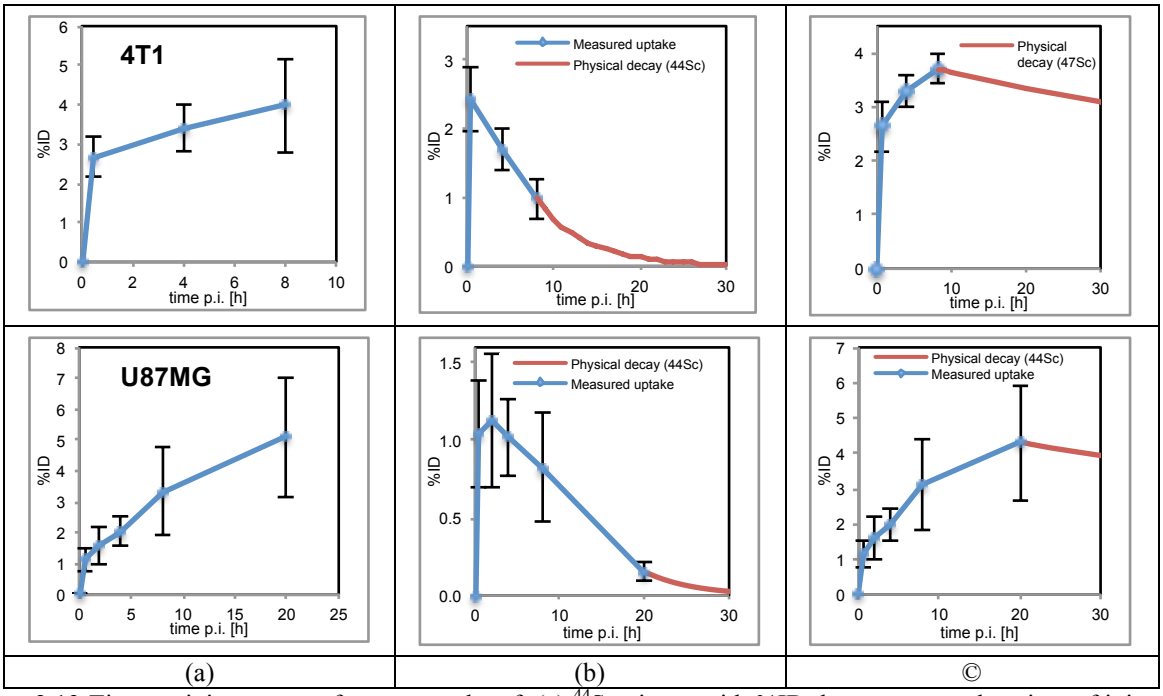

Figure 2.13 Time-activity curves of tumor uptake of: (a) ^{44}Sc-citrate with %ID decay-corrected to time of injection; (b) ^{44}Sc-citrate and (c) ^{47}Sc-citrate with %ID considering physical decay over time.

The total cumulative decays in the 4T1 tumors for each non-decay corrected curve are 0.15 and 4.27 Bq-h/Bq for ^{44}Sc and ^{47}Sc, respectively; and in the U87MG tumors 0.14 and 4.79 Bq-h/Bq for ^{44}Sc and ^{47}Sc, respectively. After logging in these two values in the dose-to-sphere model of OLINDA, the total absorbed dose to spheres of unit-density material with masses between 10 mg and 6 kg are calculated. Figure 2.14 shows the output from OLINDA along with a power fit to this data.

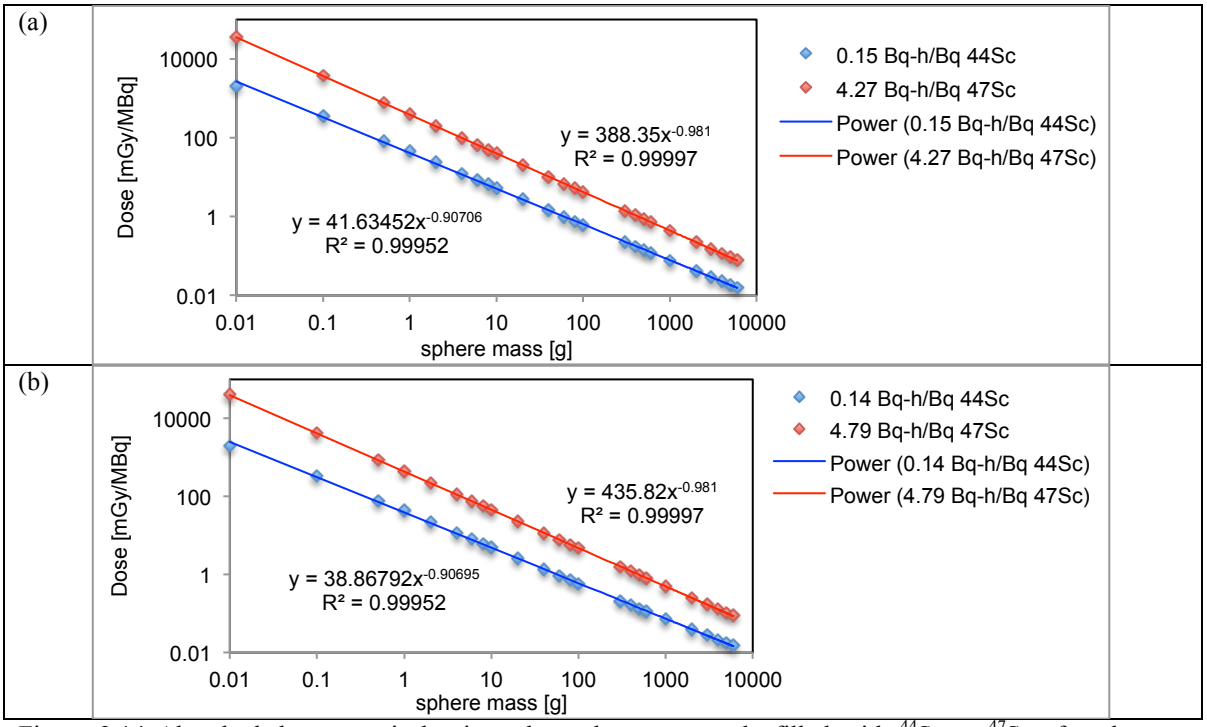

Figure 2.14 Absorbed dose to unit-density spheres homogeneously filled with ^{44}Sc or ^{47}Sc after the cumulative number of decays indicated in the legend, which were obtained from integration of the time-activity curves of the (a) 4T1 and (b) U87MG tumors in mice.

From the plot in Figure 2.14 we can estimate what is the necessary amount of ^{44}Sc- or ^{47}Sc-citrate that has to be administered in order to have a therapeutic effect in 4T1 or U87MG tumor-bearing mice like the ones employed in this study. The average volume of the VOIs drawn over the whole tumor (both 4T1 and U87MG) in all the PET images was 863 ± 266 mm^3, which corresponds to a mass of 0.86 ± 0.27 g, assuming that the tumors have a density of 1 g/cm^3. Therefore, we can assume that the treated tumor mass would be about 1 g and from the fitted curves in Figure 2.14 we can predict that each MBq of ^{44}Sc-citrate or ^{47}Sc-citrate that is administered into a mouse bearing 4T1 tumors would result in an absorbed dose to the tumor of 42 and 388 mGy, respectively; and each MBq of ^{44}Sc-citrate or ^{47}Sc-citrate that is administered into a mouse bearing U87MG tumors would result in an absorbed dose to the tumor of 39 and 436 mGy, respectively.

In order to estimate how much absorbed dose in the tumor is required for cancer regression we can explore what has been reported in peer-reviewed publications. A review article by Strigari et al from 2014 summarized the results from 48 publications that reported correlations between tumor absorbed dose and response after targeted radionuclide therapy (TRT) in large patient populations [80]. Table 2.10 shows these relationships.

Table 2.10 Published correlations between absorbed dose and therapeutic effect in patients.

Disease	No. of patients	Agent	Endpoint	Threshold dose	Ref.
Differentiated thyroid cancer	26	[^{131}I]NaI	Response	80 Gy	[81]
	23		Ablation	49 Gy	[82]
Neuroblastoma	27	^{131}I-mIBG	Partial response	70 Gy	[83]
Neuroendocrine tumors	13	^{90}Y-DOTA-octreotide	>20% shrinkage	230 Gy	[84]
Non-Hodgkin's lymphoma	20	^{131}I-tositumab	>50% shrinkage	2 Gy	[85]
	10		>80% shrinkage	4.5 Gy	[86]
Liver tumors	71	^{90}Y-microspheres (Ivalon)	>50% reduction	225 Gy	[87]
	36	^{90}Y-microspheres (glass)	Partial or complete response	205 Gy	[88]
	73	^{90}Y-microspheres (resin)	50% TCP	150 Gy	[89]
Bone pain palliation	6	^{153}Sm-EDTMP	Stable disease	21 Gy	[90]

mIBG: metaiodobenzylguanidine
TCP: Tumor Control Probability
EDTMP: ethylenediamine tetra(methylene phosphonic acid)

Alternatively, we can look at the relationship between tumor doses and tumor responses that has been observed in preclinical studies involving human colon cancer xenografts in small animals. Table 2.11 reproduces such review from an article by Connett et al [12].

Table 2.11 Published correlations between absorbed dose and therapeutic effect in colon cancer xenografts.

Tumor model	Radionuclide	mAb	Tumor size [g]	Mean tumor dose [Gy]	Tumor response	Ref.
GW39	^{64}Cu	1A3	0.2	5.86	82%	[12]
			0.6	3.30	GI	
	^{67}Cu		0.2	12.69	93%	
			0.6	7.06	GI	
	^{131}I	NP4	< 0.2	24.00	55%	[91]
			0.3 – 0.45	72.00	55%	[92]
	^{90}Y		0.3	16.03	GI	[93]
COLO 205	^{131}I	250-30.6	0.27	7.00	GI	[94]
T380	^{131}I	35,B7,B17	0.5	56.42	GI	[95]
LS174T	^{131}I	17-1A	0.52	9.53	GI	[96]
	^{90}Y		0.52	17.90	GI	
	^{90}Y	ZCE 025	< 0.5	34.00	GI	[97]

mAb: monoclonal Antibody
GI: Growth Inhibition

Therefore, under the conservative assumption that up to 230 Gy are required for tumor response, the amount of ^{44}Sc-citrate or ^{47}Sc-citrate that would have to be administered in order to have observable tumor regression in a mouse bearing a 1 g 4T1 tumor would be 5524 and 592 MBq, respectively; and in a mouse bearing 1 g U87MG tumor it would be 5917 and 528 MBq, respectively. Mouse models with tumors that are ≤ 100 mg (with a diameter < 0.6 cm, assuming that the tumor is spherical), like the ones found in early stages of cancer [98, 99], would require at least one order of magnitude less administered activity as seen in Figure 2.14, due to the exponential of the fitted curve that is approximately equal to one. However, this prediction depends upon the assumption that tumors smaller than the xenografts employed in this study will also display similar %ID uptake values.

In order to predict toxicities in normal organs of a mouse under such TRT treatment, the absorbed doses were estimated using the absorbed fraction (AF) data in a 27 g mouse obtained by Stabin et al. [56]. Table 2.12 shows the *S*-values for ^{47}Sc obtained after substitution of this data in Equation 2.5. S_γ and S_β are the *S*-values of the 159 keV gamma and the sum of the two β^- emissions with average energies of 143 and 204 keV, respectively.

Table 2.12 *S*-values of ^{47}Sc in a 27.0 g mouse. All values are in units of mGy/MBq-h.

		Source organs					
		Heart		**Liver**		**Spleen**	
		S_γ	S_β	S_γ	S_β	S_γ	S_β
Target organs	**Other tissues**	0.05	0.27	0.05	0.23	0.05	0.33
	Skeleton	0.09	0	0.07	0.04	0.08	0
	Lungs	0.43	1.57	0.26	1.95	0.32	0
	Heart	2.80	610.64	0.22	0.08	0.21	0
	Liver	0.20	0.09	0.82	112.74	0.57	6.49
	Kidneys	0.05	0	0.14	0.11	0.14	0
	Stomach	0.10	0	0.25	0.16	0.82	8.41
	Intestines	0.05	0	0.15	0.09	0.10	0
	Spleen	0.04	0	0.12	1.19	1.59	653.04
	Testes	0	0	0.04	0	0.03	0
	Bladder	0	0	0	0	0	0

For the 4T1 tumor-bearing mice, the cumulative decays per MBq in the heart, liver and spleen, obtained from the integration of the non-decay corrected time-activity curves, were 0.38, 4.49 and 1.89 MBq-h, respectively. For the U87MG tumor-bearing mice, the cumulative decays per MBq in these same organs were 0.53, 5.01 and 1.81 MBq-h, respectively. These cumulative decays per source organ can be obtained from the EXM portion of the OLINDA/EXM software after inputting the %ID values in each source organ or by "manual" integration using Equation 2.8:

$$\tilde{A} = \int_0^\infty \%ID(t=0)e^{-\lambda_e t}dt = \%ID(t=0)/\lambda_e \qquad \text{Equation 2.8}$$

where *%ID(t = 0)* is the fitted parameter that multiplies the exponential in the fitted functions to the decay-corrected time-activity curves; and λ_e is the effective decay constant in each source organ, which is equal to the sum of the biological and physical decay constants, λ_b and λ_p. The biological decay constant in each source organ is the fitted parameter in the exponent of the fitted functions to the time-activity curves and is related to the biological half-life ($t_{1/2,b}$) by the equation $\lambda_b = \ln(2)/t_{1/2,b}$. Likewise, the physical decay constant is related to the more familiar physical decay half-life by the equation $\lambda_p = \ln(2)/t_{1/2}$. After some algebra on Equation 2.8, the equation from which we can obtain the cumulative disintegrations that occur in each of the source organs is the following:

$$\tilde{A} = \frac{\%ID(t=0)}{\lambda_b} \cdot \frac{t_{1/2}}{\left(t_{1/2}+\frac{\ln(2)}{\lambda_b}\right)} \qquad \text{Equation 2.9}$$

The multiplication of the accumulated decays per source organ by the summation of the *S*-values results in the absorbed dose per target organ in units of mGy/MBq. The absorbed doses in the target organs of each of the two animal models are shown in Table 2.13.

Table 2.13 Absorbed doses from ^{47}Sc-citrate in a 27.0 g mouse. All values are in units of mGy/MBq.

		Absorbed doses in 4T1 mouse				**Absorbed doses in U87MG mouse**			
		Source organs			**Total dose**	**Source organs**			**Total dose**
		Heart	**Liver**	**Spleen**		**Heart**	**Liver**	**Spleen**	
Target organs	**Other tissues**	0.12	1.25	0.72	2.09	0.17	1.40	0.69	2.26
	Skeleton	0.03	0.49	0.16	0.68	0.05	0.54	0.15	0.74
	Lungs	0.76	9.92	0.61	11.29	1.06	11.07	0.58	12.71
	Heart	233.11	1.34	0.40	234.84	325.12	1.49	0.38	327.00
	Liver	0.11	509.89	13.33	523.33	0.15	568.94	12.77	581.86
	Kidneys	0.02	1.12	0.27	1.40	0.02	1.24	0.25	1.52
	Stomach	0.04	1.86	17.43	19.32	0.05	2.07	16.69	18.81
	Intestines	0.02	1.09	0.20	1.31	0.03	1.22	0.19	1.43
	Spleen	0.01	5.89	1237.25	1243.15	0.02	6.57	1184.88	1191.47
	Testes	0	0.17	0.06	0.23	0	0.20	0.05	0.25
	Bladder	0	0.00	0.00	0.00	0	0	0	0

Clearly, the critical organs are the source organs where most of the radioactivity is accumulated. Hence, a therapeutic administration of 592 MBq ^{47}Sc-citrate that would deposit 230 Gy on a 1 g 4T1 tumor xenograft will also imply an absorbed dose of 139, 310 and 736 Gy in the heart, liver and spleen, respectively, which would make this treatment toxic, due to their maximum tolerated doses of 50, 40 and 50 Gy, respectively [100, 101], assuming that these limits that were derived from human subjects also apply to rodents. Likewise, a therapeutic administration of 528 MBq of ^{47}Sc-citrate in a mouse bearing a 1-gram U87MG tumor will imply an absorbed dose of 124, 307 and 629 Gy in the heart, liver and spleen, respectively, which will also be toxic. However, if the tumor in the mouse has a mass of 100 mg, that is, one order of magnitude lower than the size in our study, then the therapeutic dose of ^{47}Sc-citrate needed would be 62 MBq and 55 MBq (also one order of magnitude lower than the dose needed to treat a 1 g tumor), for the 4T1 and U87MG animal models, respectively, according to the OLINDA results in Figure 2.14. In this case the absorbed doses to the critical organs would also be one order of magnitude lower and below the toxicity threshold, except for the spleen. Again, this prediction depends upon the assumption that tumors smaller than the ones employed in this study will maintain similar %ID uptake values.

2.3.10 *Availability of ^{47}Sc and future work*

Even though ^{47}Sc holds great promise as a therapeutic payload in targeted therapy, its availability for clinical applications does not seem feasible in the short term.

In the previous section we have demonstrated that between 50 and 600 MBq of ^{47}Sc-citrate are sufficient to deliver a therapeutic dose of ~230 Gy to a tumor with a mass between 0.1 and 1 g in a 18 to 23 g mouse with a body surface area (BSA) between 67 and 75 cm^2 [102]. For a standard 73.7 kg adult human with a BSA of 18,000 cm^2 [103], the amount of activity that would have to be administered in order deliver the same dose to tumors of the same size can be estimated to be at least two orders of magnitude higher, that is, between 5 and 60 GBq, based on the BSA ratio between species. This estimated range per patient agrees with the total amount of activity of the analogous "soft" beta emitters ^{177}Lu ($t_{1/2}$ = 6.65 d; 11.6% β_1, $E_{\beta1\ max}$ = 177 keV; 79.4% β_2, $E_{\beta2\ max}$ = 498 keV; 10.4% γ, E_γ = 208 keV) and ^{131}I ($t_{1/2}$ = 8.03 d; 89.6% β_1, $E_{\beta1\ max}$ = 606 keV; 7.2% β_2, $E_{\beta2\ max}$ = 334 keV) that is currently being administered in clinical trials in the form of ^{177}Lu-DOTATATE [104-111], ^{177}Lu-DOTATOC [112], ^{177}Lu-PSMA [113-116], ^{177}Lu-DOTA-girentuximab [117], ^{177}Lu-DOTA-pentixather [118], ^{131}I-MIP-1095 (targets PSMA) and ^{131}I-mIBG [119-124].

Therefore, a constant supply of batches of tens or even hundreds of GBq of ^{47}Sc at a reasonable price would have to be available if clinical trials with this nuclide are ever to be performed. Based on the production capabilities that several institutions have recently reported in scientific journals, which are summarized in Table 2.14, none of them will be able to comply with such necessary demand. The only option that will be able to provide batches of tens of GBq at saturation will be the Facility for Rare Isotope Beams (FRIB) [125] in the form of ^{47}Ca/^{47}Sc generators (^{47}Ca $t_{1/2}$ = 4.54 d), according to predicted yields from simulations [126].

Table 2.14 Recent publications with production capabilities of ^{47}Sc from potential suppliers.

Nuclear reaction	**Target**	**Energy [MeV]**	**Current [μA]**	**Yield [MBq/μAh]**	**Sat. Yield [MBq]**	**Ref.**
^{44}Ca(α,p)^{47}Sc	^{44}CaO	28.1	10	0.78	904	[79]
^{48}Ti(γ,p)^{47}Sc	^{nat}Ti foil	22	1000	4.2e-3 / g target	487 / g	[127]
	^{48}TiO$_2$	22	1000	3.3e-3 / g target	383 / g	
^{48}Ca(γ,n)^{47}Ca	^{nat}CaCl$_2$	39	1000	4.2e-4 / g target	65 / g	[128]
	^{48}CaCl$_2$	39	1000	0.33 / g target	5.1e+4 /g	[129]
^{47}Ti(n,p)^{47}Sc	^{47}TiO$_2$	> 1 (1.5e14 n cm^2-s)	-	-	25 / mg target	[130]

Nevertheless, the current production capability of hundreds of MBq of ^{47}Sc per batch is sufficient for preclinical studies in small animals, which will provide valuable information before therapeutic amounts of ^{47}Sc for human patients become available. For instance, such preclinical studies will demonstrate whether the predicted amount of ^{47}Sc-citrate for tumor control and the associated toxicities to critical organs are accurate.

There are two production routes accessible with our PETtrace cyclotron. From the excitation function of the ^{46}Ca(d,n)^{47}Sc reaction modeled by TALYS [131], we can predict that 8.2 MeV deuterons on thick targets of the

commercially available 4.9% isotopically-enriched $^{46}CaCO_3$ (56 mg/cm^2) or ^{46}CaO (60 mg/cm^2) yield 0.41 and 0.67 MBq/μAh, respectively. However, the extremely high cost of $^{46}CaCO_3$ at $105 per mg[1], due to the 0.004% natural abundance of ^{46}Ca, makes this option impractical. Alternatively, from the cross section data for the $^{50}Ti(p,\alpha)^{47}Sc$ reaction, also from TALYS, we can anticipate that 16 MeV protons on a thick target of commercially available 55.4% isotopically-enriched ^{50}Ti as TiO_2 anatase powder (273 mg/cm^2) will yield 0.55 MBq/μAh. A price of $17.50 per mg* of $^{50}TiO_2$ makes the second route feasible. The radiochemical separation procedure will be based on the work of Pietrelli et al. [132] and Kolsky et al. [133], in which TiO_2 is dissolved in hot H_2SO_4 with extra 10:1 molar ratio sulfate anions to titanium; followed by evaporation to dryness and then re-dissolution in 10 M HCl; to then trap, wash and release the ^{47}Sc using a TBP-functionalized extraction resin. The separated ^{50}Ti dissolved in the hydrochloric acid solution would then be precipitated by the addition of excess ammonium carbonate solution as in the procedure to recover ^{86}Sr after the separation of ^{86}Y developed by Rösch et al [134].

2.3.11 *Comparison of our separation method to previous publications*

Comparing the separation chemistry of this work with the one by Severin et al. in [28, 65] we found many improvements. First, the dissolved target is directly loaded onto the column without having to adjust the pH, which is a process difficult to automate. Second, the ^{44}Sc radioactivity is eluted at high concentration in 400 μL of DI water ready for labeling, instead of eluting in 1 mL of 0.1 M HCl. And third, 80 ± 4 % of the produced radioactive scandium was separated, compared to the overall separation efficiencies of 53% and 63%, reported in [28, 65], respectively.

We believe that our separation method based on the UTEVA resin can also be applied with $^{44}CaCO_3$ targets in order to get a highly concentrated radioactive product and also to improve the recycling efficiency of the expensive target material. This would be recovered by collecting and then processing the eluate with the bulk calcium after trapping the ^{44}Sc just like Krajewski et al. [27] did in his separation method based on Chelex 100, in which they achieved a 60% ^{44}Ca recycling efficiency. They claim to have achieved a separation yield of > 70%, which is slightly lower than our 80 ± 4 % separation yield. However, they elute in three 0.5 mL fractions of 1 M HCl, which means that the activity is at a lower concentration and also in a more acidic medium that will be more difficult to buffer for radiolabeling DOTA or DTPA, compared to the product eluate obtained with our method, 400 μL of deionized water. Of course, our eluate will also be acidic (~1 M) due to the residual H^+ ions that remain in the

[1] Personal communication with sales representative from ISOFLEX.

UTEVA resin after loading and washing with 10 M HCl. Nevertheless, it is clear that the smaller volume of our product, 400 µL, is much easier to buffer than 1.5 mL of 1 M HCl.

Muller, et al. [23] achieved a slightly higher separation efficiency of ~85% after using 50-70 mg of DGA resin and then concentrating the activity using a cation exchange resin DOWEX-50. Their isolated ^{44}Sc is in 200-400 µL of 1 M ammonium acetate. Table 2.15 compares our work with the results from these publications.

Table 2.15 Comparison of separation methods of ^{44}Sc from calcium-based targets

Method	Target	p^+ Energy [MeV]	Act. Yield [MBq/µAh]	Sep. yield [%]	Act. conc. [MBq/mL]	Matrix of sep. ^{44}Sc	Calcium conc. in sep. ^{44}Sc [mM]	ESA (chelator) [GBq/µmol]	Ref.
Filtration	^{nat}Ca (99.99%)	16	38 ± 3	40 ± 18	2527 ± 487	0.1 M HCl	2.3	54 ± 14 (DOTA)	[28]
Hydroxa-mate resin	^{nat}Ca (99.99%)	16	38 ± 3	63 ± 15	597 ± 98	0.1 M HCl	*Not reported*	50 (DOTA)	[29]
Chelex 100	$^{44}CaCO_3$ (94.53%)	9.0	8.9	70	103	1 M HCl	< 0.025	22 (DOTA)	[27]
DGA + DOWEX -50	$^{44}CaCO_3$ (97.00%)	17.6 ± 1.8	11.7	85	980	1 M NH_4OAc	*Not reported*	5.2 (DOTA)	[23]
UTEVA	^{nat}Ca (99.99%)	15.56 ± 0.04	32 ± 3	80 ± 4	1600 ± 163	~1 M HCl	1.58 ± 0.01	18.1 ± 6.7 (DOTA) 55 ± 42 (DTPA)	This work

2.4 Conclusions

In conclusion, we have described a rapid and facile method to recover ^{44}Sc from proton-irradiated metallic calcium targets with excellent yield and high chemical and radiochemical purities. Additionally, the usage of a single column and minimal washing/elution steps provides a convenient framework for the implementation of automatic separation modules. Even though the focus of this work was to study the isolation of ^{44}Sc from natural calcium targets, our procedure is readily applicable to the isolation of ^{44}Sc from isotopically enriched $^{44}CaCO_3$ targets or even liquid targets employing $Ca(NO_3)_2$ solutions. This separation system coupled to improved cyclotron production approaches might be the long waited answer to make ^{44}Sc production feasible for translation into the clinic.

Furthermore, we have demonstrated that the administration of ^{44}Sc-citrate into murine breast cancer (4T1) and human glioblastoma (U87MG) tumor-bearing mice results in high and gradually increasing tumor uptake due to the long systemic circulation properties of this radiotracer, which are explained by the ligand exchange of ^{44}Sc to transferrin *in vivo*. Moreover, from internal dosimetry calculations extrapolated to human subjects, we have demonstrated that the effective dose from > 90% pure cyclotron-produced ^{44}Sc from inexpensive natural calcium

targets administered as Sc-citrate is quite low: 72.9 μSv/MBq, comparable to that of mainstream tracers ^{68}Ga-DOTATATE or ^{68}Ga-HBED-CC-PSMA, which justifies the clinical application of this economical supply of ^{44}Sc as an alternative to other more expensive options that result in 100% pure ^{44}Sc. We have also anticipated therapeutic properties after administration of the therapeutic analog ^{47}Sc-citrate in the 4T1 and U87MG mouse cancer models.

Chapter 3 Cobalt-55 and Cobalt-58m

3.1 Introduction

3.1.1 *Cobalt-55*

Cobalt-55 ($t_{1/2}$ = 17.53 h, 76% β^+, E_{max} = 1498 keV) is an intermediate-lived positron-emitting radionuclide that is a useful radiotracer for positron emission tomography (PET) [135-143] and particularly useful for labeling proteins due to its favorable complexation with established bifunctional chelators [144-148]. Furthermore, when chelated in oxidation state 3+, the formed complex is considered inert and therefore it is less prone to interact with ligands in blood plasma and non-targeted organs due to trans-chelation [149-151].

Most of the early applications of ^{55}Co for PET in ischemic stroke are based on the assumption that radioactive cobalt ions behave similar to calcium ions *in vivo* based on *ex vivo* results in brain tissue [152]. The main hypothesis was that radioactive cobalt ions would present the same influx into damaged brain cells that is observed with calcium ions. This hypothesis, however, was questioned by the work of Stevens et al [135], who observed that the uptake of ^{55}Co after administration of $^{55}CoCl_2$ into 16 patients with a diagnosis of stroke may be better explained by an inflammatory process. Since this latter work, the use of ^{55}Co for PET of ischemic stroke, cobalt being injected as a weakly bound complex, was abandoned.

A more promising approach for the use of this radiometal is by binding it to a chelator and potentially conjugating this complex to a targeting vector. So far, only six studies have followed this chelator-based approach [144-148, 153]. Goethals et al [153] labeled ^{55}Co to ethylene diamine tetraacetic acid (EDTA) and characterized this complex for the application in the measurement of the glomerular filtration rate in kidneys via PET, a study which is commonly performed with the perfusion tracer ^{51}Cr-EDTA [154]. Srivastava et al[144], Thisgaard et al[155] and Mastren et al[146] successfully labeled ^{55}Co to bifunctional chelators (BFC) conjugated to targeting peptides or proteins, although with very low effective specific activities (ESA): 3.7, 0.21, and 2.0 GBq/μmol, respectively. Dam et al [147], has reported the highest ESA of ^{55}Co at 30 GBq/μmol by labeling a NOTA-conjugated bombesin analog under microwave heating in order to accelerate the labeling reaction.

Very interesting results were obtained by Heppeler et al [156] after comparing the binding affinities and internalization rates of the DOTA-conjugated somatostatin analog 4,7,10-tricarboxymethyl-1,4,7,10-tetraazacyclododecane-1-yl-acetyl-D-Phe-(Cys-Tyr-D-Trp-Lys-Thr-Cys)-threoninol (DOTATOC) radiolabeled with the long-lived ^{57}Co ($t_{1/2}$ = 271.8 d; 122 keV γ, 86%; 136 keV γ, 11%) and radionuclides of gallium and yttrium. It

was found that Co-DOTATOC exhibited the highest affinity towards somatostatin receptor subtype 2 (sst2) and the highest internalization rate to cells expressing this receptor. These results call for the comparison of more peptides labeled with different radiometals in order to find the tracer with the best uptake properties for more target-specific studies. Thus, by making the positron-emitter ^{55}Co available to the scientific community, it will be possible to translate these comparison studies from the *in vitro* to the *in vivo* stage with PET.

An even more interesting application of this radiometal would be as a PET label of cobalamin, also known as vitamin B_{12}, the only cobalt complex that is essential to humans. Due to its importance in the biochemical pathways that result in methylation reactions, thymidine production and mitochondrial metabolism, all of which are elevated in proliferating cancer tissue, radiolabeled vitamin B_{12} derivatives have been proven to be excellent targeting agents for high-grade tumors both in patients [157] and in small animals models [158].

Cobalt-55 can be produced with a small biomedical cyclotron using isotopically enriched target materials via the ^{58}Ni(p,α) [146, 159] or ^{54}Fe(d,n) [160-162] nuclear reactions. It has also been produced using more sophisticated or high-energy cyclotrons using natural iron targets via the ^{nat}Fe(^{3}He,p+xn) [163] and ^{nat}Fe(p,xn) [164] reactions. The ^{58}Ni(p,α) route seems the most practical since isotopically enriched ^{58}Ni is relatively inexpensive (natural abundance = 68.07%) and low-energy proton accelerators are more common than dual-particle (proton and deuteron) ones. However, the high excitation functions of the ^{58}Ni(p,2p), and ^{58}Ni(p,p+n) that ultimately result in the co-production of ^{57}Co make this option less attractive when compared to the ^{54}Fe(d,n) route that offers the highest radionuclidically pure product [160]. Nevertheless, isotopically enriched ^{54}Fe is relatively expensive due to its natural abundance of 5.84% and therefore recycling it after each separation process becomes mandatory.

Of the three publications in which isotopically enriched ^{54}Fe targets have been employed [155, 161, 162], only the one by Zaman et al clearly reports a numerical value of the recycling efficiency of the expensive target material of 80%. In this publication, the target was made by pressing a mixture of $^{54}Fe_2O_3$ and aluminum powder onto a pellet and the maximum deuteron current from a 14 MeV beam that was applied was merely 4 μA [161]. Sharma et al reduced Fe_2O_3 to metallic iron at 800 °C in a H_2 atmosphere and then pressed the resulting elemental ^{54}Fe powder into a pellet. Nevertheless, the maximum current that they were able to apply to this target was merely 3 μA using a 12 MeV deuteron beam [162]. Thisgaard et al prepared the ^{54}Fe targets by electrodeposition over a silver disk based on a modified electroplating method described by Zaman and Qaim [160]. In this case the maximum deuteron

current from an 8.5 MeV beam was 18 μA, although their maximum electroplated thickness was merely 7.0 mg/cm^2, which barely generated 25 MBq/μAh [155].

Avrigeanu et al [165] performed cross-section measurements by irradiating thin foils of natural iron using the stacked foil technique with a 19.74 MeV deuteron beam and found that the ^{54}Fe(d,n)^{55}Co excitation function (Figure 3.1(a)) reaches a maximum of ~158 mb at 6.71 MeV. The predicted thick target production yield from this excitation function integrated over the energy on the impinging particles available from our PETtrace, 8.2 MeV (the measurement of the energy of the deuteron beam is presented in Appendix B), as they are slowed down in the target material is 23.2 MBq/μAh. Likewise, from the ^{58}Ni(p,α) excitation functions that were measured by Khandaker et al [166] (Figure 3.1(b)) we can predict a thick target yield with our 16 MeV proton beam of 15.6 MBq/μAh. As I will present in this chapter, the experimental target yields that we measured are between 39 and 51% of these predicted yields, due to the narrow surface area of the electroplated targets as compared to the total extent of the beam transverse area (Appendix C).

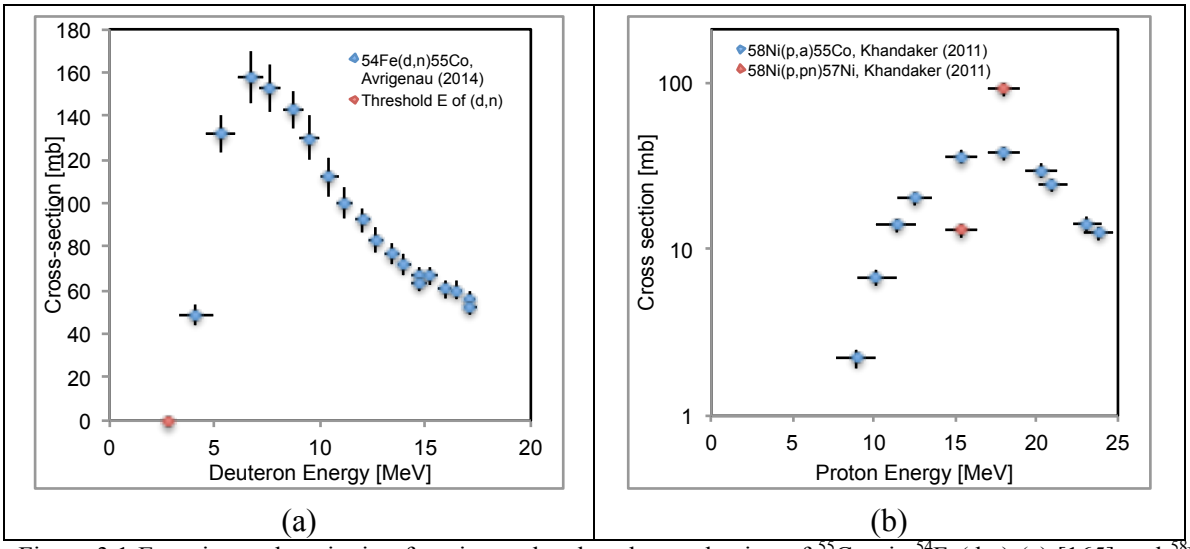

Figure 3.1 Experimental excitation functions related to the production of ^{55}Co via ^{54}Fe(d,n) (a) [165] and ^{58}Ni(p,α) (b) [166].

The radiochemical separation methods for ^{55}Co that have been published so far involve large ion exchange resin columns (> 4.0 cm × 1.0 cm Ø) that result in a final eluate of more than 5 mL volume [146, 159], which necessitates for a lengthy evaporation step in a large vessel that potentially causes a variable loss of radioactivity in the vessel's surface or in the glassware of the evaporator. In order to circumvent this problem, extraction resins with higher trapping capacity compared to the traditional ion exchange resins have proven to be more practical particularly because they allow the elution of highly concentrated radiometals in solution with high specific activity [167-169].

In this chapter, I will present methods for the production of high specific activity ^{55}Co using a biomedical cyclotron. The methods includes: (1) electrodeposition of thick ^{54}Fe or ^{58}Ni targets; (2) irradiation at high beam current using a water jet cooled target holder; (3) ^{55}Co separation and purification involving the extraction resin N,N,N',N'-tetrakis-2-ethylhexyldiglycolamide, commercially known as DGA Branched (Eichrom) [14]; and (4) efficient recycling of the ^{54}Fe or ^{58}Ni target material. We have successfully electroplated ^{54}Fe and ^{58}Ni at thicknesses of 24-65 mg/cm^2 and 90-214 mg/cm^2, respectively, both on silver disk substrates. These targets have been bombarded with deuteron beams of up to 65 μA and proton beams of up to 40 μA, respectively. Enriched ^{54}Fe targets with thickness > 52.3 mg/cm^2 yield 10.3 ± 0.8 MBq/μAh (n = 7), so batches of up to 670 MBq ^{55}Co are feasible after 1 hour of irradiation, with measured effective specific activities (ESA) of 27 ± 18 GBq/μmol of NOTA. Ni-58 targets > 90.1 mg/cm^2 thick yield 9.3 ± 0.6 MBq/μAh (n = 3) and 1 hour-long irradiations result in 370 MBq of ^{55}Co with an ESA of 10.1 ± 5.7 GBq/μmol NOTA. The ESA or reactivity of ^{55}Co towards the other mainstream chelators such as DOTA, HBED and TETA was also quantified.

The presented methods for the production of ^{55}Co will allow its widespread production for PET imaging at medical centers throughout the world. Moreover, the production method from iron targets can be easily adapted for the preparation of the therapeutic radionuclide ^{58m}Co from either proton or deuteron bombardment on isotopically enriched ^{58}Fe or ^{57}Fe, respectively.

3.1.2 *Cobalt-58m*

The internal conversion decay of ^{58m}Co ($t_{1/2}$=9.10 h, 100% IC) (Figure 3.2) results in the emission of characteristic x-ray photons, conversion electrons and Auger electrons. The three main conversion electrons from the K, L and M orbitals have energies of 17.2, 24.0 and 24.8 keV, respectively, and are emitted with probabilities per decay of 73.0, 23.5 and 3.4%, respectively [170]. Additionally, about three low energy Auger electrons with energies < 8 keV are emitted per decay [171]. The linear energy transfer (LET) of these low-energy electrons in unit-density matter covers a range from 2 to 18 keV/μm [172], which is at least one order of magnitude greater than the LET of energetic beta particles emitted by established therapeutic radionuclides such as ^{177}Lu and ^{90}Y.

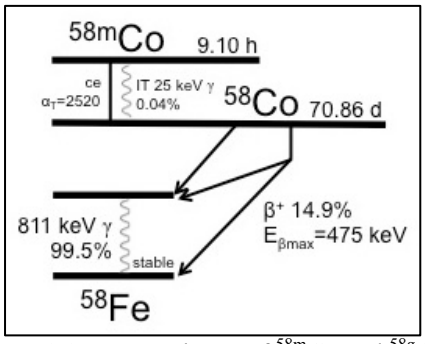

Figure 3.2 Decay scheme of ^{58m}Co and ^{58g}Co.

Furthermore, the range in water of conversion and Auger electrons is less than 10 μm, at least one order of magnitude lower compared to the range >100 μm for the main beta particle emitted by ^{177}Lu [44]. This short path length renders Auger and conversion electrons suitable for treatment of minimal disease such as micro-metastasis or residual tumor after surgical resection of a primary lesion.

However, since the short range of Auger electrons is less than the dimension of a typical cell, it has been claimed that the emitting radionuclide must be localized in proximity to the cancer cell nucleus in order to affect the DNA and cause cytotoxicity. Indeed, higher toxicity has been observed experimentally when the radionuclide is directed to the cell nucleus [173]. Nevertheless, high cytotoxicity has also been observed when a non-internalizing antibody labeled with the Auger-electron emitter ^{125}I was directed to the cell membrane and not the nucleus [174].

Besides the cancer cell nucleus and membrane, another potential target for the Auger electrons is the blood vessels that supply the tumor cells. The hypothesis is that killing tumor capillary endothelial cells will starve the tumor of oxygen and nutrients. This strategy has been explored with the alpha particle emitter ^{213}Bi labeled to an antibody that targets the surface of capillaries and blood vessels in lung cancer [175]. Following this idea, we decided to target the Auger-emitter ^{58m}Co to the vasculature of murine breast cancer cells, 4T1, in a BALB/c mouse model using the anti-CD105 antibody TRC105 (TRACON Pharmaceuticals) as the delivery vehicle. The analogous diagnostic nuclide ^{55}Co was also labeled to TRC105 and injected into the 4T1 tumor-bearing mice in order to verify the targeting efficiency of the antibody and also to estimate the absorbed dose to the tumor and the normal organs caused by the therapeutic ^{58m}Co. Thus, ^{55}Co and ^{58m}Co represent a perfect theranostic pair since exactly the same element, in this case cobalt, can be bound to a targeting vector and act either as a diagnostic label for treatment planning and monitoring of disease through PET imaging or as a radiotoxic therapeutic.

CD105 or endoglin, is a protein that is overexpressed on the surface of proliferating endothelial cells that is essential for angiogenesis, the process of new blood vessel formation. It is particularly overexpressed on tumor-

associated vascular and lymphatic endothelial cells [176]. For this reason, several anti-CD105 antibodies have been engineered either for therapy to block its cancer proliferation signaling or for diagnosis. One of such antibodies is TRC105 (also called c-SN6j) [176]. Even though the antibody by itself has been shown to cause tumor growth delay and even tumor regression in human breast cancer xenografts [177], it has also been labeled to the Auger electron-emitter ^{125}I in order to enhance its antitumor efficacy [178]. Indeed, significant tumor growth suppression was observed after treatment with two doses of 10 μCi of ^{125}I-SN6j compared to a control group injected with ^{125}I-labeled IgG [178].

The therapeutic potential of ^{58m}Co has been recognized theoretically [179-181] and experimentally [182]. Experimentally, Thisgaard et al demonstrated that ^{58m}Co-DOTATATE was significantly more efficient in cell killing per cumulated decay than ^{111}In- and ^{177}Lu-DOTATATE after exposing pancreatic tumor cells AR42J in vitro [182]. However, as far as we know, the therapeutic potential of ^{58m}Co has not been demonstrated *in vivo*.

Furthermore, ^{58m}Co decays to the positron emitter ^{58g}Co ($t_{1/2}$=70.86 d, 14.9% β^+) (Figure 3.2), which carries benefits and disadvantages. The two main advantages are that ^{58g}Co can be employed to quantify the otherwise "silent" ^{58m}Co and that it can be imaged and quantified in vivo via Positron Emission Tomography (PET). This second possibility is particularly important for therapy applications because it allows the quantification of radionuclide concentration in target and non-target tissue for dosimetry calculations. The main disadvantages are that ^{58g}Co has a long half-live and that it emits a prominent 811 keV gamma with a branching ratio of 99.5% [170] that will inevitably deposit dose in normal tissue and that will have to be controlled after excretion for radiation safety reasons.

The production of ^{58m}Co can be carried out either by proton bombardment on isotopically enriched ^{58}Fe as it was done by Thisgaard et al [181, 182], or by deuteron bombardment on ^{57}Fe. From the excitation functions of the ^{58}Fe(p,n) and ^{57}Fe(d,n) reactions published by Sudar and Qaim [183] (Figure 3.3), the thick target yields of ^{58m}Co with the 16 MeV protons and 8.2 MeV deuterons available with our PETtrace cyclotron are 395 and 33 MBq/μAh, respectively. However, thick targets of ^{58}Fe (440 mg/cm^2 [184]) are prohibitively expensive since they would cost about $13,300 due to the price of ^{58}Fe at US$30/mg^2. Much thinner targets can be used instead with acceptable production yields still attainable. For instance, Thisgaard et al [181], has reported a production yield of 10.7

[2] Personal communication with sales representative from ISOFLEX.

MBq/μAh from the bombardment of 7.0 mg/cm^2 ^{58}Fe with 10.1 MeV. Alternatively, thick targets of ^{57}Fe (73 mg/cm^2 [184]) are economically feasible to make since ^{57}Fe costs US$6/mg*.

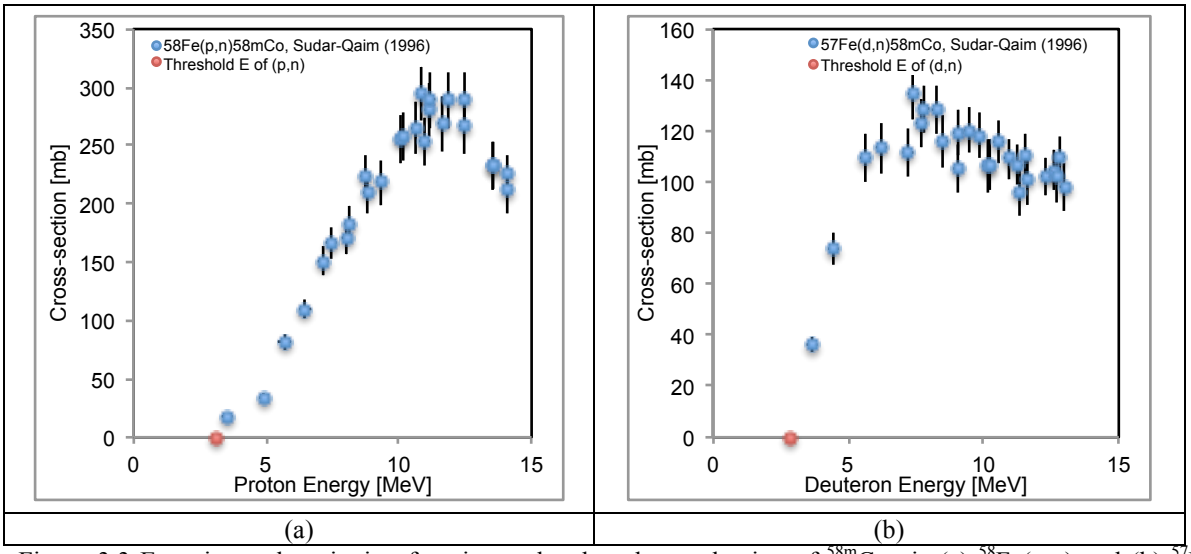

(a) (b)

Figure 3.3 Experimental excitation functions related to the production of ^{58m}Co via (a) ^{58}Fe(p,n) and (b) ^{57}Fe(d,n) [185].

In this chapter I will: 1) develop a production method of high-specific activity and high-radionuclidic purity ^{58m}Co that is efficient and economic; 2) evaluate the therapeutic antitumor effects after application of ^{58m}Co labeled to TRC105 (^{58m}Co-NOTA-TRC105) into 4T1 tumor bearing mice; and 3) demonstrate that ^{58g}Co can be used to image and quantify the biodistribution in vivo of the administered agent post-therapy.

In this chapter, I will also present the biodistribution and pharmacokinetics of injected ^{55}Co-citrate in murine breast cancer (4T1) tumor-bearing Balb/c mice and immunosupressed nude mice bearing tumors of human glioblastoma (U87MG) in order to verify whether unlabeled or weakly bound ^{55}Co has intrinsic targeting properties as we have shown with unlabeled ^{44}Sc, and to characterize the organs in which de-chelated ^{55}Co from a targeting construct could potentially accumulate in case the radiolabel is not stably bound to the vector.

3.2 Materials and Methods

Optima grade hydrochloric acid (32-35% HCl) comes from Aristar Ultra, VWR (West Chester, PA). Ethanol, 200 proof, and L-Ascorbic acid (TraceSELECT, >99.9998%) and 28% ammonium hydroxide solution in H_2O (NH_4OH, ≥ 99.99% trace metals) were purchased from Sigma-Aldrich (St. Louis, MO). The chelators NOTA (1,4,7-triazacyclononane-1,4,7-triacetic acid), DOTA (1,4,7,10-tetraazacyclododecane-1,4,7,10-tetraacetic acid) and TETA (1,4,8,1 l-tetraazacyclotetradecane-1,4,8,11-tetraacetic acid) were purchased from Macrocyclics (Dallas, TX). The

chelator HBED (N,N'-Di(2-hydroxybenzyl)ethylenediamine-N,N'-diacetic acid) comes from Strem Chemicals (Newburyport, MA). Isotopically enriched ^{54}Fe (99.93% ^{56}Fe, 0.06% ^{56}Fe, 0.005% ^{57}Fe, 0.005% ^{58}Fe), ^{57}Fe (95.06% ^{57}Fe, 0.04% ^{54}Fe, 3.06% ^{56}Fe, 1.86% ^{58}Fe) and ^{58}Ni (99.48% ^{58}Ni, 0.505% ^{60}Ni, 0.005% ^{61}Ni, 0.005% ^{62}Ni, 0.005% ^{64}Ni) were purchased from ISOFLEX (San Francisco, CA). Silver disks (1.90 cm diameter × 0.56 mm thickness) were obtained from Artisan Jewelers (Sarasota, FL). Platinum wire (99.997%, 0.25 mm diameter) and ammonium oxalate monohydrate (99.0-101.0%) were purchased from Alfa Aesar (Ward Hill, MA). 99% 4-(2-hydroxyethyl)-1-piperazineethanesulfonic acid (HEPES) was purchased from Acros Organics. Sodium hydroxide (1 M) solution was prepared from NaOH pellets from Fisher Scientific. Trace metal grade sulfuric acid, sodium citrate ($Na_3C_6H_5O_7 \cdot 2H_2O$ or Na_3Cit), ammonium acetate, methanol and ethylene diamine triacetic acid (EDTA) were also purchased from Fisher Scientific (Pittsburg, PA). TLC silica gel 60 plates and iron test strips were bought from EMD Chemicals (Darmstadt, Germany). Ion exchange resin (AG1-X8) was purchased from Bio-Rad (Hercules, CA). Extraction chromatography resin DGA, branched (50-100 μm) was purchased from Eichrom (Lisle, IL). A 50 ppm multi-element standard for calibration and Agilent's 4200 Microwave Plasma Atomic Emission Spectroscopy (MP-AES) system come from Agilent Technologies (Santa Clara, CA). Deionized water (>18 $M\Omega \cdot cm^{-1}$) was obtained from a Milli-Q filter, Millipore (Billerica, MA). Phosphate buffer saline (PBS) was purchased from Thermo Scientific.

3.2.1 *Cyclotron targetry, irradiations and target yields*

The electroplating procedure for iron was an adaptation of the methodology reported by Vosburgh et al [186]. Briefly, 62.2 ± 10.8 mg of ^{54}Fe (n = 13) or 81.0 ± 7.6 mg of ^{57}Fe (n = 6) metallic powder were dissolved in 5 mL 6 M HCl, the Fe ions were turned to oxidation state 3+ by the addition of 100 μL 30% H_2O_2 and the solution was evaporated to near dryness (< 1 mL). The residue was diluted with 15 mL of saturated ammounium oxalate (concentration ~ 44 mg/mL H_2O) followed by a pH adjustment to between 2 and 3 with either 1 M NaOH or 1 M HCl.

The electroplating procedure for nickel was very similar to the one previously reported for production of ^{64}Cu from ^{64}Ni targets [187-189]. Briefly, 100.0 to 196.8 mg of isotopically enriched metallic ^{58}Ni powder (n = 4) was dissolved in 6 M HNO_3, dried down and re-dissolved in 2.3 mL of 2.4 M H_2SO_4 followed by adjustment to pH ~9 with 1.5-1.8 mL of 28% NH_4OH and the addition of 270-300 mg of $(NH_4)_2SO_4$.

Each electroplating solution was quantitatively transferred to an electrolytic cell, as the one described in Appendix D. To prepare the iron deposits, the cell was operated at 7.0 V with an average current at the beginning of the process of 157 mA for 22 ± 3 h. Nickel was electroplated applying 3.0 to 3.6 V and 30 to 116 mA across the electrodes for 2 to 3 days. The electroplating was ended when the electrolyte solutions were fully clear and the colorimetric nickel or iron strips indicated that 0 to 0.05 mg of metal remained in solution.

During irradiation, the back of the disks is in direct contact with a water jet stream for cooling, as shown in Figure 3.4. Irradiations were performed on the UW-Madison PETtrace cyclotron using 8.2 MeV deuterons and 16 MeV protons with maximum currents of 60 μA and 40 μA on the iron and nickel targets, respectively. After irradiation, the targets were dismounted from the cyclotron and weighted with a balance in order to verify that no mass was lost during irradiation.

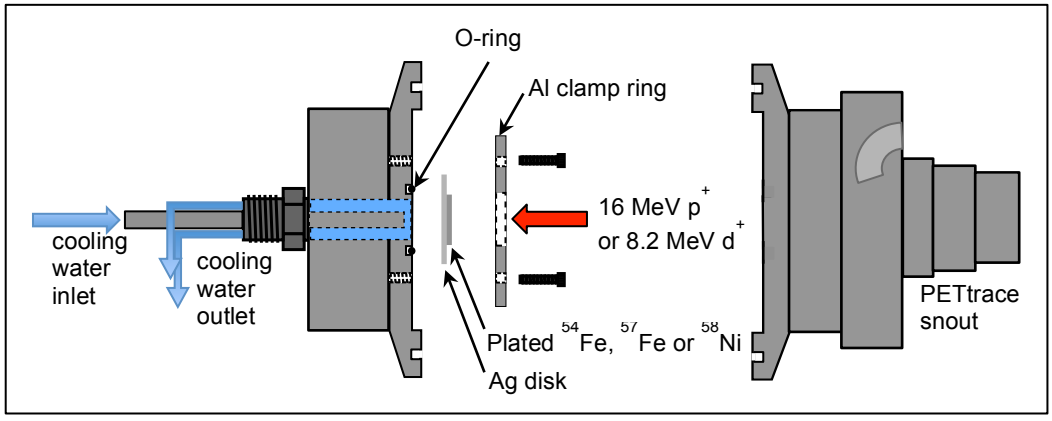

Figure 3.4 Schematic of how the electroplated iron or nickel targets are mounted into one of the ports of the cyclotron.

Co-55 activities for separation yield quantification were measured with a Capintec CRC-Dual PET (Capintec, Ramsey NJ) dose calibrator using the calibration setting 481 suggested by the manufacturer. However, the actual activity from ^{55}Co and other radionuclidic impurities was measured from the gamma intensities of 10 μL samples placed at distances with known efficiency calibration from a 60 cm^3 high purity germanium (HPGe) detector (Canberra C1519) (FWHM = 2.7 keV @ 1333 keV). Gamma-ray spectrum analysis software package, Maestro-32 MCA Emulator (Ortec, Oak Ridge TN), was used to collect and analyze the gamma-ray spectra. The gamma lines used to determine yields are listed in Table 3.1. The dead time was always kept below 10% and the acquisition time was set so that the statistical uncertainty from the number of counts per peak was kept below 1%. From the accurate activity value of ^{55}Co it was observed that the Capintec measurement with the calibration setting 481 was overestimating the actual ^{55}Co activity from the HPGe measurement by 93 ± 11% (n = 9) when the assayed ^{55}Co had

a radionuclidic purity >99.99%, after it was already isolated from the co-produced ^{52}Mn or ^{57}Ni from ^{54}Fe(d,α) and ^{58}Ni(p,pn), respectively. Hence, the Capintec reading had to be multiplied by 0.52 throughout our studies, including the quantification of administered doses to small animals and calibration of the PET scanner, in order to have accurate activity values.

Table 3.1 Gamma emissions used for production yield and separation efficiency quantifications

Nuclide	Reaction	Gamma energies [keV]	Branching ratio
^{55}Co	^{54}Fe(d,n)	477*	0.202
	^{58}Ni(p,α)	931	0.75
^{57}Co	^{56}Fe(d,n)	122	0.8560
	^{60}Ni(p,α)		
^{58g}Co	^{57}Fe(d,n)	811	0.9945
^{58m}Co	^{57}Fe(d,n)	24.9	0.000397
^{57}Ni	^{58}Ni(p,pn)	1378	0.817
^{52}Mn	^{54}Fe(d,α)	744	0.900
^{56}Mn	^{58}Fe(d,α)	847	09885
^{24}Na	^{23}Na(d,n)	1369	0.9999

* The 477 keV gamma peak was used instead of the 931 keV gamma because there is partial overlap with the 936 keV gamma from ^{52}Mn, which has a BR of 94.5%

Production yields of ^{58m}Co and ^{58g}Co from ^{57}Fe(d,n) were quantified via two methods: 1) indirectly via quantification of ^{58g}Co activity over time (E_γ = 811 keV) using an efficiency-calibrated HPGe detector, fitting the data points with the Bateman equation that contains the initial activities of the parent and daugher radionuclides, as it was done by Thisgaard et al. [181]; and 2) via direct quantification of ^{58m}Co (E_γ = 24.9 keV) using an efficiency-calibrated low-energy HPGe detector as it was done by Sudár and Qaim [183]. The sample employed for this purpose was the 10 µL aliquot drawn from the 3.1 mL target dissolution.

For method 1), the ^{58g}Co activity as a function of time after End of Bombardment (EoB), $A_g(t)$ was fitted with the following expression to obtain the generated ^{58m}Co and ^{58g}Co activity at EoB, $A_{m,0}$ and $A_{g,0}$, respectively:

$$A_g(t) = A_{g,0}\left[\frac{r\cdot\lambda_g}{\lambda_g-\lambda_m}\left(e^{-\lambda_m t} - e^{-\lambda_g t}\right) + e^{-\lambda_g t}\right] \qquad \text{Equation 3.1}$$

where, $r = A_{m,0}/A_{g,0}$ and λ_g and λ_m are the decay constants for the ground and metastable states, respectively.

3.2.2 *Radiochemical Separations*

The radiochemical separation of radio-cobalt from iron was performed in aqueous solution using the partition properties of the involved elements between HCl, HCl-Ethanol, the anion exchange resin AG1-x8 (Bio-Rad) and the extraction resin *N,N,N',N'*-tetrakis-2-ethylhexyldiglycolamide (DGA, branched) [190-192]. First, the electroplated surface was exposed to 3 mL of 6 M HCl, heating the back side of the disk with a heater set to 90°C. Only the front face of the electroplated target was exposed to HCl by use of a teflon mask with an inserted O-ring that seals against

the surface of the substrate disk. After the iron was completely dissolved in approximately 20 minutes, 100 μL of 30% H_2O_2 was added to turn the iron ions to the 3+ oxidation state. In order to quantify the produced radioactivity of the cobalt and manganese nuclides, a 10 μL sample from this solution was collected for gamma spectroscopy using a High Purity Germanium (HPGe) detector (Canberra C1519) and a low-energy HPGe detector with a beryllium window (Canberra GL0110P), both efficiency-calibrated at fixed distances with NIST-traceable radioactive sources and connected to the software Maestro (version 6.08, Ortec).

Afterwards, the iron solution was diluted with 57 mL of ethanol (EtOH) (200 proof, Sigma-Aldrich) to a concentration of ~0.3 M HCl and 95% EtOH. This new target solution was then transferred to a 60 mL syringe connected to a peristaltic-pump driven automated module similar to the one we have previously described in Chapter 2 for ^{44}Sc production [169], which sent the new solution in steps of 20 mL into an anion exchange column (AG1-x8, 1.5 cm diameter, 6.3 cm long), pre-equilibrated with 20 mL of 0.3 M HCl / 95% EtOH solution, with the flow rate being induced by gravity. The stable iron target material and the cobalt and manganese radionuclides were quantitatively retained in the column as expected from the distribution coefficients > 10^3 for these elements in anion exchange media reported by Pietrzyk [191]. The radioactive cobalt and manganese nuclides were quantitatively eluted in 10 mL of 4 M HCl, while the expensive target material was quantitatively retained in the column, a behavior that is explained by the retention properties of the chloro-complexes in anion exchange media reported by Kraus and Nelson [190]. Next, the 10 mL solution of 4 M HCl containing the radionuclides of interest was diluted to a concentration of ~8 M HCl by adding 10 mL of concentrated (12.1 M) HCl. This solution was then transferred to the reservoir of a second peristaltic-driven automated module to which a 300 mg DGA column loaded in a 0.5 cm diameter column cartridge, pre-equilibrated with 3 mL of 8 M HCl, was connected. In this case the flow rate at 1.1 mL/min was dictated by the peristaltic pump. In this chromatography setting, the radioactive cobalt was retained in the resin while radioactive manganese was eluted [192]. In order to quantitatively separate the manganese from the trapped cobalt, the resin was washed with 10 mL of 8 M HCl. Subsequently, the radioactive cobalt was eluted in fractions of 200 μL of 2 M HCl pushed by the peristaltic pump. The two fractions with the largest amount of radioactivity were mixed together and dried down in ~15 min at 100 °C under a stream of argon. The residue was re-dissolved in 100 μL of 0.1 M HCl, which constituted the separated stock of $^{xx}CoCl_2$ (xx = 55 or 58m) ready for radiolabeling. A 2-5 μL aliquot from the separated stock was assayed with both the high energy and low energy HPGe to accurately quantify the separation yield. The isotopically enriched ^{54}Fe or ^{57}Fe was eluted from the AG1-x8

column in 20 mL of 0.1 M HCl. This solution was dried to ~1 mL at 125 °C under a flow of N_2 and the residue was reconstituted into the 15 mL saturated ammonium oxalate electrolyte for re-electrodeposition. The electroplated iron mass was compared to the original target mass before irradiation in order to quantify the iron recycling yield. Figure 3.5 shows a schematic of this separation procedure.

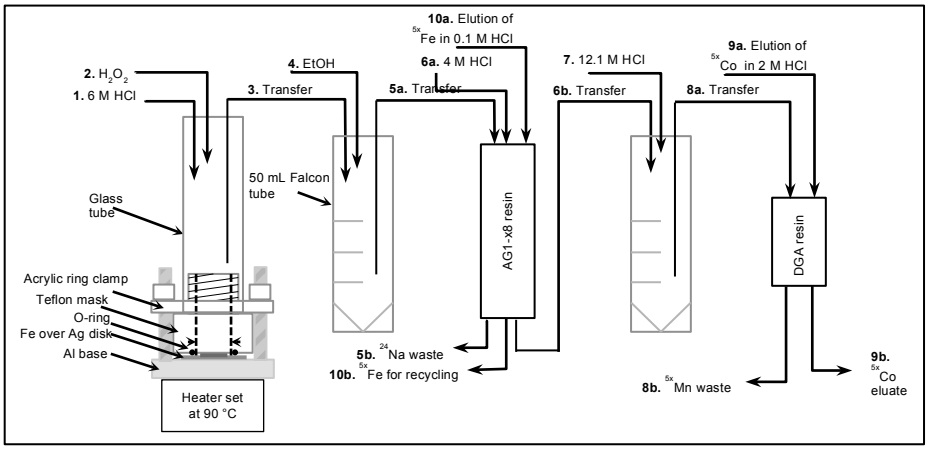

Figure 3.5 Schematic of the radiochemical separation of ^{5x}Co from ^{5x}Fe.

Similarly, the irradiated ^{58}Ni was dissolved off the silver disk in 7 mL of concentrated HCl at 90 °C in 0.5 to 1 h, followed by a dilution with 2 mL of deionized H_2O to a concentration of ~9 M HCl and then by a transfer to a 0.5 cm diameter column filled with 300 mg DGA branched resin at 1.0 mL/min with the peristaltic pump-driven module. Co-55 is trapped in the resin and the isotopically enriched ^{58}Ni that flows through is collected for recycling. A rinse of 18 mL of 9 M HCl is applied to the resin to remove the remaining bulk nickel target material as well as traces of other metals, such as copper. The elution of ^{55}Co was carried out by pumping 200 µL fractions of 3 M HCl through the loaded resin. The two or three most concentrated fractions were combined in a 1.5 mL centrifuge vial, evaporated to dryness at 100 °C under argon flow, and the residue was re-dissolved in 100 µL of 0.1 M HCl, which constituted the separated stock of $^{55}CoCl_2$. The elution profile for the main elements involved in the separation, i.e. nickel, cobalt and copper, was obtained by collecting fractions from a separation run with volumes of 3 mL in the loading (9 mL) and washing steps (18 mL), followed by fractions of 200 µL in the elution step. 64 MBq of radionuclidically pure ^{64}Cu in 5 µL of 0.1 M HCl (a novel separation method for this nuclide will be presented in Chapter 4) was mixed with the target solution to serve as a tracer for copper. The fractions were then analyzed by gamma ray spectrometry using ^{55}Co and ^{57}Ni (from ^{58}Ni(p,pn)) as the other radiotracers. The recovered isotopically-enriched nickel solution was evaporated to dryness, re-dissolved in 3mL of 6 M HNO_3 in order to digest possible organic material from the extraction resin, evaporated to dryness again, and the electroplating solution was

reconstituted and transferred to an electroplating cell as described before. Figure 3.6 shows the schematic of this separation procedure.

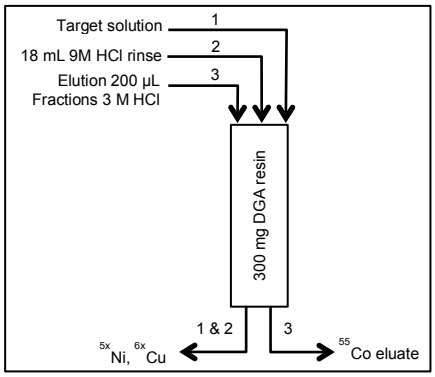

Figure 3.6 Schematic of the radiochemical separation of ^{5x}Co from ^{58}Ni.

The radionuclidic purity and identity of ^{55}Co in the separated product was confirmed by gamma spectroscopy and by half-life verification after logging the decaying signal from a sample placed inside a dose calibrator (Capintec CRC-Dual PET) that feeds an electrometer (Keithley 6517A) connected to a data acquisition program in LabVIEW. The total acquisition time was 161 hours and 108 hours on samples from ^{55}Co separated from ^{54}Fe and ^{58}Ni, respectively, with a sampling interval of 60 seconds. This data was fit to a mono-exponential function and a decay half-life was quantified and compared to the accepted value for ^{55}Co, 17.53 h [193].

Trace metal analysis was performed on samples from four and three ^{55}Co separation runs using ^{54}Fe and ^{58}Ni targets, respectively. Ten µL samples from the target solutions and 2-20 µL from the ^{55}Co separated stock were analyzed for trace metal quantification with Agilent's Microwave Plasma Atomic Emission Spectroscopy system (4200 MP-AES).

3.2.3 *Effective Specific Activity of ^{55}Co and ^{58m}Co with Mainstream Chelators*

The effective specific activity or reactivity of ^{5x}Co was evaluated by titrating equal amounts of $^{5x}CoCl_2$ solution (0.25 µL from the separated stock) with increasing amounts (0 to 300 ng) of the chelators NOTA, DOTA, TETA and HBED at pH 7.5 in 0.25 M HEPES buffer at room temperature for 30 min. The labeling yield in each reaction vial was assessed by thin layer chromatography (TLC) using silica gel plates (60 F254, EMD Chemicals) and 1:1 MeOH:10%NH_4AOc mobile phase, with the activity distribution in the plates quantified by autoradiography using a Packard Cyclone Phosphor-Plate imaging system (Perkin Elmer). The reactivity is defined as the ratio of activity decay-corrected to EoB to the amount of chelator in moles that results in 50% labeling yield, multiplied by two.

3.2.4 *Image quality of ^{55}Co*

The same miniature Derenzo phantom employed in Chapter 2, Section 2.2.6 [47] was used to evaluate the spatial resolution of ^{55}Co PET images using an Inveon microPET/CT rodent model scanner. The phantom was filled with 0.1 M HCl solution containing 29.5 MBq and data was collected for ~20 min until one billion coincident counts were acquired by the software. The raw data was collected in a histogram and reconstructed using the two-dimensional filtered back projection algorithm (FBP2D), without attenuation correction, using a matrix size of 512 × 512 pixels. Image quality was evaluated by visual inspection of transaxial slices in the middle of the phantom and by profile analysis in the region in which the minimum spatial resolution was observed.

3.2.5 *Preparation of ^{55}Co- and ^{58m}Co-NOTA-TRC105*

NOTA conjugation to TRC105 was carried out by mixing the NOTA derivative para-isothiocyanato-benzyl-NOTA (p-SCN-Bn-NOTA) (Macrocyclics) dissolved in dimethyl sulfoxide (DMSO) to a solution containing TRC105 at pH 8.5 – 9.0 with a 25:1, chelator to antibody molar ratio. After 2 hours of reaction time at room temperature, the conjugate NOTA-TRC105 was purified by size exclusion chromatography with a PD-10 column (GE Healthcare) using phosphate-buffered saline (PBS) as the mobile phase. The concentration of the conjugated protein was measured by analyzing a 1 μL sample with a UV-Vis spectrophotometer Nanodrop One (Thermo Scientific).

For radiolabeling with ^{55}Co (from ^{54}Fe) or ^{58m}Co, 20 and 90 μL of each respective separated stock with $^{5x}CoCl_2$ was buffered to pH ~7.5 by adding 1.0 mL of 0.25 M HEPES and then ~190 or ~860 μg, respectively, of TRC105-NOTA from the 3.8 μg/μL antibody stock that was eluted from the PD-10 column. One to two hours later, each of these solutions was purified by size exclusion chromatography with a PD-10 column and PBS mobile phase collecting five fractions of 400 μL. Each fraction and the PD-10 column were assayed with the dose calibrator in order to quantify the radiolabeling yield per fraction. The two most concentrated fractions from each radiolabeling were mixed and used for the animal studies.

3.2.6 *Biodistribution and pharmacokinetics of ^{55}Co-citrate and ^{55}Co-NOTA-TRC105 in tumor-bearing mice*

The calibration factor for quantification of ^{55}Co activity concentration in volumes of interest (VOI) of the PET images was obtained following the quantification calibration procedure indicated in the Inveon microPET/CT

scanner manual, which was explained in Chapter 2, Section 2.2.7, using a 130 mL cylinder phantom filled with ^{55}Co dissolved in 0.1 M HCl at a concentration of 384 ± 2 kBq/mL.

Murine breast cancer (4T1) tumors were established in four- to five-week-old female Balb/c mice by subcutaneous injection of approximately 2×10^6 murine mammary carcinoma 4T1 cells, into the upper right flank of 18 mice. Tumor sizes were monitored and mice were used for the imaging and radiotherapy experiments when the axis of the quasi-ellipsoid tumors reached lengths of 6 - 9 and 5 - 8 mm, 11 days after inoculation. The total body mass of these mice at this time was 19.5 ± 1.0 g. One group of three mice was used for the assessment of ^{55}Co-citrate biodistribution, another group of three mice was used for the study of ^{55}Co-NOTA-TRC105 biodistribution and 3 groups of 4 mice were used for the targeted radiotherapy study with ^{58m}Co-NOTA-TRC105.

Human glioblastoma (U87MG) cells were used for tumor inoculation when they reached ~80% confluence. U87MG tumors were established in four- to five-week-old female athymic nude mice by subcutaneously injecting 5×10^6 cells, suspended in 100 µL of 1:1 mixture of DMEM medium and matrigel, into the lower flank of three mice. The tumor sizes were monitored every alternate day, and *in vivo* experiments were carried out when the diameter of the tumors reached 6 – 8 mm length in the long axis (typically, 3 weeks after inoculation). The total body mass of these mice at this time was 23.0 ± 1.2 g.

The ^{55}Co-citrate stock solution for injection was prepared by diluting 50 µL of the separated $^{55}CoCl_2$ stock solution with 600 µL of 10 mM sodium citrate ($Na_3C_6H_5O_7\bullet2H_2O$ or Na_3Cit) (Fisher Scientific) with the pH adjusted to ~7 by adding 10 µL of 1 M Na_2CO_3. Doses of 6.6 ± 0.2 MBq of ^{55}Co-citrate in 200 µL were administered to each mouse of groups of three mice bearing either 4T1 or U87MG tumors and static PET scans were performed at 0.5, 4 and 24 hours post-injection (p.i.) on the 4T1 group and at 1, 5, 8 and 24 h p.i. on the U87MG group.

From the mixture of the two most concentrated fractions of ^{55}Co-NOTA-TRC105 eluted from the PD-10 column (800 µL total), 200 µL fractions with 7.8 ± 0.4 MBq ^{55}Co were administered into each mouse of another group of three 4T1 tumor-bearing mice and PET scans were performed at 4, 24 and 48 hours p.i.

PET acquisitions were set to collect at least 40 million coincident counts per mouse, which implicated scanning times of 1 - 15 min. Static images were reconstructed using the OSEM3D algorithm and then analyzed with the Inveon Research Workplace software. Volumes of interest were drawn on the whole volume of the delineable organs: liver, kidneys, bladder and tumor for the images obtained from ^{55}Co-citrate; and heart, liver and tumor for

the ones obtained from ^{55}Co-NOTA-TRC105. For both radiotracers, muscle uptake was quantified by drawing two ellipsoidal VOIs, each of 100 – 200 mm^3, flanking the urinary bladder in regions with low activity uptake where the adductor and biceps femoris muscles are located. The uptake data from each of the VOIs is decay-corrected to time of injection and expressed as percentage injected dose per gram (%ID/g). Whole body VOIs of each mouse were drawn and the whole body %ID was obtained by multiplication of the %ID/g by the volume of the VOI, assuming that 1 cm^3 = 1 g. The %ID of each delineable organ and tumor was calculated in the same manner.

The %ID versus time plots of the whole body was fit into mono-exponential decay functions in order to calculate the whole body biological half-life of each radiotracer. In the case of ^{55}Co-NOTA-TRC105, a mono-exponential fit to the time-activity curve from the ROI covering the heart was used to obtain the circulation half-life of the radiolabeled antibody. The time-activity curves of the delineable and remaining organs were used for internal dosimetry estimations as explained in Section 4.2.7.

3.2.7 *Internal dosimetry of ^{55}Co-citrate and ^{55}Co-NOTA-TRC105 in humans*

The internal dosimetry of ^{55}Co-citrate and ^{55}Co-NOTA-TRC105 was estimated for a standard adult male of 73.7 kg as defined by Cristy and Eckerman [49] using the OLINDA/EXM software [50]. The organ %ID/g data from small animals was extrapolated to %ID per organ in human using the mass method by Kirschne [52]. Only the biodistribution data from U87MG tumor-bearing mice was employed in the extrapolation to estimate the absorbed dose in humans from ^{55}Co-citrate. Details about the methodology for internal dosimetry were already explained in Chapter 2, Section 2.2.8.

3.2.8 *Tumor dosimetry of ^{55}Co- and ^{58m}Co-NOTA-TRC105 in mice*

The absorbed dose delivered to the 4T1 tumors by accumulated ^{55}Co- and ^{58m}Co-NOTA-TRC105 was estimated using the dose-to-sphere model included in the OLINDA software after inputting the total cumulative decays or disintegrations inside the tumor (which we will assume to be spherical) per administered activity in units of Bq-h/Bq, as it was done in Chapter 2, Section 2.2.9. This value is obtained by trapezoidal integration of the non-decay-corrected time-activity curve of the tumor up to the last time point that was measured (48 hours p.i.) and then by integration from this time point up to infinity assuming that there is only physical decay of the radiotracer.

3.2.9 *Tumor Therapy Study and PET Imaging with the theranostic parent-daughter pair ^{58m}Co and ^{58g}Co*

Three groups of four mice were created from the 4T1 tumor models that were prepared as explained in Section

4.2.6. For testing the therapeutic effect of ^{58m}Co-NOTA-TRC105, one group was intravenously (i.v.) administered with two doses of 151±14 MBq (n = 8), one on day zero and the other one on day 5. The control animals consisted of 1) a non-treated group, in which each mouse was i.v. injected on the same time points as the treated group with PBS; and 2) a non-radiactive treated group, in which each mouse was i.v. injected on the same time points as the treated group with 140 µg of TRC105 diluted in 200 µL of PBS. The body weight was indicated as the average of the individual relative body weight (RBW = W_x/W_0; W_x: weight at day x; W_0: weight at day 0). The tumor volume (V) was determined according to the equation for an ellipsoid volume $V=\pi\times L\times S^2/6$, where L is the long axis and S is the short axis. The values were expressed as the average of the individual relative tumor volumes (RTV = V_x/V_0; V_x: volume at day x; V_0: volume at day 0). The study was ended on day 22. The rate of tumor growth in every group of animals was determined from the slope of the RTV-versus–time curve fitted by linear regression. Statistical comparisons of slopes were made by use of the *F* test ($P < 0.05$).

PET scans were acquired on days 2, 7 (48 h post-injection of each therapeutic dose) and 14 and a PET/CT scan was performed on day 22. Since the positron annihilation signal came from the ^{58g}Co daughter, the % injected dose per gram (%ID/g) of this radionuclide in the tumor and organs was calculated by volume of interest (VOI) analysis assuming that all the ^{58m}Co activity injected was already converted to ^{58g}Co at the time of injection. Moreover, the ^{58g}Co activity co-injected along with the ^{58m}Co therapeutic dose was considered in the %ID/g calculation and estimated to be 3.6±0.5 MBq (n = 8). Imaging was performed using an Inveon microPET/CT (Siemens) setting the acquisition to at least 40 million coincident counts per mouse, which implicated scanning times of 15-20 min per mouse. Static images were reconstructed using three-dimensional ordered subset expectation maximization. Figure 3.7 shows the timeline of the therapy study.

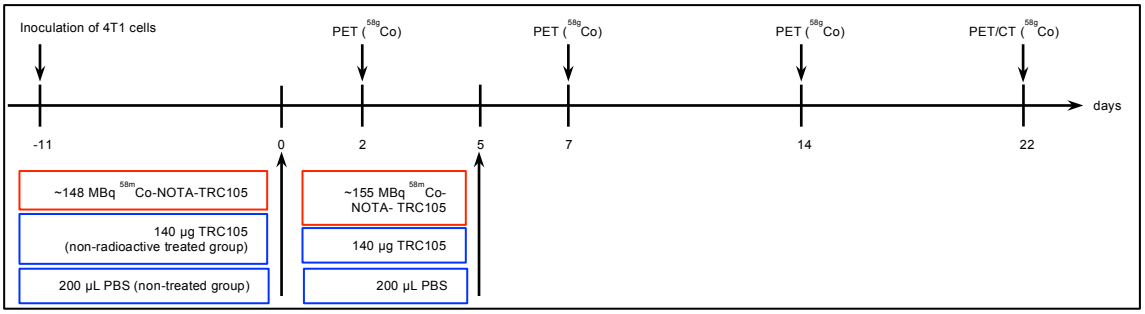

Figure 3.7 Timeline of the therapy study with ^{58m}Co-NOTA-TRC105

3.3 Results and Discussion

3.3.1 *Cyclotron targetry, irradiations and target yields*

The iron electroplating efficiency was 93 ± 4% (n = 18). The average ^{5x}Fe mass lost after each irradiation was 0.6 ± 0.5 mg (n = 13), that is, < 1% of the initial iron target material. This demonstrates that the presented iron electroplating method allows the fabrication of high quality targets for high power irradiations of up to 492 W (8.2 MeV × 60 μA, since there was total degradation of the deuteron beam in the target).

The ^{58}Ni electroplating efficiency was 94 ± 1% (n = 3). The ^{58}Ni mass loss after each irradiation was negligible, that is, within the 0.1 mg error offered by the weighting balance. Hence, the obtained nickel targets electroplated over silver allow for high power irradiations of up to 640 W (16 MeV × 40 μA, although only ~ 2 - 5 MeV are degraded in the electroplated ^{58}Ni and the rest in the silver backing). With both methods, high production yields are attainable after short irradiation times using high deuteron or proton currents.

Table 3.2 lists the experimental activity yields at end of bombardment (EoB) involved in the production of ^{55}Co and how they compare to the predicted yields from published experimental excitation functions. To have a better perception of this data, yields are plotted versus thickness in Figures 3.8(a) and (b).

Table 3.2 Activity yields related to the production of ^{55}Co and comparison to predicted yields from published excitation functions.

Target	Q [μAh]	Δx [mg/cm^2]	^{55}Co Yield [MBq/μAh]	% of predicted from [165]	% of predicted from [166]	^{52}Mn Yield [kBq/μAh]	% of predicted from [165]	^{57}Ni Yield [MBq/μAh]	% of predicted from [166]
^{54}Fe	60.0	24.3	5.5	48%	-	63	50%	-	-
	80.0	46.1	8.9	45%	-	74	43%	-	-
	50.0	49.0	8.1	39%	-	71	41%	-	-
	120.0	47.1	9.9	49%	-	80	47%	-	-
	70.0	37.6	7.7	45%	-	71	45%	-	-
	120.0	46.3	9.4	47%	-	87	51%	-	-
	70.0	45.3	9.5	48%	-	74	44%	-	-
	120.1	65.4	11.3	50%	-	87	50%	-	-
	60.0	59.2	11.2	50%	-	83	48%	-	-
	120.0	58.1	10.6	48%	-	79	45%	-	-
	44.1	52.3	10.0	47%	-	84	48%	-	-
	120.0	63.9	8.8	39%	-	68	39%	-	-
	87.5	61.2	9.9	44%	-	78	45%	-	-
	45.0	58.6	10.4	45%	-	78	45%	-	-
^{58}Ni	10.0	110.2	8.6	-	89%	-	-	1.1	58%
	25.0	214.2	9.5	-	65%	-	-	1.3	64%
	20.0	201.5	9.9	-	69%	-	-	1.0	52%

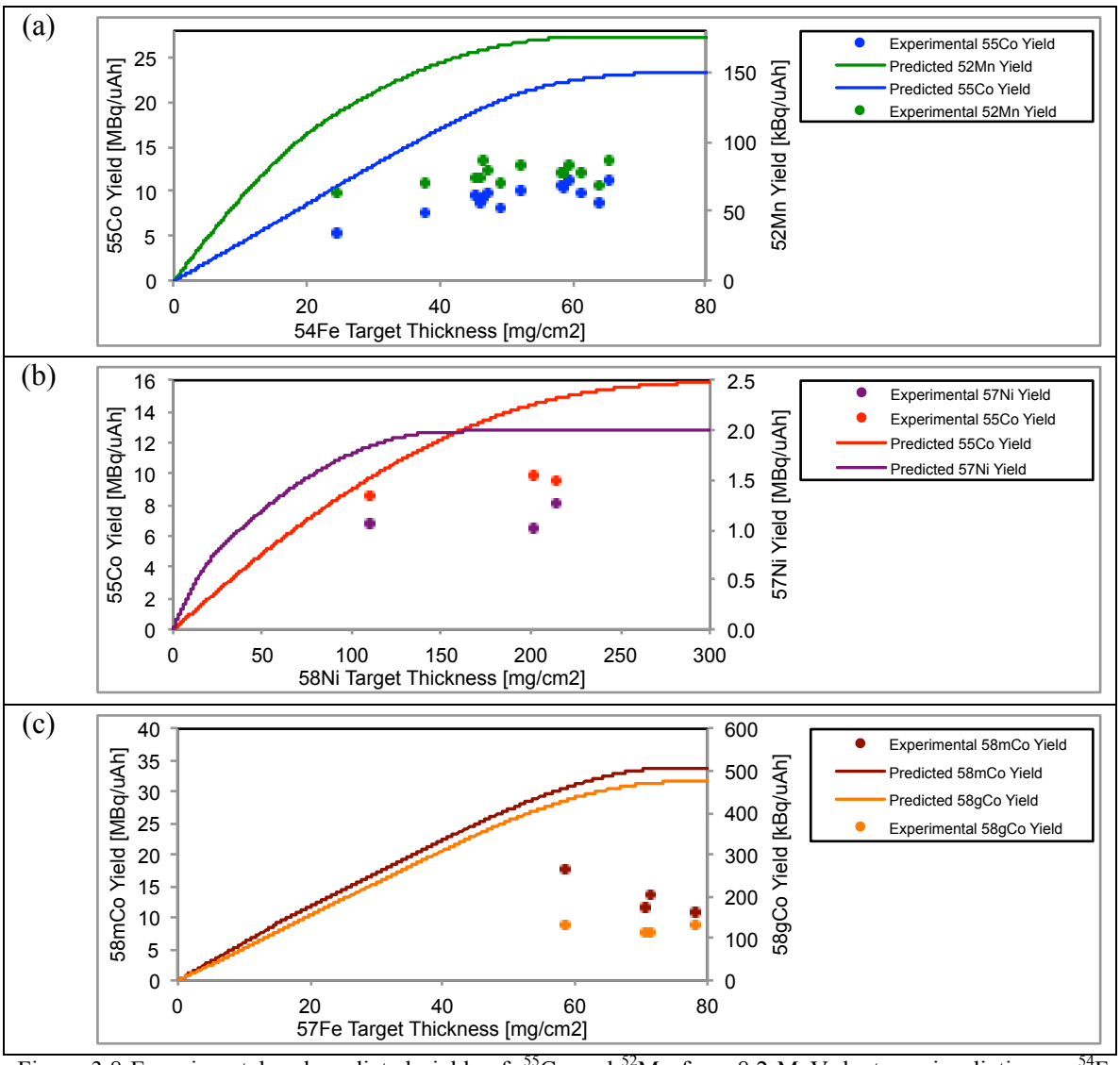

Figure 3.8 Experimental and predicted yields of: ^{55}Co and ^{52}Mn from 8.2 MeV deuteron irradiation on ^{54}Fe targets (a); ^{55}Co and ^{57}Ni from 16 MeV proton irradiation on ^{58}Ni targets (b); ^{58m}Co and ^{58g}Co after deuteron irradiation on ^{57}Fe targets (c). The scale for the ^{55}Co and ^{58m}Co yields is on the y-axis on the left side of the plot and the scale for the other nuclides' yields is on the y-axis on the right side of the plot.

Clearly, the ^{55}Co yields from thick ^{54}Fe and ^{58}Ni targets are comparable. The average and standard deviation of the ^{55}Co yields from all the irradiations on ^{54}Fe, except for the one on a thin 24.3 mg/cm^2 target, are 9.7 ± 1.1 MBq/μAh; and from the three irradiations on ^{58}Ni the ^{55}Co yields are 9.3 ± 0.6 MBq/μAh. Thus, using currents of 60 μA deuterons or 40 μA protons in a typical 1 hour long irradiation would generate batches of 582 and 372 MBq ^{55}Co, respectively.

Co-58m and ^{58g}Co yields at EoB were 13.5±3.1 and 0.13±0.02 MBq/μAh, respectively (n = 4). Therefore, a typical irradiation with 60 μA for 2 h resulted in a ^{58m}Co yield of 1.6 GBq. These results from four irradiations on ^{57}Fe targets are shown in Figure 3.8(c). Figure 3.9 shows the fits to data points of ^{58g}Co activity measured over time

that allowed for the quantification of ^{58g}Co and ^{58m}Co activity at EoB. Table 3.3 contains the irradiation settings and resulting yields from each production run. The main radionuclidic impurity in the separated product was ^{57}Co from ^{56}Fe(d,n), which accounted for a production yield of 0.04±0.01 MBq/μAh.

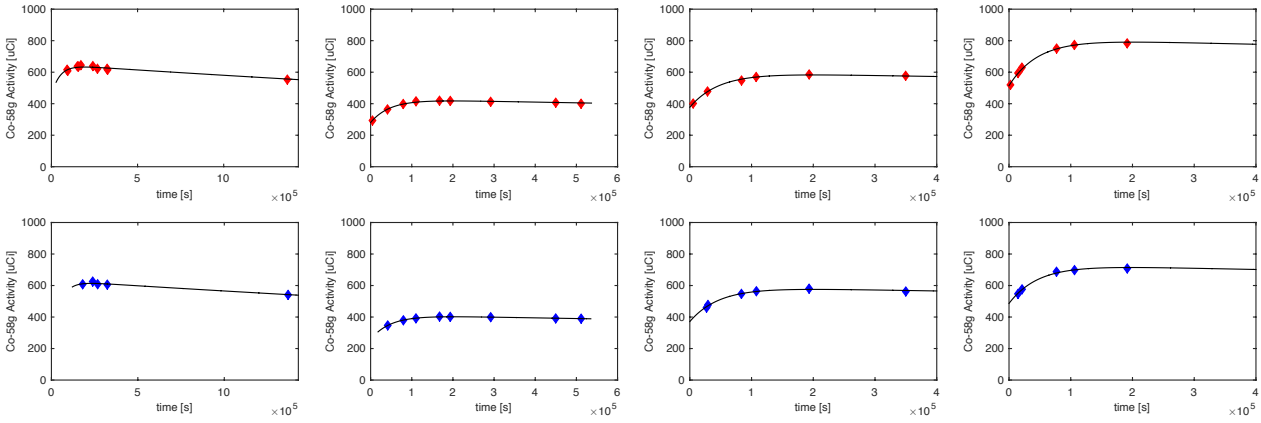

(a) (b) (c) (d)

Figure 3.9 Bateman's equation fits to ^{58g}Co activity values measured at > 6 time points after EoB. Each column corresponds to a production run. The data points in red color were obtained from quantitative gamma spectroscopy on a 10 μL sample from each target dissolution. The data points in blue color come from quantification of a 2-5 μL sample from each separated stock.

Table 3.3 Activity yields related to the production of ^{58m}Co and comparison to predicted yields from published excitation functions.

Target	**Q [μAh]**	**Δx [mg/cm^2]**	**^{58m}Co Yield [MBq/μAh]**	**% of predicted from [185]**	**^{58g}Co Yield [kBq/μAh]**	**% of predicted from [185]**	**^{57}Co Yield [kBq/μAh]**
^{57}Fe	124.0	78.2	11.0	33%	135	27%	38
	90.0	70.6	11.5	35%	115	23%	35
	120.0	71.6	13.5	41%	118	23%	37
	120.0	58.7	17.8	59%	158	28%	52

The ^{58m}Co production yields were also quantified using an efficiency-calibrated low energy HPGe detector looking at the 24.9 keV signature gamma emitted by ^{58m}Co. The yields obtained with this method agree within ± 5% of the those obtained from the fitted parameter to Bateman's equation. Figure 3.10 shows one of the gamma spectra at low energies obtained from one of the separated stocks of ^{58m}Co.

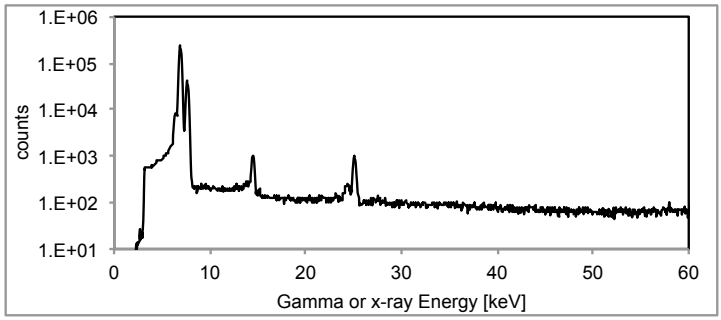

Figure 3.10 Gamma spectrum at low energies with gamma rays at 14.4 and 24.9 keV from ^{57}Co and ^{58m}Co, respectively. The overlapping peaks in the range 6 - 8 keV correspond to the characteristic x-rays from iron.

All experimental yields are on average 46 ± 12% (n = 42) of predicted yields calculated from experimental excitation functions either because these are not correct or because the irradiated surface of the electroplated targets is smaller than the proton and deuteron beam transverse area. The latter is the most probable reason since it is unlikely that all the referenced excitation functions have the same margin of error. In order to verify this, the proton and deuteron beam transverse area was measured by autoradiography of proton- or deuteron-irradiated nickel foils (0.05 mm thick), without the aluminum ring clamp that could potentially collimate the beam and thus hide the maximum extent of the beam strike. The details of this measurement are explained in Appendix C, but the conclusion was that even though the proton beam strike from the PETtrace is centered on the solid target support, it has an elliptical shape with a long and short axis of 1.55 and 1.1 cm respectively, which covers an area that is larger than the electroplated surface (Ø = 0.9 – 1.1 cm), and hence causes a loss of up to 41% and 42% of the proton and deuteron beam intensity, respectively. The details on how these percentage losses were calculated are explained in Appendix C.

3.3.2 *Radiochemical Separation*

The radio-cobalt separation efficiency from iron was 95 ± 3% (n = 11) in 50 μL of 0.1 M HCl. The whole separation process from EoB to the re-dissolution of the separated cobalt took 3 hours 40 minutes. The ^{54}Fe and ^{57}Fe recycling yields after twelve and four production runs on the same target material were 94 ± 4% and 94 ± 3%, respectively. This renders the production of ^{55}Co and ^{58m}Co economical since the replenishment of relatively expensive target material will only be required at an affordable rate.

The ^{55}Co separation efficiency from ^{58}Ni was 92 ± 5% (n = 3) in 100 μL of 0.1 M HCl. The whole separation process took 2 hours. The ^{58}Ni recycling yield after three production runs on the same target was 94 ± 1%.

Both production routes depend on the extraction properties of DGA resin in HCl solution, which were published by Pourmand and Dauphas [192]. Cobalt in HCl solution is expected to be trapped in the DGA resin when the mobile phase solution has a concentration ≥ 8 M HCl, at which the distribution coefficient (log K_d) for cobalt is > 10, while the log K_d for nickel and manganese is < 10^{-1}. Cobalt is expected to release from the column in HCl at a concentration ≤ 3 M, at which the distribution coefficient towards the resin for this element is ≤ 1. This separation method was successfully verified when the amount of DGA resin packed in a 0.5 cm diameter column is ≥ 300 mg. Lower amounts of resin resulted in lower trapping efficiencies (data not shown). Figure 3.11 shows the ^{55}Co elution

profiles from DGA in terms of the percentage of the total radioactivity produced at EoB eluted in each 200 µL fraction.

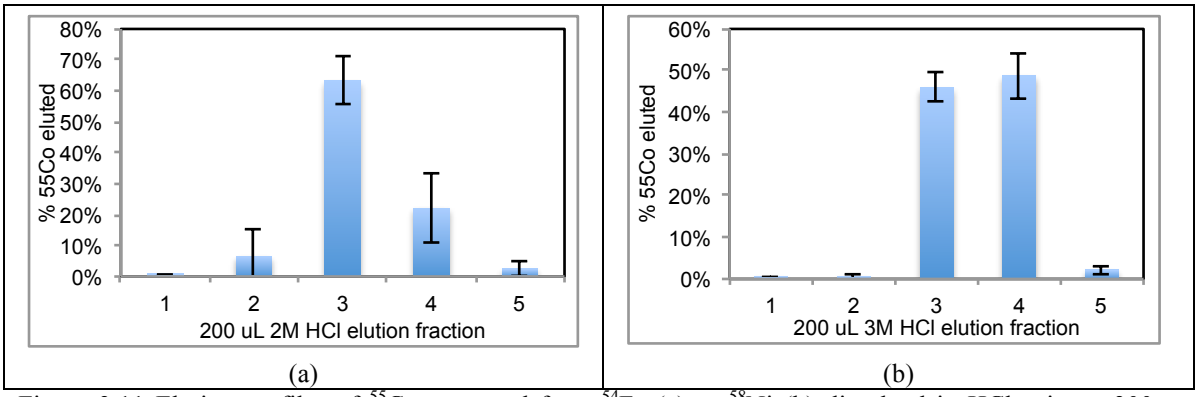

Figure 3.11 Elution profiles of ^{55}Co separated from ^{54}Fe (a) or ^{58}Ni (b) dissolved in HCl using a 300 mg DGA branched resin packed into a 0.5 cm ID column with a flow rate of 1.1 mL/min.

Figure 3.12 shows the complete elution profiles of the main elements involved in the separation of radio-cobalt using a 300 mg DGA branched column in percentage per fraction and in cumulative percentage of the total radioactivity produced at EoB.

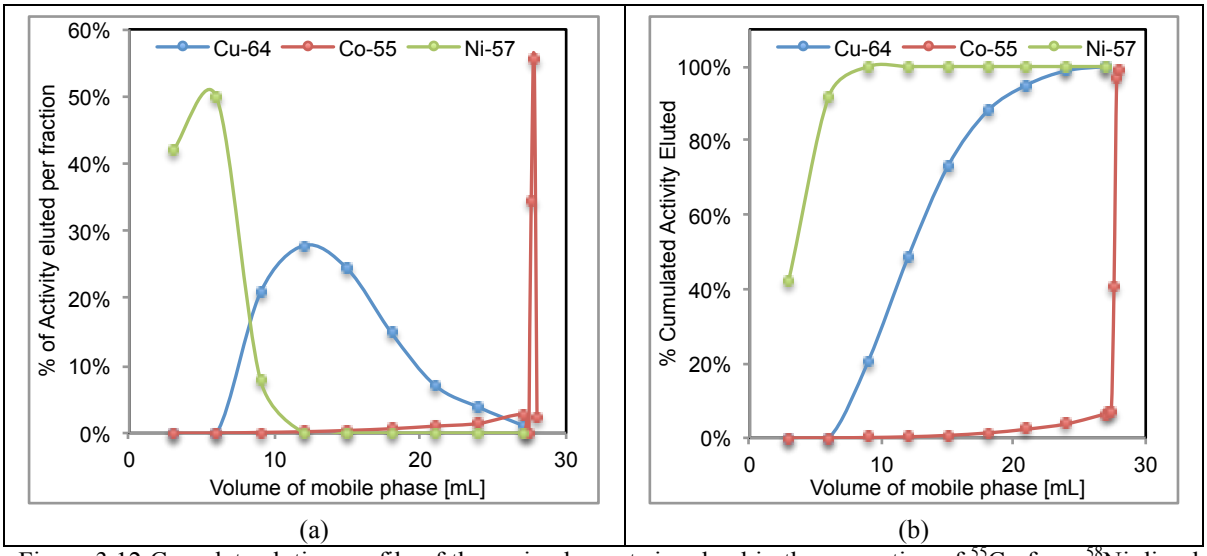

Figure 3.12 Complete elution profile of the main elements involved in the separation of ^{55}Co from ^{58}Ni dissolved in HCl in terms of percentage per volume (a) and cumulative percentage per total volume (b).

The γ-spectra, with a broad energy range of 28-1600 keV, of ^{55}Co and ^{58m}Co from isotopically enriched iron targets before and after the purification process are shown in the first two rows of Figure 3.13. The unpurified ^{55}Co and ^{58m}Co target samples contained significant levels of non-cobalt radionuclidic impurities, such as radio-manganese (^{52}Mn (744 keV) and ^{56}Mn (847 keV), respectively) and ^{24}Na (1369 keV), which could be completely removed after the purification process (Figure 4.13 (a) and (b), second column), resulting in ^{55}Co and ^{58m}Co with

radionuclidic purities at EoB of 99.995 ± 0.001% (n = 10) and 98.7 ± 0.1% (n = 4), respectively. Likewise, the γ-spectra of ^{55}Co from ^{58}Ni targets before and after the separation procedure is shown in the last row of Figure 3.13. In this case the main radionuclidic impurity that was removed in the final product was ^{57}Ni (1378 keV), and final radionuclidic purity at EoB was 98.8 ± 0.3 % (n = 3). Table 3.4 presents the details of the radionuclidic components of each separated product.

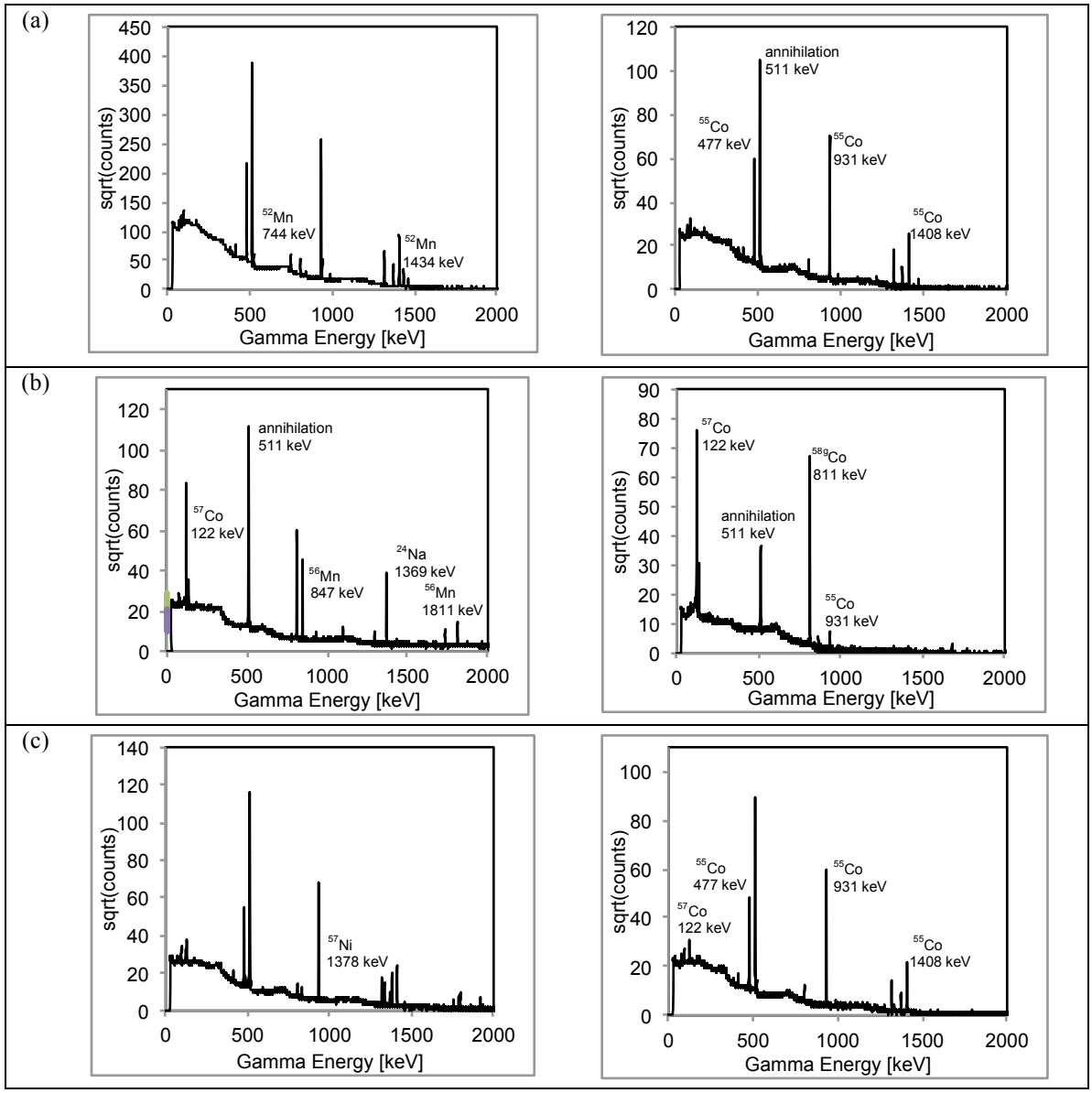

Figure 3.13 Gamma spectra of the target solutions before separation (first column) and of the separated stocks (second column). The separated product in rows (a) and (b) show the absence of gamma peaks from the impurities ^{52}Mn (E_γ=744, 1434 keV) and ^{56}Mn (E_γ=847, 1811 keV) from ^{54}Fe(d,α) and ^{58}Fe(d,α), respectively, and ^{24}Na (E_γ=1369 keV) from ^{23}Na(d,p). Row (c) shows the absence of the gamma peaks from ^{57}Ni (E_γ=1378 keV) from ^{58}Ni(p,pn). The gamma peaks at 122 and 811 keV are characteristic of ^{57}Co and ^{58g}Co, respectively.

Table 3.4 Longed-lived radionuclidic components in the separated radio-cobalt

Desired product	Target	% abundance	Reaction	Product	% in separated stock at EoB
^{55}Co	^{54}Fe	99.93%	^{54}Fe(d,n)	^{55}Co	99.995 ± 0.001%
			^{54}Fe(d,α)	^{52}Mn	0.0011 ± 0.0003%
	^{56}Fe	0.06%	^{56}Fe(d,n)	^{57}Co	0.0025 ± 0.0004%
			^{56}Fe(d,α)	^{54}Mn	*unobserved*
	^{57}Fe	0.005%	^{57}Fe(d,n)	^{58g}Co	*unobserved*
^{55}Co	^{58}Ni	99.48%	^{58}Ni(p,α)	^{55}Co	98.8 ± 0.3%
			^{58}Ni(p,pn)	^{57}Ni	*unobserved*
	^{60}Ni	0.505%	^{60}Ni(p,α)	^{57}Co	1.2 ± 0.3%
	^{61}Ni	0.005%	^{61}Ni(p,α)	^{58g}Co	0.003%
^{58m}Co	^{57}Fe	95.06%	^{57}Fe(d,n)	^{58m}Co	98.7 ± 0.1%
				^{58g}Co	0.93 ± 0.03%
	^{56}Fe	3.04%	^{56}Fe(d,n)	^{57}Co	0.29 ± 0.01%
	^{54}Fe	0.04%	^{54}Fe(d,n)	^{55}Co	0.19%

Figure 3.14 shows the decay logging from samples of separated stocks of ^{55}Co from ^{54}Fe and ^{58}Ni targets. The exponential fit to the logged activity reading from the dose calibrator indicates that the half-life of the separated product from ^{54}Fe and ^{58}Ni is 17.645 ± 0.005 h and 17.80 ± 0.01 h, respectively, which is 0.66 ± 0.03% and 1.5 ± 0.1% greater, respectively, than the accepted value for ^{55}Co: 17.53 h [193]. The latter measurement is larger due to the presence of a higher percentage of ^{57}Co impurity as shown in Table 3.4.

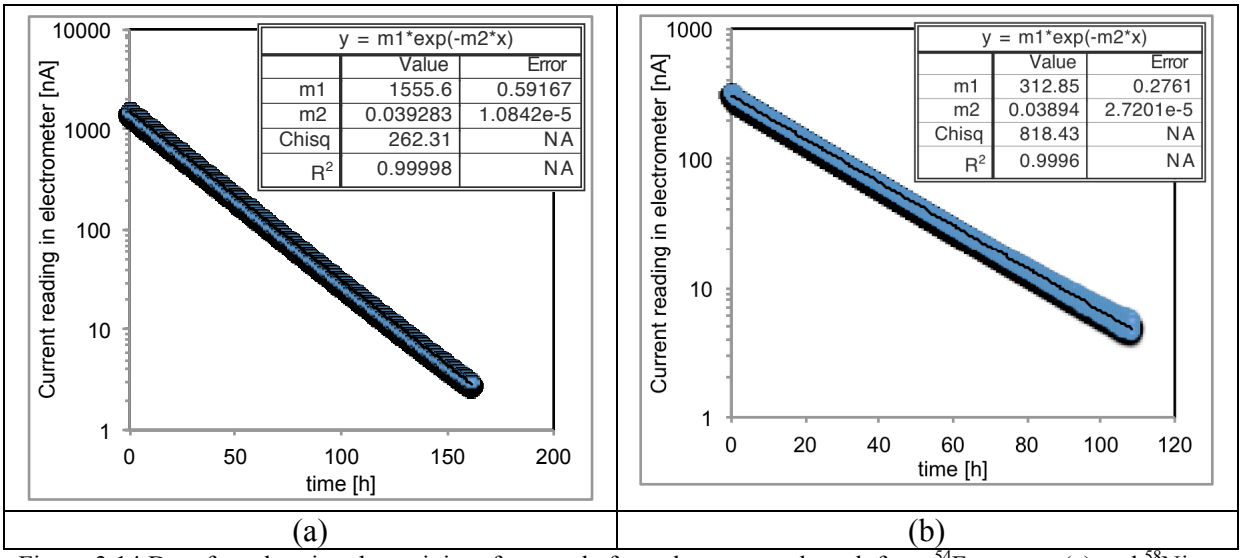

(a) (b)

Figure 3.14 Data from logging the activity of a sample from the separated stock from ^{54}Fe targets (a) and ^{58}Ni targets (b) every 10 seconds for 161 hours and 108 hours, respectively, and exponential fits to the data which indicates that the half-life of the radioactivity in the samples is 17.645 ± 0.005 h and 17.80 ± 0.01 h, respectively.

Ten µL samples from the target solutions as well as 2-20 µL samples from the separated stocks were analyzed for trace metal quantification with Agilent's 4200 MP-AES system. The main metal impurities found in the separated stock of ^{55}Co from ^{54}Fe targets are: cobalt (268 µM), copper (275 µM), nickel (150 µM), silver (95 µM), iron (55 µM) and zinc (48 µM). The main metal impurities in the separated stock of ^{55}Co from ^{58}Ni targets are:

cobalt (2.76 mM), nickel (2.05 mM), silver (148 μM), zinc (125 μM), iron (87 μM) and copper (87 μM). These results are summarized in Table 3.5, along with the corresponding separation factor for each element.

Table 3.5 Results form trace metal analysis on the separated stock of ^{55}Co used for labeling experiments.

Target	Element	Mass [μg]	Molarity [μM]	Separation Factor*
^{54}Fe	Cobalt	1.6 ± 0.2	268 ± 38	-
	Copper	1.7 ± 1.0	275 ± 153	3.6×10^3
	Nickel	0.9 ± 0.8	150 ± 140	5.2×10^3
	Silver	1.0 ± 0.3	95 ± 23	4.2×10^3
	Iron	0.3 ± 0.2	55 ± 41	4.8×10^5
	Zinc	0.3 ± 0.1	48 ± 23	6.4×10^3
^{58}Ni	Cobalt	16.2 ± 9.1	2755 ± 1545	-
	Nickel	12.0 ± 10.0	2046 ± 1705	2.0×10^4
	Silver	1.6 ± 0.9	148 ± 84	8.3×10^2
	Zinc	0.8 ± 0.3	125 ± 40	3.8×10^3
	Iron	0.5 ± 0.3	87 ± 58	1.2×10^3
	Copper	0.6 ± 0.4	87 ± 55	1.2×10^3

* Calculated by dividing the mass in the target solution over the mass in the separated stock.

As it was mentioned in Section 3.3.1, a typical 60 μAh irradiation on a ≥ 37 mg/cm^2 thick ^{54}Fe target generates ~582 MBq ^{55}Co. 95% of this activity is separated, dried down and re-dissolved in 100 μL of 0.1 M HCl, which represents ~553 MBq ^{55}Co with an activity concentration of 5530 GBq/L. Therefore, the effective specific activity (ESA) of the separated ^{55}Co from such representative irradiation would be 5530 GBq/L divided by the total molar concentration of metal impurities shown in Table 3.5, that is, 891 μM, which equals 6.2 GBq/μmol of metal impurities. Likewise, a typical 40 μAh irradiation on a ≥ 110 mg/cm^2 thick ^{58}Ni target would result in a separated stock of ^{55}Co with a concentration of 3420 GBq/L, and the division of this over the total molar concentration of metal impurities, 5248 μM, results in a ESA of 0.65 GBq/μmol of metal impurities. Both of these ESA are between 2 to 10 times lower than the ESA that are obtained from the titration experiments with mainstream chelators, as it will be presented in the following section 3.3.3 and the reason is because not all metal impurities have the same affinity towards the chelator. In other words, not all metal impurities compete for the coordination by the chelator with the same strength.

3.3.3 *Effective Specific Activity of ^{55}Co and ^{58m}Co with Mainstream Chelators*

The retention factors (R_f) of unlabeled ^{5x}Co, ^{5x}Co-NOTA, ^{5x}Co-DOTA, ^{5x}Co-HBED and ^{5x}Co-TETA in the plates after the TLC method were 0.2, 0.5, 0.3, 0.8 and 0.7, respectively. The effective specific activities of ^{55}Co from ^{54}Fe targets with NOTA, DOTA, HBED and TETA, decay-corrected at EoB, were 27 ± 18, 9 ± 5, 17 ± 10 and 14 ± 7 GBq/μmol, respectively. The ESA of ^{55}Co from ^{58}Ni with NOTA is 10 ± 6 GBq/μmol. These results are shown in Figure 3.15.

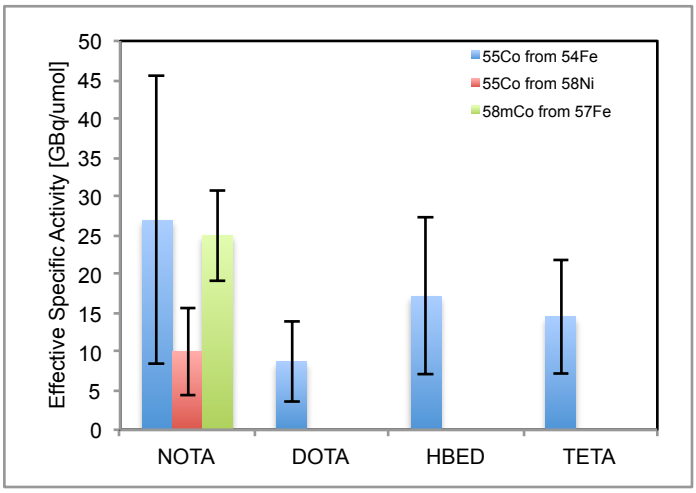

Figure 3.15 Comparison of effective specific activities with mainstream chelators NOTA, DOTA, HBED and TETA of isolated ^{55}Co from ^{54}Fe targets; and of ^{55}Co from ^{58}Ni targets and ^{58m}Co from ^{57}Fe targets when chelated with NOTA.

The thermodynamic stability constants (log K_{ML}) between metals and ligands, such as the chelators employed in this work, provide a convenient gauge of the ligand's relative affinity for a specific metal [61]. However, the differences between the log K_{ML} values of cobalt with the four chelators used to characterize ^{55}Co from ^{54}Fe do not explain by themselves the differences in the measured ESA. For instance, since the stability constants of cobalt chelated with NOTA, DOTA, TETA and HBED are 17.8, 19.3, 16.6 and 19.4, respectively [63], it would be expected that the highest ESA should have be measured with HBED followed by DOTA, NOTA and TETA. However, this was not the case because the amount of other non-radioactive metallic impurities different from cobalt and the affinity of these impurities towards the chelators (inferred from their log K_{ML} values) also need to be taken into account, since both of these factors define how strong is the competition of the impurities for the chelator against ^{55}Co. From the results in Table 3.5, the main non-radioactive metal contaminants in the final product are cobalt and copper and the latter has thermodynamic stability constants when chelated with NOTA, DOTA, TETA and HBED of 20.1, 22.7, 21.7 and 22.9, respectively [63]. Thus, copper is a weaker competitor for the chelation with NOTA compared to the other three chelators and a relatively strong competitor for the chelation with DOTA. This explains in part the order in ESA that was measured in our separated product.

3.3.4 *Image quality of ^{55}Co*

The image quality of ^{55}Co was assessed by visual inspection of the reconstructed microPET images from a Derenzo phantom. As seen in Figure 3.16(a), clear resolution was observed down to a rod diameter of 1.5 mm. Figure 3.16(b) shows the gray intensity profile from a 2.10 mm (10 pixels) wide region of interest that covers the

bottom row of 1.5 mm diameter rods on the image. Each peak was fitted with a gaussian curve revealing a full width at half maximum (FWHM) of 3.7 ± 1.2 mm. The average peak to valley ratio in this profile was 1.28 ± 0.10. These measurements will be compared to those from Derenzo phantoms filled with the other radionuclides that were covered in this thesis in Appendix A.

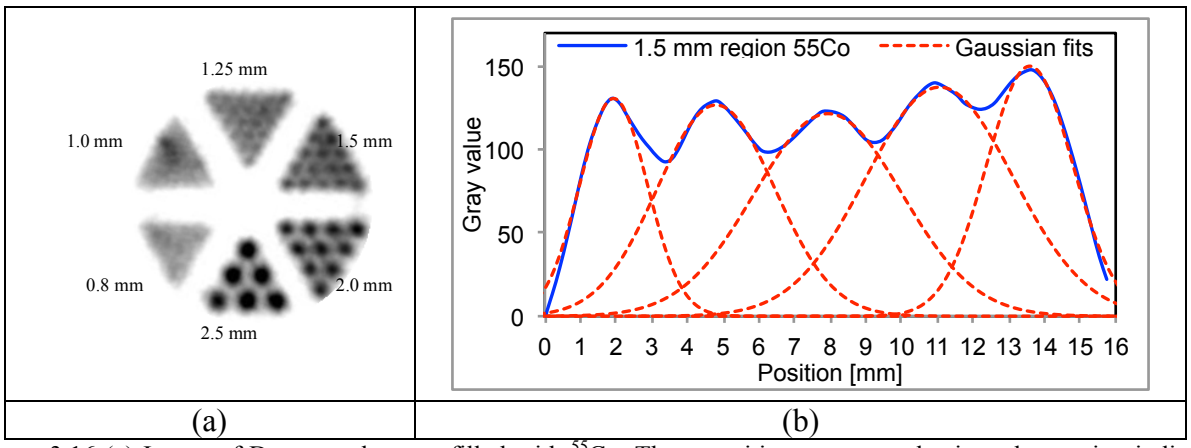

Figure 3.16 (a) Image of Derenzo phantom filled with ^{55}Co. The quantities next to each triangular section indicate the diameter of each of the rods, which are separated from center to center by twice the diameter distance. As the figure shows, rods up to 1.5 mm can be easily resolved in PET images of ^{55}Co. (b) Profile distribution of ^{55}Co from the 1.5-mm rods.

The relatively low spatial resolution is the result of the high maximum energy of 1499 keV of the main positron emitted by ^{55}Co [193], which has a mean and maximum range in water of 2.148 and 7.795 mm, respectively [194].

3.3.5 *Preparation of ^{55}Co- and ^{58m}Co-NOTA-TRC105*

After mixing 20 and 90 µL from each separated stock (0.18 and 1.42 GBq of ^{55}Co and ^{58m}Co at EoB, respectively) with ~190 and ~860 µg NOTA-TRC105, respectively, in 230 µL PBS and waiting for 1 to 2 h, the purification of ^{55}Co- and ^{58m}Co-NOTA-TRC105 resulted in a total labeling yield of 74% and 90±2% (n=3), respectively, in 4 fractions of 400 µL of PBS. However, only the two most concentrated fractions were mixed together and then employed for the animal studies. These fractions accounted for 43% and 67±4%, respectively, of the initial activity, which corresponds to 77 MBq ^{55}Co and ~ 990 MBq ^{58m}Co at EoB. Taking into account that the radiochemical separation takes ~3.7 h and that the labeling reaction was allowed to take ~1-2 h, the decay-corrected labeling yield from ^{58m}Co must be multiplied by a factor of 0.64 from decay. In the case of ^{55}Co, the labeling was done the day after production, specifically 22 hours after EoB, which accounts for a decay factor of 0.41. Therefore, the actual activity that was administered for PET imaging and targeted radioimmunotherapy was actually 32 MBq ^{55}Co and ~640 MBq ^{58m}Co in 800 µL of PBS, respectively. These formulations were split in 200 µL doses for administration into the 4T1 tumor bearing mice.

3.3.6 *Biodistribution and pharmacokinetics of ^{55}Co-citrate and ^{55}Co-NOTA-TRC105 in tumor-bearing mice*

PET scans were performed after administration of ^{55}Co-citrate at 0.5, 4 and 24 hours post-injection (p.i.) on three 4T1-tumor bearing mice and at 1, 5, 8 and 24 h p.i. on three U87MG-tumor bearing mice. Figure 3.17(a) and (b) show the coronal and sagittal maximum intensity projection (MIP) images of one of the mouse from each group. In both tumor models, no circulation of ^{55}Co-citrate in the blood pool was observed since the %ID/g intensity in the heart is similar to that found in the muscles or any other background tissue. Both tumor models showed very small uptake, although in the U87MG xenograft it was sufficient for visible contrast when the intensity scale bar is set to a maximum of 10 %ID/g as shown in Figure 3.17(a). Constant urinary excretion is visible throughout every time point as seen by the high intensity in signal in the kidneys and urinary bladder. The last time point, at 24 h p.i., clearly shows that ^{55}Co-citrate has almost cleared from every organ.

On the contrary, PET scans at 4, 24 and 48 h p.i. of ^{55}Co-NOTA-TRC105 show prominent systemic circulation of the radiolabeled antibody and gradually increasing concentration of radioactivity in the 4T1 tumor Figure 3.17(c). High accumulation in the liver and spleen is a common characteristic of full antibodies due to the binding of their Fc component to receptors found in lymphocytes and macrophages, which eventually accumulate in sinusoid capillaries found in these organs [195].

Figure 3.18 shows the biodistribution over time and the time-activity curves in terms of %ID/g and %ID, respectively, from quantifications of VOIs covering the whole body, tumor, adductor and biceps femoris muscles and the delineable organs: liver, kidneys and urinary bladder in the subjects injected with ^{55}Co-citrate; and heart, liver and spleen in those injected with ^{55}Co-NOTA-TRC105. The %ID plots also include exponential fits to the whole body VOI from which the biological half-life of ^{55}Co-citrate was quantified as 13.8 h and 13.9 h in the 4T1- and U87MG-tumor bearing mice, respectively. Similarly, exponential fits to the whole body and heart time-activity curves from the 4T1 tumor-bearing mice administered with ^{55}Co-NOTA-TRC105 reveal whole body biological and circulation half-lives of 239.8 h and 56.0 h, respectively.

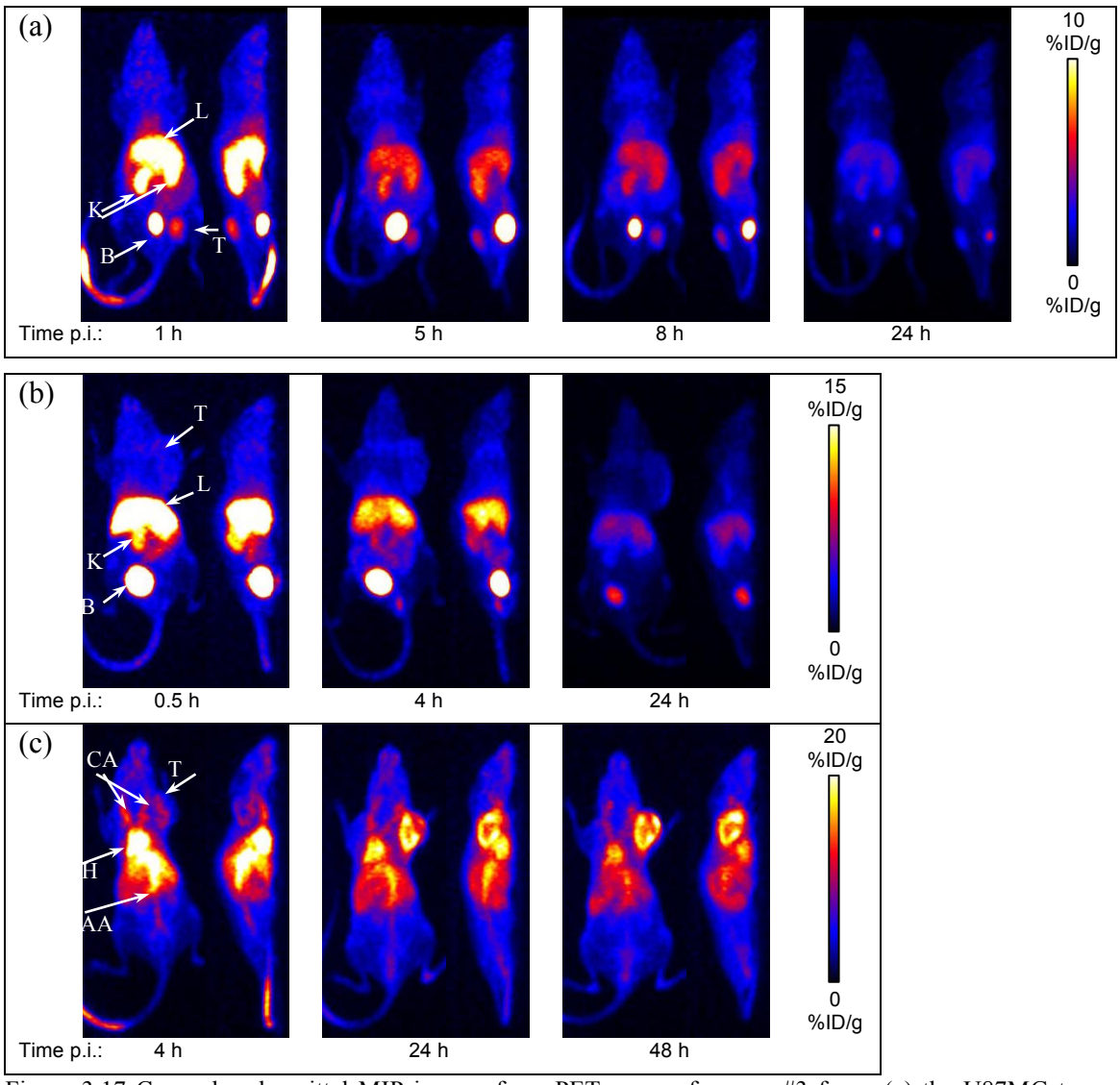

Figure 3.17 Coronal and sagittal MIP images from PET scans of mouse #3 from: (a) the U87MG tumor-bearing group at 1, 5, 8 and 24 h injected with ^{55}Co-citrate; (b) the 4T1 tumor-bearing group at 30 min, 4, and 24 h p.i of ^{55}Co-citrate; and (c) the 4T1 tumor-bearing group at 4, 24 and 48 h p.i of ^{55}Co-NOTA-TRC105. The ^{55}Co uptake level is color coded by the %ID/g bar shown on the right of each set of images. The PET scans for the other two mice in each group show the same trend in biodistribution of each ^{55}Co-labeled agent. T: tumor; L: liver; K: kidneys; B: bladder; CA: carotid arteries; H: heart; AA: abdominal aorta.

The biodistribution of ^{55}Co-citrate is useful to understand the fate of ^{55}Co that de-chelates or exchanges ligand from the targeting bioconjugate vector to ligands in non-specific tissues. Our results indicate that ^{55}Co has a low retention in the body, having cleared by more than 70% after 24 h p.i. in both tumor models via the liver, kidneys and ultimately the urinary bladder (Figures 3.18 (a) and (b)). Furthermore, even though there is a significant tumor uptake of ^{55}Co-citrate in both tumor models (2.2 ± 0.9, 2.0 ± 0.8, 1.8 ± 0.6 and 1.2 ± 0.3 %ID/g at 1, 5, 8 and 24 h p.i., respectively, in the U87MG tumor and 2.4 ± 0.3, 2.0 ± 0.2 and 1.5 ± 0.1 %ID/g at 0.5, 4 and 24 h p.i., respectively, in the 4T1 tumor), this gradually clears over time and is more that two times lower of what is typically

observed with a radiolabeled antibody such as ^{55}Co-NOTA-TRC105, which displayed %ID/g values of 5.3 ± 0.6, 12.1 ± 2.2 and 12.7 ± 1.9 at 4, 24 and 48 h p.i., respectively. Therefore the overestimation of uptake in the tumor due to inclusion of de-chelated ^{55}Co uptake in the quantification will not affect the measurement significantly. As it will be shown in Chapter 4, ^{64}Cu-citrate shows biodistribution properties opposite to ^{55}Co-citrate, namely a long whole body biological half-life and high uptake and long retention time in several organs and in both 4T1 and U87MG tumor xenografts.

The biodistribution of ^{55}Co-NOTA-TRC105 in 4T1 tumor-bearing mice shown in Figure 3.18(c) agrees with that of ^{64}Cu-DOTA-TRC105, ^{64}Cu-NOTA-TRC105, ^{89}Zr-DFO-TRC105, ^{66}Ga-NOTA-TRC105 and ^{52}Mn-DOTA-TRC105 in the same tumor model [196-200], which is not surprising due to the high thermodynamic stability of all the metal-chelate pairs involved in these studies. The high tumor uptake is due to the binding of TRC105 to the CD105 receptors that are overexpressed in vascular endothelial cells undergoing angiogenesis, which seek to satisfy the demand for vasculature by the proliferating tumor cells [201, 202].

From the biodistribution chart it can be seen that the tumor contrast in terms of tumor-to-muscle (T/M) ratio does not change significantly over time with ^{55}Co-citrate in both tumor models, since both the tumor and muscle uptake decrease over time almost at the same rate. The average and standard deviation of all the T/M ratios is 3.4 ± 0.5 for ^{55}Co-citrate in U87MG tumor-bearing mice and 1.8 ± 0.4 for ^{55}Co-citrate in 4T1 tumor-bearing mice. On the contrary, the T/M ratio of the uptake of ^{55}Co-NOTA-TRC105 rapidly increases over time with values of 2.5 ± 0.5, 5.8 ± 1.4 and 5.7 ± 1.0 at 4, 24 and 48 h p.i. Likewise, the tumor-to-liver (T/L) contrast gradually increases over time with T/L ratios of 0.4 ± 0.1, 1.2 ± 0.2 and 1.5 ± 0.3 in the same incremental times post-injection, which means that for PET scans beyond 48 h p.i. ^{55}Co-NOTA-TRC105 is a good radiotracer for liver metastasis.

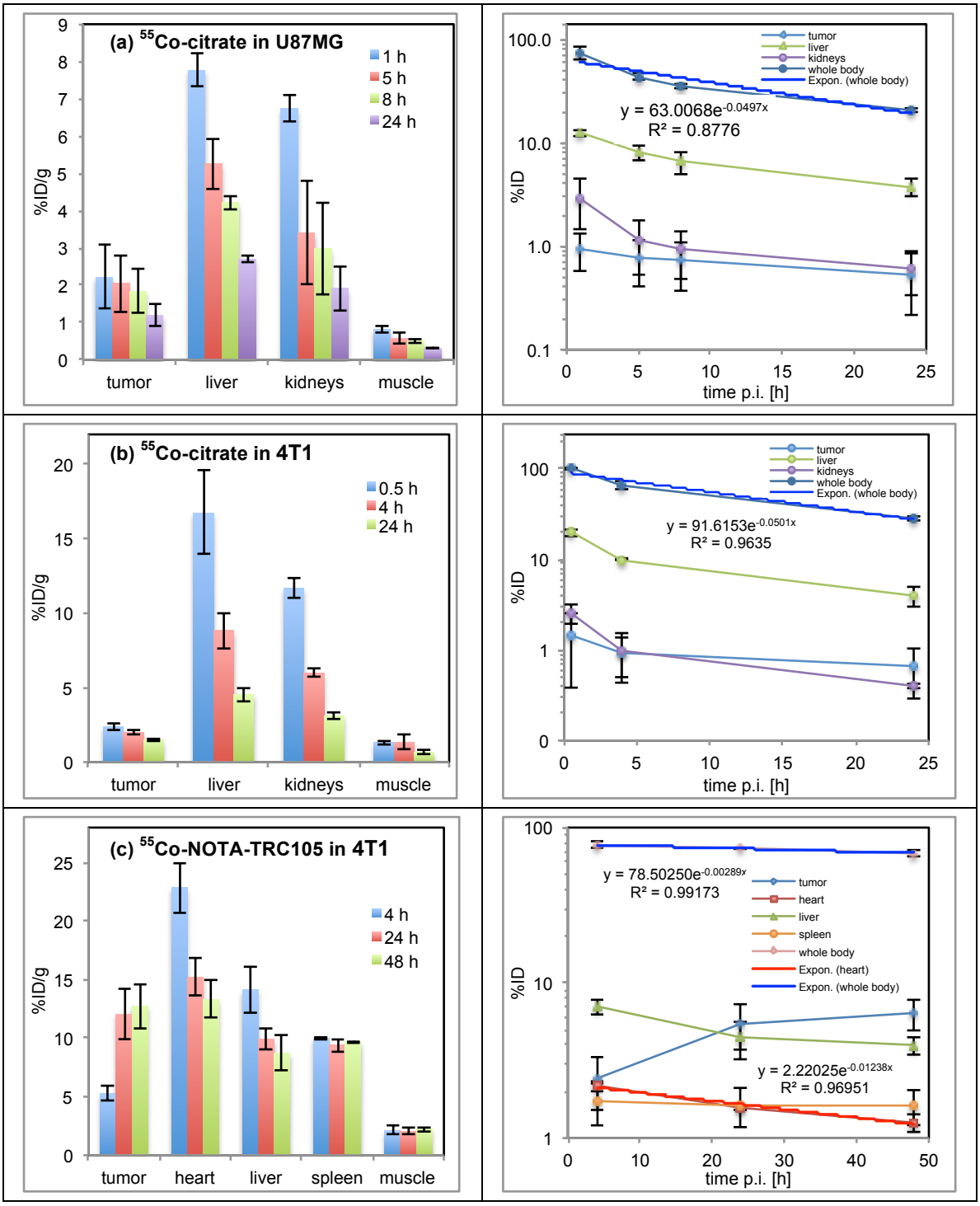

Figure 3.18 Quantitative PET data presented as biodistribution charts in terms of %ID/g and time-activity curves in terms of %ID from: ^{55}Co-citrate in mice bearing U87MG tumors (a) and 4T1 tumors (b); and ^{55}Co-NOTA-TRC105 in mice bearing 4T1 tumors (c). All data is decay-corrected to time of injection. Error bars represent standard deviation from quantifications in three mice.

An important implication of the observed tumor targeting is that the diagnostic label ^{55}Co can be substituted by the therapeutic emitter of low-energy electrons ^{58m}Co in order to deliver these high-LET emissions to the tumor cells

for cancer treatment. In the following two sections on internal dosimetry the therapeutic potential of ^{58m}Co-NOTA-TRC105 will be evaluated.

3.3.7 *Internal dosimetry of ^{55}Co-citrate, ^{55}Co-NOTA-TRC105 and ^{58m}Co-NOTA-TRC105 in humans*

Only the biodistribution data from U87MG tumor-bearing mice was employed for the estimation of human dosimetry after administration of ^{55}Co-citrate, since more time points post-injection in this tumor model were analyzed. Table 3.6 shows the %ID uptake values of ^{55}Co-citrate and ^{55}Co-NOTA-TRC105 extrapolated to a 73.7 kg standard adult male as defined by Cristy and Eckerman [49], using the mass extrapolation method by Kirschne [52], with the whole body mass per U87MG and 4T1 mouse set to the average values of 23.0 g and 19.5 g, respectively.

Table 3.6 Extrapolation to %ID uptake of ^{55}Co in standard adult male organs from studies in mice.

Organ	**Organ mass in human male adult [g] [49]**	**Conversion factors %ID/g in mouse to %ID in human**		**%ID ^{55}Co-citrate**				**%ID ^{55}Co-NOTA-TRC105**		
		23.0 g (U87MG)	**19.5 g (4T1)**	**1 h**	**5 h**	**8 h**	**24 h**	**4 h**	**24 h**	**48 h**
Heart	840	0.265	0.224	-	-	-	-	5.1	3.4	3.0
Spleen	183	0.057	0.048	-	-	-	-	0.5	0.5	0.5
Liver	1910	0.596	0.505	4.6	3.1	2.5	1.6	7.1	5.0	4.4
Kidneys	299	0.093	0.079	0.6	0.3	0.3	0.2	-	-	-
Urinary bladder	-	-	-	12.7	3.1	0.9	0.5	-	-	-
Remaining organs	Balance	Balance	Balance	57.2	37.2	31.4	18.4	64.6	64.9	60.3

After setting these %ID uptake values in the EXM portion of the OLINDA software and fitting them to mono-exponential functions, the software automatically calculated the cumulative number of decays in each source organ and then the absorbed dose in every target organ considered by the software as well as the total body effective dose. The doses deposited by the therapeutic analogue ^{58m}Co-NOTA-TRC105 were obtained from OLINDA by keeping the pharmacokinetic data from ^{55}Co-NOTA-TRC105 and replacing the cobalt nuclide by ^{58m}Co. The effective doses were estimated as 81.5 μSv/MBq ^{55}Co-citrate, 172 μSv/MBq ^{55}Co-NOTA-TRC105 and 1.86 μSv/MBq ^{58m}Co-NOTA-TRC105 injected. Figure 3.19 shows the absorbed dose to each target organ after administration of each one of these agents.

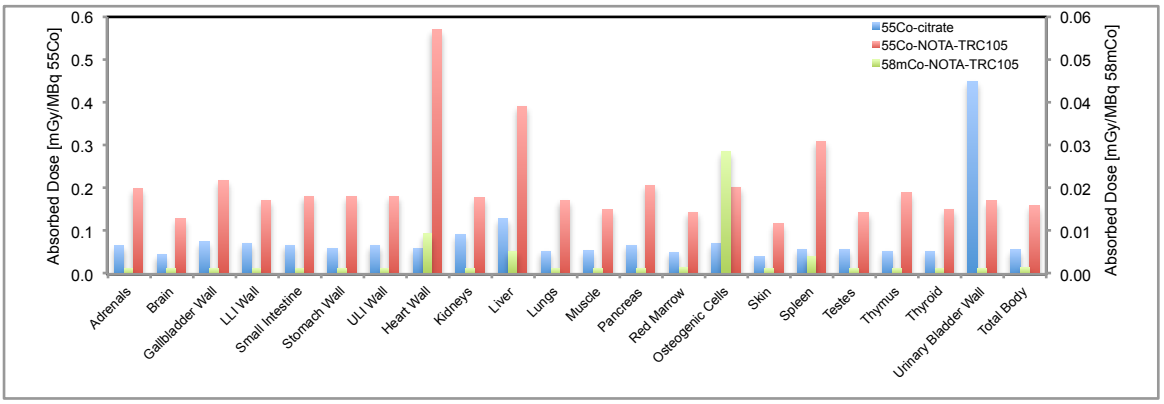

Figure 3.19 Absorbed dose to the organs of a standard adult male after administration of ^{55}Co-citrate, ^{55}Co-NOTA-TRC105 or ^{58m}Co-NOTA-TRC105. The scale on the left side is for ^{55}Co and the scale on the right side if for ^{58m}Co. Notice that there is one order of magnitude difference between them.

Clearly, the urinary bladder wall is the critical organ after the administration of ^{55}Co-citrate, with an absorbed dose of 449 μGy/MBq. The heart wall and the liver are the critical organs after administration of ^{55}Co-NOTA-TRC105, with absorbed doses of 570 and 391 μGy/MBq, respectively. These absorbed doses suggest that a typical activity for a PET scan of between 19 and 74 MBq ^{55}Co [135, 136, 138, 139, 142, 203] labeled to either one of these radiotracers can be safely administered into a patient without reaching the 50 mGy annual limit to any organ recommended by the FDA [75].

The critical tissue after injection of the therapeutic analogue ^{58m}Co-NOTA-TRC15 is predicted to be the osteogenic cells with an absorbed dose of 28.6 μGy/MBq. All the other tissues receive < 10 μGy/MBq and most of them < 2 μGy/MBq. This is not surprising due to the shallow penetration of the low energy emissions of ^{58m}Co. The emitted electrons have energies < 24.8 keV with a range in tissue < 10 μm [41]; and the most energetic gamma emitted has an energy of 24.9 keV with mean free path (the reciprocal of the linear attenuation coefficient) in tissue that is < 30 mm [41]. Thus, most of the dose caused by ^{58m}Co is absorbed in the source organs where the radiotracer is accumulated, which in the case of ^{58m}Co-NOTA-TRC105 are the heart, liver and spleen. OLINDA indicates that the osteogenic cells receive the highest dose per administered activity due to the uptake in the remaining organs, which includes the bones. So the bones as a source organ are the cause of the high dose to the osteogenic cells, which is a 10 μm layer (single cell thickness) that surrounds the trabecular and cortical bone surfaces [204-206]. Thus, all the energy from electrons emitted by ^{58m}Co with < 6 μm range are absorbed within this layer, making it the critical organ. Fortunately, osteogenic cells are not a very radiosensitive tissue [206] and electrons are stopped before reaching the highly radiosensitive marrow space that is enclosed within bone tissue. Indeed, not just higher

injected activities of low-energy electron emitters compared to beta emitters are tolerated in small animals [207], most importantly, higher absorbed doses in the blood are tolerated if the source of the radiation is a low-energy electron emitter [208].

3.3.8 *Tumor dosimetry of ^{55}Co- and ^{58m}Co-NOTA-TRC105 in mice*

The absorbed dose delivered to the 4T1 tumors in mice by ^{55}Co-NOTA-TRC105 and the predicted dose that will be delivered by the therapeutic ^{58m}Co-NOTA-TRC105 was estimated using the dose-to-sphere model of OLINDA, which only requires the total cumulative decays or disintegrations inside the tumor per administered activity in units of MBq-h/MBq. This value was obtained by trapezoidal integration of the non-decay-corrected time-activity curve of the tumor up to the last time point that was measured (48 hours p.i.) and then by integration from this time point up to infinity assuming: 1) that the uptake phase in the tumor is over, 2) that there is no biological clearance and 3) that there is only physical decay of the radiotracer. The formula for this latter integration is Equation 2.7 from Chapter 2 of this dissertation. Thus, after substitution for the physical half-lives, the integrals are 0.57×%ID(t = 48 h) and 0.01×%ID(t = 48 h) for ^{55}Co and ^{58m}Co, respectively.

Figure 3.20(a) shows the tumor uptake over time of ^{55}Co-NOTA-TRC105 obtained from VOI analysis of the PET images in units of %ID decay-corrected to the time of injection. Figures 3.20(b) and (c) show this same data after consideration of decay of ^{55}Co and ^{58m}Co, respectively; including the continuation of the time-activity curve after the last measured time point, assuming that only physical decay occurs up to infinity

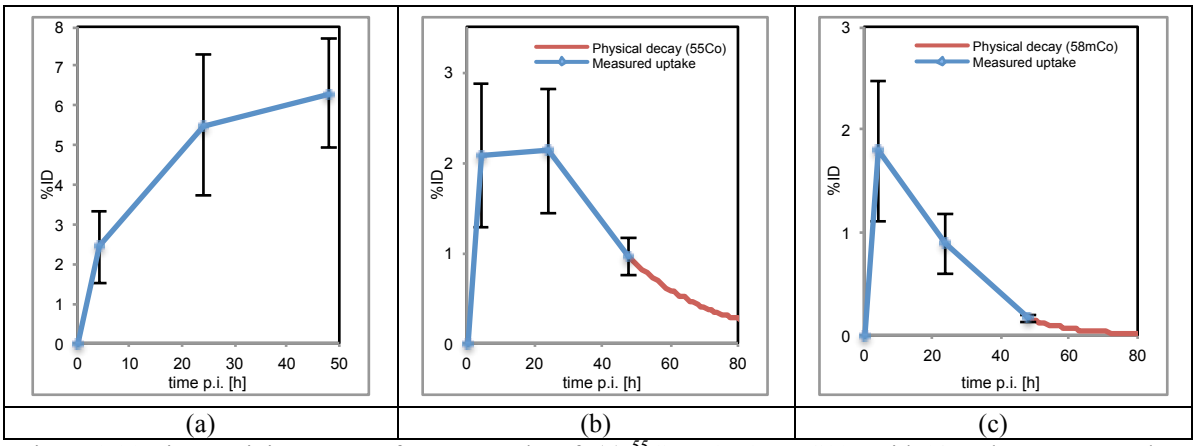

Figure 3.20 Time-activity curves of tumor uptake of: (a) ^{55}Co-NOTA-TRC105 with %ID decay-corrected to time of injection; (b) ^{55}Co-NOTA-TRC105 and (c) ^{58m}Co-NOTA-TRC105 with %ID considering physical decay over time.

The total cumulative decays in the 4T1 tumors for each non-decay corrected curve are 0.87 and 0.43 Bq-h/Bq for ^{55}Co and ^{58m}Co, respectively. After logging in these two values in the dose-to-sphere model of OLINDA, the

total absorbed dose to spheres of unit-density material with masses between 10 mg and 6 kg are calculated. Figure 3.21 shows the output from OLINDA along with a power fit to this data.

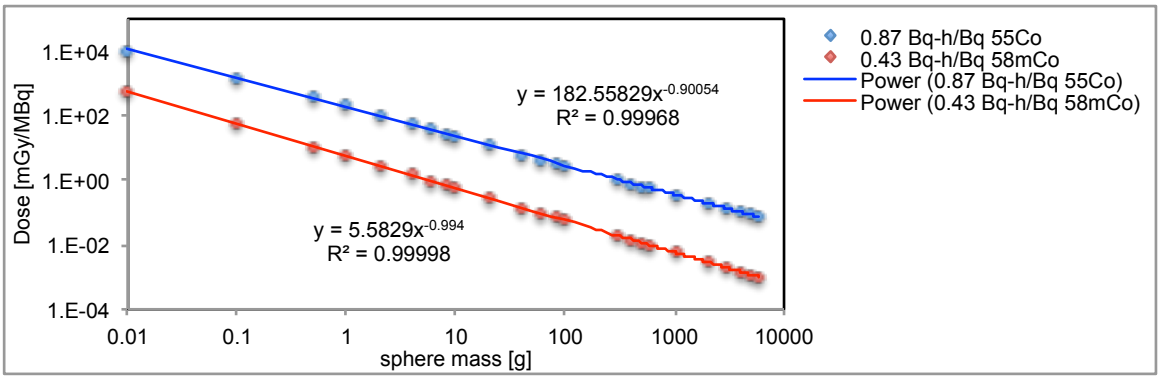

Figure 3.21 Absorbed dose to unit-density spheres homogeneously filled with ^{55}Co or ^{58m}Co after the cumulative number of decays indicated in the legend, which were obtained from integration of the time-activity curves of ^{55}Co-NOTA-TRC105 in 4T1 tumors in mouse models.

From the plot in Figure 3.21 we can estimate what is the necessary amount of ^{55}Co- or ^{58m}Co-NOTA-TRC105 that has to be administered in order to have a therapeutic effect in 4T1 tumor-bearing mice like the ones employed in this study. The average volume of the VOIs drawn over the whole tumor in all the PET images was 494 ± 201 mm^3, which corresponds to a mass of 0.49 ± 0.20 g, assuming that the tumors have a density of 1 g/cm^3. Therefore, we can assume that the treated tumor mass would be about 0.5 g and from the fitted curves in Figure 3.21 we can predict that each MBq of ^{55}Co- or ^{58m}Co-NOTA-TRC105 that is administered into a mouse bearing 4T1 tumors would result in an absorbed dose to the tumor of 341 and 11 mGy, respectively. Hence, under the conservative assumption that up to 230 Gy are required for tumor response, as it was explained in section 2.3.9, the amount of ^{55}Co- or ^{58m}Co-NOTA-TRC105 that would have to be administered in order to have observable tumor regression in a mouse bearing a 0.5 g 4T1 tumor would be 0.68 and 20.69 GBq, respectively.

However, the absorbed dose from ^{58m}Co that was calculated using the sphere model only takes into account the nominal energy emitted per decay and does not take into account the enhancement in cytotoxicity caused by low energy electrons when they deposit their energy in the DNA or in the nucleus of cells to which they are targeted. This enhancement in cytotoxicity could be interpreted as a multiplication on the absorbed dose, similar to the multiplication by a weighting factor in health physics in order to estimate the equivalent dose caused by high-LET radiation such as alpha particles [209]. This enhancement in cytotoxicity has been quantified *in vitro* in cell cultures using the relative biological effectiveness (RBE) concept that relates the amount of absorbed dose from low-LET radiation, such as an external beam of 662 keV gammas from a ^{137}Cs source, to the absorbed dose from incorporated

high-LET radiation such as that caused by alpha emitters or by DNA-targeted Auger emitters, when both absorbed doses result in a cell survival fraction of 37% (D_{37}). For instance, ^{125}I-labeld deoxyuridine (a DNA targeting molecule) and ^{210}Po (an alpha emitter) have an RBE between 4 and 9 because 0.5 to 1 Gy deposited by these radiations has the same cell killing effect (D_{37}) as ~4.5 Gy deposited by an external beam of 662 keV gammas [172]. Hence, if the TRC105 antibody delivers the ^{58m}Co payload to the vicinity of the endothelial cells nuclei, perhaps up to 9 times less activity would have to be administered in order to cause tumor regression in small animal xenograft.

3.3.9 *Tumor therapy study and PET imaging with the theranostic parent-daughter pair ^{58m}Co and ^{58g}Co*

Figure 3.22 shows the results of the therapy study. The three groups show a constant tumor growth but the groups treated with ^{58m}Co-NOTA-TRC105 and TRC105 show a slower growth rate. By the end of the study on day 22, the RTVs are 8.2 ± 3.1, 9.8 ± 5.3 and 13.8 ± 3.5 for the ^{58m}Co-NOTA-TRC105 treated, the TRC105 non-treated and the PBS non-treated groups, respectively. However, the RBW plot in Figure 3.22(b) clearly shows a drop in body mass in the treated group during the first 7 days after injection of the first dose, which indicates that the radiation dose caused general toxicity.

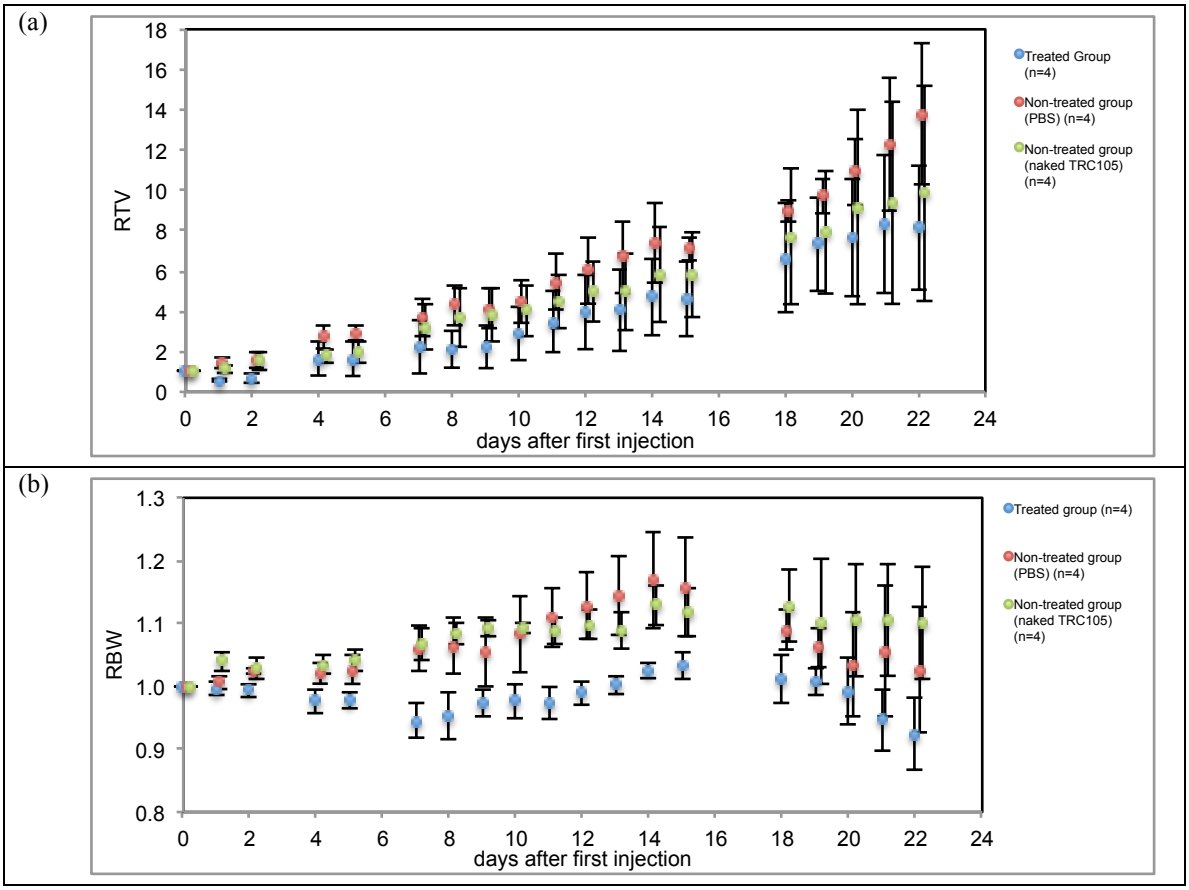

Figure 3.22 Relative tumor size (a) of 4T1-bearing mice after treatment with 151±14 MBq (4.1±0.4 mCi) of ^{58m}Co-NOTA-TRC105 on days 0 and 5. Control animals were injected with non-radioactive TRC105 and PBS on the same days. (b) Relative body weight of the two groups.

Statistical comparisons with the *F* test of the slopes from each group in the RTV versus time curves reveal that there is statistically significant differences ($P < 0.05$) between the group treated with ^{58m}Co-NOTA-TRC105 and the non-treated group injected with PBS and also between the group treated with non-radioactive TRC105 and the non-treated group. However, there is no statistically significant difference ($P > 0.05$) between the groups injected with ^{58m}Co-NOTA-TRC105 and "naked" TRC105. This is not surprising since it is known that TRC105 by it self has therapeutic properties due to it's anti-angiogenic effects [210]. ^{58m}Co-labeled TRC105 had no significant effect in the tumor growth most likely because the amount of activity that was administered was too low. From the tumor dosimetry results obtained in section 3.3.8 using the "macroscopic" MIRD formalism, we estimated that ^{58m}Co-NOTA-TRC105 delivers 11.1 mGy/MBq to a 0.5 g tumor, and since we only administered, on average, a total of 303 MBq into each mouse, the total absorbed dose to the tumor xenograft was merely 3.4 Gy, which is one to two orders of magnitude lower than the typical amount required for regression of solid tumors [80]. However, we were

hoping to observe an enhancement effect in case the dose from the low energy electrons emitted by ^{58m}Co reached the sensitive nucleus of the endothelial cells that are the target of the TRC105 antibody.

Figure 3.23(a) shows the coronal MIP images obtained from the PET scans that were performed on days 2, 7, 14 and 22, as it was outlined in the timeline shown in Figure 3.7. Figures 3.23(b) shows the biodistribution of the ^{58g}Co activity in the segmentable organs and tumor lesion in %ID/g. Figure 3.23(c) shows the comparison of %ID values of ^{55}Co-NOTA-TRC105 versus ^{58g}Co-NOTA-TRC105, both at 48 h p.i. The agreement of these values justifies the continuation of the time-activity curve of ^{55}Co-NOTA-TRC105 that was shown in Figure 3.18(c), with the data points of ^{58g}Co-NOTA-TRC105 at days 14 and 22. Exponential fits to the %ID values in the heart and whole body reveal circulation and biological half-lives of 5.3 and 6.7 days, respectively, which are 128% higher and 33% lower, respectively, than the half-lives calculated in section 3.3.6 from the fits to only three data points using ^{55}Co-NOTA-TRC105. It can be seen that from day 14 on (9 days p.i. of the second dose) the agent has almost cleared from every organ except the tumor. Quantitatively from the PET data, the %ID remaining in the whole body on days 2, 7, 14 and 22 is 84.8 ± 3.9, 58.1 ± 4.8, 32.0 ± 7.3 and 13.9 ± 6.7, respectively, while the tumor uptake is 6.0 ± 5.3, 5.8 ± 3.0, 7.1 ± 2.6 and 6.3 ± 3.3 %ID at these time points. The retention of ^{58g}Co in the tumor is explained by the residualizing effect of most radiometals, which are retained intracellularly in lysosomes after they are transported through the cell membrane via receptor-mediate endocytosis of the radiolabeled antibody [211-213].

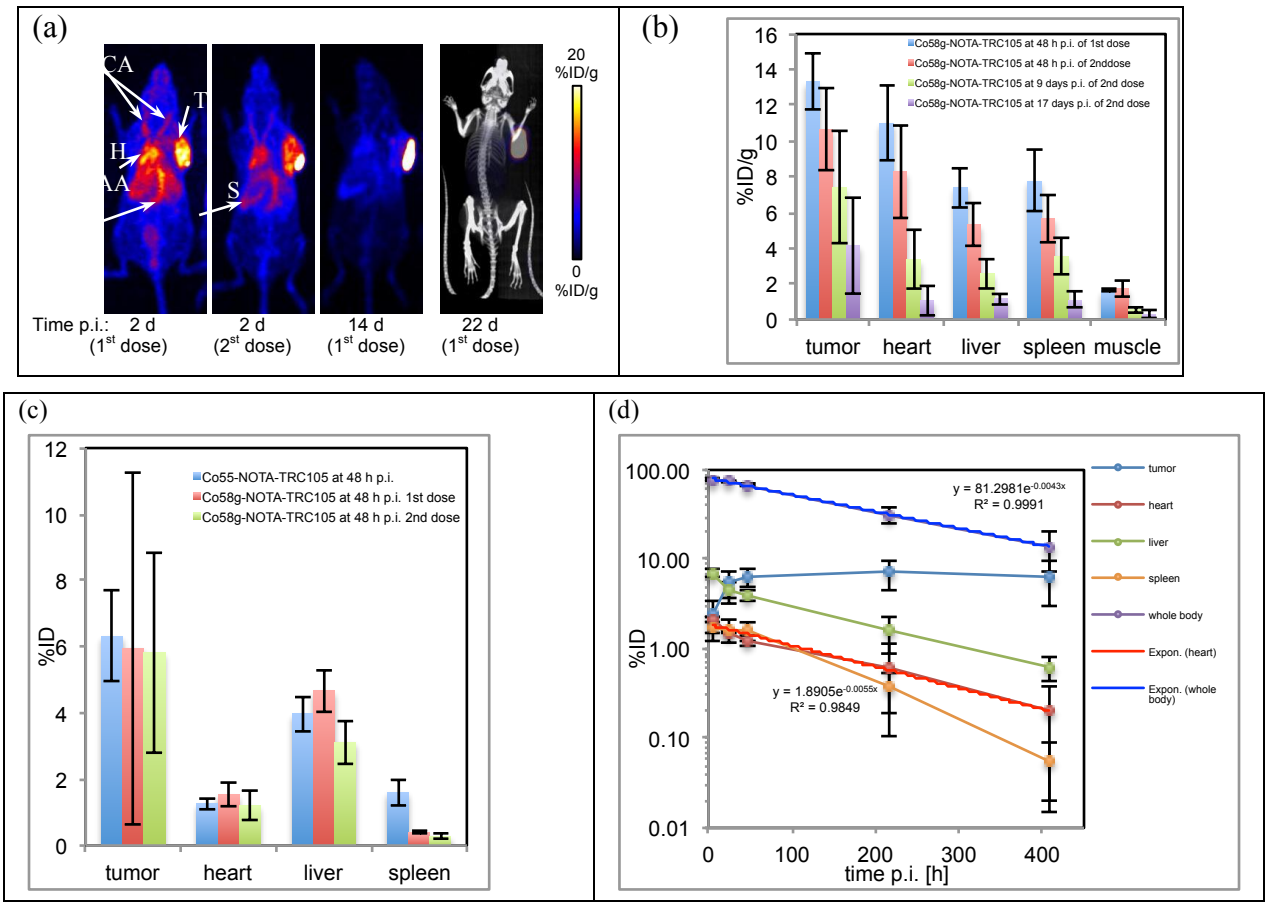

Figure 3.23 (a) Coronal MIP images from PET scans of 4T1 tumor-bearing mouse #1 at 48 h, 96 h, 14 d and 22 d p.i. of the first therapeutic dose of ^{58m}Co-NOTA-TRC105. Only the last PET scan was complemented by a x-ray computed tomography (CT) scan. The ^{58g}Co uptake level is color coded by the %ID/g bar shown on the right. The PET images of the other three mice show the same trend in biodistribution. (b) Biodistribution chart in terms of %ID/g from the PET images. (c) Comparison of the %ID values at 48 h p.i. of ^{55}Co-NOTA-TRC105 and ^{58g}Co-NOTA-TRC105. (d) Time-activity curves in terms of %ID combining the data from ^{55}Co-NOTA-TRC105 at 4, 24 and 48 h p.i. with the data from ^{58g}Co-NOTA-TRC105 at 14 and 22 d p.i. of the first therapeutic dose of ^{58m}Co-NOTA-TRC105. All data is decay-corrected to time of injection. Error bars represent standard deviation from quantifications in all the mice in each group. CA: carotid arteries; H: heart; AA: abdominal aorta; T: tumor; S: spleen.

For the quantification of the ^{58g}Co uptake in the PET images we considered the amount of ^{58g}Co that was co-injected with the ^{58m}Co plus the ^{58g}Co that was generated by the decay of it's parent, ^{58m}Co. As a matter of fact, the reasons of why the first scan was performed 48 h p.i. of the therapeutic dose, were: 1) to verify that the uptake at 48 h agreed to that obtained from the PET analogue ^{55}Co-NOTA-TRC105 (section 3.3.6); and 2) because at this time ^{58m}Co had almost completely decayed to ^{58g}Co. In fact, it has decayed by 97% from the computation 1-exp(-ln(2)*48h/9.1h), which we assumed it was 100% in order to be able to use the simplified Bateman equation that relates the activity of the daughter nuclide generated by total decay of the parent nuclide:

$$A_{daughter}\left(t \gg t_{\frac{1}{2}parent}\right) \approx A_{parent}\frac{\lambda_{daughter}}{\lambda_{parent}-\lambda_{daughter}}e^{-\lambda_{daughter}\cdot t} = A_{parent}\cdot 0.00538\cdot e^{-\frac{\ln(2)}{t_{\frac{1}{2}daughter}}\cdot t}$$

Equation 3.2

where A_{parent} is the activity of ^{58m}Co at the time of injection. This amount of generated activity of the daughter (^{58g}Co) was decay corrected to the time of injection of each dose using the daughter's half-life (70.86 h), as if it had been already present from this time point, and then added to the co-injected activity of ^{58g}Co that was present at the time of injection. Table 3.7 presents the average activities that were injected into the group of four mice in each of the two therapeutic doses and the total amount of ^{58g}Co from which the PET images are generated and from which the uptake values were quantified after making the assumptions that are pointed out in the next paragraph.

Table 3.7 Activities at time of injection of each therapeutic dose.

Dose #	**^{58m}Co [MBq]**	**^{58g}Co generated [MBq]**	**^{58g}Co co-injected [MBq]**	**Total ^{58g}Co [MBq]**
First	146.2 ± 11.6	1.2 ± 0.1	2.0 ± 0.2	3.2 ± 0.3
Second	156.3 ± 16.8	1.4 ± 0.2	2.5 ± 0.3	3.9 ± 0.5

Since the %ID/g values from the PET scans are decay corrected to the time of injection of the first therapeutic dose, the total amount of ^{58g}Co from the second dose was decay-corrected 5 days to the time of the first injection and added to the total activity from the first dose. Hence, the total amount of ^{58g}Co that was input in the PET analysis software was 3.2 MBq, from the first dose for the analysis of the scan on day 2, plus 3.9*exp(ln(2)*5 d / 70.86 d = 4.1 MBq, from the second dose, which is equal to 7.3 MBq total for the analysis of the images from days 5, 19 and 22, even though in reality only 3.2 + 3.9 = 7.1 MBq of ^{58g}Co had been administered into each mouse as shown in Table 3.7.

Similar to how it was done in section 3.3.7, the internal dosimetry of ^{58g}Co-NOTA-TRC105 in a 73.7 kg standard adult male as defined by Cristy and Eckerman [49], was estimated with OLINDA from the time-activity curves shown in Figure 3.23(d) after extrapolation to %ID values in human. The effective dose in this case turns out to be 0.76 mSv/MBq ^{58g}Co, which even though seems high in a per MBq basis, it is not so when we consider that the amount of MBq of ^{58g}Co that will be administered is at least two orders of magnitude lower than the amount of MBq of therapeutic ^{58m}Co that would be injected, as we can see in Equation 3.2. Furthermore, the estimated ED conservatively assumes that all of the ^{58g}Co generated by ^{58m}Co is present right after administration, which is not true, since it takes ~48 h p.i. to build up to ~100% as we explained before. Hence, the ED is actually lower.

As it was mentioned in section 3.3.2, the separation of ^{58m}Co from ^{57}Fe takes ~3.7 hours and the radiolabeling takes ~1 h. Hence the radiotherapeutic agent would be ready for injection ~5 hours post-EoB. From the results in

Table 3.4, at this time point the radionuclidic purity of ^{58m}Co is as follows: 97.9 ± 0.1% ^{58m}Co, 1.58 ± 0.04% ^{58g}Co, 0.43 ± 0.01% ^{57}Co and 0.22% ^{55}Co. Thus, assuming that a therapeutic dose of 37 GBq ^{58m}Co would have to be administered into a human patient, that would imply that 599 MBq ^{58g}Co, 161 MBq ^{57}Co and 83 MBq ^{55}Co would also be co-injected. Table 3.8 shows the effective dose contributions from these impurities, which were calculated with OLINDA after substitution of the cobalt radionuclide in the software, keeping the same time-activity curve for ^{5x}Co-NOTA-TRC105 shown in Figure 3.23(d) after extrapolation to %ID values in human. Table 3.8 also includes other published dosimetry results from clinically established targeted radiotherapy agents for comparison.

Table 3.8 Comparison of typical activities and resulting ED in a standard male patient of established TRT agents and the ^{58m}Co-NOTA-TRC105 presented in this work.

Nuclide	$t_{1/2}$	**Electron or β⁻ ave. E [keV]**	**Electron or β⁻ ave. Range [mm]**	**Targeting vector**	**Activity injected [GBq]**	**Effective Dose (ED) [mSv/MBq]**	**Total ED [mSv]**	**Ref.**
^{58m}Co	9.1 h	23	0.005	TRC105	37	0.0019	70	This work
^{58g}Co	70.9 d	-	-		0.60	0.76	456	
^{57}Co	272 d	-	-		0.16	0.14	22	
^{55}Co	17.5 h	-	-		0.08	0.17	14	
^{111}In	2.8 d	32	0.009	pentetreotide	3.7	0.073	270	[214]
^{131}I	8.0 d	190	0.18	tositumomab (Bexxar)	1.8 - 5.6	-	650 – 750	[215]
^{177}Lu	6.6 d	149	0.12	PSMA-617	1 to 3 cycles of 6.0	0.037 – 0.083 per cycle	222 - 498 per cycle	[216]
^{90}Y	2.7 d	934	2.7	ibritumomab (Zevalin)	max. 1.2	-	230 - 790	[217]

However, as it was pointed out in Chapter 2, section 2.2.8, the effective dose concept is not appropriate for therapy cases in which acute effects from radiation are prevalent due to the fact that excessively high amounts of radioactivity are administered. Nevertheless, we believe that the ED is a good metric that allows us to compare the ^{58m}Co-labeled radio-immunotherapeutic employed in this work with other established agents such as those referenced in Table 3.8.

Even though the long half-life of ^{58g}Co may seem as an inconvenience, the fact that it can be used as a diagnostic probe for PET for many days after therapy seems very convenient. For instance, the change in %ID/g uptake in the tumor can be used as a diagnostic metric to evaluate the efficacy of the treatment caused by ^{58m}Co. In Figure 3.23(b) we can see how the %ID/g values after 48 h p.i. decrease over time even though the %ID values at these same time points remain almost fixed, as shown by the time-activity curve of the tumor in Figure 3.23(d). The reason is because the mass of the tumor is increasing over time, indicating that the therapy was not successful.

Hence, if the therapy had been successful, the trend in %ID/g in the tumor over time would be incremental since a fixed amount of %ID is being divided over a shrinking mass of tumor.

3.3.10 *Future work (increase production yield of ^{58m}Co)*

The production capacity of ^{58m}Co with our PETtrace dual particle cyclotron can be increased considerably if, instead of bombarding 8.2 MeV deuterons on thick enriched ^{57}Fe targets, we irradiate ≤ 16 MeV protons on thin targets of enriched ^{58}Fe, as it was reported by Thisgaard et al [181]. From the measured excitation function of the ^{58}Fe(p,n)^{58m}Co reaction by Sudar and Qaim [183] show in Figure 3.3(a), we can expect the production yields versus proton energy and target thickness shown in Figure 3.24.

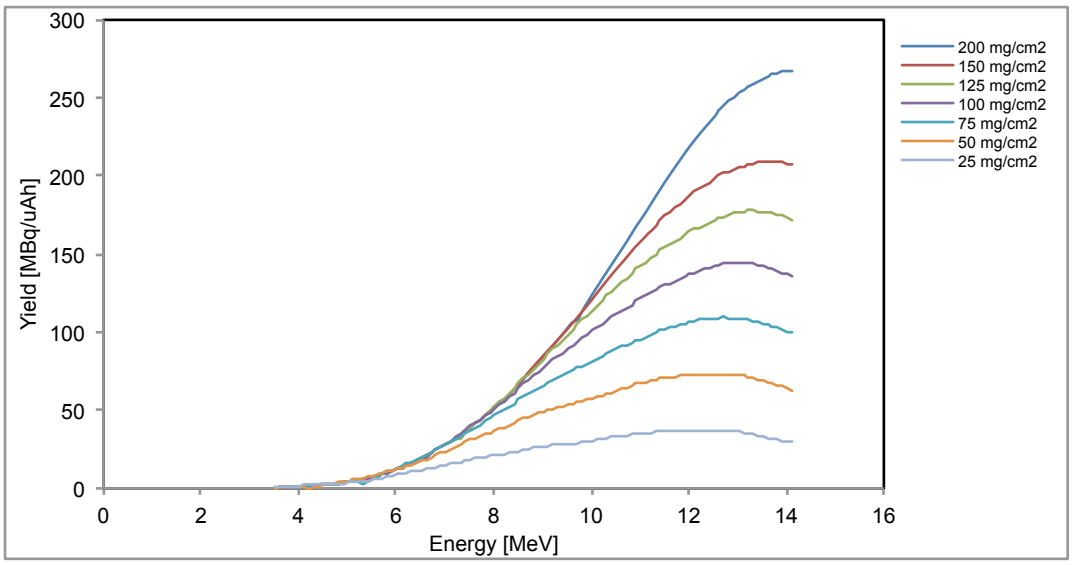

Figure 3.24 Thin target yields of ^{58m}Co from ^{58}Fe based on the ^{58}Fe(p,n)^{58m}Co cross-section data measured in the range from 3.54 to 14.12 MeV by Sudar and Qaim [183].

Clearly, the optimum incoming proton energy on the target depends on its thickness and since isotopically enriched ^{58}Fe has a market price of ~US$30/mg[3], a thick target for 16 MeV (435 mg/cm^2 [184]) may not be economically feasible to make. Thus, assuming that a 100 mg target electroplated over 1 cm^2 is a practical choice, we can see from Figure 3.24 that the optimum proton energy for this target would be 13.0 MeV with a resulting thin target yield of 145 MBq/μAh, which is more than ten times greater than the yield that we have reported in this chapter from deuterons on thick ^{57}Fe targets (13.5±3.1 MBq/μAh). However, since the electroplated surface of ~1.0 cm^2 is narrower than the PETtrace proton beam transverse area (See Appendix C), we can expect about ~50% of the predicted yield or ~72.5 MBq/μAh. Now, assuming that a proton current of up to 50 μA is feasible, batches of ~37

[3] Personal communication with sales representative from ISOFLEX.

GBq ^{58m}Co are attainable after a 10 hour long irradiation. Alternatively, irradiations can be performed using the the 11 MeV proton beam from the CTI RDS 112 cyclotron, whose beam transverse area is < 1.0 cm^2 (data not shown) is about the same size as the 1.0 cm^2 electroplated surface with ^{58}Fe, and therefore the experimental yields in this case should closely match the predicted yields shown in Figure 3.24. However, maximum proton currents of 20 μA are available with the RDS 112 cyclotron, which is less than half of the maximum current that can be delivered with the PETtrace cyclotron, so the increment in production yield may not be reflected in larger batches of ^{58m}Co per unit-time of irradiation. For instance, a 100 mg/cm^2 ^{58}Fe target irradiated with 11 MeV protons on the RDS 112 cyclotron should generate ~120 MBq/μAh (from Figure 3.24), and therefore a 10 hour-long irradiation with 20 μA would generate ~24 GBq ^{58m}Co, which is lower than the ~37 GBq that are expected after shooting on a similar 100 mg/cm^2 ^{58}Fe target with 50 μA for 10 hours using 13.0 MeV protons after degradation of the 16 MeV protons from the PETtrace.

3.3.11 *Comparison of our separation methods to previous publications and clinical perspective*

Comparing the separation chemistry methods of this work with previously reported methods [146, 155, 159, 161, 162, 181, 182] we found many improvements. First, more than 99.99% of the co-produced ^{52}Mn from ^{54}Fe(d,a) was removed from the separated ^{55}Co; second, more than 95% of the produced ^{55}Co in either ^{58}Ni or ^{54}Fe targets was isolated at a very high concentration in ≤ 600 μL, which is volume that can be easily evaporated for reconstitution in any desired volume of any desired acid or buffered solution; and third, we have reported the highest effective specific activity of ^{55}Co and the second highest of ^{58m}Co toward established chelators. All of these improvements are due to the chromatographic method that we have discovered using a small column filled with DGA branched resin. Table 3.9 compares our work with the results from previous publications.

Table 3.9 Comparison of production methods of radio-cobalt for biomedical applications

Sep. Method	**Target**	**p^+ or d^+ Energy [MeV]**	***i* [μA]**	**A Yield [MBq/μAh]**	**^{5x}Co Sep. yield [%]**	**Vol. of eluted ^{5x}Co [mL]**	**Nuclidic impurities at EoB**	**ESA [GBq/μmol] (chelator)**	**Target recycling efficiency [%]**	**Ref.**
AEC	plated ^{58}Ni (99.87%)	15 - 9	10	9.6	*Not reported*	15	0.5% ^{57}Co	*Not reported*	*Not reported*	[159]
AEC	plated ^{58}Ni (99.48%)	15	30	6 ± 1	92 ± 3	10	0.2% ^{57}Co	1.96 (DOTA)	95 ± 3	[146]
SPEC (DGA)	^{58}Ni (99.48%)	16 - 11	40	9.3 ± 0.6	92 ± 5	0.4	1.2 ± 0.3% ^{57}Co	10 ± 6 (NOTA)	94 ± 1	This work
Solvent extrac-tion + AEC	pressed $^{54}Fe_2O_3$/Al powder (91.6%)	12.6 - 5	4	13	*Not reported*	40	0.06% ^{57}Co <0.01% ^{52}Mn <0.02% ^{56}Co	*Not reported*	> 80	[161]
AEC	pressed ^{54}Fe (97.08%)	12	3	62.9	90	40	0.016% ^{57}Co	*Not reported*	*Not reported*	[162]
AEC	plated ^{54}Fe (99.84%)	8.5	18	1.4	> 97	8 - 10	*Not reported*	> 0.21 (DOTA)	*Not reported*	[155]
AEC	plated ^{58}Fe (99.86%)	10.1	18	10.7	> 97	8 - 10	0.85% ^{58g}Co	> 4 (DOTA)	*Not reported*	[155, 181]
AEC + Chroma-fix 30-PS-HCO_3	"	"	"	"	"	0.2	"	84 (DOTA)	"	[182]
AEC + SPEC (DGA)	^{54}Fe (99.93%)	8.2	60	10.3 ± 0.8	94 ± 3	0.4 – 0.6	0.002% ^{57}Co 0.001% ^{52}Mn	27 ± 18 (NOTA) 9 ± 5 (DOTA) 17 ± 10 (HBED) 15 ± 7 (TETA)	94 ± 4	This work
"	^{57}Fe (95.06%)	8.2	"	13 ± 3	96 ± 2	"	0.93% ^{58g}Co 0.29% ^{57}Co	25 ± 6 (NOTA)	94 ± 3	This work

AEC: Anion Exchange Chromatography
SPEC (DGA): Solid Phase Extraction Chromatography with DGA resin

The first highlight of the three production methods reported in this chapter compared to the other ones presented in Table 3.9, is that we have used the highest bombardment currents without any compromise in target integrity. In terms of radiochemical separation, our method to isolate ^{55}Co from ^{58}Ni is clearly superior to any of the reported methods shown in Table 3.9, especially with regards to the volume in which ^{55}Co is separated and the effective specific activity. Our method separates ^{55}Co in 400 μL, a volume that can be quickly evaporated even in the original 1.5 mL vial where the separated fractions are collected, which avoids the use of a large vessel (>10 mL) connected to a rotoevaporator in which a variable loss of radioactivity may be lost in the large surface area of the glassware as it is difficult to re-dissolve all the activity off the walls of the vessel with a small volume (< 1 mL) of diluted HCl acid. Similarly, in our separation method of ^{55}Co from ^{54}Fe, the use of the DGA branched extraction resin in the

second part of the separation allows for: 1) the elution of the separated activity in a small volume of 400 to 600 μL that is easy to evaporate; 2) the almost complete removal of ^{52}Mn impurities; and 3) a separated ^{55}Co with the highest reported effective specific activity. However, the introduction of a post-purification step with a Chromafix 30-PS-HCO_3 by Thisgaard et al [182], allows for the concentration of the activity in an even smaller volume (200 μL) with an order of magnitude improvement in ESA, although they only applied this extra step in the production of ^{58m}Co and not in the production of ^{55}Co.

Furthermore, we are the first research group that has reported the effective specific activity of ^{55}Co with HBED, which has recently become very relevant in the field of nuclear medicine since the HBED-PSMA molecule labeled with ^{68}Ga is increasingly becoming the workhorse for detection and monitoring of prostate cancer [218]. Hence, this discovery opens the possibility of introducing the Auger and conversion electron emitter ^{58m}Co for therapy of prostate cancer with the HBED-CC-PSMA targeting vehicle.

The main contribution of our production method for ^{58m}Co is that we have demonstrated that there is a more economical alternative to the proton irradiation of expensive ^{58}Fe (~US$30/mg). In this work, we have irradiated isotopically enriched ^{57}Fe (~US$6/mg) with 8.2 MeV deuterons and, as it is shown in Table 3.9, our measured production yields from thick targets is higher than the production yield obtained by Thisgaard et al [181], after irradiation of 10.1 MeV protons on a thin ^{58}Fe target (7.0 mg/cm^2). The reason ^{57}Fe, is much cheaper than ^{58}Fe, even though they both have similar natural abundances of 2.119% and 0.282%, respectively, is because ^{57}Fe already has a steady demand in the market of Mössbauer spectroscopy [219]. Thus, the availability of the ^{57}Fe target material is less subject to variations in supply and price, although deuteron accelerators are less common than their proton counterparts.

From a clinical perspective, the ^{55}Co production yields that were obtained in this work would be able to supply activities for several patient studies. Co-55 has been administered to human subjects for PET imaging with injected activities that range from 19 to 74 MBq [135, 136, 138, 139, 142, 203]. These administered activities depend on the positron branching ratio of the radionuclide (77% for ^{55}Co), the pharmacokinetics of the radiolabeled tracer and the annual dose constraint of 50 mSv[75] for adult research subjects. This means that 1 hour-long irradiations on either ^{54}Fe or ^{58}Ni targets with the specifications and separation yields that were presented in Sections 3.2.1 and 3.3.2, could provide sufficient ^{55}Co activity for between 5 and 32 patients, or one half of these, between 2 and 16 patients, if the activity needs to be transported overnight, assuming that one half-life has elapsed from EoB.

3.4 Conclusions

We have developed efficient methods for the production of GBq amounts of the positron emitter ^{55}Co and its therapeutic pair ^{58m}Co with high specific activities at EoB that allows for quantitative radiolabeling of chelator-conjugated targeting vectors, such as antibodies, in ratios ≤ 45 MBq ^{55}Co and ≤ 31 MBq ^{58m}Co per nmol of NOTA-conjugated protein.

We have presented a novel electroplating method for iron that allows for the elaboration of thick targets that can sustain high power irradiations of up to 492 W and that allows for the recovery of expensive isotopically enriched iron after a "wet" radiochemical separation process.

Compared to previously published methods, the introduction of the extraction resin DGA branched greatly simplified the radiochemical separation of radio-cobalt from both iron or nickel-based targets, because it allows to elute the separated nuclide in < 0.6 mL instead of tens of milliliters.

The application of ^{58m}Co in a radiotherapy study demonstrates the feasibility to perform targeted radioimmunotherapy with this radionuclide, and the potential of ^{58g}Co-based PET scans to assess the biodistribution of the ^{58m}Co-labeled agent *in vivo*. The PET analogue ^{55}Co radiolabeled to the same targeting construct allows to predict the targeting efficiency of the radiotherapeutic and for internal dosimetry estimations and treatment planning before substitution with the therapeutic analogue ^{58m}Co.

PET imaging and quantification of the biodistribution over time of ^{55}Co-citrate in tumor-bearing mice demonstrated that it is rapidly excreted via the urinary system with a biological half-life of 13.8 h, indicating that this radiometal is not prone to interact with biological ligands in the bloodstream nor in organ or tumor tissues as it is the case with other radiometals such as ^{44}Sc and ^{64}Cu.

Chapter 4 Improvements to production methods of more conventional radiometals: Copper-61, Copper-64 and Yttrium-86

4.1 Introduction

The majority of current separation methods for emerging positron-emitting radiometals such as ^{61}Cu, ^{64}Cu and ^{86}Y involve cumbersome and lengthy manipulations mainly because of the requirements of either: 1) large ion exchange resin columns (> 4.0 cm × 1.0 cm Ø), which entail large mobile phase volumes (> 4 mL) [188, 189, 220-223]; 2) more than one chromatographic step [134, 224, 225]; or 3) precise pH adjustments [226]. However, a prominent disadvantage of these methods is that the solution with the separated radiometal usually consists of > 4 mL volume, which necessitates for a lengthy evaporation step in a large vessel that potentially causes a variable loss of radioactivity in the vessel's surface or in the glassware of the evaporator. Furthermore, these requirements complicate the automation of the separation process, which mandates frequent intervention by a radiochemist and increased radiation exposure. In order to circumvent these problems, extraction resins with higher trapping capacity compared to the traditional ion exchange resins have proven to be more practical particularly because they allow for the elution of highly concentrated radiometals in solution with high specific activity [167-169]. In this chapter novel chromatographic methods for the production of high specific activity ^{61}Cu, ^{64}Cu and ^{86}Y with the extraction resin N,N,N',N'-tetrakis-2-ethylhexyldiglycolamide, commercially known as DGA Branched (Eichrom) [192] will be presented.

As a proof that the obtained specific activities for ^{64}Cu and ^{86}Y were high enough for practical radiolabeling of chelator-conjugated targeting vectors, the anti-CD105 antibody TRC105 was conjugated to NOTA and CHX-A"-DTPA, radiolabeled to ^{64}Cu and ^{86}Y, respectively, and administered to 4T1-tumor bearing mice. The biodistribution data from the organs with highest uptake was used for internal dosimetry estimations extrapolated to humans using the OLINDA/EXM software and the biodistribution in the tumor was used to predict the feasibility of targeted radiotherapy with the theranostic nuclide ^{64}Cu and its beta emitter analogue ^{67}Cu, as well as the therapeutic analogue of yttrium, ^{90}Y.

The biodistribution and pharmacokinetics of ^{64}Cu-citrate via PET in murine breast cancer (4T1) tumor-bearing Balb/c mice and human glioblastoma (U87MG) tumor-bearing immunosupressed nude mice will also be presented in order to elucidate whether this metal shows passive tumor targeting properties, like ^{44}Sc, and to characterize the organs in which de-chelated ^{64}Cu from a targeting construct could potentially accumulate in case the radiolabel is

not stably bound to the vector. ^{86}Y-citrate was administered into a single mouse bearing a 4T1 tumor, also to verify whether there is significant passive tumor targeting of weakly bound yttrium, although the bone seeking properties of these agent are well known [227-230].

Cu-64 ($t_{1/2}$ = 12.7 h; 17.4% β^+, $E_{\beta+max}$ = 653 keV; 39.0% β^-, $E_{\beta-max}$ = 579 keV; E.C. 45%, Figure 4.1(a)) is important for several reasons: 1) it possesses instrinsic theranostic properties that allows to detect and treat cancer lesions; 2) the favorable excitation function of the ^{64}Ni(p,n) reaction allows to economically produce tens of GBq after a reasonably short irradiation time in a small biomedical cyclotron; 3) it can be used as a surrogate for treatment planning for targeted radiotherapy with the beta emitter ^{67}Cu ($t_{1/2}$ = 2.58 d; 57% β_1, $E_{\beta1\ max}$ = 377 keV; 22% β_2, $E_{\beta2\ max}$ = 468 keV; 20% β_3, $E_{\beta3\ max}$ = 562 keV, Figure 4.1(b)), which is a much better therapeutic radionuclide compared to ^{64}Cu due of its longer half-live and because it emits less energetic, and hence less penetrating, gamma photons; and 4) its coordination to established chelators such as NOTA, DOTA and TETA is well understood [61]. Furthermore, the intermediate half-life of ^{64}Cu is very advantageous because: 1) it allows to monitor, via PET imaging, molecules with slow pharmacokinetics such as full antibodies; 2) once it is accumulated in a target lesion, it allows to concentrate a large number of decays that can result in absorbed doses at a therapeutic scale even after the administration of relatively low amounts of activity; and 3) it allows to ship activity to medical institutions that are far from a centralized production facility, where the activity can still be used the following day after production.

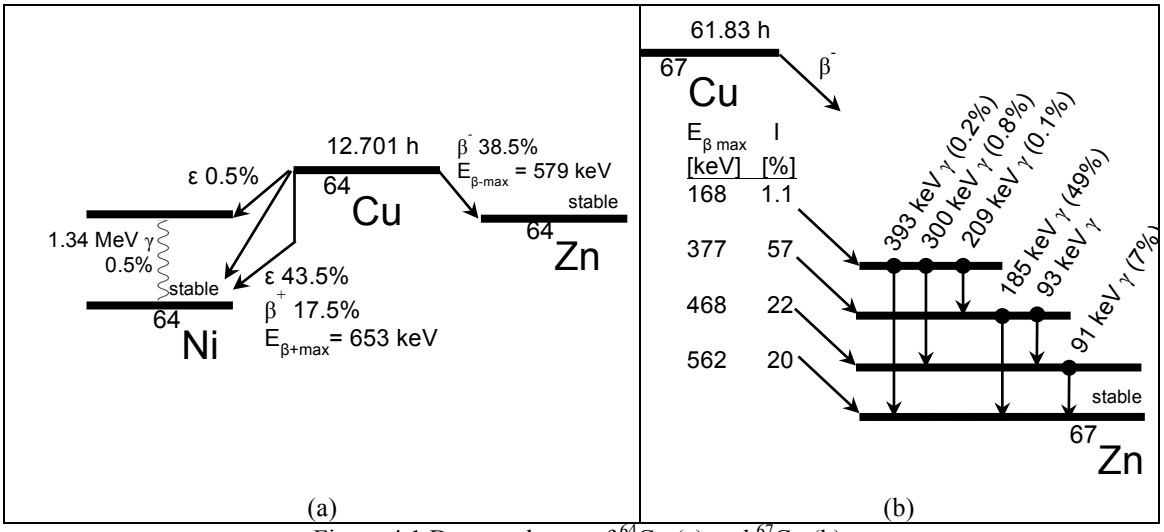

Figure 4.1 Decay scheme of ^{64}Cu (a) and ^{67}Cu (b).

Cu-61 ($t_{1/2}$ = 3.33 h; 61% β^+, $E_{\beta+max}$ = 1215 keV) serves as an alternative to ^{64}Cu to radiolabel PET radiotracers for diagnosis, but is offers limited applicability for treatment planning due to its relatively short half-life. It's two main advantages compared to ^{64}Cu are that: 1) it can be used to monitor targeting vectors that rapidly accumulate in

target tissue generating sufficient tumor-to-background contrast, without the need to leave the patient burdened with an relatively long-lived radionuclide that can affect the patient's family and the general public following release from the hospital; 2) if a low energy deuteron accelerator is available, it can be produced from inexpensive target material (^{60}Ni or even natural nickel), which makes the target recycling efficiency less critical.

Yttrium-86 is not the best positron emitter for medical imaging due to its emission of more than 97 prompt gammas with energies that range from 132 to 3877 keV; although only 8 of these have intensities > 15% and energies between 443 keV and 1921 keV. Nevertheless, it is the best positron emitter for clinical applications that can be used as a PET surrogate of the widely used therapeutic beta emitter ^{90}Y ($t_{1/2}$ = 2.67 d; 99.99% β, $E_{\beta\,max}$ = 2280 keV, Figure 4.2), and therefore it can be used to assess the biodistribution and to predict the absorbed dose that will be delivered by ^{90}Y-labeled antibodies and microspheres, both of which are already widely used in the clinic [215, 231-233].

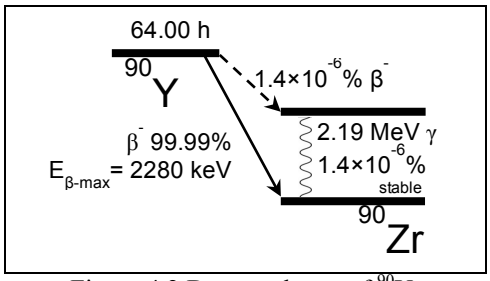

Figure 4.2 Decay scheme of ^{90}Y.

Copper-64 can be produced with a small biomedical cyclotron after proton irradiation on isotopically enriched ^{64}Ni. Metallic nickel has a reasonably high thermal conductivity of 91 $W \cdot m^{-1} \cdot K^{-1}$ that allows for relatively high proton current irradiations of up to 30 μA (with a corresponding power deposition of ~60 W, assuming a typical proton beam degradation within the nickel of ~2 MeV, from 11 to 9 MeV) with water-jet cooling on the back of the target. From the ^{64}Ni(p,n)^{64}Cu excitation function measured by Rebeles et al [234], shown in Figure 4.3(a), the thin target yields shown in Figure 4.3(b) were estimated. Clearly, very high production yield are feasible even on relatively thin targets that are ≤ 100 mg/cm^2, if the incident proton beam has energy in the neighborhood of 10 to 12 MeV. Indeed, thin targets are the most practical and economical option for ^{64}Cu production, since isotopically enriched ^{64}Ni is relatively expensive (US$25/mg[4]) due to its natural abundance of 0.9255%. Figure 4.3(a) also contains the measured excitation function of the ^{64}Ni(p,α)^{61}Co [235], that generates a short-lived impurity with a

[4] Quote from ISOFLEX in 2015

half-life of 1.65 h, which is fully separated from the desired ^{64}Cu product using the radiochemical separation method that will be presented in this chapter.

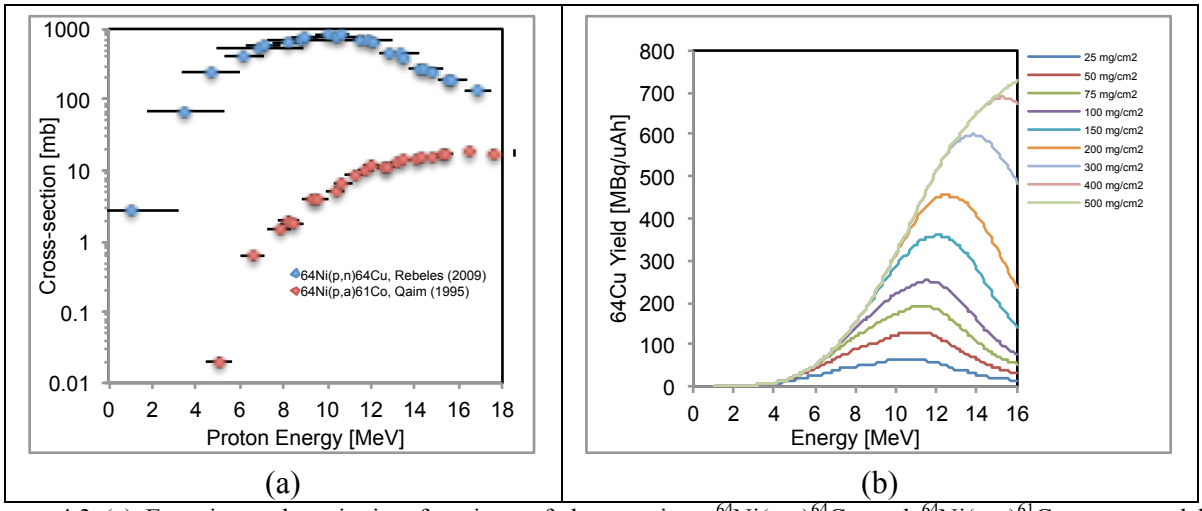

Figure 4.3 (a) Experimental excitation functions of the reactions ^{64}Ni(p,n)^{64}Cu and ^{64}Ni(p,α)^{61}Co, measured by Rebeles et al. [234] and Qaim et al. [235], respectively. (b) Predicted thin target yields of ^{64}Cu versus incident proton energy based on the same ^{64}Ni(p,n)^{64}Cu cross-section data. Each curve corresponds to a ^{64}Ni target with the thickness indicated in the legend.

Copper-61 can be produced either by proton irradiation on isotopically enriched ^{61}Ni (with a price of US$50/mg[5]) or via deuteron irradiation on ^{60}Ni, which can be accomplished without isotopic enrichment since all the other nickel components lead to short-lived ($t_{1/2}$ < 10 min) radio-copper products. However, the use of isotopically enriched ^{60}Ni (with a price of US$1/mg[†]) allows for a close to four-fold increment in production yield due to the natural abundance of ^{60}Ni of 26.223% and also for a significant reduction in the production of ^{56}Co ($t_{1/2}$ = 77.2 d) from the ^{58}Ni(d,α) reaction on 68.077% abundant ^{58}Ni. Anyhow, deuteron bombardment of nickel targets inevitably leads to the production of radio-cobalt impurities, which have to be radiochemically separated from the desired ^{61}Cu product. The separation method that will be presented in this chapter accomplishes this without compromising the separation efficiency of ^{61}Cu significantly (86 ± 9%). From the measured ^{nat}Ni(d,x)^{61}Cu excitation function by Takacs et al [236, 237], extrapolated to 100% ^{60}Ni (Figure 4.4(a)), the predicted thick target yields of ^{61}Cu, after bombardment of 8.2 MeV deuterons, is 231 MBq/μAh.

[5] Quote from ISOFLEX in 2009

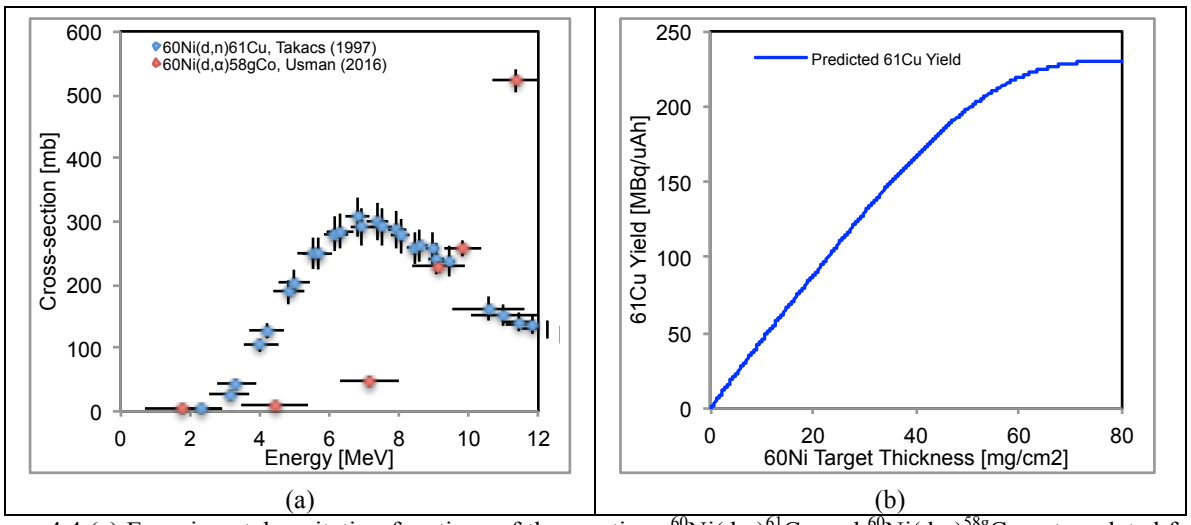

Figure 4.4 (a) Experimental excitation functions of the reactions ^{60}Ni(d,n)^{61}Cu and ^{60}Ni(d,α)^{58g}Co extrapolated from the cross-section measurements after natural nickel irradiation performed by Takacs et al. [236] and Usman et al. [238], respectively. (b) Predicted thin target yields of ^{61}Cu versus ^{60}Ni target thickness after irradiation with 8.2 MeV deuterons based on the same ^{60}Ni(d,n)^{61}Cu cross-section data.

Yttrium-86 with > 98% radionuclidic purity can be produced by proton irradiation on isotopically enriched ^{86}Sr, which can only be purchased as strontium carbonate ($SrCO_3$), a white powder with a low thermal conductivity < 10 $W \cdot m^{-1} \cdot K^{-1}$ [239] that decomposes to strontium oxide (SrO) and carbon dioxide (CO_2) at > 675 °C in vacuum [240]. This latter characteristic constrains $^{86}SrCO_3$ targets to low power, and hence low current, irradiations since the release of CO_2 into the cyclotron's vacuum chamber raises the pressure, which affects the transmission of the proton beam due to scattering. As a matter of fact, the PET trace cyclotron control system automatically stops an irradiation if the cyclotron's vacuum pressure reaches a threshold value of ~2.0×10^{-5} mbar. However, due to the favorable excitation function of the ^{86}Sr(p,n) reaction [241] (Figure 4.5(a)) acceptably high activity production yields are achievable even after low current bombardment on $^{86}SrCO_3$ targets as seen in Figure 4.5(b). For instance, the predicted thick target yield from bombardment of 312 mg/cm^2 $^{86}SrCO_3$ with 16 MeV protons is 320 MBq/μAh. The market price of $^{86}SrCO_3$ at US$9/mg obligates for target recycling, which is easily achievable with high efficiency following published methods [134, 226].

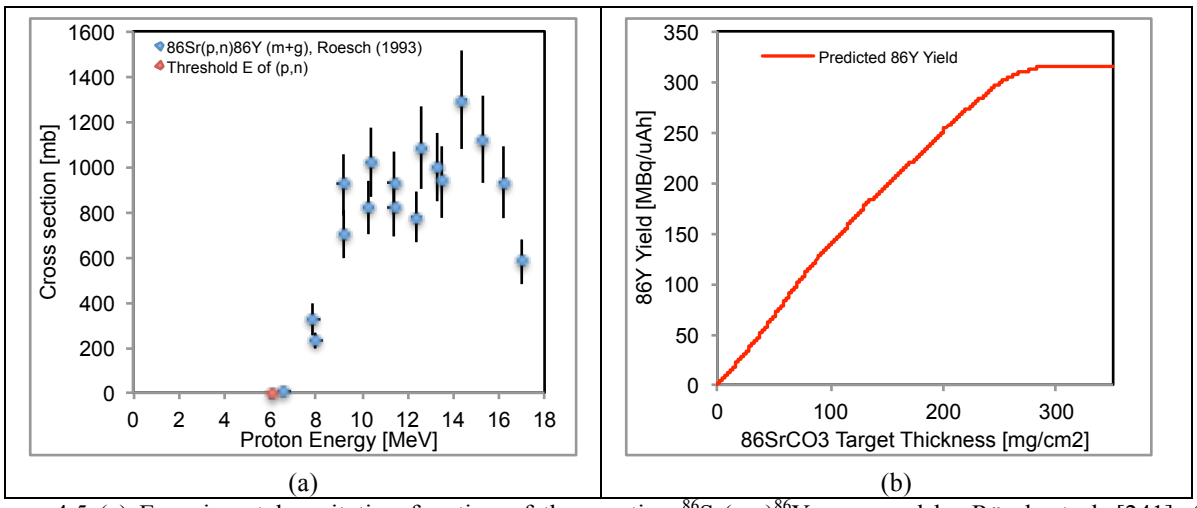

Figure 4.5 (a) Experimental excitation function of the reaction $^{86}Sr(p,n)^{86}Y$ measured by Rösch et al. [241]. (b) Predicted thin target yields of ^{86}Y versus $^{86}SrCO_3$ target thickness after irradiation with 16 MeV protons based on the same $^{86}Sr(p,n)^{86}Y$ cross-section data.

4.2 Materials and Methods

Optima grade hydrochloric acid (32-35% HCl) and nitric acid (67-70% HNO_3) come from Aristar Ultra, VWR (West Chester, PA). The cyclic chelators NOTA (1,4,7-triazacyclononane-1,4,7-triacetic acid) and DOTA (1,4,7,10-tetraazacyclododecane-1,4,7,10-tetraacetic acid) were purchased from Macrocyclics (Dallas, TX). The acyclic chelator DTPA (diethylenetriamine-pentaacetic acid) was obtained from Acros Organics (Geel, Belgium). Isotopically enriched ^{64}Ni (99.32% ^{64}Ni, 0.47% ^{62}Ni, 0.13% ^{58}Ni, 0.07% ^{60}Ni, 0.01% ^{61}Ni), ^{60}Ni (99.60% ^{60}Ni, 0.32% ^{58}Ni, 0.06% ^{61}Ni, 0.02% ^{62}Ni, <0.01% ^{64}Ni) and $^{86}SrCO_3$ (96.40% ^{86}Sr, 2.26% ^{88}Sr, 1.33% ^{87}Sr, 0.01% ^{84}Sr) were purchased from ISOFLEX (San Francisco, CA). Silver and gold disks (1.90 cm diameter × 0.56 mm thickness) were obtained from Artisan Jewelers (Sarasota, FL). A 1.5" diameter niobium rod was obtained from Eagle Alloys Corporation (Talbott, TN). Platinum wire (99.997%, 0.25 mm diameter) and 99.999% ammonium sulfate $(NH_4)_2SO_4$ were purchased from Alfa Aesar (Ward Hill, MA). Trace metal grade sulfuric acid, sodium citrate ($Na_3C_6H_5O_7 \cdot 2H_2O$ or Na_3Cit), ammonium acetate and methanol were purchased from Fisher Scientific (Pittsburg, PA). 28% ammonium hydroxide solution in H_2O (NH_4OH, ≥ 99.99% trace metals) comes from Sigma-Aldrich. TLC silica gel 60 plates and nickel test strips were bought from EMD Chemicals (Darmstadt, Germany). Extraction chromatography resin DGA, branched (50-100 μm) was purchased from Eichrom (Lisle, IL). A 50 ppm multi-element standard for calibration and Agilent's 4200 Microwave Plasma Atomic Emission Spectroscopy (MP-AES) system come from Agilent Technologies (Santa Clara, CA). Deionized water (>18 $M\Omega \cdot cm^{-1}$) was obtained from a Milli-Q filter, Millipore (Billerica, MA). Phosphate buffer saline (PBS) was purchased from Thermo Scientific.

4.2.1 *Cyclotron targetry, irradiations and target yields*

Isotopically enriched ^{60}Ni was electroplated over 0.56 mm thick silver disks following the method explained in Chapter 3 for ^{58}Ni targets; while ^{64}Ni was plated over 0.56 mm thick gold disks following published methods [187-189]. Briefly, isotopically enriched metallic nickel powder (55.6 to 70.1 mg of ^{60}Ni or 38.5 to 106.5 mg of ^{64}Ni) was dissolved in 6 M HNO_3, dried down and re-dissolved in 2.3 mL of 2.4 M H_2SO_4 followed by pH-adjustment to ~9 with 1.5-1.8 mL of 28% NH_4OH and the addition of 270-300 mg of $(NH_4)_2SO_4$. The solution was then transferred to a electrolytic cell, like the one described in Appendix D, in which 2.5-3.5 V and 20-200 mA/cm^2 was applied for 2-3 days using a platinum anode at 1 cm from the cathode disk, where the exposed surface for electrodeposition was a 0.9-1.1 cm^2 circle (1.1 to 1.2 cm diameter). The electroplating was ended when the electrolyte solution was fully clear and the colorimetric nickel strip indicated that 0 to 0.05 mg of nickel remained in solution.

Isotopically enriched $^{86}SrCO_3$ (125.2 to 173.9 mg) was transferred into a crucible made of niobium (0.41 mm deep, 1.2 cm Ø, shown in Figure 4.6), pressed with 4270 psi using a hydraulic press (Dake Corporation, model 972200) and covered with a 0.05 mm niobium foil that seals against a viton O-ring concentric to the depression.

Irradiations were performed on a GE PETtrace that delivers 16 MeV protons or 8.2 MeV deuterons at the beam port. Targets were mounted in a solid target support, which connects to one of the beam ports and seals the target's rear surface against a jet of cooling water for heat dissipation during bombardment, as shown in Figure 4.6. Ni-64 targets were placed behind a 0.25 mm molybdenum foil that degrades the nominal proton energy to ~11.0 MeV according to a SRIM simulation [184]. Ni-60 targets were irradiated without degradation with the nominal deuteron energy from the cyclotron. Also from SRIM simulations, the proton energy after the niobium foil covering the pressed $^{86}SrCO_3$ is 15.2 MeV and the cavity thickness filled with $SrCO_3$ degrades the proton beam energy from 15.2 to 10.8 MeV, covering ~55% of the thick target yield predicted from the ^{86}Sr(p,n)^{86}Y excitation function measured by Rösch et al [241].

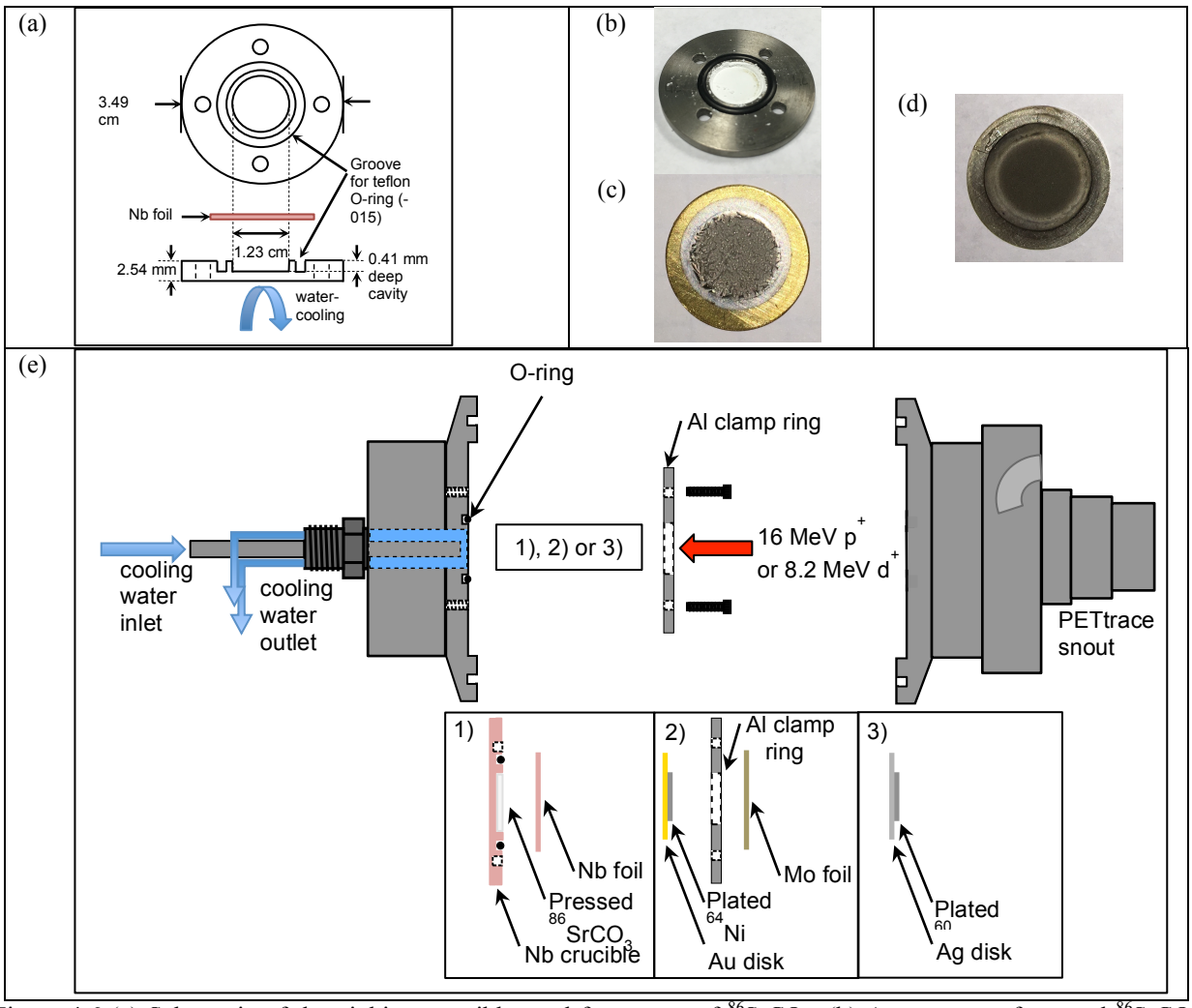

Figure 4.6 (a) Schematic of the niobium crucible used for targets of $^{86}SrCO_3$. (b) Appearance of pressed $^{86}SrCO_3$ inside the depression of the Nb crucible. (c) ^{64}Ni electroplated over a gold disk. (d) ^{60}Ni electroplated over a silver disk. (e) Schematic of how each target is mounted into one of the ports of the cyclotron.

After irradiation, the targets were dismounted from the cyclotron, dried and weighted in order to quantify possible mass loss during irradiation. Table 4.1 summarizes the targetry settings.

Table 4.1 Irradiation parameters

Nuclide	Target material	% enrichment	Reaction	Thickness [mg/cm^2]	E_{in} [MeV]	max. *i* [μA]	Irradiation time [min]
^{64}Cu	^{64}Ni over Au	99.32	$^{64}Ni(p,n)$	37 – 83	11.0	30	60 – 360
^{61}Cu	^{60}Ni over Ag	99.60	$^{60}Ni(d,n)$	54 – 63	8.2	60	30 – 120
^{86}Y	$^{86}SrCO_3$ over Nb	96.40	$^{86}Sr(p,n)$	111 – 154	15.2	4	60 – 120

The nickel targets were dismounted and dissolved in 3 mL 12.1 M HCl at 90 °C for 30 to 60 min. Only the front face of the electroplated nickel target was exposed to HCl by use of a teflon mask with an inserted O-ring that seals against the surface of the substrate disk. To dissolve the irradiated $^{86}SrCO_3$, the entire niobium support was exposed to 6 mL 9 M HCl inside a 50 mL beaker. Ten μL samples were drawn from each target solution for activity

quantification using a 60 cm^3 high purity germanium (HPGe) detector (Canberra C1519) (FWHM = 2.7 keV @ 1333 keV), efficiency-calibrated at fixed distances with NIST-traceable radioactive sources and connected to the gamma-ray spectrum analysis software Maestro-32 MCA Emulator (version 6.08, Ortec, Oak Ridge TN); and for trace metal quantification using Agilent's Microwave Plasma Atomic Emission Spectroscopy system (4200 MP-AES). The gamma lines used to determine yields are listed in Table 4.2. The dead time was always kept below 10% and the acquisition time was set so that the statistical uncertainty from the number of counts per peak was kept below 1%.

Using radionuclidically pure samples after the radiochemical separation, the actual activity measured with the HPGe was compared to the activity reading by the Capintec CRC-Dual PET dose calibrator (Capintec, Ramsey NJ) using the calibration settings for each radionuclide suggested by the manufacturer or in other references [242], in order to determine their accuracy. The calibration numbers used were #015, #417 and #711÷2 for ^{64}Cu, ^{61}Cu and ^{86}Y, respectively. It was observed that the Capintec measurements were overestimating the actual ^{64}Cu, ^{61}Cu and ^{86}Y activities by 46 ± 9% (n = 5), 4 ± 2% (n = 5) and 16 ± 4% (n = 4), respectively. Hence, the Capintec readings had to be multiplied by 0.69, 0.96 and 0.87 throughout the PET studies, including the quantification of administered doses to small animals and calibration of the scanner, in order to have accurate activity values.

Table 4.2 Gamma emissions used for production yield and separation efficiency quantifications

Nuclide	Reaction	Gamma energies [keV]	Branching ratio
^{64}Cu	^{64}Ni(p,n)	511	0.176×2
^{61}Co	^{64}Ni(p,α)	67	0.847
^{61}Cu	^{60}Ni(d,n)	283	0.122
^{58g}Co	^{60}Ni(d,α)	811	0.995
^{86}Y	^{86}Sr(p,n)	1077	0.825
^{86m}Y	^{86}Sr(p,n)	208	0.938
^{87}Y	^{87}Sr(p,n)	485	0.898
	^{87}Sr(p,n)^{87m}Y($t_{1/2}$=13.4 h)		
^{88}Y	^{88}Sr(p,n)	898	0.937
^{85m}Sr	^{86}Sr(p,pn)	232	0.839

4.2.2 *Radiochemical Separation*

The dissolved targets were diluted with H_2O to adjust the HCl concentration to a set value shown in Table 4.3 and then manually transferred to a reservoir syringe connected to a peristaltic pump-driven automated module, from which they were delivered at a flow rate of 1.0 mL/min to a 0.5 cm diameter column filled with DGA branched resin that trapped the radionuclide of interest.

Columns were rinsed with HCl to remove remaining bulk target material as well as radionuclidic impurities such as ^{61}Co, ^{58}Co and ^{85m}Sr. Detailed loading and washing conditions are summarized in Table 4.3. The elution of the radionuclide of interest was carried out by pumping 200 µL fractions of diluted HCl through the loaded resin. The two or three most concentrated fractions were combined in a 1.5 mL centrifuge vial, evaporated to dryness at 100 °C under argon flow, and the residue was re-dissolved in 100 µL of 0.1 M HCl. Table 4.3 summarizes the chromatographic settings for each of the radiochemical separations.

The loading and washing solutions were collected in order to recover the isotopically-enriched target material as previously described for nickel in Chapter 3; and for strontium following the precipitation method by Rösch et al and Avila-Rodriguez et al [134]. Briefly, recovered isotopically-enriched nickel solutions were evaporated to dryness, re-dissolved in 3mL of 6 M HNO_3 in order to digest possible organic material from the extraction resin, evaporated to dryness again, and the electroplating solution was reconstituted and transferred to an electroplating cell as described before. In the case of ^{86}Sr, ~80 mL of saturated ammonium carbonate, $(NH_4)_2CO_3$, solution was drop-wise added to the recovered ^{86}Sr solution in HCl until a white precipitate was formed. Two hours later, when the precipitate had settled to the bottom of the flask, the supernatant was decanted and the precipitate was transferred to a 2 mL vial, in which it was treated three times with 1.5 mL saturated $(NH_4)_2CO_3$, with a 14000 rpm × 1 min centrifugation between washes, in order to have a complete conversion of $Sr(OH)_2$ to $SrCO_3$. The resulting pellet was dried at 100 °C with a flow of argon and the residue was weighted and saved for re-irradiation.

Samples from the separated product and the recycling solution were analyzed with the efficiency-calibrated HPGe detector for quantification of radionuclidic purity, separation yield and recycling efficiency.

Table 4.3 Radiochemical separation settings

Nuclide	mL of H_2O added to target solution	Mass of DGA [mg]	HCl concentration [M] and (mL) of		
			target solution	rinse solution	eluate solution
^{61,64}Cu	3	430	5.5-6.0 (6)	4.5 (3)	2.0 (0.2×4)
^{86}Y	0	100	8.0-9.0 (6)	9.0 (5)	1.0 (0.2×4)

The complete elution profile for the main elements involved in the separation of radio-copper using the DGA branched resin, i.e. copper, nickel and cobalt, was obtained by collecting fractions with volumes of 2 mL in the loading step (6 mL total), 1 mL in the 4.5 M HCl washing step (3 mL total), followed by fractions of 200 µL in the elution step, from a ^{61}Cu separation run after deuteron bombardment on a electroplated natural nickel target. The fractions were then analyzed by gamma ray spectrometry using ^{61}Cu, ^{65}Ni (from ^{64}Ni(d,n)) and ^{56}Co (from ^{58}Ni(d,α)) as radiotracers.

The radionuclidic purity and identity of ^{64}Cu and ^{86}Y in the separated product was confirmed by gamma spectroscopy and by half-life verification after logging the decaying signal from a sample placed inside a dose calibrator (Capintec CRC-Dual PET) that feeds an electrometer (Keithley 6517A) connected to a data acquisition program in LabVIEW. The total acquisition times were 26.4 hours and 49.8 hours, respectively, with a sampling interval of 60 seconds. This data was fit to a mono-exponential function and a decay half-life was quantified and compared to the accepted value for ^{64}Cu, 12.701 h [243], and ^{86}Y, 14.74 h [244]. The radionuclidic purity of ^{61}Cu in the separated product was confirmed only by gamma spectroscopy.

Trace metal analysis was performed on samples from nine, three and three ^{64}Cu, ^{61}Cu and ^{86}Y separation runs, respectively. Ten μL samples from the target solutions and 2-20 μL from the separated stocks were analyzed for trace metal quantification with Agilent's Microwave Plasma Atomic Emission Spectroscopy system (4200 MP-AES).

4.2.3 *Effective Specific Activity with Chelators*

The effective specific activity (ESA) or reactivity of each of the separated radionuclides was assayed by titrating a fixed amount of activity against increasing amounts of chelator. 1,4,7-triazacyclononane-1,4,7-triacetic acid (NOTA) was employed for ^{61}Cu and ^{64}Cu; and 1,4,7,10-tetraazacyclododecane-1,4,7,10-tetraacetic acid (DOTA) and diethylenetriamine-pentaacetic acid (DTPA) were employed for ^{86}Y. All chelation reactions were performed in acetate buffer at pH 4.5 in 250 μL and were allowed to proceed for at least 30 min. A sample from each reaction vial was analyzed by thin layer chromatography (TLC) using silica gel and 1:1 MeOH:10% NH_4OAc mobile phase. Radio-TLC plates were analyzed by autoradiography using a Packard Cyclone Phosphor-Plate imaging system (Perkin Elmer). The reactivity is defined as the ratio of activity decay-corrected to EoB to the amount of chelator in moles that results in 50% labeling yield, multiplied by two.

4.2.4 *Image quality of ^{64}Cu, ^{61}Cu and ^{86}Y*

The same miniature Derenzo phantom employed in Chapter 2, Section 2.2.6 [47] was used to evaluate the spatial resolution of ^{64}Cu, ^{61}Cu and ^{86}Y PET images using an Inveon microPET/CT rodent model scanner. The phantom was filled with 0.1 M HCl solution containing 29, 30 and 29 MBq ^{64}Cu, ^{61}Cu and ^{86}Y, respectively and data was collected for 20 - 40 min until one billion coincident counts were acquired by the software. The raw data was collected in a histogram and reconstructed using the two-dimensional filtered back projection algorithm (FBP2D), without attenuation correction, using a matrix size of 512 × 512 pixels. Image quality was evaluated by

visual inspection of transaxial slices in the middle of the phantom and by profile analysis in the region in which the minimum spatial resolution was observed.

4.2.5 *Preparation of ^{64}Cu-NOTA-TRC105 and ^{86}Y-DTPA-CHX-A"-TRC105*

NOTA conjugation to TRC105 was carried out as described in Chapter 3, section 3.2.5. Following a very similar procedure, the conjugation of DTPA-CHX-A" to TRC105 was performed by mixing [(R)-2-Amino-3-(4-isothiocyanatophenyl)propyl]-trans-(S,S)-cyclohexane-1,2-diamine-pentaacetic acid (p-SCN-Bn-CHX-A"-DTPA) (Macrocyclics) dissolved in dimethyl sulfoxide (DMSO) to a solution containing TRC105 at pH 8.5 – 9.0 with a 25:1, chelator to antibody molar ratio. After 2 hours of reaction time at room temperature, the conjugate DTPA-CHX-A"-TRC105 was purified by size exclusion chromatography with a PD-10 column (GE Healthcare) using phosphate-buffered saline (PBS) as the mobile phase. The concentration of the conjugated protein was measured by analyzing a 1 μL sample with a UV-Vis spectrophotometer Nanodrop One (Thermo Scientific).

For radiolabeling with ^{64}Cu or ^{86}Y, 5 and 25 μL of each respective separated stock with $^{64}CuCl_2$ or $^{86}YCl_3$ was buffered to pH ~4.5 by adding 0.9 mL of 0.08 M NaOAc buffer (pH ~ 4.5) and then ~125 μg of NOTA- TRC105 or ~786 μg of DTPA-CHX-A"-TRC105 from the antibody stocks that were eluted from the PD-10 column. One hour later, each of these solutions was purified by size exclusion chromatography with a PD-10 column and PBS mobile phase collecting five fractions of 400 μL. Each fraction and the PD-10 column were assayed with the dose calibrator in order to quantify the radiolabeling yield per fraction. The two most concentrated fractions from each radiolabeling were mixed and used for the animal studies.

4.2.6 *Biodistribution and pharmacokinetics of ^{64}Cu-citrate, $^{64}CuCl_2$ in PBS, ^{64}Cu-NOTA-TRC105, ^{86}Y-citrate and ^{86}Y-DTPA-CHX-A"-TRC105 in tumor-bearing mice*

The calibration factor for quantification of ^{64}Cu and ^{86}Y activity concentration in volumes of interest (VOI) of the PET images was obtained following the quantification calibration procedure indicated in the Inveon microPET/CT scanner manual, which was explained in Chapter 2, Section 2.2.7, using a 130 mL cylinder phantom filled with ^{64}Cu and ^{86}Y dissolved in 0.1 M HCl at a concentration of 482 ± 2 kBq/mL and 302 ± 14 kBq/mL, respectively.

Murine breast cancer (4T1) tumors were established in four- to five-week-old female Balb/c mice by subcutaneous injection of approximately 2×10^6 murine mammary carcinoma 4T1 cells, into the upper or lower right flank of 13 mice. Tumor sizes were monitored and mice were used for the imaging and radiotherapy experiments

when the axis of the quasi-ellipsoid tumors reached lengths of 6 - 9 and 5 - 8 mm, 11 days after inoculation. The total body mass of these mice at this time was 18.3 ± 1.1 g. Groups of three mice were used for the assessment of biodistribution of each of the four tracers: ^{64}Cu-citrate, $^{64}CuCl_2$ in PBS, ^{64}Cu-NOTA-TRC105 and ^{86}Y-DTPA-CHX-A"-TRC105. The biodistribution of ^{86}Y-citrate was obtained from a single 4T1 tumor-bearing mouse.

Human glioblastoma (U87MG) cells were used for tumor inoculation when they reached ~80% confluence. U87MG tumors were established in four- to five-week-old female athymic nude mice by subcutaneously injecting 5×10^6 cells, suspended in 100 μL of 1:1 mixture of DMEM medium and matrigel, into the lower flank of three mice. The tumor sizes were monitored every alternate day, and *in vivo* experiments were carried out when the diameter of the tumors reached 6 – 8 mm length in the long axis (typically, 3 weeks after inoculation). The total body mass of these mice at this time was 22.5 ± 0.5 g.

The ^{64}Cu-citrate and ^{86}Y-citrate stock solutions for injection were prepared by diluting 10 μL of the separated $^{64}CuCl_2$ or $^{86}YCl_3$ stock solutions with 0.6 mL of 10 mM sodium citrate ($Na_3C_6H_5O_7{\cdot}2H_2O$ or Na_3Cit) (Fisher Scientific), which automatically resulted in solutions with pH ~7. Doses of 63.4 ± 5.2 MBq and 84.3 ± 1.6 MBq ^{64}Cu-citrate in 200 μL were administered into each mouse of groups of three mice bearing 4T1 or U87MG tumors, respectively, and static PET scans were performed at 0.5, 4, 8 24 and 48 hours post-injection (p.i.) on the 4T1 group and at 1, 5, 8, 24 and 48 h p.i. on the U87MG group. 18.9 MBq of ^{86}Y-citrate was injected into a single 4T1 tumor-bearing mouse and static PET scans were performed at 0.5, 4, 24 and 48 h p.i.

From the mixture of the two most concentrated fractions of ^{64}Cu-NOTA-TRC105 and ^{86}Y-DTPA-CHX-A"-TRC105 eluted from the corresponding PD-10 column (800 μL total), 200 μL fractions with 3.7 ± 0.1 MBq ^{64}Cu or 7.1 ± 0.1 MBq ^{86}Y were administered into each mouse of the corresponding group of three 4T1 tumor-bearing mice and PET scans were performed at 4, 24 and 48 hours p.i. in both groups.

PET acquisitions were set to collect at least 40 million coincident counts per mouse, which implicated scanning times of 1.5 to 22 min, 3 to 40 min, 3 to 16 min and 1 to 8 min for the mice injected with ^{64}Cu-citrate, ^{64}Cu-NOTA-TRC105, ^{86}Y-DTPA-CHX-A"-TRC105 and ^{86}Y-citrate, respectively. Static images were reconstructed using the OSEM3D algorithm and then analyzed with the Inveon Research Workplace software. Volumes of interest were drawn on the whole volume of the delineable organs: liver, large intestine and tumor for the images obtained from ^{64}Cu-citrate; and heart, liver and tumor for the ones obtained from ^{64}Cu-NOTA-TRC105. For both radiotracers, muscle uptake was quantified by drawing two ellipsoidal VOIs, each of 100 – 200 mm^3, flanking the urinary bladder

in regions with low activity uptake where the adductor and biceps femoris muscles are located. The uptake data from each of the VOIs is decay-corrected to time of injection and expressed as percentage injected dose per gram (%ID/g). Whole body VOIs of each mouse were drawn and the whole body %ID was obtained by multiplication of the %ID/g by the volume of the VOI, assuming that 1 cm^3 = 1 g. The %ID of each delineable organ and tumor was calculated in the same manner.

The %ID versus time plots of the whole body was fit into mono-exponential decay functions in order to calculate the whole body biological half-life of each radiotracer. In the case of ^{64}Cu-NOTA-TRC105 and ^{86}Y-DTPA-CHX-A"-TRC105, mono-exponential fits to the time-activity curves from the ROIs covering the heart was used to obtain the circulation half-life of the radiolabeled antibody. The time-activity curves of the delineable and remaining organs were used for internal dosimetry estimations as explained in Section 4.2.7.

4.2.7 *Internal dosimetry of ^{64}Cu-citrate, $^{64}CuCl_2$ in PBS, ^{64}Cu-NOTA-TRC105 and ^{86}Y-DTPA-CHX-A"-TRC105 in humans*

The internal dosimetry of ^{64}Cu-citrate, $^{64}CuCl_2$ in PBS, ^{64}Cu-NOTA-TRC105 and ^{86}Y-DTPA-CHX-A"-TRC105 was estimated for a standard adult male of 73.7 kg as defined by Cristy and Eckerman [49] using the OLINDA/EXM software [50]. The organ %ID/g data from small animals was extrapolated to %ID per organ in human using the mass method by Kirschne [52]. Only the biodistribution data from 4T1 tumor-bearing mice was employed in the extrapolation to estimate the absorbed dose in humans from ^{64}Cu-citrate. Details about the methodology for internal dosimetry were already explained in Chapter 2, Section 2.2.8.

4.2.8 *Tumor and normal organ dosimetry of ^{64}Cu-citrate, $^{64}CuCl_2$ in PBS, ^{64}Cu-NOTA-TRC105, ^{67}Cu-NOTA-TRC105 and ^{90}Y-DTPA-CHX-A"-TRC105 in mice*

The absorbed dose delivered to the 4T1 tumors by accumulated ^{64}Cu-citrate, $^{64}CuCl_2$ in PBS, ^{64}Cu-NOTA-TRC105 and ^{86}Y-DTPA-CHX-A"-TRC105; and by accumulated ^{64}Cu-citrate in the U87MG tumor, was estimated using the dose-to-sphere model included in the OLINDA software after inputting the total cumulative decays or disintegrations inside the tumor (which we will assume to be spherical) per administered activity in units of Bq-h/Bq, as it was done in Chapter 2, Section 2.2.9. This value is obtained by trapezoidal integration of the non-decay-corrected time-activity curve of the tumor up to the last time point that was measured and then by integration from this time point up to infinity assuming that there is only physical decay of the radiotracer. The same analysis for

tumor dosimetry was extrapolated to the hypothetical administration of the therapeutic analogues labeled with ^{67}Cu and ^{90}Y maintaining the same pharmacokinetic data measured with the PET counterparts.

In order to estimate the absorbed dose to the normal organs of a mouse after the administration of the theranostic tracers: ^{64}Cu-citrate, $^{64}CuCl_2$ (in PBS) and ^{64}Cu-NOTA-TRC105; and the hypothetical administration of the therapeutic analogues: ^{67}Cu-citrate, $^{67}CuCl_2$ (in PBS), ^{67}Cu-NOTA-TRC105 and ^{90}Y-DTPA-CHX-A"-TRC105, we employed the absorbed fractions (AF or ϕ_k) for different source-to-target organ configurations in a 27 g transgenic mouse that were calculated and published by Stabin et al. [56], from which the *S*-values can be calculated using Equation 2.5. However, in the case of ^{90}Y-DTPA-CHX-A"-TRC105, the *S*-values for ^{90}Y found in the same publication were directly employed. The AFs reported by Stabin et al were calculated by simulating mono-energetic photons (of energies 10, 15, 20, 30, 50, 100, 200, 500, 1000, 2000 and 4000 keV) and electrons (of energies 100, 200, 400, 700, 1000, 2000 and 4000 keV) inside a voxel-based, not mathematically modeled, transgenic mouse using a Monte Carlo particle transport code. The AFs for the three main emissions of ^{64}Cu (one β^+ particle with E_{ave} = 278 keV; one β^- particle with E_{ave} = 191 keV and the 511 keV γ emissions that result from positron annihilation) and the seven main emissions of ^{67}Cu (four β^- particles of mean energies of 51, 121, 154 and 189 keV and three γ emissions of 91, 93 and 185 keV) were interpolated from the published AF values assuming that positrons and and beta particles behave as mono-energetic electrons.

Following the MIRD schema [53] for internal dosimetry, the mean absorbed dose to a target organ is then calculated by substituting the *S*-values and the cumulative activity or total number of decays in each source organ in Equation 2.6.

4.3 Results and Discussion

4.3.1 *Cyclotron targetry, irradiations and target yields*

There was no nickel mass loss in targets used for the production of ^{61}Cu and ^{64}Cu during irradiation, which demonstrates that the electroplated targets can sustain high power irradiations of at least up to 492 W (8.2 MeV × 60 μA, since there was total degradation of the deuteron beam on the ^{60}Ni targets). The average $^{86}SrCO_3$ mass lost after each irradiation was 6 ± 3 mg (n = 3), that is, 4% of the initial target material. This is the result the conversion of some $^{86}SrCO_3$ to ^{86}SrO and gaseous CO_2 due to the heat deposition by the proton beam and therefore there is no actual loss of enriched ^{86}Sr. The CO_2 release into the vacuum chamber of the cyclotron was reflected in a slight increase in pressure from 6.5×10^{-6} mbar to 1.1×10^{-5} mbar during the < 5 min beam tuning stage according to the

cyclotron's pressure sensor. Afterwards, the pressure dropped back to the baseline value of 7.0-6.0 $\times 10^{-6}$ mbar. The change in vacuum pressure was considered acceptable and therefore the presented target setup only allows for low power irradiations of up to 64 W (16 MeV × 4 μA, although only ~ 4 - 5 MeV are degraded in the $SrCO_3$ and the rest in the niobium backing). Higher currents would be attainable if $SrCO_3$ is turned into SrO before irradiation as it was demonstrated by Yoo J, et al [245]. This change in target composition would not affect the subsequent separation chemistry procedure presented in this work as SrO is soluble in HCl.

Tables 4.4, 4.5 and 4.6 lists the experimental activity yields at end of bombardment (EoB) involved in the production of ^{64}Cu, ^{61}Cu and ^{86}Y, respectively, with the irradiation settings pointed out in Table 4.1, and how they compare to the predicted yields from published experimental excitation functions. To have a better perception of this data, the respective yields are plotted versus thickness in Figures 4.7, 4.8 and 4.9.

Table 4.4 Activity yields related to the production of ^{64}Cu and comparison to predicted yields from published excitation functions.

Q [μAh]	**Δx [mg/cm^2]**	**^{64}Cu Yield [MBq/μAh]**	**% of est. from [234]**	**^{61}Co Yield at Saturation [MBq/μA]**	**% of est. from [235]**
125.0	35.9	50	56%	5	40%
24.8	37.0	54	55%	9	67%
110.0	65.5	95	58%	11	55%
116.7	69.1	73	42%	12	58%
45.0	71.3	96	53%	13	62%
10.0	77.0	127	64%	12	52%
80.0	78.6	84	42%	10	45%
65.0	80.6	109	53%	11	48%
115.0	82.8	107	52%	10	45%
30.8	84.1	142	66%	11	48%
56.0	85.6	111	52%	14	58%
26.0	92.4	109	48%	11	44%
149.7	109.0	113	43%	9	34%

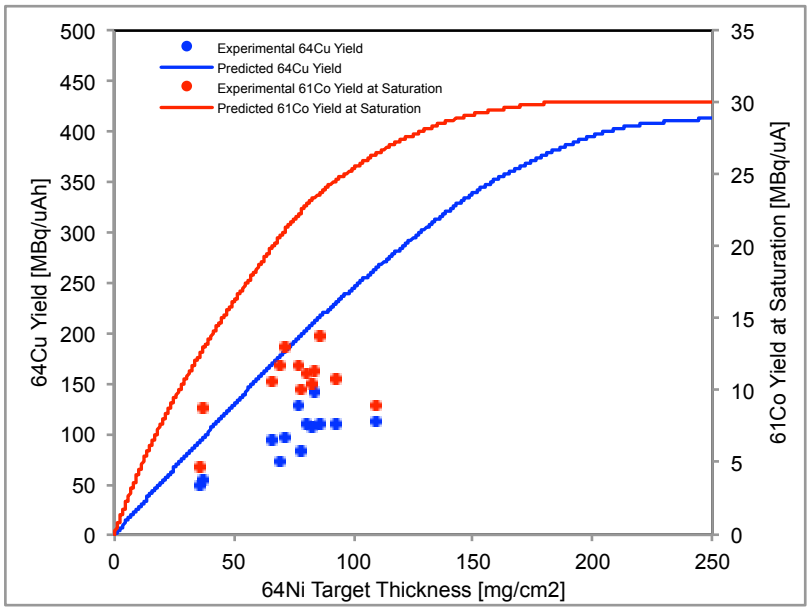

Figure 4.7 Experimental and predicted yields of ^{64}Cu and ^{61}Co from 11.0 MeV proton irradiation on ^{64}Ni targets. The scale on the left side of the plot is for ^{64}Cu yield in MBq/μAh and the scale on the right side is for ^{61}Co yield at saturation in MBq/μA.

Table 4.5 Activity yields related to the production of ^{61}Cu and comparison to predicted yields from published excitation functions.

Q [μAh]	Δx [mg/cm^2]	^{61}Cu Yield [MBq/μAh]	% of est. from [236, 237]	^{58g}Co Yield [kBq/μAh]	% of est. from [238]
60.0	51.0	69	39%	26	32%
20.0	51.9	74	41%	43	53%
79.8	64.3	70	35%	30	35%

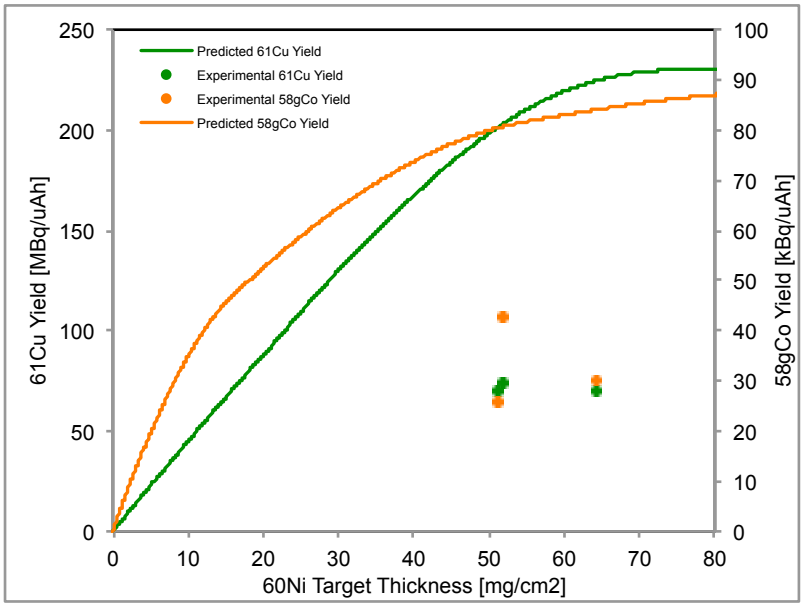

Figure 4.8 Experimental and predicted yields of ^{61}Cu and ^{58g}Co from 8.2 MeV deuteron irradiation on ^{60}Ni targets. The scale on the left side of the plot is for ^{61}Cu yield in MBq/μAh and the scale on the right side is for ^{58g}Co yield in kBq/μAh.

Table 4.6 Activity yields related to the production of ^{86}Y and comparison to predicted yields from published excitation functions.

Q [μAh]	Δx [mg/cm^2]	^{86}Y Yield (m+g) [MBq/μAh]	% of est. from [234]	^{87m}Y Yield [MBq/μAh]	^{88}Y Yield [kBq/μAh]
4.0	105.5	86	60%	1.6	13
3.0	122.0	103	64%	1.8	15
4.0	146.5	116	61%	2.1	18

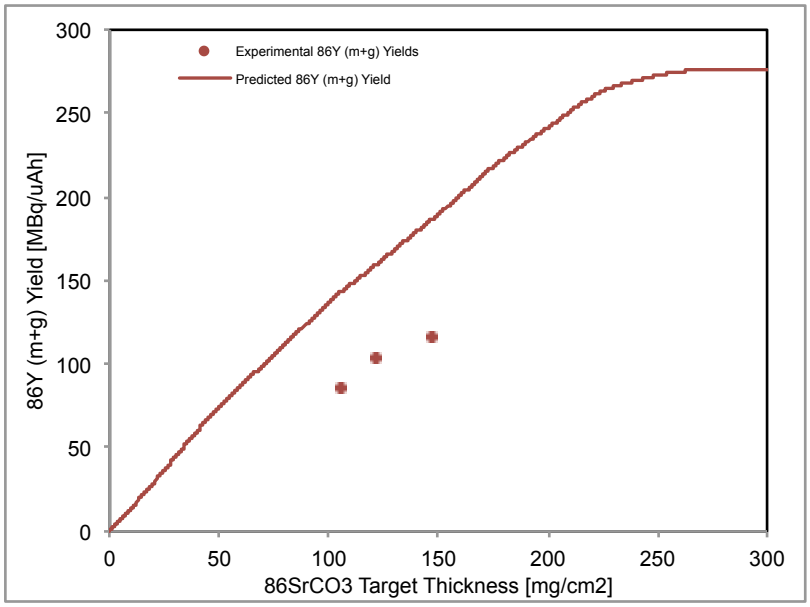

Figure 4.9 Experimental and predicted yields of ^{86}Y from 15.2 MeV proton irradiation on $^{86}SrCO_3$ targets. The ^{86g}Y activity generated by total decay of ^{86m}Y ($t_{1/2}$ = 47 min) is included and decay corrected to EoB.

The experimental ^{64}Cu, ^{61}Co, ^{61}Cu, ^{58g}Co and ^{86}Y yields are 53 ± 8%, 51 ± 9%, 39 ± 3%, 40 ± 11% and 61 ± 2%, respectively, of the predicted yields calculated from experimental excitation functions because, even though the proton beam from the PETtrace is centered on the solid target support, it covers an axial area that is larger than the electroplated surface (Ø = 0.9 – 1.1 cm) and the transverse area of the depression in the niobium crucible (Ø = 1.23 cm), that causes a loss of up to 41 and 42% of the proton and deuteron beam intensities, respectively, in the electroplated targets; and a loss of 15% in the niobium crucible. The details on how these percentage losses were calculated are explained in Appendix C.

The average and standard deviation of the ^{64}Cu yields, except for the two thin targets of 35.9 and 37.0 mg/cm^2, is 106 ± 19 MBq/μAh. The average yield of ^{61}Cu from the three irradiations on ^{60}Ni is 71 ± 3 MBq/μAh. The ^{86g}Y yield at EoB (including the contribution from the decay of ^{86m}Y) from the three production runs is 102 ± 15 MBq/μAh. Thus, using currents of 30 μA protons on ^{64}Ni, 60 μA deuterons on ^{60}Ni or 4 μA protons on $^{86}SrCO_3$, with the range in thicknesses shown in Tables 4.4, 4.5 and 4.6, a typical 1 hour long irradiation would generate

batches of 3.18 GBq ^{64}Cu, 4.26 GBq ^{61}Cu and 0.41 GBq ^{86}Y, respectively. The percentage of these batches that is actually separated with high radionuclidic purity and specific activity will be explained in the next section.

4.3.2 *Radiochemical Separation*

The radio-copper separation efficiency was 86 ± 9% (n = 10, including productions runs for both ^{64}Cu and ^{61}Cu) in 100 µL of 0.1 M HCl. The whole separation process from EoB to the re-dissolution of the separated copper took 1.8 ± 0.4 hours, having as the main bottleneck the dissolution of the nickel target in 0.5 – 1.0 hour. The ^{64}Ni and ^{61}Ni recycling yields after production/electroplating runs on the same target material were 94 ± 2% and 97 ± 1%, respectively. This renders the production of both radio-copper labels economical since the replenishment of relatively expensive target material will not be required on a regular basis.

The ^{86}Y separation efficiency from ^{86}Sr was 93 ± 6% (n = 3) in 100 µL of 0.1 M HCl. The whole separation process took 1.8 ± 0.4 hours (coincidentally the same average and standard deviation as in the radio-copper separation). The $^{86}SrCO_3$ recycling yield after three production runs on the same target was 89 ± 1%.

Both production routes depend on the extraction properties of DGA resin in HCl solution, which were published by Pourmand and Dauphas [192]. Copper in HCl solution reaches a maximum in distribution coefficient (log K_d) with DGA resin of ~10 when the acid concentration is ~6 M HCl, , while the log K_d for nickel and cobalt is < 10^{-1} and ~10, respectively. Almost quantitative radio-copper trapping (94 ± 4%) is obtained when the amount of DGA resin packed in a 0.5 cm diameter column is ≥ 420 mg. Lower amounts of resin resulted in lower trapping efficiencies (data not shown). The co-trapped radio-cobalt is washed from the resin without significantly eluting the desired radio-copper at a concentration of 4.5 M HCl, at which the distribution coefficients towards the resin for copper is still ~10 and that of cobalt has dropped to ~1. However, this HCl wash will also remove radio-copper, although in a smaller proportion and at a lower rate compared to the amount or radio-cobalt. Fortunately, quantitative removal of radio-cobalt is achieved after 3 mL of 4.5 M HCl at the expense of merely ~6% of the desired radio-copper.

Likewise, the distribution coefficients of yttrium and strontium in the DGA/HCl medium are very favorable for a separation strategy. The log K_d of yttrium is ≥ 10^4 when the concentration of HCl is ≥ 3 M, while that of strontium is ≤ 1 under the same conditions, reaching a minimum at ~ 9 M HCl. As seen in Table 4.3, this is the HCl concentration of the target solution that is aimed for before the transfer to the extraction resin.

Once the radionuclide of interest (either ^{64}Cu, ^{61}Cu or ^{86}Y) is trapped in the DGA resin, the elution is carried out in 200 µL fractions of HCl. As shown in Table 4.3, the concentration of this eluent is 2 M HCl for radio-copper and 1 M HCl for ^{86}Y. Such relatively high concentrations were selected, instead of using plain deionized H_2O or 0.1 M HCl, because at these high concentrations the log K_d values for the ubiquitous trace metals iron and zinc remain above 10^2 [192], which means that the majority of these metals will remain in the resin while the desired radionuclide is eluted with a high effective specific activity. Figure 4.10 shows the elution profiles from DGA in terms of the percentage of the total radioactivity produced at EoB eluted in each 200 µL fraction.

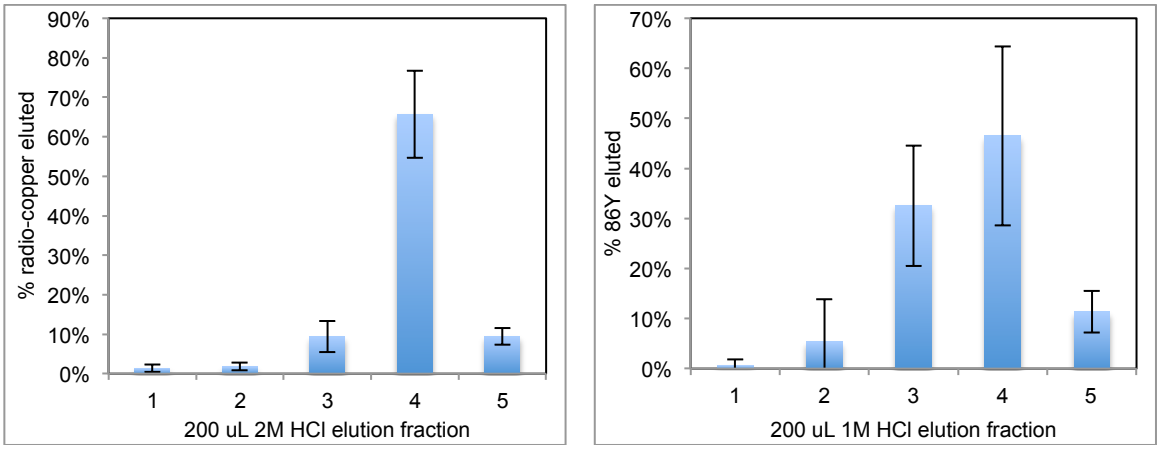

(a) (b)

Figure 4.10 Elution profiles of (a) radio-copper (^{61}Cu or ^{64}Cu) separated from isotopically enriched nickel targets in HCl solution using a > 420 mg DGA branched resin packed into a 0.5 cm ID column with a flow rate of 1.1 mL/min; and (b) ^{86}Y from ^{86}Sr dissolved in HCl using a 100 mg DGA branched resin.

Figure 4.11 shows the complete elution profiles of the main elements involved in the separation of radio-copper using a 420 mg DGA branched column in percentage per fraction and in cumulative percentage of the total radioactivity produced at EoB.

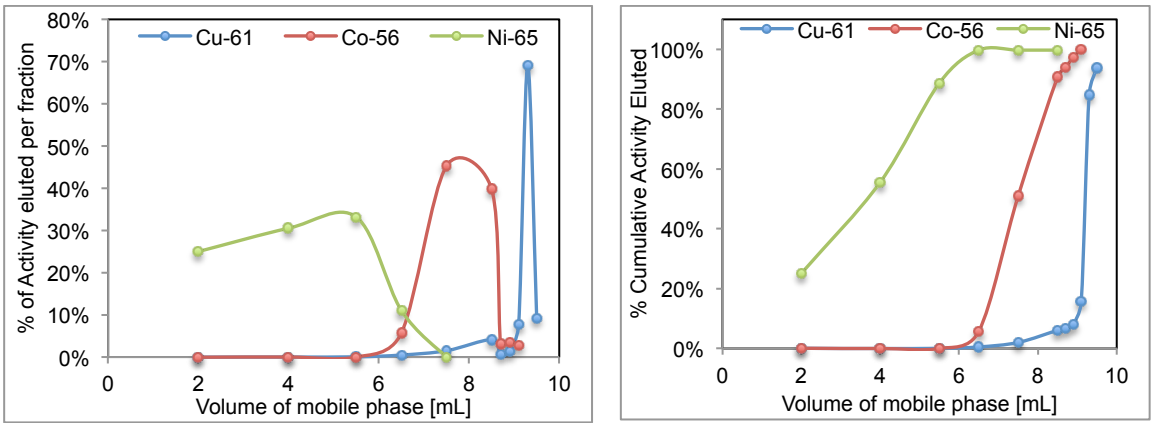

(a) (b)

Figure 4.11 Complete elution profile of the main elements involved in the separation of radio-copper from nickel-based targets dissolved in HCl in terms of percentage per volume (a) and cumulative percentage per total volume (b).

The γ-spectra of ^{64}Cu, ^{61}Cu and ^{86}Y before and after the purification process are shown in Figure 4.12. The unpurified radio-copper target samples contained significant levels of radio-cobalt radionuclidic impurities, which were completely removed after the purification process, resulting in ^{61}Cu with radionuclidic purity at EoB of 99.9998 ± 0.0001% (n = 3). The radionuclidic purity of the separated ^{64}Cu is of a similar value, although it was not directly quantified because the main impurity ^{61}Co was below the detection limit.

The main non-yttrium radionuclidic impurities generated in the $^{86}SrCO_3$ targets were the short-lived ^{85m}Sr and ^{87m}Sr, as well as traces of the long-lived ^{83}Rb from ^{86}Sr(p,α), all of which are only visible in the solution that flows through the DGA resin after trapping > 99% of the radio-yttrium. Hence, the main impurities in the desired ^{86}Y are other yttrium radionuclides generated by the stable isotopes of strontium that are not ^{86}Sr, which account for 3.6% of the target material. Furthermore, the ^{86}Sr(p,n) reaction also leads to a short-lived metastable state of ^{86}Y that decays to the desired ^{86g}Y with a half-live of 48 min. Thus, the radionuclidic purity at EoB is of little value since at this time the ^{86m}Y activity represents a large fraction of the activity and the radionuclidic purity quickly changes over time as ^{86m}Y decays and turns into the desired ^{86g}Y. Therefore, the radionuclidic purity is reported 8 hours after EoB, when ten half-lives of ^{86m}Y have elapsed, resulting in 98.3 ± 0.1 % (n = 3). Table 4.7 presents the details of the radionuclidic components of each separated product. The ^{88}Y impurity is of particular concern due to its long half=life of 106.6 days and its two prominent gamma emissions of 898 and 1836 keV, both with > 90% BR. From Table 4.7, we can see that this impurity is minimal, accounting for 0.022% of the total activity. In other words, there is only 220 Bq ^{88}Y for every MBq of ^{86}Y, 8 hours after EoB.

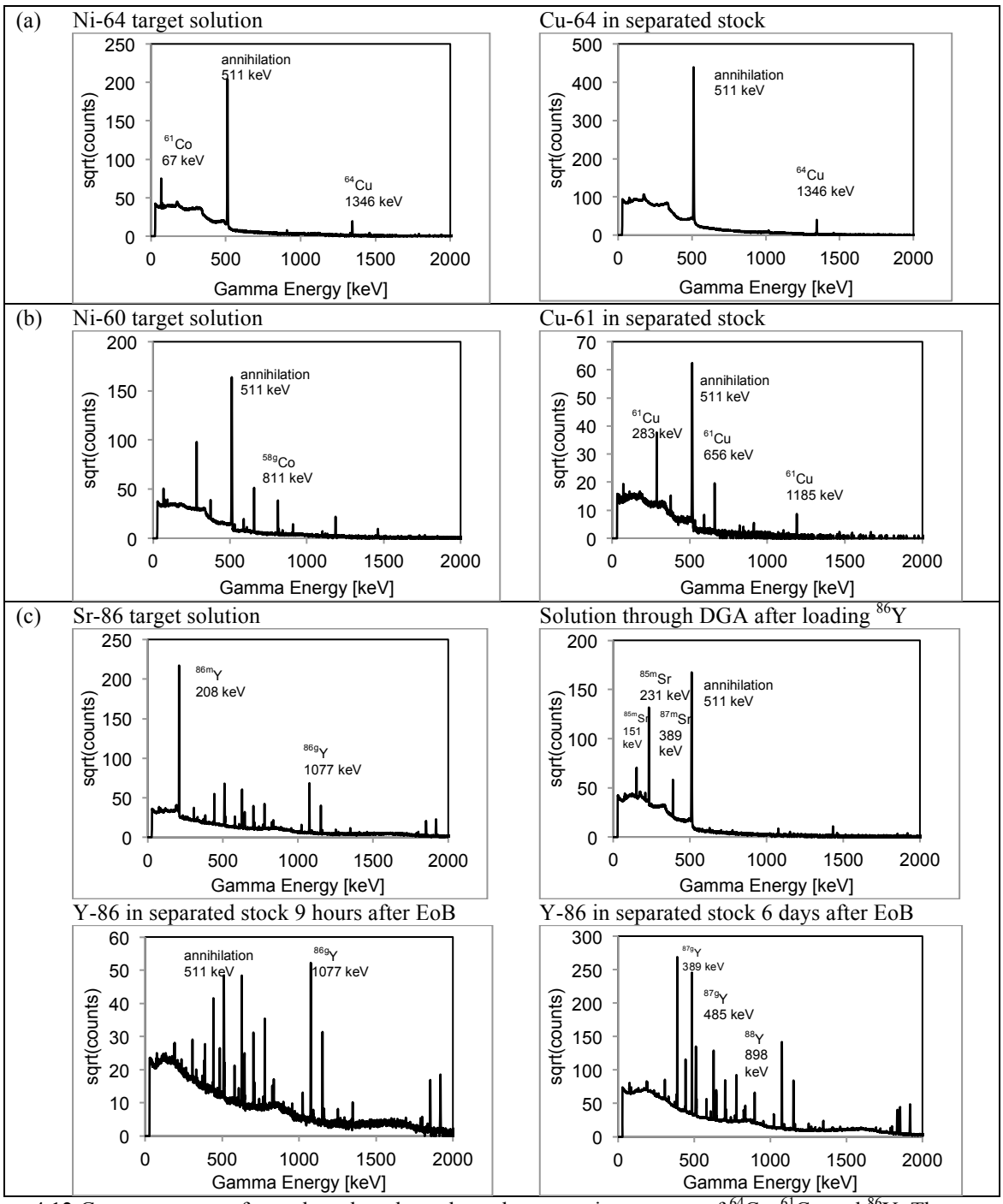

Figure 4.12 Gamma spectra of samples taken throughout the separation process of ^{64}Cu, ^{61}Cu and ^{86}Y. The spectrum from separated ^{64}Cu in row (a) shows the absence of the 67 keV gamma peak from ^{61}Co from ^{64}Ni(p,α). The spectrum from separated ^{61}Cu in row (b) shows the absence of the 811 keV gamma peak from ^{58g}Co from ^{60}Ni(d,α). The spectra in (c) display the many gamma lines emitted by ^{86g}Y with the impurities ^{87g}Y (generated from ^{87m}Y) and ^{88}Y only visible after many half-lives of ^{86}Y after EoB. The target sample shows a prominent gamma line from ^{86m}Y co-produced via ^{86}Sr(p,n), which is absent in the spectrum of the separated stock 9 hours after EoB. The spectrum of the solution that passed through the DGA resin after loading the ^{86}Y only shows the gamma lines from the short-lived strontium radionuclides that are co-eluted with the bulk ^{86}Sr target material, demonstrating the high trapping efficiency of yttrium.

Table 4.7 Radionuclidic impurities in the separated radionuclides of interest

Desired product	Target	% abundance	Reaction	Product	% in separated stock at EoB
^{64}Cu	^{64}Ni	99.32	^{64}Ni(p,n)	^{64}Cu	> 99.999%
			^{64}Ni(p,α)	^{61}Co	*unobserved*
^{61}Cu	^{60}Ni	99.60	^{60}Ni(d,n)	^{61}Cu	99.9998 ± 0.0001%
			^{60}Ni(d,α)	^{58g}Co*	0.0002 ± 0.0001%
	^{58}Ni	0.32	^{58}Ni(d,α)	^{56}Co	*unobserved*
^{86g}Y	^{86}Sr	96.40	^{86}Sr(p,n)	^{86g}Y	98.3 ± 0.1% #
			^{86}Sr(p,α)	^{83}Rb	*unobserved*
	^{88}Sr	2.26	^{88}Sr(p,n)	^{88}Y	0.022 ± 0.001%
	^{87}Sr	1.33	^{87}Sr(p,n)	^{87m}Y	1.7 ± 0.1% §

* After decay correction to EoB of all the ^{58g}Co, including the one generated from total decay of ^{58m}Co.
# Radionuclidic purity 8 h post-EoB in order to have complete decay of ^{86m}Y ($t_{1/2}$=47 min).
§ Y-87m decays to ^{87g}Y ($t_{1/2}$=79.8 h), an impurity that is not considered at EoB.

Figure 4.13 shows the decay logging from samples of separated stocks of ^{64}Cu and ^{86}Y. The exponential fit to the logged activity reading from the dose calibrator indicates that the half-life of the separated ^{64}Cu is 12.71 ± 0.06 h, which is 0.1 ± 0.5% greater than the accepted value for ^{64}Cu: 12.701 h [243]; and that of the separated ^{86}Y is measured as 14.888 ± 0.004 h, or 1.01 ± 0.03% higher than the accepted value: 14.74 h [244]. This latter discrepancy is due to the presence of impurities with longer half-lives: ^{87g}Y and ^{88}Y.

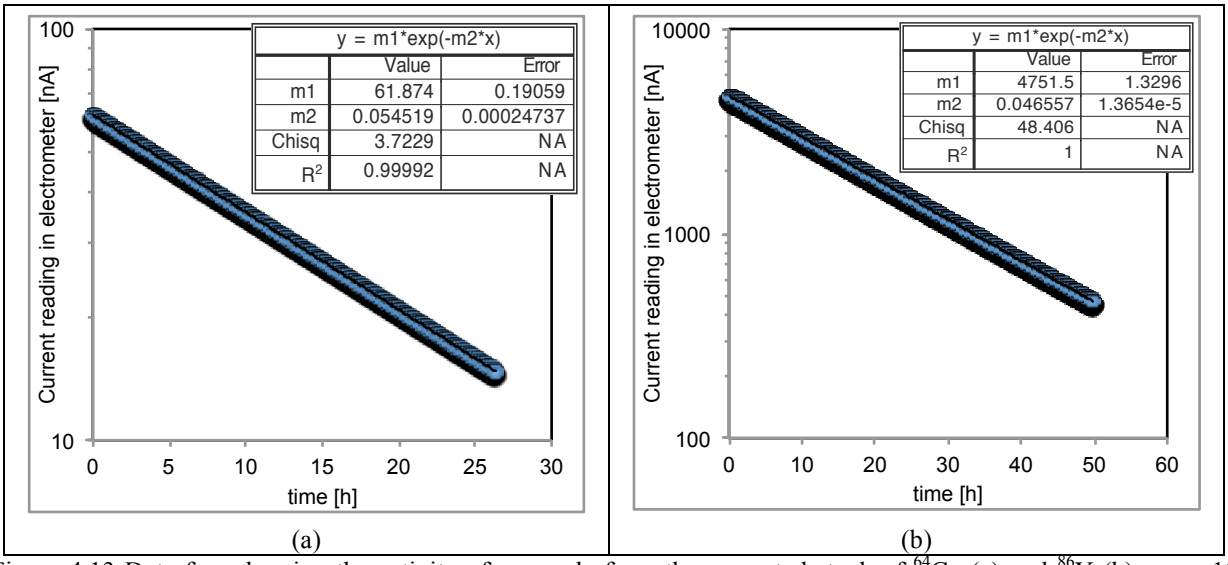

(a) (b)

Figure 4.13 Data from logging the activity of a sample from the separated stock of ^{64}Cu (a) and ^{86}Y (b) every 10 seconds for 26.4 hours and 49.8 hours, respectively, and exponential fits to the data which indicates that the half-life of the radioactivity in the samples is 12.71 ± 0.06 h and 14.888 ± 0.004 h, respectively.

Ten µL samples from the target solutions as well as 2-20 µL samples from the separated stocks were analyzed for trace metal quantification with Agilent's 4200 MP-AES system. The main metal impurities found in the separated stock of ^{64}Cu were: cobalt (380 µM), nickel (317 µM), copper (144 µM), zinc (55 µM) and iron (68 µM). In the separated stock of ^{61}Cu, the main metal impurities were: nickel (323 µM), cobalt (241 µM), copper (157 µM), silver (53 µM), zinc (52 µM) and iron (21 µM). The main impurities in the separated ^{86}Y were: zinc (4.2 mM),

cobalt (2.7 mM), iron (1.9 mM), strontium (462 μM), yttrium (312 μM), nickel (78 μM) and copper (64 μM). These results are summarized in Table 4.8, along with the corresponding separation factor for each element.

Table 4.8 Results form trace metal analysis on the germanium eluate used for labeling experiments.

Desired product	Element	Mass [μg]	Molarity [μM]	Separation Factor*
^{64}Cu	Cobalt	2.2 ± 0.8	380 ± 133	4.2×10^3
	Nickel	1.9 ± 1.5	317 ± 253	2.5×10^4
	Copper	0.9 ± 0.6	144 ± 100	-
	Zinc	0.4 ± 0.2	55 ± 35	3.2×10^3
	Iron	0.4 ± 0.3	68 ± 58	2.4×10^3
^{61}Cu	Nickel	1.9 ± 1.2	323 ± 204	1.3×10^5
	Cobalt	1.4 ± 0.9	241 ± 159	3.4×10^3
	Copper	1.0 ± 0.2	157 ± 38	-
	Silver	0.6 ± 0.3	53 ± 32	6.7×10^3
	Zinc	0.3 ± 0.2	52 ± 23	3.2×10^3
	Iron	0.11 ± 0.10	21 ± 18	4.2×10^3
^{86}Y	Zinc	27.5 ± 9.5	4208 ± 1452	6.1×10^2
	Cobalt	16.2 ± 8.9	2743 ± 1512	1.3×10^3
	Iron	10.4 ± 3.4	1854 ± 603	62
	Strontium	4.1 ± 2.7	462 ± 308	3.6×10^4
	Yttrium	2.8 ± 1.4	312 ± 159	-
	Nickel	0.5 ± 0.2	78 ± 27	1.3×10^3
	Copper	0.4 ± 0.1	64 ± 23	1.6×10^3

* Calculated by dividing the mass in the target solution over the mass in the separated stock.

As it was mentioned in Section 4.3.1, a typical 30 μAh irradiation on a ≥ 65 mg/cm^2 thick ^{64}Ni target generates ~3.18 GBq ^{64}Cu. 86% of this activity is separated, dried down and re-dissolved in 100 μL of 0.1 M HCl, which represents ~2.73 GBq ^{64}Cu with an activity concentration of 27348 GBq/L. Therefore, the effective specific activity (ESA) of the separated ^{64}Cu from such representative irradiation would be 27348 GBq/L divided by the total molar concentration of metal impurities shown in Table 4.8, that is, 964 μM, which equals 28 GBq/μmol of metal impurities. This ESA is of the same order of magnitude as the ESA that was obtained from the titration experiments with mainstream chelators that will be presented in the following section 4.3.3. A similar analysis for ^{61}Cu and ^{86}Y, after irradiations of 60 and 4 μAh, respectively, reveals that the ESA from the trace metal quantification is 43 and 0.39 GBq/μmol, respectively, which are in close agreement with the ESA obtained from the titration with NOTA and DTPA, respectively.

4.3.3 *Effective Specific Activity with Chelators*

The retention factors (R_f) of unlabeled ^{6x}Cu and ^{86}Y in plates after the TLC protocol were 0 in both cases; and those of ^{6x}Cu-NOTA, ^{86}Y-DOTA and ^{86}Y-DTPA were 0.5, 0.5 and 1.0, respectively.

The average ESA from all the production runs, decay corrected to EoB, of ^{64}Cu-NOTA, ^{61}Cu-NOTA, ^{86}Y-DOTA and ^{86}Y-DTPA are 105 ± 37, 64 ± 45, 0.5 ± 0.2 and 1.4 ± 0.5 GBq/μmol, respectively.

The measured ESA of ^{64}Cu is between 40 and 60% of the average ESA reported by McCarthy et al [188], Avila-Rodriguez et al [189] and Thieme et al [246], while that of ^{61}Cu falls within the ESA range reported in the publications of McCarthy et al [220] and Bradshaw et al [247]. This indicates that the reported radiochemical separation method results in radio-copper with sufficient quality for labeling macrocyclic chelators such as NOTA, TETA (1,4,8,11-tetraazacyclotetradecane-tetraacetic acid) and ATSM (diacetylbis(4-N-methyl-3-thiosemicarbazone)).

The measured ESA of ^{86}Y with DTPA is ~40% of that reported by Garmestani et al. [224]. Measured with DOTA, the ESA obtained in this work is ~60% of that reported by Reischl et al. [248] and one, two and three orders of magnitude lower than that reported by Park et al. [225], Avila-Rodriguez et al. [226] and Yoo et al. [245], respectively. In future work, we will try to increase the ESA by dissolving the $^{86}SrCO_3$ off the niobium crucible exposing only the target material by use of a O-ring sealed teflon mask as done with the electroplated nickel targets. Nevertheless, the ESA obtained so far was sufficiently high for radiolabeling with 82% yield a DTPA-CHX-A"-conjugated antibody by mixing 786 μg (5.2 nmol) of protein per 37 MBq of ^{86}Y, as it will be explained in section 4.3.5.

The measured Y-DTPA reactivity is about three times higher than with DOTA even though the thermodynamic stability constants (log K_{ML}) of these two complexes, 22.05 and 24.0 [63], respectively, would predict the opposite. The reason is because the three main metal impurities in the separated $^{86}YCl_3$: zinc, cobalt and iron, all have higher log K_{ML} values when bound to DOTA, compared to DTPA, and hence all are stronger competitors for the coordination of DOTA. The log K_{ML} values of Zn-DOTA, Zn-DTPA, Co-DOTA, Co-DTPA, Fe(II)-DOTA and Fe(II)-DTPA are 18.7, 18.2, 19.3, 18.8, 19.8 and 16.2, respectively [63].

In order to have a better idea of what is the required ESA in a clinical setting, we can look at the reported values in articles in which ^{64}Cu- or ^{86}Y-labeled antibodies or peptides have been administered to patients without any adverse effect in the biodistribution or pharmacokinetics of the radiotracer. It will be assumed that the molecular weight of intact antibodies is 150 kDa [249] unless the actual values are explicitly indicated in the referenced publications. Philpott et al. [250], reports that 5.0 mg (33 nmol) of antibody labeled with 333 to 407 MBq was injected and that each antibody was conjugated with ~1.8 TETA chelators; therefore, the ESA range in this case was 10.1 – 12.3 GBq/μmol antibody or 5.6 – 6.9 GBq/μmol chelator. Cutler et al. [251], administered the same antibody as Philipott, but reports labeling up to four times more antibody, 20 mg (133 nmol), per 370 MBq of ^{64}Cu, indicating

that in this case the ESA for human administration was four times lower, that is, 1.4 – 1.7 GBq/μmol chelator. Thakur et al. [252] and Tripathi et al. [253] injected a diaminodithiol-conjugated peptide (^{64}Cu-TP3805; MW=3983 Da) with an ESA of 44.4 GBq/μmol. In the study published by Mortimer et al. [254], 5 to 50 mg of DOTA-conjugated trastuzumab labeled with 364 to 512 MBq were administered to the patients, which implies that the ESA was between 1.1 and 15.4 GBq/μmol assuming a 1:1 chelator-to-antibody molar ratio. Lockhart et al. [255] reports the injection of ^{64}Cu-DOTA-patritumab with an ESA of 555 – 2220 GBq/μmol antibody, although the number of chelators per antibody was not specified. Förster et al. [256] reports the administration of ^{86}Y-DOTATOC (DOTA-D-Phe^{1}-Tyr^{3}-octreotide; MW=1421 Da) with an ESA of 11 – 24 GBq/μmol. Jamar et al. [257] administered the same ^{86}Y-labeled octreotide analogue with a ESA range of 0.7 to 52.6 GBq/μmol. Table 4.9 summarizes these reported values and whether the ESA of the produced radionuclides presented in this chapter are within the same order of magnitude.

Table 4.9 Effective Specific Activities employed in the clinic

Nuclide	ESA [GBq/μmol]	Comparison of ESA in this work	References
^{64}Cu	5.6 – 6.9	>	[250]
	1.4 – 1.7	>	[251]
	44.4	>	[252, 253]
	1.1 – 15.4	>	[254]
	555 - 2220	<	[255]
^{86}Y	11 – 24	<	[256]
	0.7 – 52.6	>	[257]

4.3.4 *Image quality of ^{64}Cu, ^{61}Cu and ^{86}Y*

The image quality of ^{64}Cu, ^{61}Cu and ^{86}Y was assessed by visual inspection of the reconstructed microPET images from a Derenzo phantom. As seen in the images on the left column of Figure 4.14, clear resolution was observed down to a rod diameter of 1.25, 1.25 and 1.5 mm, when the phantom was filled with ^{64}Cu, ^{61}Cu and ^{86}Y, respectively. The plots on the right column of Figure 4.14 shows the gray intensity profile from 2.10 mm (10 pixels) wide regions of interest that covers the bottom row of the 1.5 mm diameter rods on each image. Each peak was fitted with a gaussian curve revealing full width at half maximum (FWHM) values of 3.0 ± 0.6, 3.5 ± 0.8 and 4.0 ± 0.8 mm, respectively. The average peak to valley ratios in each profile were 1.38 ± 0.22, 1.35 ± 0.17 and 1.21 ± 0.13, respectively. These measurements will be compared to those from Derenzo phantoms filled with the other radionuclides that were isolated throughout this work in Appendix A.

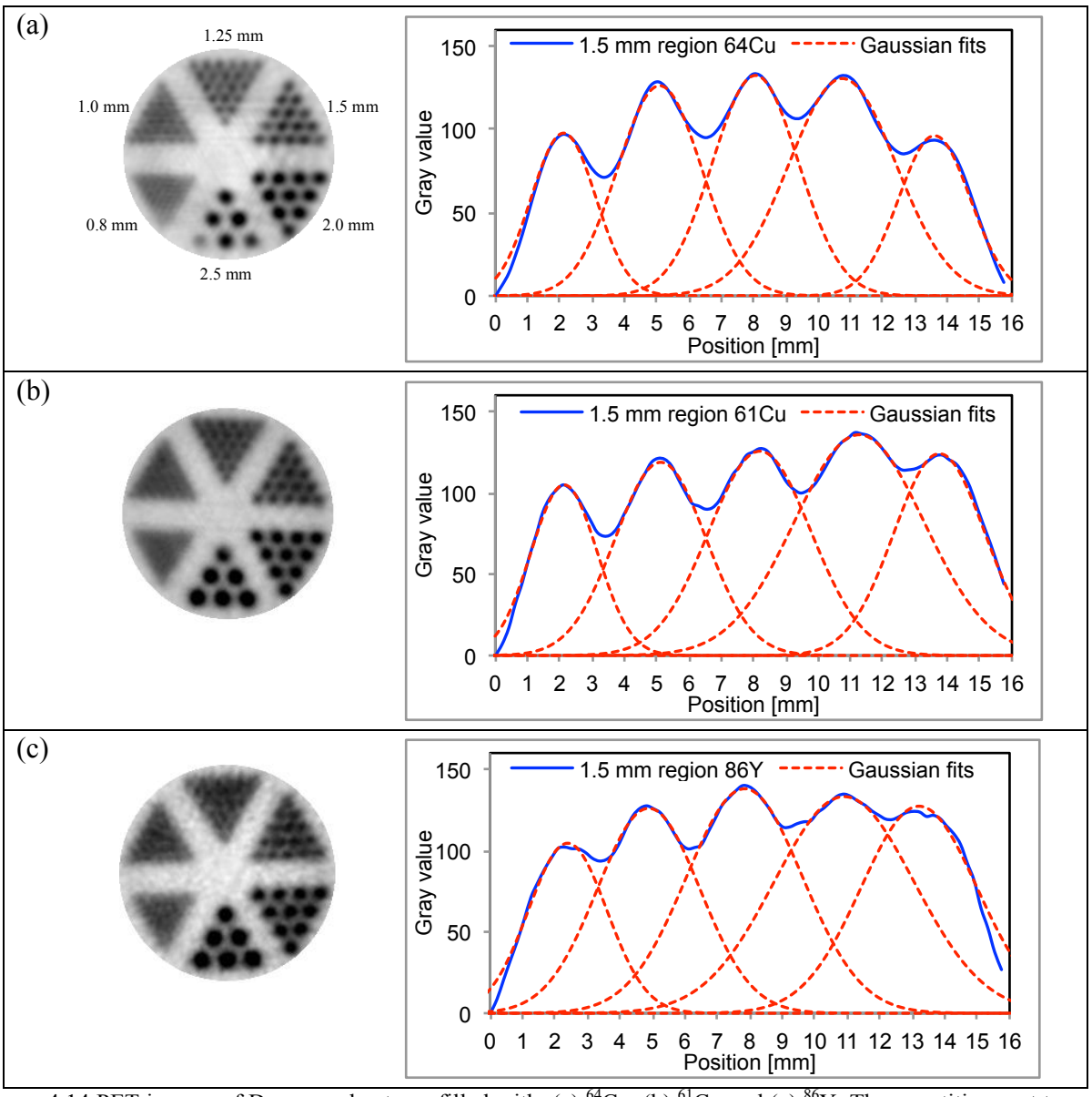

Figure 4.14 PET images of Derenzo phantoms filled with: (a) ^{64}Cu, (b) ^{61}Cu and (c) ^{86}Y. The quantities next to each triangular section in (a) indicate the diameter of each of the rods, which are separated from center to center by twice the diameter distance. Rods up to 1.25 mm can be easily resolved in PET images of ^{64}Cu and ^{61}Cu and rods up to 1.5 mm with ^{86}Y. The profile distribution plots from the bottom row of 1.5-mm rods in each image is shown in the right column.

Cu-64 offers an excellent spatial resolution due to the low maximum energy of its only positron emission with a maximum energy of 653 keV, which has a mean and maximum range in water of 0.560 and 2.935 mm, respectively [194]. In fact, the resolution that is visualized with the Derenzo image is lower than the mean range of the positron due to the intrinsic resolution limit of the Inveon scanner, quantified as 1.62 mm in the radial direction using a ^{22}Na (β^+ E_{max} = 546 keV) point source, by Kemp et al [258]. In fact, this explains why the spatial resolution of ^{61}Cu is

comparable to that of ^{64}Cu even though the mean positron range of the main positron emitted by the former, with a maximum energy of 1216 keV and a branching ratio of 51%, is more than three times higher at 1.805 mm [194].

The relatively low spatial resolution of the ^{86}Y image is the result of the high maximum energy of 1221 keV of the main positron emitted by ^{86}Y, with a branching ratio of 11.9%, although this nuclide also emits other positrons with higher maximum energy but at lower branching ratios, the most energetic one having a maximum energy of 3142 keV and a branching ratio of 2.0% [244]. Le Loirec and Champion have reported a mean and maximum range in water for this latter positron of 2.511 and 11.126 mm, respectively [194].

4.3.5 *Preparation of ^{64}Cu-NOTA-TRC105 and ^{86}Y-DTPA-CHX-A"-TRC105*

After mixing 5 and 25 µL from each separated stock (173 and 71 MBq of $^{64}CuCl_2$ and $^{86}YCl_3$ at EoB, respectively) with ~125 µg NOTA-TRC105 and ~786 µg DTPA-CHX-A"-TRC105, respectively, in a total volume of 1 mL NaOAc buffer (pH ~4.5) and waiting for 0.5 - 1 h, the purification of ^{64}Cu-NOTA-TRC105 and ^{86}Y-DTPA-CHX-A"-TRC105 resulted in a total labeling yield of 40% and 82%, respectively, in 4 fractions of 400 µL of PBS. However, only the two most concentrated fractions were mixed together and then employed for the animal studies. These fractions accounted for 31% and 54%, respectively, of the initial activity, which corresponded to 14 MBq ^{64}Cu and 29 MBq ^{86}Y at the time of the synthesis (the ^{64}Cu and ^{86}Y labeling was performed 21 and 5 hours after EoB, respectively). These formulations were split in 200 µL doses for administration into each 4T1 tumor bearing mice.

4.3.6 *Biodistribution and pharmacokinetics of ^{64}Cu-citrate, $^{64}CuCl_2$ in PBS, ^{64}Cu-NOTA-TRC105, ^{86}Y-citrate and ^{86}Y-DTPA-CHX-A"-TRC105 in tumor-bearing mice*

PET scans were performed after administration of ^{64}Cu-citrate at 0.5, 4, 8 24 and 48 hours post-injection (p.i.) on three 4T1-tumor bearing mice and at 1, 5, 8, 24 and 48 h p.i. on three U87MG-tumor bearing mice. PET scans on the 4T1-tumor bearing mice injected with $^{64}CuCl_2$ diluted in PBS were performed at 0.5, 4, 16, 24, 48 and 72 h p.i., the three latter scans on the Genisys4 PET/x-ray scanner (Sofie Biosciences, Culver City, CA). Figure 4.15(a), (b) and (c) show the coronal and sagittal maximum intensity projection (MIP) images of one of the mouse from each group.

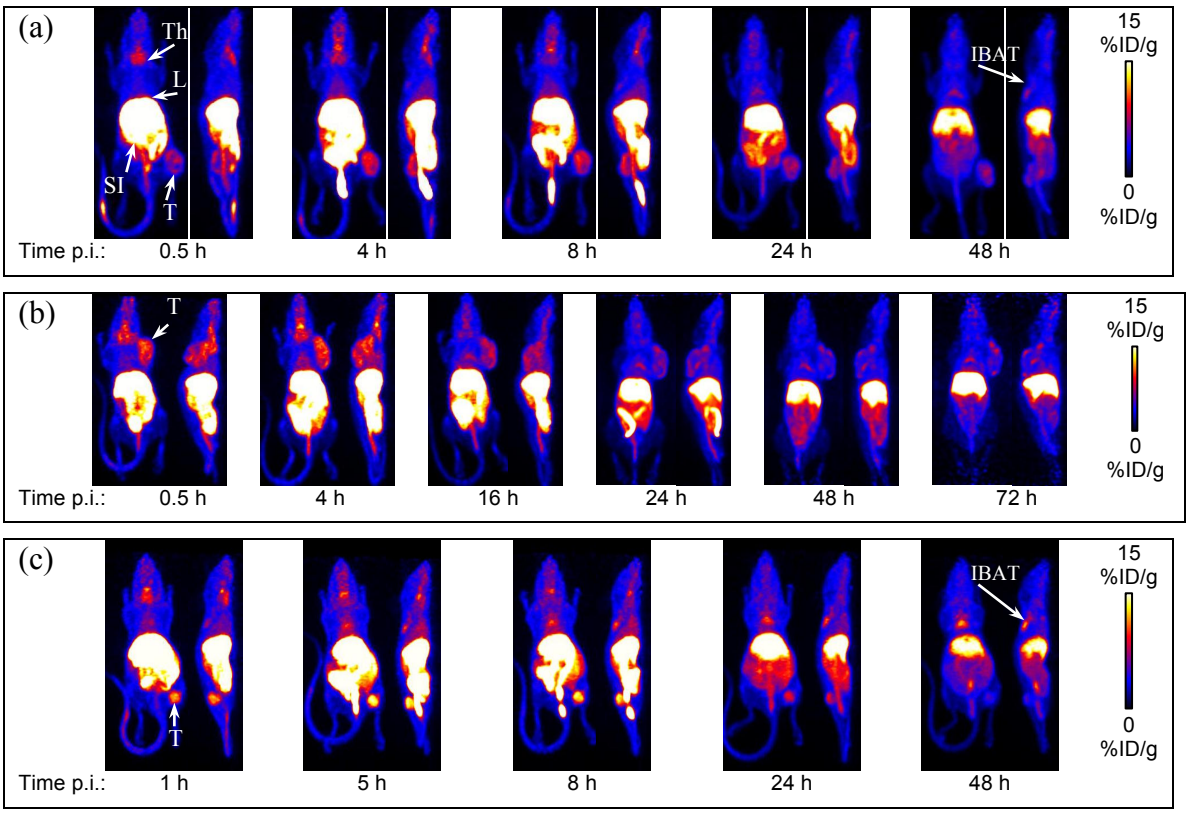

Figure 4.15 Coronal and sagittal MIP images from PET scans of mouse #3 from: (a) the 4T1 tumor-bearing group at 0.5, 4, 8 24 and 48 h injected with ^{64}Cu-citrate; (b) the 4T1 tumor-bearing group at 0.5, 4, 16, 24, 48 and 72 h p.i of $^{64}CuCl_2$ in PBS; and (c) the U87MG tumor-bearing group at 1, 5, 8, 24 and 48 h p.i of ^{64}Cu-citrate. The ^{64}Cu uptake level is color coded by the %ID/g bar shown on the right of each set of images. The PET scans for the other two mice in each group show the same trend in biodistribution of each ^{64}Cu-labeled agent. T: tumor; L: liver; SI: small intestine; Th: throat; IBAT: interscapular brown adipose tissue.

Both tumor models showed significant uptake for visible contrast when the intensity scale bar is set to a maximum of 15 %ID/g. Visually, the biodistribution over time of $^{64}CuCl_2$ diluted in PBS in 4T1-tumor bearing mice looks very similar to that of ^{64}Cu-citrate in the same tumor model. This result indicates that weakly bound ^{64}Cu to either citrate, chloride or phosphate, behaves almost identically *in vivo*, perhaps because it is quickly exchanged to ligands in the bloodstream or in tissue and because the phosphate anions in PBS, with a concentration of 10 mM, do not combine with copper forming a precipitate as it was the case with $^{44}ScCl_3$ diluted in PBS. If ^{64}Cu would form a precipitate in PBS, 100% of the activity as ^{64}Cu-phosphate would accumulate in the liver, as it was the case after administration into mice of $^{44}ScCl_3$ diluted in PBS (Figure 2.9, in section 2.3.7). With both tracers, high accumulation in the intestines and liver is evident, as well as significant accumulation in the throat region in early time points and in the brown adipose tissue found in the interscapular region in later time points. Furthermore, the persistence of high %ID/g intensity in the liver and bowel throughout the studies, indicates that weakly bound ^{64}Cu has a very slow clearance rate from these organs. Figure 4.16 shows the biodistribution over time and the time-

activity curves in terms of %ID/g and %ID, respectively, from quantifications of VOIs covering the whole body, tumor, adductor and biceps femoris muscles and the delineable organs: liver and intestines. The %ID plots include exponential fits to the whole body VOIs from which the biological half-life of ^{64}Cu-citrate was quantified as 48.1 h and 55.0 h in the 4T1- and U87MG-tumor bearing mice, respectively. The biological half-life of $^{64}CuCl_2$ injected in PBS solution into 4T1-tumor bearing mice is 85.5 h.

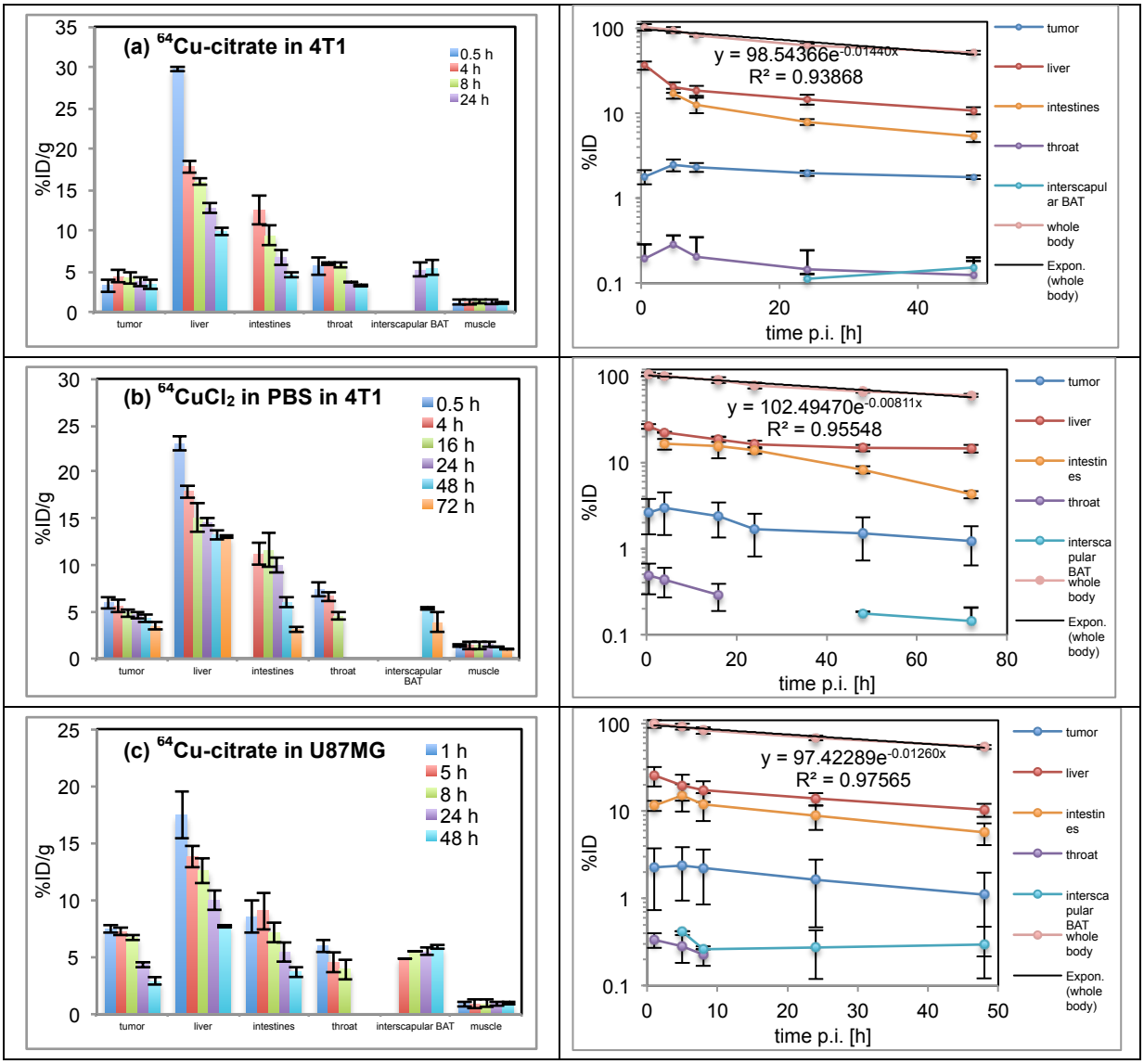

Figure 4.16 Quantitative PET data presented as biodistribution charts in terms of %ID/g and time-activity curves in terms of %ID from: ^{64}Cu-citrate in mice bearing 4T1 tumors (a) and U87MG tumors (c); and $^{64}CuCl_2$ diluted in PBS in mice bearing 4T1 tumors (b). All data is decay-corrected to time of injection. Error bars represent standard deviation from quantifications in three mice.

PET scans at 4, 24 and 48 h p.i. of ^{64}Cu-NOTA-TRC105 and ^{86}Y-DTPA-CHX-A"-TRC105 show prominent systemic circulation of the radiolabeled antibody and gradually increasing concentration of radioactivity in the 4T1

tumor (Figure 4.17). High accumulation in the liver and spleen is a common characteristic of full antibodies due to the binding of their Fc component to receptors found in lymphocytes and macrophages, which eventually accumulate in sinusoid capillaries found in these organs [195]. Below the PET scans from ^{86}Y-DTPA-CHX-A"-TRC105, Figure 5.15(c) shows the PET scans of ^{86}Y-citrate from a single 4T1 tumor-bearing mouse as a reference of how unlabeled or de-chelated ^{86}Y accumulates mainly in the skeleton.

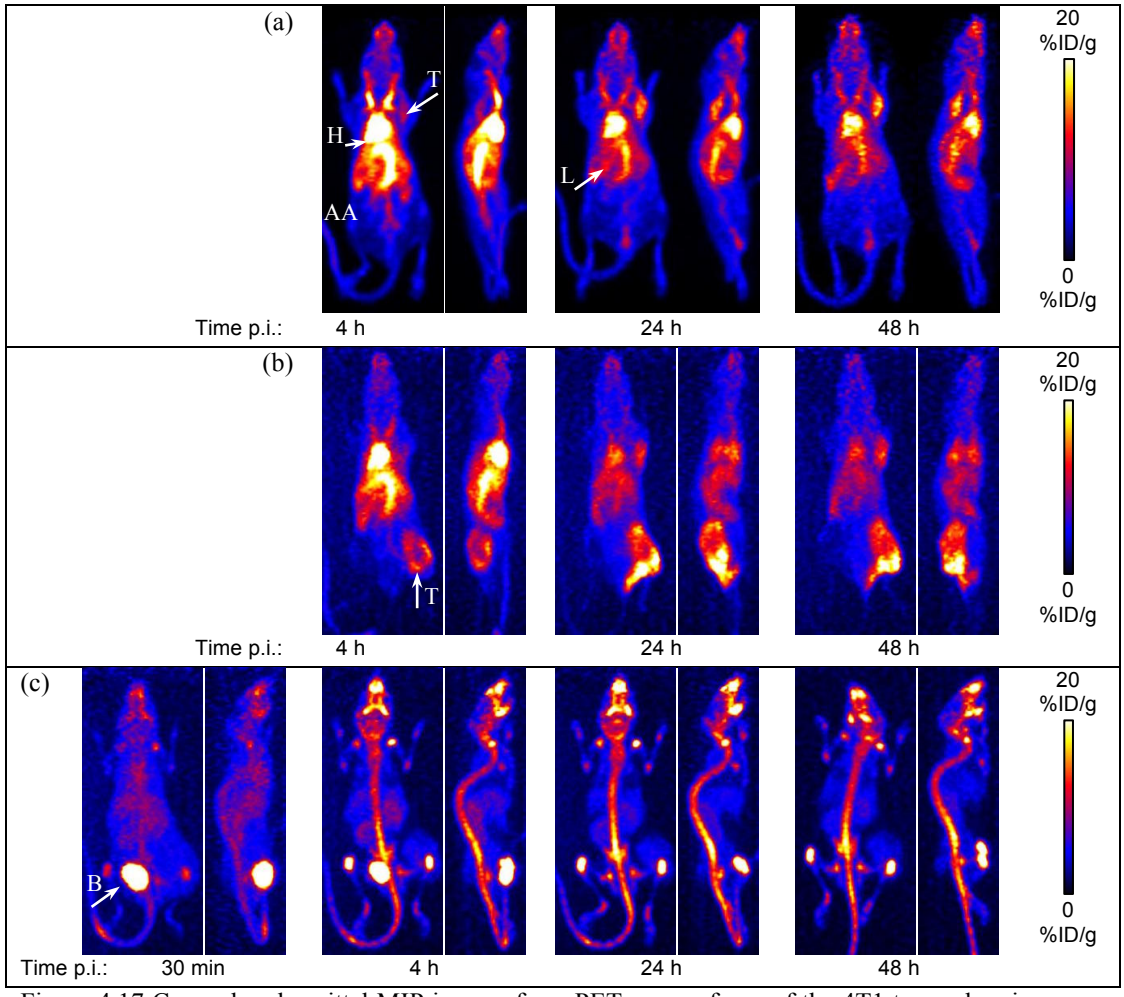

Figure 4.17 Coronal and sagittal MIP images from PET scans of one of the 4T1 tumor-bearing mouse administered with (a) ^{64}Cu-NOTA-TRC105, (b) ^{86}Y-DTPA-CHX-A"-TRC105 and (c) ^{86}Y-citrate. Uptake level is color coded by the %ID/g bar shown on the right of each set of images. T: tumor; L: liver; B: bladder; CA: carotid arteries; H: heart; AA: abdominal aorta.

Figure 4.18 shows the biodistribution over time of the radiolabeled antibodies and the time-activity curves from quantifications of VOIs covering the whole body, tumor, adductor and biceps femoris muscles and the delineable organs: heart, liver and spleen. Exponential fits to the whole body and heart time-activity curves reveal whole body biological and circulation half-lives for ^{64}Cu-NOTA-TRC105 of 282.9 h and 52.2 h, respectively; and 362.9 h and 42.1 h, respectively, for ^{86}Y-DTPA-CHX-A"-TRC105.

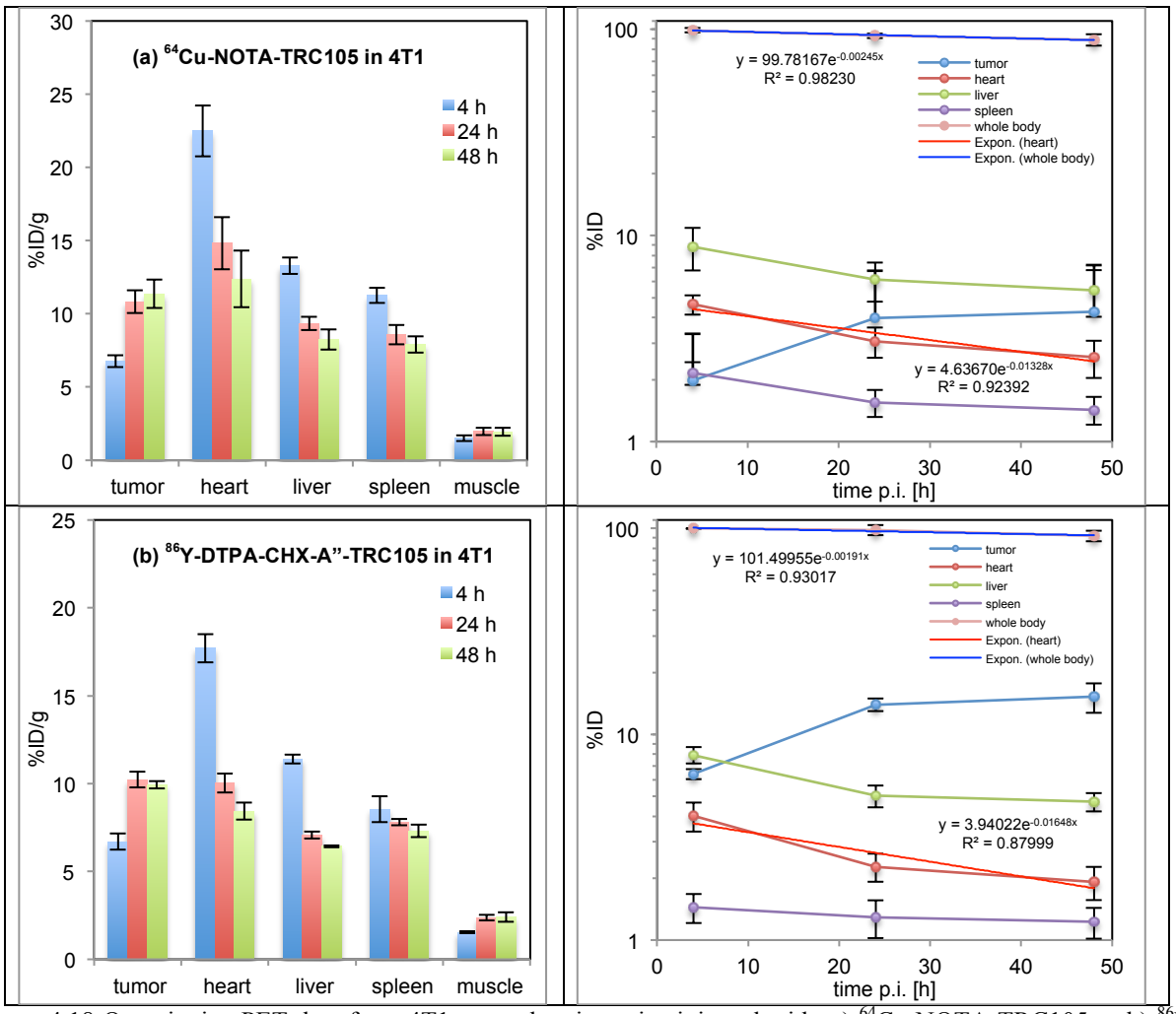

Figure 4.18 Quantitative PET data from 4T1-tumor bearing mice injected with: a) ^{64}Cu-NOTA-TRC105 or b) ^{86}Y-DTPA-CHX-A"-TRC105. All data is decay-corrected to time of injection. Error bars represent standard deviation from quantifications in three mice.

The biodistribution of weakly bound ^{64}Cu (^{64}Cu-citrate or $^{64}CuCl_2$ diluted in PBS) is useful to understand the fate of ^{64}Cu that decorporates or exchanges ligand from the targeting bioconjugate vector to ligands in non-specific tissues. Our results indicate that ^{64}Cu *in vivo* has a strong affinity towards many tissues, although particularly towards the liver and bowel, which reflects into a long retention in the body, having cleared only by 48 ± 3%, 45 ± 3% and 33 ± 3% after 48 h post-injection of ^{64}Cu-citrate in 4T1-tumor bearing mice, ^{64}Cu-citrate in U87MG tumor-bearing mice and $^{64}CuCl_2$ in 4T1-tumor bearing mice, respectively. This behavior contrasts with that of weakly bound ^{55}Co (^{55}Co-citrate), which had cleared from the whole body by more than 70% after 24 h p.i. in both tumor models (Chapter 3, section 3.3.6). Furthermore, there is significant tumor uptake of weakly bound ^{64}Cu in both tumor models, which needs to be considered in the quantification of uptake from ^{64}Cu-labeled targeted agents, in case there is suspicion of decorporation from the radiolabel. Table 4.10 compares the %ID/g uptake in the 4T1

tumor of the weakly-bound ^{64}Cu agents to that of ^{64}Cu-NOTA-TRC105 to highlight how de-chelated ^{64}Cu could potentially impact the evaluation of the targeting efficacy of this radiolabeled targeted agent.

Table 4.10 Comparison of ^{64}Cu uptake in 4T1 tumors by the targeted agent ^{64}Cu-NOTA-TRC105 and the non-targeted agents $^{64}CuCl_2$ diluted in PBS and ^{64}Cu-citrate. The uptake of ^{64}Cu-citrate in U87MG xenografts is included in the table but not compared to any other tracer.

Time p.i. [h]	**^{64}Cu-NOTA-TRC105 in 4T1 (%ID/g)**	**$^{64}CuCl_2$ in PBS in 4T1 (%ID/g)**	**ratio vs NOTA-TRC105**	**^{64}Cu-citrate in 4T1 (%ID/g)**	**ratio vs NOTA-TRC105**	**^{64}Cu-citrate in U87MG (%ID/g)**
0.5 – 1	-	6.0 ± 0.6	-	3.2 ± 0.8	-	7.4 ± 0.3
4 – 5	6.8 ± 0.4	5.6 ± 0.7	83%	4.3 ± 0.8	64%	7.3 ± 0.4
8	-	-	-	4.2 ± 0.7	-	6.7 ± 0.3
16	-	4.9 ± 0.5	-	-	-	-
24	10.8 ± 0.8	4.7 ± 0.4	44%	3.7 ± 0.6	34%	4.4 ± 0.3
48	11.4 ± 1.0	4.3 ± 0.4	38%	3.3 ± 0.5	29%	2.8 ± 0.3
72	-	3.5 ± 0.4	-	-	-	-

From the results in Table 4.10, if ^{64}Cu were to decorporate from the ^{64}Cu-NOTA-TRC105 agent, it could potentially contribute to an overestimation of the tumor uptake by up to 83% in the early time points (4 – 5 hours p.i.). However, we can rule out his possibility since the PET images from ^{64}Cu-NOTA-TRC105 show very small uptake in the bowel (Figure 4.17(a)), where decorporated ^{64}Cu would accumulate besides the liver, indicating that ^{64}Cu is stably bound to the chelator. This is actually the case based on the high thermodynamic stability of the Cu-NOTA complex (log K_{ML} = 20.1)[63].

However, other ^{64}Cu-labeled agents make use of chelators that bind ^{64}Cu with low strength, causing the radiometal to de-chelate and confound the targeting properties of the radiolabeled agent. For instance, the biodistribution of the hypoxia tracer ^{64}Cu-ATSM has been compared to that of weakly-bound ^{64}Cu (injected as ^{64}Cu-acetate) in mice bearing either murine adenocarcinoma (CaNT) or murine mammary carcinoma (EMT6) tumors, resulting in almost identical tumor uptakes beyond 2 hours post-injection [259], which raised the question of whether the copper accumulation is mediated by hypoxia or by copper metabolism.

On the other hand, the relatively high tumor targeting properties of weakly-bound ^{64}Cu make this agent a useful probe for diagnostic imaging of cancer lesions. Indeed, many research groups are beginning to use plain $^{64}CuCl_2$ to detect cancer lesions in both preclinical [8, 9, 13-15, 260] and clinical [16, 17] studies. To quantitatively demonstrate how weakly-bound ^{64}Cu is able to generate T/M contrast that is comparable to that from a targeted agent such as ^{64}Cu-NOTA-TRC105, the tumor-to-muscle (T/M) ratios were calculated and plotted in Figure 4.19.

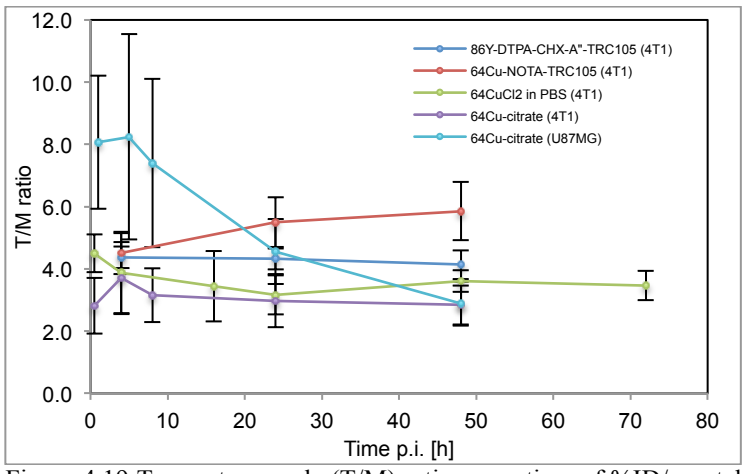

Figure 4.19 Tumor-to-muscle (T/M) ratios over time of %ID/g uptake values measured from PET images of groups of three 4T1 tumor-bearing mice injected with ^{86}Y-DTPA-CHX-A"-TRC105, ^{64}Cu-NOTA-TRC105, $^{64}CuCl_2$ in PBS and ^{64}Cu-citrate. The T/M ratios from the set of three U87MG tumor-bearing mice injected with ^{64}Cu-citrate is also included.

Clearly, the highest T/M ratio after administration of weakly bound ^{64}Cu occurs within the early time points after injection (≤ 8 h), particularly in the U87MG tumor model, in which it reaches a T/M ratio of ~ 8 merely 1 h p.i. These results suggests that if weakly-bound radio-copper were to be used as a radiotracer of cancer lesions, a better choice for a copper radionuclide that matches its pharmacokinetics is the shorter-lived ^{61}Cu. In the following section on internal dosimetry the effective dose caused by weakly-bound ^{64}Cu and ^{61}Cu will be evaluated and compared against each other.

Another important implication of the observed intrinsic tumor targeting properties of weakly-chelated ^{64}Cu is that it can be potentially used as a therapeutic due to its prominent β^- emissions, or it can be substituted by the radio-copper therapeutic ^{67}Cu. In the following two sections on internal dosimetry the therapeutic potential of weakly-bound ^{64}Cu and ^{67}Cu will also be evaluated.

The biodistribution results of ^{64}Cu-NOTA-TRC105 in 4T1 tumor-bearing mice shown in Figure 4.18(a) agree with the results published by Zhang et al [197]. The ^{86}Y-labeled analogue, ^{86}Y-DTPA-CHX-A"-TRC105, displays a similar biodistribution in the same time points (Figure 4.18(b)), which indicates that ^{86}Y is being transported by the antibody throughout the timeframe of the study, having minimal decorporation. If this were not the case, high ^{86}Y uptake would be detected in the skeleton as it is the case with ^{86}Y-citrate shown in Figure 4.18(c). The high tumor uptake of the radiolabeled antibodies is due to the binding of TRC105 to the CD105 receptors that are overexpressed in vascular endothelial cells undergoing angiogenesis, which seek to satisfy the demand for vasculature by the proliferating tumor cells [201, 202]. This targeting mechanism can be further exploited by delivering highly ionizing

radiation to the cancer lesion. In the next sections on internal dosimetry, the therapeutic efficiency of the theranostic ^{64}Cu-NOTA-TRC105 will be evaluated, as well as that of the fully therapeutic analogues ^{67}Cu-NOTA-TRC105 and ^{90}Y-DTPA-CHX-A"-TRC105.

4.3.7 *Internal dosimetry of ^{64}Cu-citrate, $^{64}CuCl_2$ in PBS, ^{64}Cu-NOTA-TRC105 and ^{86}Y-DTPA-CHX-A"-TRC105 in humans*

Only the biodistribution data from 4T1 tumor-bearing mice was employed for the estimation of human dosimetry after administration of ^{64}Cu-citrate. Table 4.11 shows the %ID uptake values of ^{64}Cu-citrate, $^{64}CuCl_2$ in PBS, ^{64}Cu-NOTA-TRC105 and ^{86}Y-DTPA-CHX-A"-TRC105 extrapolated to a 73.7 kg standard adult male as defined by Cristy and Eckerman [49], using the mass extrapolation method by Kirschne [52], with the whole body mass of the 4T1 mouse set to the average value of 18.3 g.

Table 4.11 Extrapolation of ^{64}Cu and ^{86}Y uptake in 4T1-tumor bearing mice to standard adult male organs.

Organ	Organ mass in human male adult [g] [49]	Conversion factors %ID/g in mouse to %ID in human	%ID ^{64}Cu-citrate					%ID $^{64}CuCl_2$ in PBS					
			0.5 h	4 h	8 h	24 h	48 h	0.5 h	4 h	16 h	24 h	48 h	72 h
Liver	1910	0.474	14.1	8.4	7.6	6.1	4.7	10.9	8.5	7.2	6.9	6.3	6.2
Small intestine	677	0.168	-	2.1	1.6	1.1	0.8	-	1.9	2.0	1.7	1.0	0.5
Thyroid (throat)	20.7	0.005	0.028	0.030	0.029	0.019	0.016	0.037	0.034	0.023	-	-	-
Remaining organs	Balance	Balance	89.2	85.6	74.2	56.0	46.7	95.2	91.1	81.3	69.4	59.7	53.2

Organ	Organ mass in human male adult [g] [49]	Conversion factors %ID/g in mouse to %ID in human	%ID ^{64}Cu-NOTA-TRC105			%ID ^{86}Y-DTPA-CHX-A"-TRC105		
			4 h	24 h	48 h	4 h	24 h	48 h
Heart	840	0.211	4.7	3.1	2.6	3.7	2.1	1.8
Liver	1910	0.474	6.3	4.4	3.9	5.4	3.3	3.0
Spleen	183	0.045	0.5	0.4	0.4	0.4	0.4	0.3
Remaining organs	Balance	Balance	87.7	85.4	82.2	90.5	92.4	86.9

After setting these %ID uptake values in the EXM portion of the OLINDA software and fitting them to mono-exponential functions, the software automatically calculated the cumulative number of decays in each source organ and then the absorbed dose in every target organ considered by the software as well as the total body effective dose. The dose deposited by the shorter-lived analogues of weakly bound ^{61}Cu was obtained from OLINDA by keeping the pharmacokinetic data from the ^{64}Cu-labeled tracers and replacing the nuclide accordingly. The effective doses were estimated as 22.6 μSv/MBq ^{64}Cu-citrate, 23.2 μSv/MBq ^{61}Cu-citrate, 25.2 μSv/MBq $^{64}CuCl_2$, 24.0 μSv/MBq $^{61}CuCl_2$, 25.8 μSv/MBq ^{64}Cu-NOTA-TRC105 and 249 μSv/MBq ^{86}Y-DTPA-CHX-A"-TRC105 injected. Figure 4.20 shows the absorbed dose to each target organ after administration of each one of these agents.

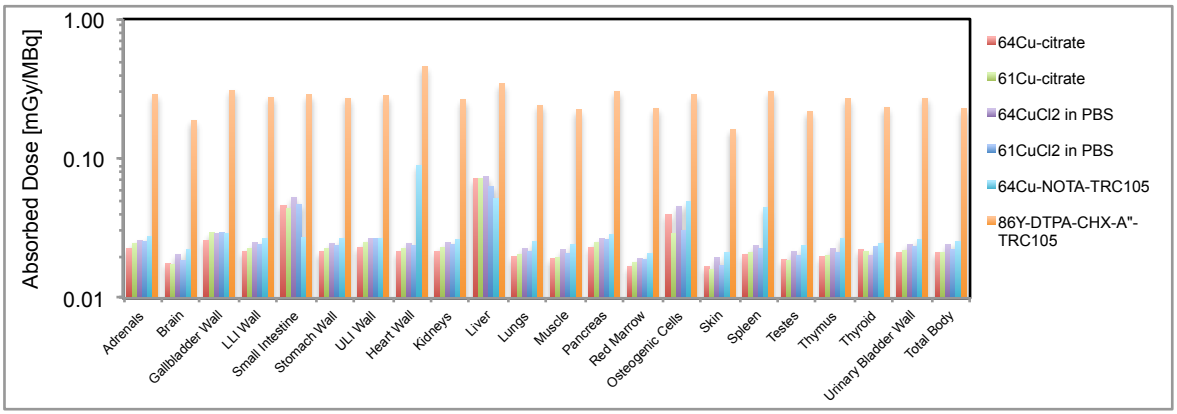

Figure 4.20 Absorbed dose to the organs of a standard adult male after administration of ^{64}Cu-citrate, ^{61}Cu-citrate, $^{64}CuCl_2$, $^{61}CuCl_2$, ^{64}Cu-NOTA-TRC105 or ^{86}Y-DTPA-CHX-A"-TRC105. The absorbed doses of the ^{61}Cu-labeled agents were estimated from the biodistribution data obtained with the ^{64}Cu-labeled analogues. Notice that the scale is in logarithmic scale.

The first important observation from Figure 4.20, is that the ^{86}Y-labeled antibody deposits about one order of magnitude more absorbed dose through every organ compared to the ^{64}Cu-labeled counterpart. This is the result of the many penetrating gamma rays that are emitted from the decaying ^{86}Y (see gamma spectrum in Figure 4.12(c)), whereas the only penetrating radiation emitted from ^{64}Cu are the 511 keV gammas from positron annihilation and a 1346 keV gamma with a minuscule branching ratio of 0.475%.

Surprisingly, both the effective dose and the absorbed doses per organ of ^{61}Cu-citrate and $^{61}CuCl_2$ is almost identical to that caused by the ^{64}Cu analogues, even though ^{61}Cu has a much shorter half-live (3.33 h vs 12.7 h). The most likely explanation for this is that ^{61}Cu emits more penetrating gammas per decay compared to ^{64}Cu, namely 3.5 times more 511 keV gammas from annihilation and two important gammas of 283 and 656 keV with branching ratios of 12% and 11%, respectively. Hence, in terms of dose per unit of injected activity, there is no advantage in using a short-lived copper nuclide against the already commercially available and logistically more accessible ^{64}Cu.

Evidently, the critical organs after administration of each radiotracer are the organs where most of the activity is accumulated. For ^{64}Cu-citrate and $^{64}CuCl_2$ the critical organ is the liver with an absorbed dose per MBq of 71.8 and 74.4 μGy/MBq, respectively. For ^{64}Cu-NOTA-TRC105 and ^{86}Y-DTPA-CHX-A"-TRC105 the critical organ is the heart wall with an absorbed dose of 89.8 and 455 μGy/MBq, respectively. These absorbed doses indicate that maximum activities of ^{64}Cu-citrate, $^{64}CuCl_2$, ^{64}Cu-NOTA-TRC105 and ^{86}Y-DTPA-CHX-A"-TRC105 that can be administered into a human male patient are 696, 672, 556 and 109 MBq, respectively, in order to comply with the recommended 50 mGy annual limit to any organ recommended by the FDA [75]. Such doses would imply effective

doses of 15.7, 16.9, 14.3 and 27.1 mSv, respectively, all of them also below the annual ED limit of 50 mSv recommended by the FDA [75].

The doses deposited in every organ by the therapeutic analogues labeled with ^{67}Cu or ^{90}Y were obtained from OLINDA by keeping the pharmacokinetic data from the ^{64}Cu- or ^{86}Y-labeled tracers and replacing the nuclide accordingly. Figure 4.21 shows these results.

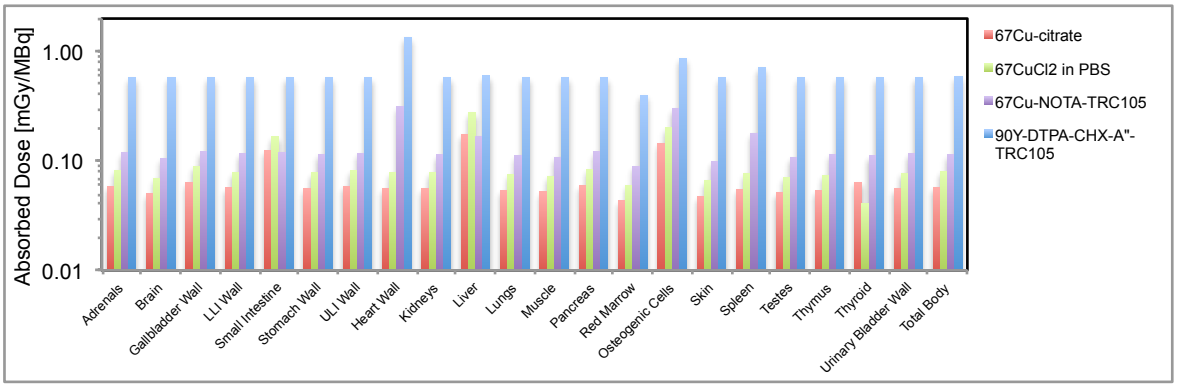

Figure 4.21 Absorbed dose to the organs of a standard adult male after administration of ^{67}Cu-citrate, $^{67}CuCl_2$, ^{67}Cu-NOTA-TRC105 and ^{90}Y-DTPA-CHX-A"-TRC105.

Once again, the critical organs are the ones in which most of the activity is accumulated: the liver, which receives an absorbed dose of 0.175 mGy/MBq ^{67}Cu-citrate or 0.275 mGy/MBq $^{67}CuCl_2$; and the heart wall, which receives an absorbed dose of 0.313 mGy/MBq ^{67}Cu-NOTA-TRC105 or 1.340 mGy/MBq ^{90}Y-DTPA-CHX-A"-TRC105. Since the maximum amount of absorbed dose that can be tolerated by these organs, measured as the probability of 50% complication within 5 years, is 40 Gy and 50 Gy, respectively [100], this means that maximum amounts of 228 GBq of ^{67}Cu-citrate, 145 GBq $^{67}CuCl_2$, 159 GBq ^{67}Cu-NOTA-TRC105 and 37 GBq ^{90}Y-DTPA-CHX-A"TRC105 can be safely administered into a patient. However, the dose limit to other more sensitive organs, such as the kidneys and red marrow, needs to be taken into account. It is recommended that these organs receive less than 28 Gy[100] and 3 Gy[217, 261, 262], respectively. Clearly, the red marrow will be the main tissue of concern due to its low tolerance to radiation and since the absorbed dose to this organ is 43.1 μGy/MBq ^{67}Cu-citrate, 59.9 μGy/MBq $^{67}CuCl_2$, 89.2 μGy/MBq ^{67}Cu-NOTA-TRC105 and 0.399 mGy/MBq ^{90}Y-DTPA-CHX-A"-TRC105, the maximum activities that can be safely administered are 69 GBq of ^{67}Cu-citrate, 50 GBq $^{67}CuCl_2$, 33 GBq ^{67}Cu-NOTA-TRC105 and 7.5 GBq ^{90}Y-DTPA-CHX-A"TRC105.

On the other hand, if ^{64}Cu were to be used as a therapeutic, meaning that large amounts of activity of this nuclide were to be administered, the critical tissues after administration of ^{64}Cu-citrate, $^{64}CuCl_2$ or ^{64}Cu-NOTA-

TRC105 would constraint the maximum amount of injectable activity to 557, 537 and 556 GBq, respectively. However, once the again, the red marrow dose limit of 3 Gy, will further constraint the maximum injectable activity based on the absorbed doses to this tissue shown in Figure 4.20 of 16.9 μGy/MBq ^{64}Cu-citrate, 19.4 μGy/MBq $^{64}CuCl_2$ and 21.0 μGy/MBq ^{64}Cu-NOTA-TRC105. Thus, the maximum activity that can be safely administered for radionuclide therapy is actually 177, 154 and 142 GBq, respectively

The necessary amount of either one of the therapeutic agents mentioned in this chapter that has to be administered in order to control a tumor in a patient depends on the tumor uptake and on the size of the tumor. For instance, Börjesson et al [263], report that a ^{89}Zr-labeled antibody (U36) administered to 20 human patients with tumors of head and neck squamous cell carcinoma results in tumor uptakes that range from 0.006 to 0.038 %ID/g, which is two to three orders of magnitude lower than what is typically observed in tumor xenografts in small animals. Therefore, the estimation of tumor dosimetry in a clinical scenario is beyond the scope of this thesis. However, from the tumor uptake data in mice that we have obtained we can estimate the absorbed dose to the implanted tumors and then predict what is the necessary amount of ^{64}Cu, ^{67}Cu or ^{90}Y-labeled agent that would result in tumor regression in our small animal models. Based on these values and the internal dosimetry in mice obtained from the biodistribution data, we can also predict the potential toxicity of such a treatment. This will be focus of the next section.

4.3.8 *Tumor and normal organ dosimetry of ^{64}Cu-citrate, $^{64}CuCl_2$ in PBS, ^{64}Cu-NOTA-TRC105, ^{67}Cu-NOTA-TRC105 and ^{90}Y-DTPA-CHX-A"-TRC105 in mice*

The absorbed dose delivered to the 4T1 tumors in mice by the theranostic agents ^{64}Cu-citrate, $^{64}CuCl_2$ and ^{64}Cu-NOTA-TRC105 and the predicted dose that will be delivered by the fully therapeutic analogues ^{67}Cu-citrate, $^{67}CuCl_2$, ^{67}Cu-NOTA-TRC105 and ^{90}Y-DTPA-CHX-A"-TRC105 was estimated using the dose-to-sphere model of OLINDA, which only requires the total cumulative decays or disintegrations inside the tumor per administered activity in units of MBq-h/MBq. This value was obtained by trapezoidal integration of the non-decay-corrected time-activity curve of the tumor up to the last time point that was measured and then by integration from this time point up to infinity assuming: 1) that the uptake phase in the tumor is over, 2) that there is no biological clearance and 3) that there is only physical decay of the radiotracer. The formula for this latter integration is Equation 2.7 from Chapter 2 of this dissertation. Table 4.12 shows the results of the trapezoidal integration and the analytical integration after the last imaged time point. The first column of plots in Figure 4.22 shows the tumor uptake over

time of each of the agents obtained from VOI analysis of the PET images in units of %ID decay-corrected to the time of injection. The second and third columns shows this same data after consideration of decay of the diagnostic (^{64}Cu or ^{86}Y) or therapeutic (^{67}Cu or ^{90}Y) nuclides, respectively, including the continuation of the time-activity curve after the last measured time point, assuming that only physical decay occurs up to infinity.

Table 4.12 Cumulative decays from each agent inside the 4T1 tumor xenograft and predicted absorbed dose based on the sphere model of the OLINDA software.

Therapeutic agent	**Trapezoidal integral of non-decay corrected %ID in tumor curve [Bq-h/Bq]**	**Analytical integral from last time point to infinity (Eq. 2.7)**	**Total cumulative decays in tumor (trapezoidal + analytical integrals) [Bq-h/Bq]**	**Average tumor mass [g]**	**mGy / MBq in tumor (from fits in Figure 5.21)**	**MBq required to deliver 230 Gy to tumor**
^{64}Cu-citrate	0.388	0.002	0.390	0.55 ± 0.05	48	4777
^{67}Cu-citrate	0.780	0.540	1.321		209	1100
$^{64}CuCl_2$	0.436	0.0001	0.436	0.42 ± 0.20	70	3292
$^{67}CuCl_2$	0.952	0.218	1.170		241	954
^{64}Cu-NOTA-TRC105	0.464	0.004	0.468	0.34 ± 0.20	92	2501
^{67}Cu-NOTA-TRC105	1.194	1.298	2.492		631	364
^{90}Y-DTPA-CHX-A”-TRC105	4.191	4.977	9.168	1.29 ± 0.29	2677	86

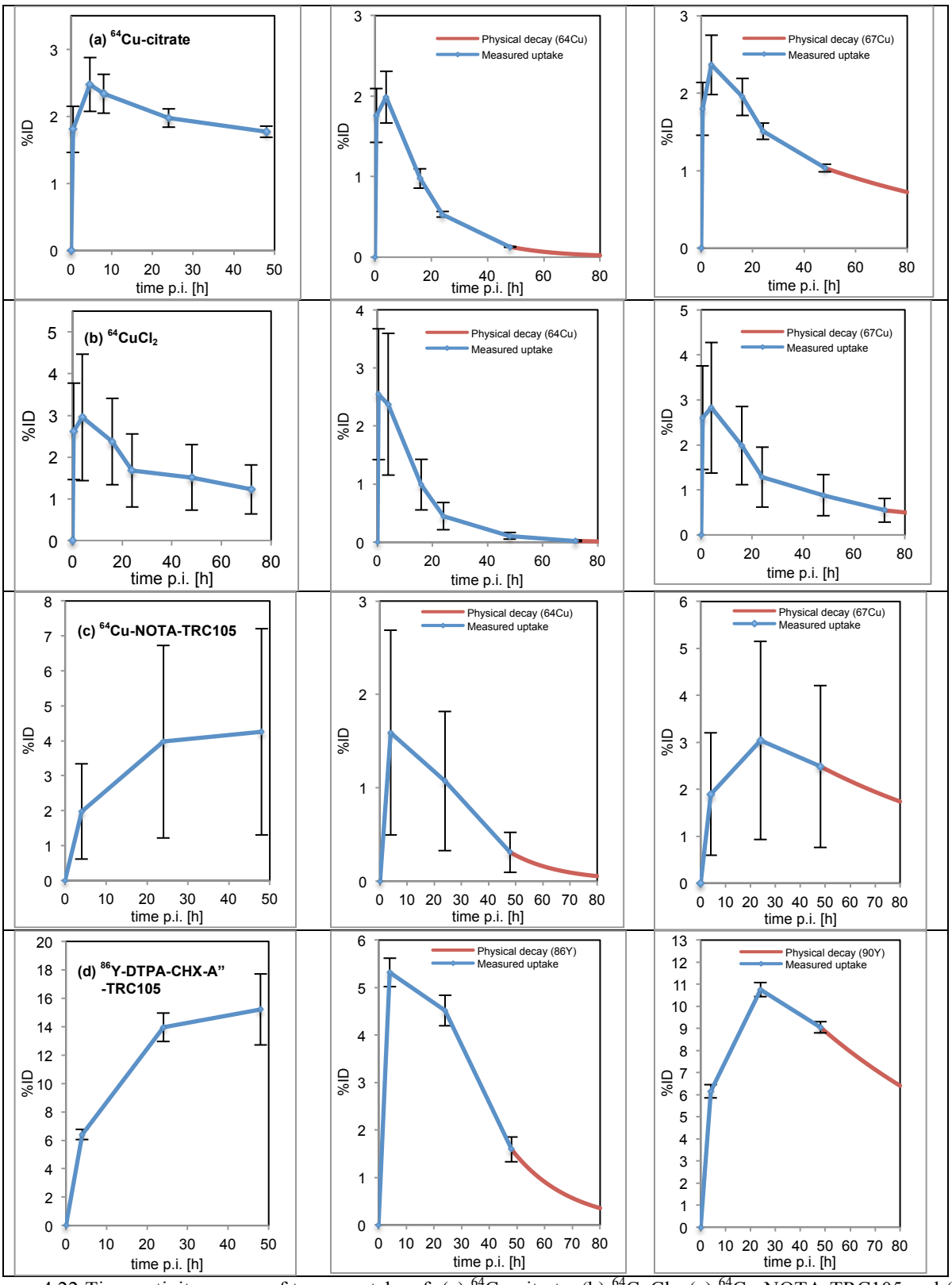

Figure 4.22 Time-activity curves of tumor uptake of: (a) ^{64}Cu-citrate, (b) $^{64}CuCl_2$, (c) ^{64}Cu-NOTA-TRC105 and (d) ^{86}Y-DTPA-CHX-A"-TRC105. The first column is in %ID decay-corrected to time of injection; the second and third columns with %ID considering physical decay over time of the diagnostic and therapeutic radionuclides, respectively.

After logging in the total cumulative decays inside each 4T1 tumor in the dose-to-sphere model of OLINDA, the total absorbed dose to spheres of unit-density material with masses between 10 mg and 6 kg are calculated. Figure 4.23 shows part of the output from OLINDA, in the range between 10 mg to 10 g, along with a power fit to each set of data.

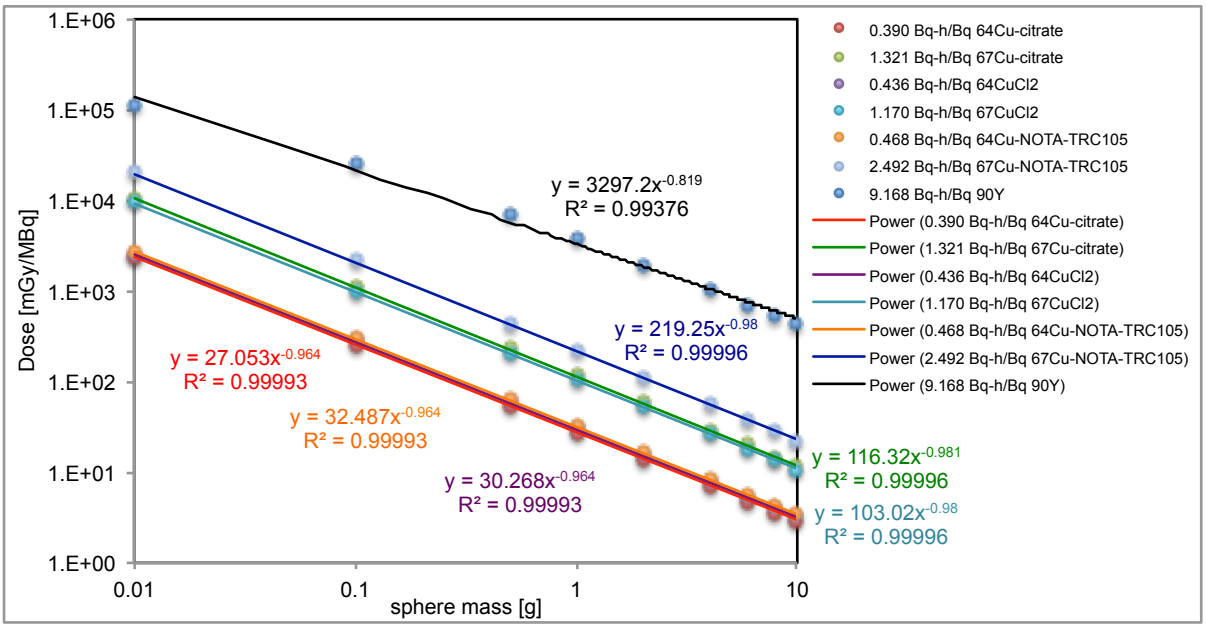

Figure 4.23 Absorbed dose to unit-density spheres homogeneously filled with ^{64}Cu, ^{67}Cu or ^{86}Y after the cumulative number of decays indicated in the legend, which were obtained from integration of the non-decay corrected time-activity curves in 4T1 tumors in mouse models of radio-copper or radio-yttrium labeled agents shown in Figure 4.22.

From the plots in Figure 4.23 we can estimate what is the necessary amount of radiolabeled agent that has to be administered in order to have a therapeutic effect in 4T1 tumor-bearing mice like the ones employed in this study. The average volume of the VOIs drawn over the whole tumor in the PET images from the mice injected with ^{64}Cu-citrate, $^{64}CuCl_2$, ^{64}Cu-NOTA-TRC105 and ^{86}Y-DTPA-CHX-A"-TRC105 was 554 ± 48, 425 ± 196, 339 ± 198 and 1286 ± 290 mm^3, respectively, which corresponds to tumor masses of 0.55 ± 0.05, 0.42 ± 0.20, 0.34 ± 0.20 and 1.29 ± 0.29 g, respectively, assuming that the tumors have a density of 1 g/cm^3. Thus, from these tumor masses and the fitted power functions in Figure 4.23 we can predict the absorbed dose delivered to the tumor per administered MBq of radiolabeled agent. Table 4.12 summarizes these estimates and the activity of each agent that would have to be administered in order to have observable tumor regression under the conservative assumption that up to 230 Gy are required for tumor response, an assumption based on the review article by Strigari et al [80] as it was explained in section 2.3.9. However, in order to be able to compare the predicted therapeutic efficacy between agents, a tumor

mass of 0.5 g was assumed for every mouse xenograft, resulting in the tumor absorbed doses per MBq shown in Table 4.13.

Table 4.13 Predicted absorbed dose to a 0.5 g 4T1 tumor xenograft based on the sphere model of the OLINDA software.

Therapeutic agent	**mGy / MBq in 0.5 g tumor (from fits in Figure 5.21)**	**MBq required to deliver 230 Gy to 0.5 g tumor**
^{64}Cu-citrate	53	4357
^{67}Cu-citrate	230	1002
$^{64}CuCl_2$	59	3894
$^{67}CuCl_2$	203	1132
^{64}Cu-NOTA-TRC105	63	3628
^{67}Cu-NOTA-TRC105	433	532
^{90}Y-DTPA-CHX-A"-TRC105	5816	40

Clearly, the ^{90}Y-labed antibody delivers the highest dose per MBq accumulated in the tumor, resulting in the lowest amount of activity required to control, that is to deliver 230 Gy, to a 0.5 g tumor xenograft in a mouse. There are three main reasons for this: first, ^{90}Y emits beta particles that are 4 to 5 times more energetic than the ones emitted by either ^{64}Cu and ^{67}Cu, therefore it delivers about the same factor more energy per unit mass or absorbed dose to its surroundings (as long as the radius of the spherical volume of mass is larger than the mean range of the beta particles from ^{90}Y, that is, 4 mm [41], which is actually the case for a 0.5 g or 0.5 cm^3 sphere); second, compared to ^{64}Cu, ^{90}Y has 5 times longer half-life, which means that once it is accumulated and retained in the tumor it will accumulate decays in this tissue for a longer time resulting in many more total cumulated decays; in other words, the integral of the time-activity curve in the tumor will result in a larger value as seen in Table 4.12; and third, compared to the ^{64}Cu-labeled antibody, the ^{86}Y-labeled analogue showed about a factor of 3 better targeting efficiency as seen in Figures 4.22 (c) and (d). The reason for this is that the average mass of the tumor xenografts in the mice injected with ^{86}Y-DTPA-CHX-A"-TRC105 are 3.8 times larger that the average tumor mass of the ones injected with the ^{64}Cu-labeled counterpart, and therefore, even though the %ID/g uptakes in the tumor are comparable between agents, as seen in Figure 4.18, the %ID values turn out to be higher with the former agent.

The ^{67}Cu analogues are more effective radiotherapeutics compared to the ^{64}Cu counterparts due to the decay properties of the former nuclide. Namely, the emission of a beta particle with 100% probability per decay against 38.5% β^- emission by ^{64}Cu; and an almost five fold difference in half-live (61.8 h vs 12.7 h), which results in a larger number of cumulative decays in the target tissue, as explained before. However, ^{67}Cu is as not readily available as ^{64}Cu. For instance, with the novel radiochemical separation method presented in section 4.2.2, ^{64}Cu can be produced from a single batch of ^{64}Ni target material, after recycling, two or three times within a week, and due to

the high yields of the ^{64}Ni(p,n) reaction, shown in Figure 4.3(b) and Figure 4.7, tens or even hundreds of GBq of ^{64}Cu per run can be produced for a fractionated therapy regimen. Thus, many doses of ^{64}Cu-labeled radiotherapeutic can be injected within a week in order to compensate for the relatively short half-live of ^{64}Cu.

Another important observation from Table 4.13 is that due to the intrinsic tumor targeting properties of weakly-bound radio-copper, the ^{6x}Cu-citrate and $^{6x}CuCl_2$ agents are able to deliver doses per MBq that are comparable to that of the tumor targeted agent ^{6x}Cu-NOTA-TRC105. However, the high accumulation of the former agents in non-targeted tissue such as the liver and intestines most likely will result in high absorbed doses to these organs and therefore in unacceptable toxicity.

In order to predict toxicities in normal organs in a mouse injected with either one of the therapeutic agents covered in this chapter, the *S*-values for ^{64}Cu and ^{67}Cu were estimated after interpolation from the absorbed fraction (AF) data for mono-energetic photons and electrons within the organs of a 27 g mouse obtained by Stabin et al. [56] and then by substitution of these values in Equation 2.5 from the MIRD schema [53] for internal dosimetry. On the other hand, the *S*-values for ^{90}Y found in the same publication by Stabin et al. were directly employed. The beta and positron emissions from ^{64}Cu or ^{67}Cu were assumed to have fixed average energies and only the organs with the highest uptake, that is, the delineable organs from the PET images, were considered as source organs. Table 4.14 shows the nuclear data of the main emissions from ^{64}Cu and ^{67}Cu that were considered in the *S*-values. Tables 4.15 and 4.16 show the calculated *S*-values for ^{64}Cu and ^{67}Cu, where S_{γ}, $S_{\beta-}$ and $S_{\beta+}$ represent the *S*-values of the γ, β^- and positron emissions, respectively, in units of mGy/MBq-h. Table 4.17 shows the *S*-values of ^{90}Y[56] of the main source organs involved in the biodistribution of ^{86}Y-DTPA-CHX-A"-TRC105, in order to have them as a comparison to the calculated *S*-values of ^{64}Cu and ^{67}Cu and as a reference to the estimated absorbed doses per organ.

Table 4.14 Nuclear data of ^{64}Cu and ^{67}Cu considered for the calculations of *S*-values in mouse.

Nuclide	**Radiations**	**Yield [Bq^{-1}-s^{-1}]**	**Energy (average for β^- and β^+) [keV]**
^{64}Cu	β^+	0.1760	278.2
	γ from β^+ annihilation	0.3520	511.0
	γ_1	0.0048	1346.0
	β^-	0.3850	190.7
^{67}Cu	β^-_1	0.0110	51.0
	β^-_2	0.5700	121.0
	β^-_3	0.2200	154.0
	β^-_4	0.2000	189.0
	γ_1	0.0700	91.3
	γ_2	0.1610	93.3
	γ_3	0.4870	184.6

Table 4.15 *S*-values of ^{64}Cu in a 27.0 g mouse. All values are in units of mGy/MBq-h.

		Source organs											
		Small intestine			Liver			Heart			Spleen		
		S_γ	$S_{\beta-}$	$S_{\beta+}$	S_γ	$S_{\beta-}$	$S_{\beta+}$	S_γ	$S_{\beta-}$	$S_{\beta+}$	S_γ	$S_{\beta-}$	$S_{\beta+}$
Target organs	**O. T.**	0.10	0.10	0.10	0.09	0.12	0.11	0.10	0.14	0.14	0.09	0.17	0.15
	Skeleton	0.08	0	0	0.11	0.02	0.03	0.14	0	0	0.13	0	0
	Lungs	0.14	0	0	0.51	1.09	1.25	0.84	0.89	1.27	0.68	0	0
	Heart	0.12	0	0	0.31	0.05	0.08	5.09	272.64	172.77	0.37	0	0
	Liver	0.31	0.05	0.06	1.53	50.50	32.41	0.41	0.05	0.08	1.09	3.44	3.54
	Kidneys	0.54	0.08	0.13	0.28	0.06	0.08	0.09	0	0	0.28	0	0
	Stomach	0.25	0.07	0.09	0.50	0.09	0.14	0.20	0	0	1.68	4.49	4.91
	S. I.	1.41	41.99	27.11	0.30	0.05	0.07	0.10	0	0	0.21	0	0
	Spleen	0.03	0	0	0.21	0.63	0.66	0.09	0	0	2.42	288.09	173.80
	Testes	0.24	0	0	0.07	0	0	0	0	0	0.07	0	0
	Bladder	0	0	0	0	0	0	0	0	0	0	0	0

Table 4.16 *S*-values of ^{67}Cu in a 27.0 g mouse. All values are in units of mGy/MBq-h.

		Source organs							
		Small intestine		Liver		Heart		Spleen	
		S_γ	$S_{\beta-}$	S_γ	$S_{\beta-}$	S_γ	$S_{\beta-}$	S_γ	$S_{\beta-}$
Target organs	**Other tissues**	0.05	0.15	0.05	0.18	0.05	0.21	0.05	0.25
	Skeleton	0.06	0	0.07	0.03	0.09	0	0.08	0.001
	Lungs	0.06	0	0.25	1.34	0.39	1.06	0.30	0
	Heart	0.04	0	0.16	0.05	2.69	537.45	0.22	0
	Liver	0.14	0.06	0.80	98.95	0.19	0.06	0.54	4.81
	Kidneys	0.27	0.09	0.14	0.08	0.04	0	0.13	0.00
	Stomach	0.14	0.08	0.25	0.11	0.09	0.002	0.77	6.18
	Small intestine	0.75	82.04	0.14	0.07	0.05	0	0.09	0.00
	Spleen	0.02	0	0.11	0.88	0.04	0	1.49	580.59
	Testes	0.12	0	0.04	0	0	0	0.03	0.00
	Bladder	0	0	0	0	0	0	0	0.00

Table 4.17 *S*-values of ^{90}Y in a 27.0 g mouse published by Stabin et al [56]. All values are in units of mGy/MBq-h.

		Source organs		
		Liver	Heart	Spleen
Target organs	**Other tissues**	12.89	17.24	11.23
	Skeleton	8.39	3.24	7.34
	Lungs	74.16	162.00	114.12
	Heart	33.73	1753.20	18.50
	Liver	399.60	33.95	183.60
	Kidneys	15.95	0.01	4.79
	Stomach	41.04	2.65	320.04
	Small intestine	17.21	0.03	4.00
	Spleen	186.48	17.24	6228.00
	Testes	0	0	0.001
	Bladder	0	0	0

Table 4.18 shows the cumulative decays per MBq of injected agent in each of the source organs that is obtained from the integration of their respective non-decay corrected time-activity curves, which can be done with the EXM portion of the OLINDA/EXM software or "manually" after some algebra on the parameters of the fitted mono-exponential functions, as it was explained in section 2.3.9.

Table 4.18 Cumulative decays in each of the main organs where the therapeutic agent accumulates

	Accumulated decays in units of [MBq-h/MBq] in:			
Therapeutic agent	**Small intestine**	**Liver**	**Heart**	**Spleen**
^{64}Cu-citrate	2.11	3.48	-	-
^{67}Cu-citrate	4.30	7.17	-	-
$^{64}CuCl_2$	2.64	3.67	-	-
$^{67}CuCl_2$	6.66	11.5	-	-
^{64}Cu-NOTA-TRC105	-	1.35	0.691	0.337
^{67}Cu-NOTA-TRC105	-	3.86	1.88	0.986
^{90}Y-DTPA-CHX-A"-TRC105	-	3.30	1.39	0.991

The multiplication of the accumulated decays per source organ by the corresponding *S*-value and their summation results in the absorbed dose per target organ in units of mGy/MBq. The results from this computation are shown in Table 4.19.

Table 4.19 Absorbed doses from ^{64}Cu, ^{67}Cu and ^{90}Y-labeled agents in a 27.0 g mouse. All values are in units of mGy/MBq.

	Agent:	**^{64}Cu-citrate**			**^{67}Cu-citrate**			**$^{64}CuCl_2$**			**$^{67}CuCl_2$**		
		Source organs		**Total**	**Source organs**		**Total**	**Source organs**		**Total**	**Source organs**		**Total**
		SI	**Liver**	**dose**	**SI**	**Liver**	**dose**	**SI**	**Liver**	**dose**	**SI**	**Liver**	**dose**
Target organs	**O. T.**	0.6	1.1	1.8	0.8	1.6	2.5	0.8	1.2	2.0	1.3	2.6	3.9
	Skeleton	0.2	0.5	0.7	0.2	0.7	0.9	0.2	0.6	0.8	0.4	1.1	1.5
	Lungs	0.3	9.9	10.2	0.3	11.4	11.7	0.4	10.4	10.8	0.4	18.3	18.7
	Heart	0.3	1.5	1.8	0.2	1.5	1.7	0.3	1.6	1.9	0.3	2.4	2.7
	Liver	0.9	293.9	294.7	0.9	715.2	716.1	1.1	309.9	311.0	1.3	1147.2	1148.5
	Kidneys	1.6	1.5	3.0	1.6	1.5	3.1	2.0	1.6	3.5	2.4	2.5	4.9
	Stomach	0.9	2.5	3.4	0.9	2.6	3.5	1.1	2.7	3.8	1.4	4.1	5.5
	Intestines	148.8	1.5	150.2	356.0	1.5	357.5	186.1	1.6	187.7	551.3	2.4	553.7
	Spleen	0.1	5.2	5.3	0.1	7.1	7.2	0.1	5.5	5.6	0.1	11.4	11.5
	Testes	0.5	0.3	0.8	0.5	0.3	0.8	0.6	0.3	0.9	0.8	0.4	1.2
	Bladder	0	0	0	0	0	0	0	0	0	0	0	0

	Agent:	**^{64}Cu-NOTA-TRC105**				**^{67}Cu-NOTA-TRC105**				**^{90}Y-DTPA-CHX-A"-TRC105**			
		Source organs			**Total**	**Source organs**			**Total**	**Source organs**			**Total**
		Heart	**Liver**	**Spleen**	**dose**	**Heart**	**Liver**	**Spleen**	**dose**	**Heart**	**Liver**	**Spleen**	**dose**
Target organs	**O. T.**	0.3	0.4	0.1	0.8	0.5	0.9	0.3	1.6	34.5	51.6	11.2	97.3
	Skeleton	0.1	0.2	0.0	0.4	0.2	0.4	0.1	0.6	6.5	33.6	7.3	47.4
	Lungs	2.1	3.8	0.2	6.1	2.7	6.1	0.3	9.2	324.0	296.6	114.1	734.8
	Heart	311.3	0.6	0.1	312.0	1015.5	0.8	0.2	1016.5	3506.4	134.9	18.5	3659.8
	Liver	0.4	114.0	2.7	117.1	0.5	385.0	5.3	390.8	67.9	1598.4	183.6	1849.9
	Kidneys	0.1	0.6	0.1	0.7	0.1	0.8	0.1	1.0	0.0	63.8	4.8	68.6
	Stomach	0.1	1.0	3.7	4.9	0.2	1.4	6.9	8.4	5.3	164.2	320.0	489.5
	Intestines	0.1	0.6	0.1	0.7	0.1	0.8	0.1	1.0	0.1	68.8	4.0	72.9
	Spleen	0.1	2.0	156.5	158.6	0.1	3.8	573.9	577.8	34.5	745.9	6228.0	7008.4
	Testes	0.0	0.1	0.0	0.1	0.0	0.1	0.0	0.2	0.0	0.0	0.0	0.0
	Bladder	0	0	0	0	0	0	0	0	0.0	0.0	0.0	0.0

Clearly, the critical organs are the source organs where most of the radioactivity is accumulated, specifically the liver, for the weakly-chelated radio-copper agents; and the heart, for the radio-labeled antibodies. Thus, the administration of the necessary amount of activity to have a therapeutic effect in a 0.5 g tumor, shown in Table 4.13, will also imply absorbed doses that are above the tolerance limits of these organs: 40 and 50 Gy, respectively [100], assuming that these limits that were derived from human subjects also apply to rodents. The maximum amount of activity of each agent that can be administered into a tumor-bearing mouse in order to stay right below these limits is 135 MBq ^{64}Cu-citrate, 55 MBq ^{67}Cu-citrate, 128 MBq $^{64}CuCl_2$, 34 MBq $^{67}CuCl_2$, 160 MBq ^{64}Cu-NOTA-TRC105, 59 MBq ^{67}Cu-NOTA-TRC105 and 13 MBq ^{90}Y-DTPA-CHX-A"-TRC105. From the fitted power functions in

Figure 4.23, such activities would only deposit 7.1, 12.6, 7.6, 6.9, 10.1, 25.5 and 75.6 Gy to a 0.5 g tumor xenograft, respectively. However, if the tumor xenograft had a mass that is one order of magnitude lower than the size in our study, then these same activities would deposit one order of magnitude higher absorbed dose in the tumor, making the treatment with ^{67}Cu- and ^{90}Y-labeled TRC105 likely effective, assuming that 230 Gy is the required dose to have tumor response. On the other hand, even though the absorbed doses to the tumor caused by the ^{64}Cu-labeled agents are quite low, a fractionated regimen that allows the normal tissue to recover between cycles and that accumulates hundreds of Gy in the tumor over many cycles can still be tested for effectiveness.

Other interesting prediction from the fitted power functions in Figure 4.23 is the mass of the tumor xenograft that would receive 230 Gy when the maximum activity of each agent, to stay below the toxicity threshold of the critical organ, is administered. Such analysis reveals that 135 MBq ^{64}Cu-citrate, 55 MBq ^{67}Cu-citrate, 128 MBq $^{64}CuCl_2$, 34 MBq $^{67}CuCl_2$, 160 MBq ^{64}Cu-NOTA-TRC105, 59 MBq ^{67}Cu-NOTA-TRC105 and 13 MBq ^{90}Y-DTPA-CHX-A"-TRC105 would be able to control tumor xenografts that have masses of 14, 26, 14, 14, 20, 53 and 128 mg, respectively. This prediction depends upon the assumption that such small tumor xenografts will maintain similar %ID uptake values as those measured in our studies.

Our predictions agree with published results in which the therapeutic effectiveness of ^{64}Cu-labeled agents has been demonstrated in preclinical studies in mice. In a publication by Qin et al [10], two groups of mice bearing melanoma tumors (B16F10 and A375M) with diameters of 0.5 – 0.8 cm (65 – 268 mg, assuming that they are spherical and that $\rho = 1$ g/cm^3) at the beginning of the therapy showed a slower tumor growth rate compared to control groups after administration of 74 MBq $^{64}CuCl_2$, as well as negligible toxicity in the liver and kidneys from histology analysis. The pharmacokinetics of $^{64}CuCl_2$ in both of these tumor models resembled the pharmacokinetics that was observed in our studies with 4T1 and U87MG xenografts, that is, tumor uptakes between 3 and 6 %ID/g over 1 to 72 h p.i. and significant uptake in the liver throughout the study between 10 and 30 %ID/g. Therefore, and since they do not mention any dosimetry analysis in their study, we can estimate that the absorbed dose delivered to the tumor and liver per administered MBq $^{64}CuCl_2$ was similar to the estimations obtained in our work (power fit in Figure 4.23 and results in Table 4.19). Hence, the 72 MBq $^{64}CuCl_2$ in their study probably delivered between 8 and 31 Gy to the tumor and ~23 Gy to the liver. The former quantity was probably sufficient to cause a detectable slower tumor growth rate, although not tumor remission, and the latter quantity is much lower than the 40 Gy toxicity threshold [100]. Other studies have demonstrated the therapeutic effectiveness of ^{64}Cu-ATSM [18] and ^{64}Cu-labeled

anti-human colorectal cancer monoclonal antibody (1A3) [12] in tumor xenografts in hamsters (whole body mass = 200 g). The experimental results from the latter study can be compared to the predictions from our study that also involves the ^{64}Cu-labeled antibody TRC105, although an extrapolation between animal species is required. In this study, 87.5% of the hamsters bearing small tumors (0.43 ± 0.25 g) of human colon cancer (GW39) treated with 74 MBq ^{64}Cu-1A3 or 14.8 MBq ^{67}Cu-1A3 were disease free 7 months after the treatment. Extrapolating their experimental setup to a 20 g mice, the average tumor size would be 0.043 g and the required activities for the same tumor regression would be 7.4 MBq ^{64}Cu-1A3 and 1.48 MBq ^{67}Cu-1A3. From our predictions and assuming that the TRC105 and 1A3 antibodies show similar tumor uptakes, such activities would deliver 5.0 and 7.1 Gy, respectively, which actually agrees very well with the tumor doses of 5.86 Gy and 1.269 Gy, respectively, that they have reported in their publication after administering 10 times more activity, on a 10 times heavier rodent that bears a 10 times larger tumor. This actually demonstrates that our assumption that 230 Gy are required for tumor control is extremely conservative.

4.3.9 *Comparison of our separation methods to previous publications and clinical perspective*

The main advantages of the radiochemical separation method for radio-copper presented in this chapter are: 1) the radionuclide is separated in a small volume (0.4 - 0.6 mL), which can be easily evaporated without having variable losses of radioactivity in the vessel and without compromising the effective specific activity; 2) the separated isotopically enriched nickel material is also separated in a small volume (8 - 9 mL), which can be reconstituted into the electrolyte for re-electrodeposition into a target within the same day of production. This latter improvement, has allowed us to recycle a target within 24 hours after separation, which we believe will make the theranostic ^{64}Cu more readily available for fractionated targeted radiotherapy regimens that can compensate for its relatively short half-live compared to established therapeutic radionuclides. And 3) we have achieved the highest radionuclidic purity for ^{61}Cu of 99.9998% at EoB, which is particularly important for this nuclide due to the generation of long-lived radio-cobalt impurities. All of these improvements are due to the chromatographic method that we have developed using a small column (4.4 cm ×0.5 cm Ø) filled with DGA branched resin. Table 4.20 compares our work with the results from previous publications.

The radiochemical separation method for ^{86}Y that was presented in this chapter offers similar advantages to those that were pointed out for the radio-copper separation method. First, the separated nuclide is contained in a small

volume (0.4 – 0.6 mL); second, the separated isotopically enriched strontium material is also separated in a small volume (10 - 11 mL) of acid, which can be easily turned alkaline in order to precipitate the strontium carbonate for re-irradiation. This can also be done within the same day of production, having a target ready for another production run the following day. Table 4.21 compares our production method with previous publications.

Table 4.20 Comparison of production methods of radio-copper for biomedical applications

Separation Method	**Column specs. (h×Ø)**	**Target mass [mg/cm^2] (material)**	**Energy [MeV] (particle)**	***i*** **[µA]**	**A Yield [MBq/µAh]**	**^{6x}Cu Sep. yield [%]**	**Vol. of eluted ^{6x}Cu [mL]**	**Nuclidic impurities at EoB**	**ESA [GBq/µmol] (chelator)**	**Vol. of eluted enriched Nickel [mL]**	**Target recycling efficiency [%]**	**Ref.**
AEC	(4×1 cm)	23 - 69 (^{64}Ni)	15.5 (p^+)	15 - 45	83 - 185	*Not reported*	4	0.01-0.04% ^{55}Co	234 - 734 (TETA)	12	90.5 ± 4.0	[188]
AEC	(15×1.5 cm)	17 (^{64}Ni)	12.5 (p^+)	40	389 ± 111	93 ± 8	12	*Not reported*	0.04 (ATSM)	27	*Not reported*	[221]
AEC	(5×1.5 cm)	25 - 225 (^{64}Ni)	11.4 (p^+)	30	322	> 95	5	*Not reported*	696 ± 122 (TETA)	25	> 96	[189]
AEC	(7×1 cm)	*Not reported*	16.1 (p^+)	0.1	*Not reported*	92 ± 3	13	*Not reported*	*Not reported*	10	95 ± 4	[222]
AEC	*Not reported*	122 - 213 (^{64}Ni)	10 (p^+)	15	135	> 95	1.2	*Not reported*	70 - 426 (TETA)	4	95	[246]
AEC	(4×1 cm)	44 - 89 (^{64}Ni)	12 (p^+)	50	73	*Not reported*	*Not reported*	< 1% ^{55}Co	56 - 186 (ATSM)	*Not reported*	94	[264]
CEC	(9×1 cm)	182 ± 13 (^{64}Ni)	12 (p^+)	10	521 ± 12	88 ± 3	*Not reported*	< 0.01%	*Not reported*	60	94	[223]
SPEC (DGA)	(4.4×0.5 cm)	35.9 - 109 (^{64}Ni)	11.0 (p^+)	30	50 - 142	86 ± 9%	0.4 - 0.6	< 0.001% ^{61}Co	105 ± 37 (NOTA)	8 - 9	94 ± 2%	This work
"	"	51 - 64 (^{60}Ni)	8.2 (d^+)	60	69 - 74	"	"	< 0.001% ^{58g}Co	64 ± 45 (NOTA)	"	97 ± 1%	This work
AEC	(4×1 cm)	93 - 107 (^{60}Ni)	8.1 (d^+)	20	41 - 90	*Not reported*	4	0.04% ^{58g}Co	48 - 189 (TETA)	12	90.5 ± 4.0	[188, 220]

AEC: Anion Exchange Chromatography
CEC: Cation Exchange Chromatography
SPEC (DGA): Solid Phase Extraction Chromatography with DGA resin

Table 4.21 Comparison of production methods of ^{86}Y for biomedical applications

Separation Method	**Column specs. (h×Ø)**	**Target mass [mg/cm^2] (material)**	**p$^+$ Energy [MeV]**	***i*** **[µA]**	**A Yield [MBq/ µAh]**	**^{86}Y Sep. yield [%]**	**Vol. of separated ^{86}Y [mL]**	**ESA [GBq/µmol] (chelator)**	**Vol. of separated enriched ^{86}Sr [mL]**	**Target recycling efficiency [%]**	**Ref.**
Co-preciptitation with La + CEC	(4×0.4 cm)	166 ($^{86}SrCO_3$)	14 - 10	3 - 8	155	~90	< 1	*Not reported*	10	> 90%	[134]
Electrolysis (× 2)	-	67 ($^{86}SrCO_3$)	15.1	10	48 ± 8	88 ± 6	0.1 - 0.3	0.8 (DOTA)	50	*Not reported*	[248]
SPEC (× 2)	(10×1 cm) & 1 mL bed vol.	113 ($^{86}SrCO_3$)	13.8	10	39 - 74	75 - 80	3	3.3 (DTPA)	~130	80 - 85	[224]
SPEC (× 2) + CEC	(10×2.5 cm), (5×1 cm) & (5.5×0.5)	*Not reported*	*Not reported*	*Not reported*	*Not reported*	80 - 90	0.6 - 0.8	5.6 (DOTA)	*Not reported*	*Not reported*	[225]
Electrolysis (× 2)	-	155 (^{86}SrO)	14.5	2 - 6	166	> 90	2	430 ± 281 (DOTA or DTPA)	~30	*Not reported*	[245]
Precipitation + Filtration	-	50 – 119 ($^{86}SrCO_3$)	11	10 - 20	35 - 48	88 ± 3	4	55 ± 30 (DOTA)	~30	> 90	[226]
SPEC (DGA)	(×0.5 cm)	111 – 154 ($^{86}SrCO_3$)	15.2	4	102 ± 15	93 ± 6	0.4 - 0.6	0.5 ± 0.2 (DOTA) 1.4 ± 0.5 (DTPA)	10 - 11	89 ± 1	This work

CEC: Cation Exchange Chromatography
SPEC: Solid Phase Extraction Chromatography

From the irradiation conditions listed in Table 4.1 and the average production yields and separation efficiencies presented in sections 4.3.1 and 4.3.2, a typical 1 hour irradiation yields 3.18 GBq ^{64}Cu, 4.26 GBq ^{61}Cu and 0.41 GBq ^{86}Y. From a clinical perspective, ^{64}Cu and ^{86}Y have been administered to human subjects for PET imaging with injected activities that range from 130 to 925 MBq of ^{64}Cu [250-255, 265-268] and 100 to 385 MBq of ^{86}Y [227, 256, 257, 269, 270]. In the case of ^{61}Cu, there are no published studies in which this nuclide has been administered to humans. However, 150 to 370 MBq have been administered to 20-25 kg canines [247, 271], from which we can assume that a 70 kg human patient would require roughly four times more activity, that is, between 600 and 1480 MBq. These administered activities are chosen based on the half-live of the radionuclide, its positron branching ratio (17.6%, 61.4% and 31.9% for ^{64}Cu[243], ^{61}Cu[272] and ^{86}Y[244], respectively), the pharmacokinetics of the radiolabeled tracer and the annual dose constraint of 50 mSv [75] for adult research subjects. This means that the hypothetical yields following 1 hour long irradiations could potentially provide sufficient activities of ^{64}Cu, ^{61}Cu and ^{86}Y for 3 to 24, 2 to 7 and 1 to 4 patient studies, respectively.

4.4 Conclusions

The production methods described herein for ^{61}Cu, ^{64}Cu and ^{86}Y have provided sufficient yields, purities and effective specific activities for clinical PET applications. Furthermore, the low variance in separation yields demonstrates that the DGA branched extraction resin allows for very reproducible results. This is largely due to small elution volumes, which avoid the use of a rotary evaporator. Moreover, we have demonstrated the facile semi-automation of these separation methods using a peristaltic pump-driven module under LabVIEW control.

As a proof of the high specific activity of the separated ^{64}Cu and ^{86}Y, these radiometals were labeled to a chelator-conjugated antibody (TRC105) with a radiolabeling yield $\geq$ 40% using $\leq$ 411 μg of protein per 37 MBq (decay-corrected to EoB) of radiometal.

Furthermore, based on the existence of therapeutic analogues of copper and yttrium, namely, ^{64}Cu itself, ^{67}Cu and ^{90}Y, the tumor-targeting properties of the ^{64}Cu- and ^{86}Y-labeled antibodies was expanded beyond their use as diagnostic probes to their application as treatment planning probes. Thus, the biodistribution data of these agents in tumor-bearing mice, obtained via PET, was exploited to predict the amount of ^{64}Cu, ^{67}Cu or ^{90}Y activity that is required to deliver therapeutic amounts of absorbed dose to a tumor xenograft and to determine the maximum amount of injected activity that can be tolerated by the rodent.

PET imaging and quantification of the biodistribution over time of weakly bound ^{64}Cu in tumor-bearing mice demonstrated that this metal has a slow clearance rate from the body being retained mainly in the liver and the small intestine. Furthermore, it showed significant uptake in 4T1 and U87MG tumor xenografts, with the highest uptake in early time points (1 - 4 h p.i.) that can be between 64% and 83% of that observed with the ^{64}Cu-labeled TRC105, indicating that the tumor targeting of copper-labeled vectors needs to be carefully analyzed in order to discard uptake from de-chelated radio-copper; and that weakly-bound radio-copper can be used as a probe to detect the two kinds of cancer cells used in our studies and perhaps other kinds of cancer.

Chapter 5 Germanium-69 and Germanium-68

5.1 Introduction

5.1.1 *Germanium-69 as a label to SPION and a surrogate of ^{68}Ge*

Germanium-69 (^{69}Ge, $t_{1/2}$ = 39.05 h, 21% β^+, E_{max} =1205 keV) is a novel positron emitting radionuclide whose potential is yet to be explored for positron emission tomography (PET) imaging [273]. The adequately long half-life of ^{69}Ge, makes it an ideal choice for immuno-PET imaging using ^{69}Ge-labeled antibodies. Also, the production route of this radioisotope is simple and cost-effective [274]. However, the major limitation in the use of this novel radioisotope is its complex coordination chemistry in aqueous medium and the unavailability of suitable radiolabeling techniques for the preparation of ^{69}Ge-based radiopharmaceuticals. It has been reported that the predominant germanium species in aqueous media are $Ge(OH)_4$, $[GeO(OH)_3]^-$, $[GeO_2(OH)_2]^{2-}$, and $[[Ge(OH)_4]_8(OH)_3]^{3-}$ with the distribution of each species depending on the total concentration and the pH of the medium [275, 276], making it a major challenge for radiolabeling with ^{69}Ge using traditional chelator-based methods.

Fortunately, the incorporation of another germanium isotope, ^{68}Ge ($t_{1/2}$ = 279 d, 100% EC)), into metal oxides such as TiO_2, ZrO_2, CeO_2, SnO_2, Fe_2O_3, Fe_3O_4, Al_2O_3, et cetera, has long been reported for the preparation of clinically useful ^{68}Ge/^{68}Ga generators [277-279]. In these generators, ^{68}Ge remains selectively adsorbed in a chromatographic column containing metal oxide sorbent, and the daughter isotope ^{68}Ga ($t_{1/2}$ = 68 min, 88% β^+, E_{max} = 1899 keV)) can be regularly eluted out using a suitable solvent for a prolonged period of time (generally, ca. 1 year). The strong binding affinity of germanium ions to these metal oxides has also been demonstrated by the fact that the breakthrough of ^{68}Ge from the generator column is less than 0.01% on multiple ^{68}Ga-elutions over the period of 1 year [277, 280].

Inspired by these, we hypothesized that using a suitable water-soluble metal oxide as a platform, ^{69}Ge-labeled metal oxides could be synthesized simply by mixing metal oxide with ^{69}Ge ions, forming intrinsically radiolabeled particles without the assistance of any chelators (Figure 5.1). In this chapter, I will demonstrate how super-paramagnetic iron oxide nanoparticle (SPION) can be employed for this purpose and also how this nanoplatform can be applied for simultaneous PET and magnetic resonance imaging (MRI) [281, 282]. The synergistic combination of PET (with high sensitivity) and MRI (with high resolution and exquisite soft tissue contrast) has attracted tremendous interest over the last decade, and PET/MRI scanners are now being used in clinical practices [283]. The

future of PET/MRI scanning will greatly benefit from the use of dual-modality PET/MRI probes, such as the one presented in this work.

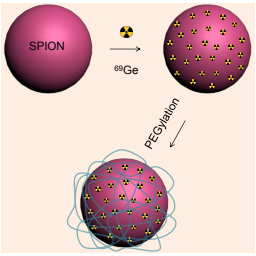

Figure 5.1 Schematic illustration of chelator-free synthesis of ^{69}Ge-metal oxides.

Ideally, no breakthrough of the parent nuclide ^{68}Ge should be present in the eluate with the daughter nuclide ^{68}Ga in clinical ^{68}Ge/^{68}Ga generators. This is very critical due to the long half-life of the parent nuclide, which after co-administration with the daughter nuclide, could impart a large absorbed dose in case it is retained in the subject's body. Ge-69, as a shorter-lived and positron-emitting analogue of ^{68}Ge, precisely allows determining the risks associated with ^{68}Ge breakthrough by using it as a surrogate in biodistribution, pharmacokinetic and internal dosimetry studies. In this chapter, I will also estimate the absorbed dose per organ and effective dose that result from the administration of ^{69}Ge diluted in phosphate buffer saline (PBS) using the pharmacokinetic data obtained from murine breast cancer (4T1) tumor-bearing Balb/c mice as an input to the OLINDA software [50]. The internal dosimetry of ^{68}Ge will be estimated from the same pharmacokinetic data after replacing ^{69}Ge by ^{68}Ge in the original OLINDA file. The reason the mice in this study have a tumor xenograft is because we wanted to verify whether unlabeled or weakly bound ^{69}Ge has intrinsic targeting properties as we have shown with unlabeled ^{44}Sc and ^{64}Cu.

5.1.2 *Targetry considerations and predicted yields*

Both ^{69}Ge and ^{68}Ge are produced by proton bombardment on natural gallium targets composed of 60.108% ^{69}Ga and 39.892% ^{71}Ga via the ^{69}Ga(p,n) and ^{69}Ga(p,2n) reactions, respectively. The co-produced ^{71}Ge ($t_{1/2}$ = 11.43 d) from the ^{71}Ga(p,n) reaction has no effect on the imaging properties of ^{69}Ge since it decays 100% by electron capture with no gamma emission. However, the decay process of ^{71}Ge will result in a cascade of Auger electrons caused by the filling of vacancies left by the nuclear-captured electron and the subsequent conversion electrons, which makes this nuclide a potential candidate for targeted radiotherapy due to the highly localized nature of this kind of emitted electrons [172].

Due to the importance of ^{68}Ge production, there has been extensive research in the measurement of the ^{nat}Ga(p,x)^{68}Ge excitation function. The International Atomic Energy Agency (IAEA) recommends to use the one

measured by Takacs et al. [284]. However, this is not the case for the ^{nat}Ga(p,n)^{69}Ge and ^{nat}Ga(p,nα)^{65}Zn reactions, which have to be interpolated from the ^{69}Ga(p,n)^{69}Ge and ^{69}Ga(p,nα)^{65}Zn excitation functions that have been measured using enriched ^{69}Ga targets [42, 285]. Furthermore, these experimental functions have to be decreased by 20%, as suggested by Takacs et al. [43], due to the use of incorrect cross-section data of the monitor reaction ^{nat}Mo(p,x)^{96}Tc by the authors. The relevant excitations functions for $^{68/69}$Ge production from natural gallium targets in the energy neighborhood of our 16 MeV proton cyclotron are shown in Figure 5.2. The ^{58}Ni(p,α) cross section data is included in the figure because nickel-gallium (NiGa) alloys were the main targets for production as it will be explained in later sections.

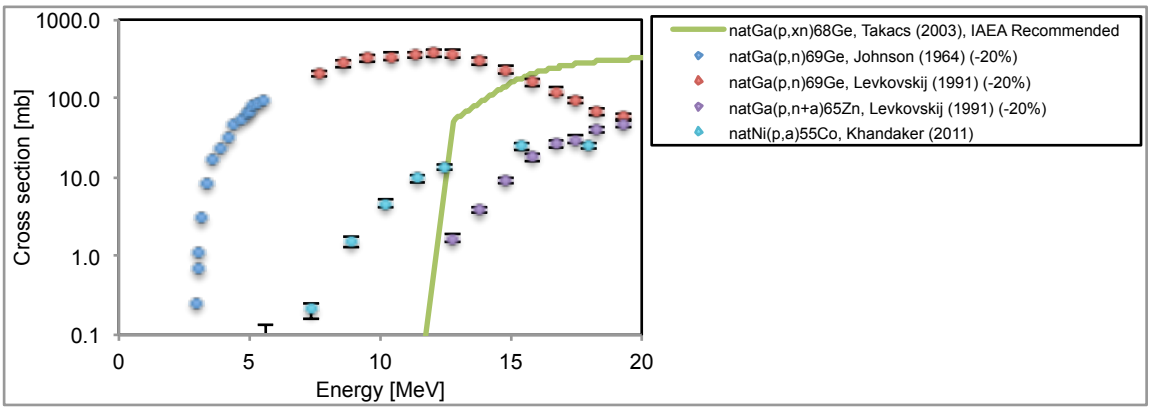

Figure 5.2 Experimental excitation functions related to the production of ^{69}Ge and ^{68}Ge from NiGa targets.

From the experimental ^{nat}Ga(p,n)^{69}Ge excitation function, with a maximum of ~375 mb at 12 MeV, we can expect a high production yield of ^{69}Ge using 16 MeV protons from our PETtrace cyclotron. However, in order to avoid the production of ^{68}Ge, the energy of the proton beam has to be degraded to an energy below 11.4 MeV, the threshold energy for the ^{69}Ga(p,2n)^{68}Ge reaction [286], where the excitation function still has a large cross section value of ~360 mb. A thick gallium target for this energy, that is, one that would degrade the energy from 11.4 to 3 MeV, the threshold energy for the ^{69}Ga(p,n)^{69}Ge reaction, needs to be 420 μm or 256 mg/cm^2, according to the proton range in gallium obtained from a SRIM (Stopping and Range of Ions in Matter) simulation [44]. The estimated ^{69}Ge thick target yield for such a target is 52.5 MBq/μAh .

The ^{nat}Ga(p,2n)^{68}Ge excitation function has a maximum cross-section value of 321.8 mb at 20.5 MeV. At the maximum energy available from our cyclotron, 16 MeV, the cross section is 216.4 mb or about 2/3 of the maximum. However, a low production yield is expected since this is inversely proportional to the half-life of the radionuclide being produced, which in this case is 271 days. The estimated ^{68}Ge thick target yield for a 370 μm thick natural

gallium target that degrades the proton enegy from 16 to 11.4 MeV is 127 kBq/μAh.

Gallium targetry is very complicated due to the low melting point of metallic gallium (29.8 °C) and the fact that this molten metal in contact with other solid metals tends to mix rapidly creating alloys, which many times are brittle [287]. This is particularly the case when gallium mixes with aluminum [288], a common metal used in solid target supports due to its excellent thermal conductivity that allows efficient cooling. Niobium, on the other hand, does not react with liquid gallium at a temperature < 400 °C [289], and this is why large-scale production of ^{68}Ge in Brookhaven National Laboratory (BNL) [290] and Los Alamos National Laboratory (LANL) [291] is carried out by irradiating water-cooled targets made of gallium encapsulated in niobium containers with proton beams of 30 MeV at 85 μA and ~60 MeV at 125 μA, respectively [292], albeit niobium's low thermal conductivity that is about a quarter of that of aluminum, 54 vs 235 W/mK, at room temperature.

Other gallium-based compounds that have higher melting points and are less corrosive than metallic gallium are gallium oxide (Ga_2O_3) [293] and the alloy $NiGa_4$ [294], with melting points of 1900 °C and > 800 °C, respectively. These target materials are employed in the ^{68}Ge large-scale production facilities of iThemba Laboratories in South Africa [295] and Cyclotron Co. in Obninsk, Russia, respectively [292]. Each of these compounds has challenges, however. For instance, Ga_2O_3 is a dielectric powder that does not allow high current irradiations; and $NiGa_4$ introduces one extra element in bulk quantities, nickel, plus the radionuclidic contaminants ^{5x}Co and ^{6x}Cu from the ^{6x}Ni(p,α) and ^{6x}Ni(p,n) reactions, respectively, each of which has to be purified from the final radioactive germanium product. Another drawback is the lower molar percentage of gallium in the target composition since a thick target of Ga_2O_3 and $NiGa_4$ is only 40% and 80% of gallium, respectively, and hence the ^{6x}Ge production yields would be lower compared to those from a thick 100% metallic gallium target.

Inspired by these targetry methods, in this chapter I will present target designs for the irradiation of molten gallium and electroplated NiGa alloy targets that allow the large-scale production of ^{69}Ge with our 16 MeV proton PETtrace cyclotron, as well as the production of MBq quantities of ^{68}Ge that can be used to prepare a small ^{68}Ge/^{68}Ga generator for small animal and micro-PET scanner performance studies.

5.1.3 *Separation chemistry considerations*

The separation of the produced ^{68}Ge from irradiated gallium-based targets has been achieved by distillation of $^{68}GeCl_4$ [296, 297], ion exchange chromatography [293] and liquid-liquid extraction using CCl_4. The latter being the one employed in large-scale production facilities in BNL, LANL, iThemba and Obnisnk due to the > 90% ^{68}Ge

recovery yield and > 99.9% radionuclidic purity with a gallium separation factor > 1×10^6 [291, 292]. The liquid-liquid extraction of the nonpolar $GeCl_4$ to the organic solvent CCl_4 is carried out from gallium targets dissolved in either H_2SO_4 or HCl, the aqueous phases. Several extractions between these two phases are required for a quantitative recovery and extreme precautions are necessary to avoid the formation of volatile $^{68}GeCl_4$ at room temperature in HCl solutions > 6 M [273]. The requirement of this multistep chemical process and the manipulation of large radioactivities of long-lived isotopes such as ^{68}Ge ($t_{1/2}$ = 270.8 d), ^{65}Zn ($t_{1/2}$ = 244.26 d, 50.6% γ, E_γ = 1115 keV) from the ^{69}Ga(p,αn) reaction and ^{57}Co ($t_{1/2}$ = 271.79 d, 85.6% γ, E_γ = 122) from ^{60}Ni(p,α) in case $NiGa_4$ alloys are employed, makes the production of large amounts of ^{68}Ge not appropriate for small PET facilities. This, however, is not the case for the production and isolation of ^{69}Ge using a much simpler separation method based on the extraction resin N,N,N',N'-tetra-n-octyldiglycolamide (DGA) in diluted HNO_3 medium as it will be explained in this chapter.

5.2 Materials and Methods

Materials for cyclotron targetry and separation chemistry

Ultra pure grade 67-70% nitric acid (HNO_3) comes from Aristar Ultra, VWR (West Chester, PA). 99.9999% natural gallium pellets, 99.99% gallium(III) oxide, 99% nickel(II) sulfate hexahydrate ($NiSO_4 \cdot 6H_2O$) and 28% ammonium hydroxide solution in H_2O (NH_4OH, ≥ 99.99% trace metals) come from Sigma Aldrich. Trace metal grade 93-98% sulfuric acid (H_2SO_4) and ethylene diamine triacetic acid (EDTA) were purchased from Fisher Scientific (Pittsburg, PA). 99.999% ammonium sulfate $(NH_4)_2SO_4$ was purchased from Alfa Aesar (Ward Hill, MA). Gold disks (1.90 cm diameter × 0.61 mm thickness) were obtained from Artisan Jewelers (Sarasota, FL). A 1.5" diameter niobium rod was obtained from Eagle Alloys Corporation (Talbott, TN). Extraction chromatography resin DGA, branched (50-100 μm) was purchased from Eichrom (Lisle, IL). A 50 ppm multi-element standard for calibration and Agilent's 4200 Microwave Plasma Atomic Emission Spectroscopy (MP-AES) system come from Agilent Technologies (Santa Clara, CA). Deionized water (>18 $M\Omega \cdot cm^{-1}$) was obtained from a Milli-Q filter, Millipore (Billerica, MA). Phosphate buffer saline (PBS) was purchased from Thermo Scientific.

Materials for synthesis of nanoparticles

Iron chloride hexahydrate ($FeCl_3 \cdot 6H_2O$, >99%) was purchased from Acros. Oleic acid (NF/FCC), ethyl(dimethylaminopropyl) carbodiimide / N-hydroxysulfosuccinimide (EDC/S-NHS) and hydrochloric acid (HCl) were purchased from Fisher Scientific. Poly(acrylic acid), 1-octadece, tetraethylorthosilicate (TEOS),

Polyoxyethylene (5) nonylphenylether branched (Igepal CO-520 (NP-5)), ammonia (30%), copper chloride dihydrate ($CuCl_2 \cdot 2H_2O$), sodium citrate dihydrate, sodium sulfide nonahydrate ($Na_2S \cdot 9H_2O$), germanium (IV) oxide (99.999%), copper (I) chloride (≥ 99.995%), sodium tartrate dibasic dihydrate, and cyclohexane (≥ 99.9%) were purchased from Sigma-Aldrich (St. Louis, MO). Hydrogen peroxide was purchased from Fluka Analytical. Diethylene glycol (DEG, 99%) was purchased from Alfa Aesar. PD-10 columns were purchased from GE Healthcare (Piscataway, NJ). Maleimide polyethylene glycol amine (Mal-PEG_{5k}-NH_2) was obtained from Creative PEGworks. All chemicals were used as received without further purification.

5.2.1 *Cyclotron targetry, irradiations and target yields*

Germanium-69 was produced by bombarding electroplated nickel-gallium (NiGa) alloy targets with 11.0 MeV protons, after degradation of the 16.0 MeV proton beam from the cyclotron with a 0.25 mm thick molybdenum foil. Germanium-68 was produced by two methods: 1) irradiating natural gallium encapsulated in a niobium crucible with a 0.05 mm thick niobium foil facing the proton beam, degrading it down to 15.2 MeV; and 2) irradiating electroplated NiGa alloys without a degrader.

Molten gallium was encapsulated on a 0.41 mm deep, 1.23 cm diameter, depression machined on the center of a 2.54 mm thick niobium disk. A concentric groove for a teflon O-ring was machined to seal the molten gallium against the niobium degrader foil. According to a SRIM simulation [44], the cavity thickness encapsulates a thick gallium target for ^{68}Ge production, which degrades the proton beam energy from 15.2 to 9.5 MeV, below the threshold energy for the ^{69}Ga(p,2n)^{68}Ge reaction, 11.4 MeV [286]. Figure 5.3 shows the schematic of the niobium crucible (a), the appearance of molten gallium inside it (b) and how it is mounted into one of the ports of the cyclotron (c). A maximum proton current of 15 μA was employed in this target arrangement.

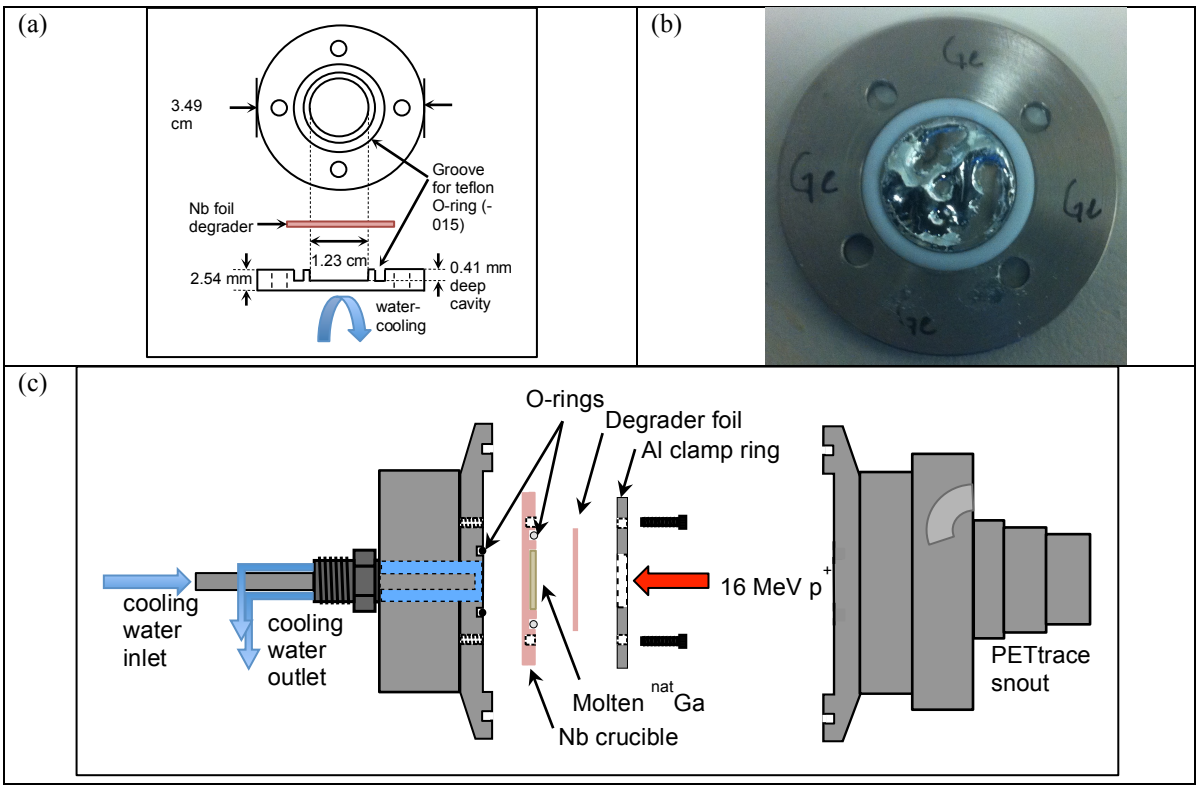

Figure 5.3 (a) Schematic of the niobium crucible. (b) Appearance of molten gallium inside it. (c) Schematic of how the crucible is mounted into one of the ports of the cyclotron.

The nickel-gallium mixture with the greatest gallium molar fraction that forms a homogeneous solid phase alloy is $NiGa_4$ with a melting point at ~900 °C [298]. Such NiGa alloy can be manufactured by direct melting and mixing using an induction furnace as described by Loch et al. [294] or by electrodeposition over a gold surface from an ammonium sulfate electrolyte as described by Adam-Rebeles et al. [299]. Inspired by these publications, we were able to fabricate NiGa targets using both methods. However, only the electroplated ones were sufficiently stable and homogenous for high power targetry. The NiGa alloys produced by melting on an induction furnace (EIA Power Cube 45/900) were used as standards for characterization of the electroplated NiGa targets via x-ray fluorescence spectroscopy (XRF).

The electroplating solution was made by dissolving 65.9 ± 2.7 mg of Ga_2O_3 in 8 mL of H_2SO_4 (27%) at 110 °C and stirring overnight, followed by a pH adjustment to 1.5 using ~ 10 mL of concentrated NH_4OH and then adding 43.8 ± 3.7 mg of $NiSO_4*6H_2O$, dissolving it at 65 °C and stirring. The solution is then transferred to the electrolytic cell, as the one described in Appendix D. The optimum electroplating parameters in terms of total mass deposition efficiency, in the shortest amount of time, and with a smooth, dense and homogenous surface are summarized in Table 5.1. One of the plated targets was heated at 400 °C for 15 min in an argon atmosphere to verify that the

melting point of the alloy was higher that this temperature and that no reaction between traces of gallium and the gold substrate was present. The target did not melt and looked intact after this experiment, even under 10x magnification on an optical microscope, which indicated that the alloy was indeed able to sustain high power irradiations. The electroplated NiGa target was mounted on the water-cooled solid target support for irradiation (Figure 5.4) and was able to sustain currents up to 40 μA.

Table 5.1 Electroplating cell parameters for plating NiGa over a gold surface (n = 8).

Molar Ga^{3+} : Ni^{2+} in solution	4 : 1
Cell volume	18 – 19 mL
pH	1.5
Potential between electrodes	3.8 ± 0.2 V
Current density (DC)	37 ± 11 mA/cm^2
Electroplated surface	0.9 cm^2
Anode Material	Platinum
Distance between electrodes	1 cm
Electrodeposition time	3 ± 1 days
Deposited mass per run:	34.2 ± 4.9 mg/cm^2
Deposited thickness:	52 ± 8 μm

Up to three electroplating runs over the same gold disk resulted in a maximum cumulated thickness of 98.6 mg/cm^2 (151 μm). The average and standard deviation of three of such cumulated runs was 85.4 ± 12.0 mg/cm^2. However, in order to get thicker targets more efficiently, we have assembled a larger cell with a capacity of 50 mL, with which, after two electroplating runs over the same gold disk using the same electroplating parameters outlined in Table 5, except for a plating time of 6 days per run, we have been able to electroplate a target that is 245.3 mg/cm^2 (375 μm) thick. As it will be shown in section 5.3.1, this represents a thick target for the production of both ^{69}Ge and ^{68}Ge with our cyclotron.

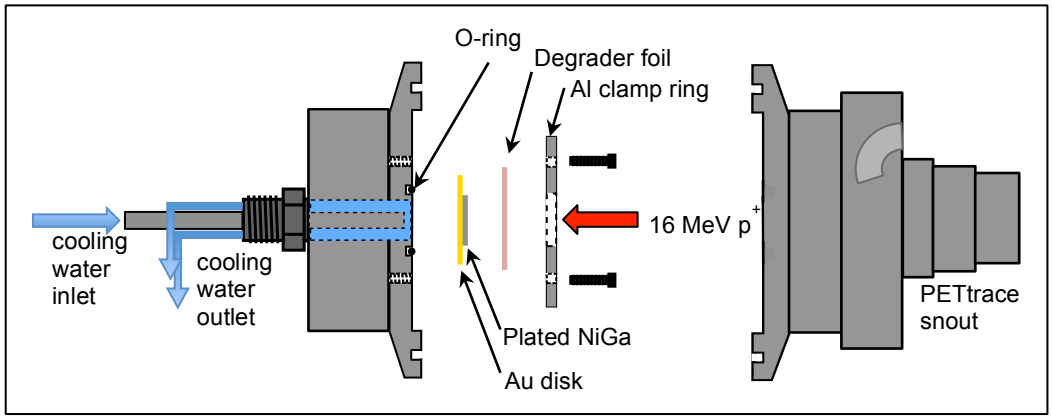

Figure 5.4 Schematic of how the electroplated NiGa is mounted into one of the ports of the cyclotron.

The elemental composition of the electroplated NiGa targets was determined by x-ray fluorescence spectroscopy (XRF) using a ^{109}Cd excitation source ($t_{1/2}$ = 461 d, 100% EC, Ag $E_{x\text{-}ray}$ = 22 keV, 86%) made in-

house after proton irradiation on a silver disk and a HPGe detector for low-energy gamma spectrometry with a beryllium window (Canberra GL0110P). The characteristic x-rays used for the identification of gallium and nickel were 9.26 keV and 7.48 keV, respectively. The setup for this measurement is shown in Figure 5.5.

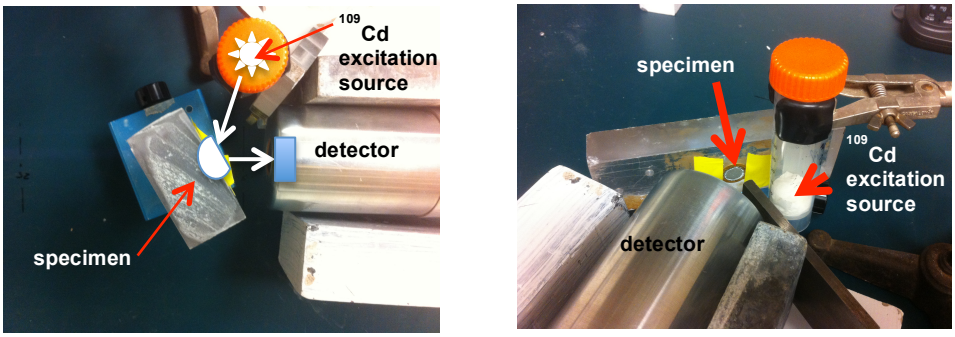

(a) (b)

Figure 5.5 Top view (a) and side view (b) of the experimental setup for XRF spectroscopy of the electroplated NiGa targets

In order to make this measurement quantitative, a relationship between the ratios of count rates from the Ga and Ni characteristic x-rays to known Ga:Ni molar ratios from a series of standard GaNi alloys was established. Standards with Ga:Ni molar ratios of 1.0, 2.0, 2.9, 3.7, 4.0 and 5.2 were fused in an induction furnace (EIA Power Cube 45/900) and analyzed by XRF spectroscopy with a gold disk placed behind the specimens to replicate the composition of the electroplating alloys.

As with the electroplated alloys, the fused alloys were heated to 400 °C for ~15 min in an argon atmosphere in order to verify that their melting point was indeed higher than this temperature and that they were not corrosive in contact with metallic components of our solid target support, such as aluminum and silver, at this high temperature. Hence, piece of $NiGa_4$ foil was placed on top of a silver disk in this heating experiment. Unfortunately, even though the foil stayed as a solid, we could detect spots of corrosion over the silver disk, indicating the presence of heterogeneities in the alloy, in which pure gallium had not fused with nickel. This result demonstrated that even though the fused alloys have a high melting point, they are not homogenous enough to ensure that the solid target support components will not be corroded by traces of pure gallium that could potentially come into contact with them.

The produced activities of ^{69}Ge and other radionuclidic impurities were measured using an efficiency calibrated 60 cm^3 high purity germanium (HPGe) detector (Canberra C1519) (FWHM = 2.7 keV @ 1333 keV). Gamma-ray spectrum analysis software package, Maestro-32 MCA Emulator (Ortec, Oak Ridge TN), was used to collect and analyze the gamma-ray spectra. The gamma lines used to determine yields are listed in Table 5.2. The dead time was

always kept below 10% and the acquisition time was set so that the statistical uncertainty from the number of counts per peak was kept below 1%.

Table 5.2 Gamma emissions used for yield and radionuclidic purity quantification

Nuclide	Reaction	Gamma energy [keV]	Branching ratio
^{69}Ge	^{69}Ga(p,n)	1107	0.36
^{68}Ge/^{68}Ga	^{69}Ga(p,2n)	1077	0.03
^{55}Co	^{58}Ni(p,α)	931	0.75
^{57}Co	^{60}Ni(p,α)	122	0.86
^{197m}Hg	^{197}Au(p,n)	134	0.33
^{65}Zn	^{69}Ga(p,αn)	1115	0.51

5.2.2 *Radiochemical separation*

After irradiation, the NiGa target was allowed to decay overnight to avoid unnecessary radiation exposure from the short-lived radiocopper products that originate from the nickel target material. The molten gallium inside the niobium crucible or the electroplated NiGa were exposed to 5 mL of concentrated nitric acid using a teflon mask with an inserted O-ring that seals against the surface of the substrate disk in a setup that is very similar to the electrolytic cell but without any electricity involvement. Nitric acid was chosen for dissolution instead of hydrochloric acid for two reasons: first, to avoid the formation of the volatile complex $GeCl_4$ and second, to take advantage of the favorable germanium extraction properties of the N,N,N′,N′-tetra-n-octyldiglycolamide (DGA) extraction resin in HNO_3 solution published by Pourmand and Dauphas [192]. The gallium-based material was fully dissolved at room temperature after 1 hour under constant stirring, the solution was then diluted by adding 5 mL of concentrated HNO_3 and then transferred with a pipette to the reservoir syringe of the module employed in chapter 2 for ^{44}Sc separation [169], but with a set of syringes and tubing exclusively dedicated for ^{69}Ge separation to avoid cross-contamination. From the target solution, a 50 µL sample was taken for gamma spectroscopy and quantification of radioactivity yields using an energy and efficiency-calibrated HPGe detector.

The separation of ^{69}Ge from the bulk target material and other radionuclidic impurities (^{197m}Hg and ^{55}Co) was carried out using 200 mg of DGA extraction resin packed in a 5 mm diameter column (length = 1.9 cm). On passing the target solution through the chromatographic column, ^{69}Ge was trapped in the resin, which could subsequently be rinsed with 5 mL of concentrated HNO_3 and then eluted in fractions of 200 µL of deionized water (Figure 5.6). The three most concentrated fractions were mixed together, evaporated to dryness and then reconstituted in 100 µL of 0.1 M HCl, which represented the separated stock for radiolabeling of SPION and for preparation of ^{69}Ge diluted in pH 7 buffered solution for administration into tumor-bearing mice.

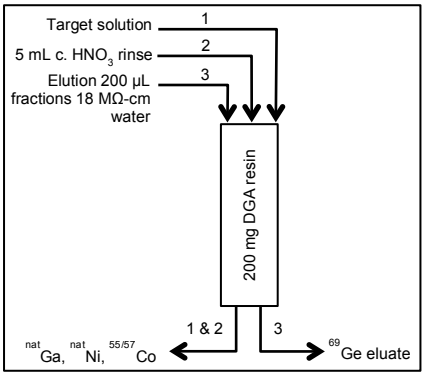

Figure 5.6 Schematic of the radiochemical separation of ^{69}Ge.

The radionuclidic purity and identity of ^{69}Ge in the separated product was confirmed by gamma spectroscopy and by half-life verification after logging the decaying signal from a sample placed inside a dose calibrator (Capintec CRC-Dual PET) that feeds an electrometer (Keithley 6517A) connected to a data acquisition program in LabVIEW. The total acquisition time was 147 hours and the sampling was done every 10 seconds. This data was fit to a mono-exponential function and a decay half-life was quantified and compared to the accepted value for ^{69}Ge, 39.05 h [300].

One of the electroplated $NiGa_3$ targets with a thickness of 82.7 mg/cm^2 was processed in a "cold" separation run, that is, without irradiation, in order to quantify the amount of trace metal contaminants in the separated product and also to quantify the separation factors for each metal impurity. A 50 µL sample from the target solution as well as the combination of the 200 µL separated fractions 3 to 5 that are known to contain most of the ^{69}Ge from real production runs, were analyzed for trace metal quantification with Agilent's Microwave Plasma Atomic Emission Spectroscopy system (4200 MP-AES).

5.2.3 *Image quality of ^{69}Ge*

The same miniature Derenzo phantom employed in chapter 2 [47] was used to evaluate the spatial resolution of ^{69}Ge PET images using an Inveon microPET/CT rodent model scanner. The phantom was filled with 0.1 M HCl solution containing 21 MBq and data was collected for ~30 min until one billion coincident counts were acquired by the software. The raw data was collected in a histogram and reconstructed using the two-dimensional filtered back projection algorithm (FBP2D), without attenuation correction, using a matrix size of 512 × 512 pixels. Image quality was evaluated by visual inspection of transaxial slices in the middle of the phantom and by profile analysis in the region in which the minimum spatial resolution was observed.

5.2.4 *Synthesis of SPION, radiolabeling with ^{69}Ge, PEGylation and serum stability*

Synthesis of iron-oleate complex

Iron-oleate complex was used as the precursor for the synthesis of SPION. $FeCl_3 \cdot 6H_2O$ (3.243 g, 12 mmol) and NaOH (1.44 g, 36 mmol) was each dissolved in methanol (40 mL) under magnetic stirring. Oleic acid (12 mL, 36 mmol) was added into the $FeCl_3$-methanol solution, followed by addition of NaOH-methanol solution using a separatory funnel. The mixture was stirred overnight at room temperature. Reddish-brown product could be observed at the bottom of the flask in the next morning. The product was washed with methanol twice, and then washed with deionized water twice before drying at room temperature for 48 h. The final iron-oleate complex was in a waxy solid form.

Synthesis of SPION

SPION was synthesized following the previously reported procedure with slight modifications [301, 302]. In a typical experiment for ~10 nm sized SPION, pre-prepared iron oleate (2.9 g, ~3 mmol) was dissolved in 1-octadece (40 mL). No extra oleic acid was used. The mixture was first heated to 80 ºC to accelerate the dissolution of solid iron-oleate, and then heated to 120 ºC and maintained at this temperature for 2 h to remove air and water from the system. The reaction mixture was then directly heated to 310-320 ºC and kept at this temperature for 30 min. The black-brown mixture was then cooled down to room temperature, washed with hexane and ethanol, and collected by magnetic separation. The final product could be well-dispersed in cyclohexane.

Poly(acrylic acid) (PAA) modification of SPION

Water soluble poly(acrylic acid) (PAA) modified SPION (SPION@PAA) was first prepared by reacting oleate-coated SPION with PAA in diethylene glycol (DEG) following the reported procedure by Zhang et al. [303] with slight modifications [304]. PAA (560 mg) was added in DEG solution (20 mL) and heated to 110 ºC with vigorous stirring. No nitrogen flow was used in our case. A chloroform solution of oleic acid capped SPION (3 mL) was then injected into the hot solution. The mixture was kept at 110 ºC for 2 h. Subsequently, the system was further heated to 240 ºC and kept at this temperature for another 3 h until the solution became clear. As-synthesized SPION@PAA nanoparticles were washed with ethanol and cyclohexane, and collected by magnetic separation. The final sample could be well-dispersed in water (pH 7-8).

Radiolabeling of SPION@PAA with ^{69}Ge

In order to label SPION@PAA with ^{69}Ge, 40 µL from the separated stock containing 37 MBq (1 mCi) of ^{69}Ge was added to 600 µL of SPION@PAA (3.1 mM Fe, dispersed in 1 mM sodium hydroxide solution, pH 7–8) in an Eppendorf tube. Then, the pH was carefully adjusted to ~7 by addition of ~2 µL of 1 M Na_2CO_3 solution in order to achieve the best labeling efficiency since the pH-dependent sorption behavior of germanium ions to iron oxide has been well documented with the optimum range found to be pH 4–8 [305]. The mixture was kept under constant shaking at 500 rpm and 37 ºC. Radiolabeling yield of ^{69}Ge-SPION@PAA was then determined at different time intervals using radio-thin layer chromatography (radio-TLC). The radio-TLC protocol employs aluminum backed silica gel plates as the stationary phase and sodium tartrate/methanol (9:1; 0.01 M) solution as the mobile phase with the autoradiography done by exposing the developed plates to a phosphor plate that is read with a Cyclone Phosphor-Plate imaging system (Perkin Elmer). After the radiolabeling procedure, unlabeled free ^{69}Ge was separated from ^{69}Ge-SPION@PAA by passing through a PD-10 column, preconditioned with PBS.

PEGylation of ^{69}Ge-SPION

For polyethylene glycol (PEG) modification, 500 µL of ^{69}Ge-SPION@PAA in PBS was mixed with a suitable amount of EDC/S-NHS (62.5 µL, 2 mg/mL) and activated for 15 min at pH 4–5. Two mg of Mal-PEG_{5k}-NH_2 and sodium carbonate (Na_2CO_3) (2 µL, 0.1 M) were then added and reacted at room temperature for 2 h (pH 7–8). To purify and collect ^{69}Ge-SPION (with either PAA or PEG at the surface) for further studies, PD-10 column was used to remove the free ^{69}Ge from ^{69}Ge-SPION as described above. The ^{69}Ge-SPION was subsequently concentrated by using a centrifugal filter (molecular weight cut off: 10 kDa), and re-dispersed in PBS before injection into mice.

Serum stability studies

For serum stability studies, ^{69}Ge-SPION@PAA and ^{69}Ge-SPION@PEG were incubated in complete mouse serum at 37 ºC for up to 24 h. Portions of the mixture were sampled at different time points and filtered through 100 kDa cut off filters. The filtrates were collected, and the radioactivity was measured. The radiochemical purity of 'intact' ^{69}Ge-SPION (i.e. SPION@PAA or SPION@PEG retaining ^{69}Ge) was calculated using the equation (total radioactivity - radioactivity in filtrate)/total radioactivity.

5.2.5 *In Vivo PET Imaging, Biodistribution Studies and In Vivo MR Imaging*

All the animal studies were conducted under a protocol approved by the University of Wisconsin Institutional Animal Care and Use Committee.

The calibration factor for quantification of ^{69}Ge activity concentration in volumes of interest (VOI) of the PET images was obtained following the quantification calibration procedure indicated in the Inveon microPET/CT scanner manual, which was explained in chapter 2, section 2.2.7, using a 130 mL cylinder phantom filled with ^{69}Ge dissolved in 0.1 M HCl at a concentration of 155 ± 5 kBq/mL.

Tumors were established in four- to five-week-old female Balb/c mice by subcutaneous injection of approximately 2×10^6 murine mammary carcinoma 4T1 cells, into the lower flank of three mice. Tumor sizes were monitored and mice were used for the imaging experiments when the axis of the quasi-ellipsoid tumors reached lengths of 6 - 9 and 5 - 8 mm, 10 days after inoculation. The total body mass of the mice at this time was 18.0 ± 1.0 g.

The ^{69}Ge diluted in phosphate buffer stock solution ($^{69}GeCl_4$ in PBS or simply ^{69}Ge-PBS) for injection was prepared by mixing 10 µL of the separated stock in 0.1 M HCl with 600 µL of phosphate buffer saline (PBS) (Thermo Scientific) and 2 µL of 2 M Na_2CO_3 for pH adjustment to ~7. A dose of 3.64 ± 0.05 MBq of ^{69}Ge-PBS in 200 µL was administered to each mouse and static PET scans were performed at 0.5, 3 and 6 hours post-injection (p.i.). The acquisition was set to collect at least 40 million coincident counts per mouse, which implicated scanning times of 5 - 22 min. Static images were reconstructed using the OSEM3D algorithm and then analyzed with the Inveon Research Workplace software. Volumes of interest were drawn on the whole volume of the delineable organs: liver, kidneys and bladder, as well as the whole tumor volume. Muscle uptake was quantified by drawing two ellipsoidal VOIs, each of 100 – 200 mm^3, flanking the urinary bladder in regions with low activity uptake where the adductor and biceps femoris muscles are located. The uptake data from each of the VOIs is decay-corrected to time of injection and expressed as percentage injected dose per gram (%ID/g). Large prismatic VOIs were drawn to occupy the whole body of each mouse and the whole body %ID was obtained by multiplication of the %ID/g by the volume of the VOI, assuming that 1 cm^3 = 1 g. The %ID of each delineable organ and tumor was calculated in the same manner.

The %ID versus time plot of the whole body was fit into a mono-exponential decay function in order to calculate the whole body biological half-life of ^{69}Ge-PBS. The time-activity curves of the delineable and remaining organs were used for internal dosimetry estimations as explained in section 5.2.8.

For *in vivo* PET imaging and biodistribution studies of SPION, 200 µL of ^{69}Ge-SPION@PEG (1.85 ± 0.05 MBq) was i.v. injected into normal BALB/c mice (n = 3) and PET scans were performed at different time intervals.

After the last PET scans at 36 h p.i., biodistribution studies were carried out to confirm that the %ID/g values based on PET imaging truly represented the radioactivity distribution in mice. For in vivo lymph node mapping with PET, 40 μL of ^{69}Ge-SPION@PEG (0.74 MBq ± 0.05) was subcutaneously injected into the left footpad of mouse. The time points of 0.5 h, 2 h and 20 h post-injection were chosen for serial PET scans.

All the MRI experiments were performed using a 4.7 T small-animal scanner (Agilent Technologies, Santa Clara, CA). In vivo imaging was carried out before contrast agent administration and at several time points post-injection of 200 μL (or 40 μL) of Ge-SPION@PEG (7.77 mM Fe) in PBS solution for liver imaging or lymph node mapping. To detect SPION accumulation, in vivo T_2*-weighted images were collected using a multi-slice gradient echo sequence with the following parameters: TR = 500 ms; TE = 12 ms; flip angle = 20°; FOV = 40 mm × 40 mm; matrix 256 × 256; NEX = 8; slice thickness = 1 mm for axial liver images and 0.5 mm for coronal lymph node mapping.

5.2.6 *Sentinel Lymph Node Mapping with ^{69}Ge-SPION@PEG*

As a proof-of-concept, non-invasive PET/MR dual-modality sentinel lymph nodes (SLNs) mapping using ^{69}Ge-SPION@PEG was also demonstrated. Typically, SLNs are the first sites of primary tumor metastasis and therefore successful imaging of SLNs has been considered as an important strategy for tracking cancer metastasis in the clinical context [306]. Upon subcutaneous injection of ^{69}Ge-SPION@PEG solution (40 μL, 0.37 ± 0.05 MBq) into the left footpad of normal BALB/c mice, serial PET scans were performed.

5.2.7 *Internal dosimetry of $^{69}GeCl_4$ in PBS, $^{68}GeCl_4$ in PBS and ^{69}Ge-SPION in humans*

The internal dosimetry of ^{69}Ge-PBS, ^{68}Ge-PBS and ^{69}Ge-SPION was estimated for a standard adult male of 73.7 kg as defined by Cristy and Eckerman [49] using the OLINDA/EXM software [50]. The organ %ID/g data from small animals was extrapolated to %ID per organ in human using the mass method by Kirschne [52]. Details about the methodology for internal dosimetry were already explained in chapter 2, section 2.2.8. The internal dosimetry of ^{68}Ge-PBS in 4T1 tumor-bearing mice was obtained by replacing ^{69}Ge for ^{68}Ge in the original OLINDA file, without modification to the original ^{69}Ge-PBS pharmacokinetic data.

5.3 Results and discussion

5.3.1 *Cyclotron targetry, irradiations and target yields*

The molten gallium target encapsulated in the niobium crucible was able to sustain up to 15 μA without causing a peritectic reaction between gallium and the enclosing niobium, which occurs when the temperature is > 400 °C

[289]. Higher currents were not tested to avoid risk of damage to components of our solid target system and therefore the maximum current that is attainable, before niobium and gallium react in the target, remains unknown.

Figure 5.7 shows the typical macroscopic and microscopic appearance of the electroplated NiGa alloys, demonstrating the homogeneity and smoothness of the deposit.

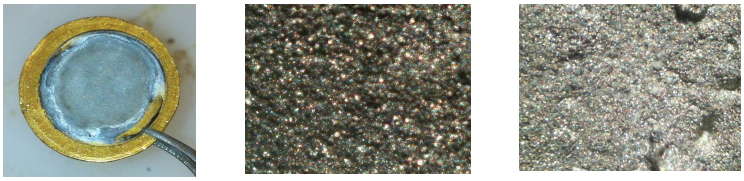

(a) (b) (c)

Figure 5.7 (a) Macroscopic appearance of NiGa electroplated over a gold disk and microscopic appearance from an optical microscope using (b) 4x and (c) 10x magnification.

From the NiGa standard's XRF data, a linear relationship with an $R^2 = 0.97$ was found, as shown in Figure 5.8(b). After substituting the Ga:Ni count rate ratio from one of the electroplated targets into this fitted linear equation, the composition was found to be 3 to 1 Ga:Ni, which means that the molecular formula of the alloy is $NiGa_3$. Figure 5.8(a) shows a typical spectrum from one of the alloys and the linear relationship obtained from analyzing the standard alloys.

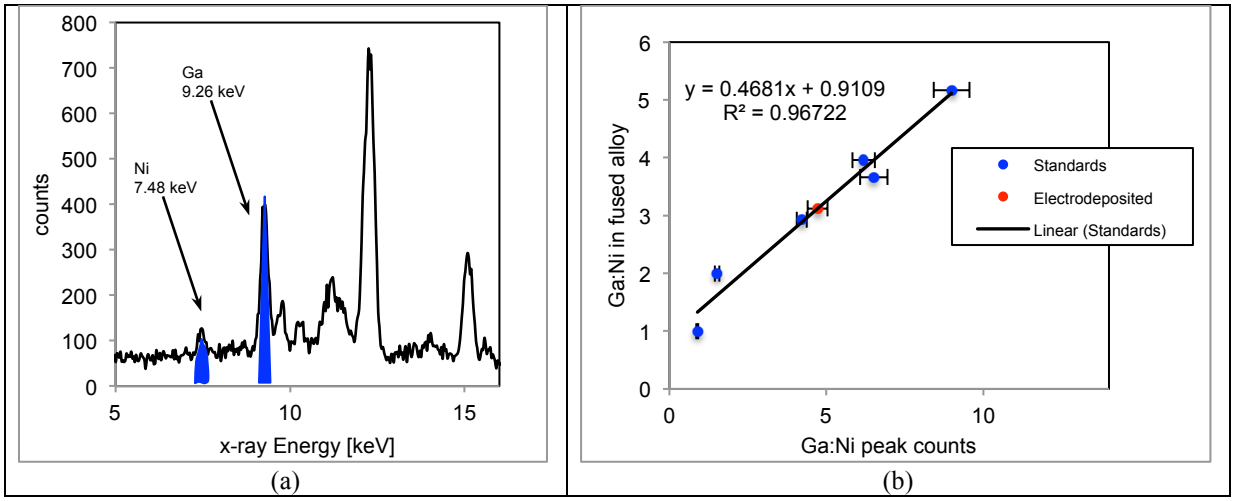

Figure 5.8 (a) X-ray spectra from a NiGa alloy electroplated over a gold disk and (b) Linear fit to the plot of Ga:Ni counts under each peak vs the molar Ga:Ni composition in the standards.

Looking at the NiGa phase diagram from Hansen [298], a $NiGa_3$ alloy with 75% molar content of gallium has a melting point of ~ 950 °C, which is between the melting points of gallium (29.8 °C) and nickel (1455 °C). Likewise, the thermal conductivity is estimated to be between that of nickel and gallium, 91 and 29 W/m-K, respectively, which in this regard makes this material comparable to niobium, with a thermal conductivity of 54 W/m-K.

A SRIM simulation of protons over $NiGa_3$ material (with an estimated density of 6.52 g/cm^3, obtained from the

addition of each component's density times their respective molar fraction, i.e. 0.25*7.81+0.75*6.10) indicates that a thick target for ^{69}Ge and ^{68}Ge production with respective proton entrance energies of 11.0 and 16.0 MeV, has to be at least 347 μm (226 mg/cm^2) and 352 μm (229 mg/cm^2) thick, respectively; with respective predicted thick target yields of 35.3 MBq/μAh (0.96 mCi/μAh) ^{69}Ge and 95.1 kBq/μAh (2.57 μCi/μAh) ^{68}Ge from the experimental excitation functions shown in Figure 5.2.

The maximum current that has been tested on a $NiGa_3$ target was 40 μA without any effect on the appearance of the target. The mass loss after a 1.5 hour-long irradiation with 40 μA on 55.5 mg $NiGa_3$ plated over 1.0 cm^2 of the gold substrate was 1.8 mg, that is, only 3% of the target mass.

Table 5.3 lists the experimental activity yields at end of bombardment (EoB) and how they compare to the predicted yields from published experimental excitation functions. To have a better appreciation of this data, yields of the germanium nuclides from $NiGa_3$ targets are plotted versus thickness in Figure 5.9.

Table 5.3 Activity yields related to the production of ^{69}Ge and ^{68}Ge and comparison to predicted yields from published excitation functions.

Target	**E_{in} [MeV]**	**Δx [mg/cm^2]**	**^{69}Ge Yield [MBq/ μAh]**	**% of predicted from [42, 285]**	**^{55}Co Yield [MBq/ μAh]**	**% of predicted from [166]**	**^{68}Ge Yield [kBq/ μAh]**	**% of predicted from [284]**	**^{65}Zn Yield [kBq/ μAh]**	**% of predicted from [42]**
Ga	15.2	239.8	31.4	40%	-	-	64.0	81%	2.5	57%
$NiGa_3$	16.0	75.9	4.1	34%	0.47	43%	37.5	63%	1.4	27%
		245.3	24.8	43%	1.04	41%	42.9	45%	1.3	20%
	11.0	35.0	5.5	62%	0.10	80%	-	-	-	-
		39.4	8.0	75%	0.14	98%	-	-	-	-
		41.5	5.7	53%	0.08	56%	-	-	-	-
		55.5	4.1	29%	0.05	29%	-	-	-	-
		68.5	8.0	45%	0.04	21%	-	-	-	-
		98.6	12.6	53%	0.09	41%	-	-	-	-
		124.9	14.0	49%	0.08	35%	-	-	-	-

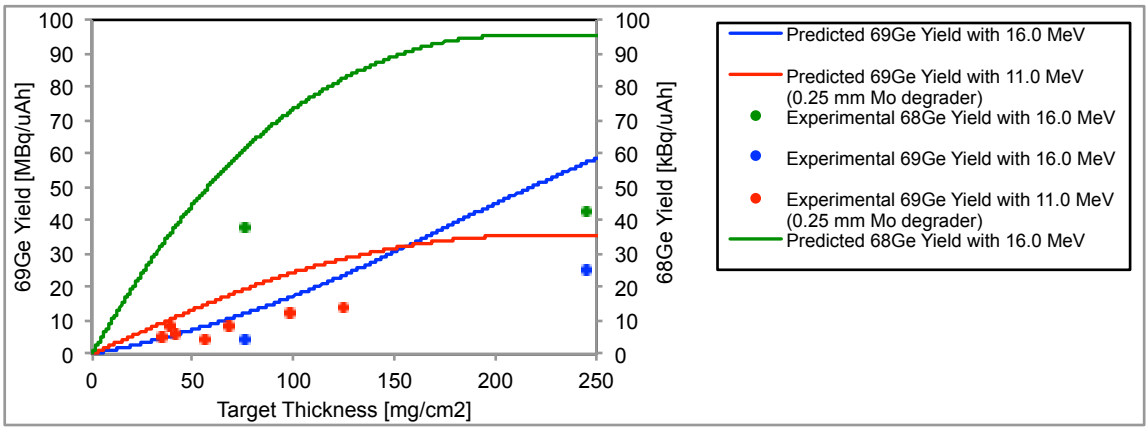

Figure 5.9 Experimental and predicted yields of ^{69}Ge and ^{68}Ge after proton irradiation on $NiGa_3$ targets. The y-axis on the left is for ^{69}Ge in units of MBq/μAh and the y-axis on the right if for ^{68}Ge in units of kBq/μAh.

The yield of ^{55}Co ($t_{1/2}$ = 17.53 h), from ^{58}Ni(p,α), is reported in Table 5.3 because this is the main radionuclidic impurity found in the target after letting decay most of the radioactive copper isotopes produced from ^{nat}Ni(p,n). Even though the radioactive copper yields were not quantified, it was assumed that the main impurities up until a few hours after EoB were ^{60}Cu ($t_{1/2}$ = 23.7 min), ^{62}Cu ($t_{1/2}$ = 9.7 min) and ^{61}Cu ($t_{1/2}$ = 3.33 h) from the proton reactions on the nickel isotopes ^{60}Ni, ^{62}Ni and ^{61}Ni with natural abundances of 26.2%, 3.63% and 1.14%, respectively. For this reason, irradiated targets were left mounted on the cyclotron overnight (~15 h) to let copper radioactivities decay to minimum levels and avoid unnecessary dose exposure. Mercury-197 ($t_{1/2}$ = 64.14 h) and ^{197m}Hg ($t_{1/2}$ = 23.8 h) from the ^{197}Au(p,n) reaction on the gold substrate were also important radionuclidic impurities. The impurity ^{65}Zn ($t_{1/2}$ = 243.93 d) from ^{69}Ga(p,αn) becomes an issue when irradiating with protons > 12.8 MeV (Figure 5.2), i.e. when producing ^{68}Ge.

The experimental yields for ^{69}Ge are on average 48 ± 13% of the predicted yields calculated from experimental excitation functions [42, 285] because the axial profile of the proton beam from the PETtrace covers an area that is larger than the electroplated surface (Ø = 0.9 – 1.1 cm) and the transverse area of the depression in the niobium crucible (Ø = 1.23 cm), which causes a loss of up to 41% of the proton beam intensity in the electroplated targets; and a loss of 15% in the niobium crucible. The details on how these percentage losses were calculated are explained in Appendix C.

The average ^{69}Ge activity yield at the end of bombardment from all the $NiGa_3$ targets irradiated with 11.0 MeV was 8.3 ± 3.7 MBq μA^{-1} h^{-1} (n = 7). Hence, the overall yield of ^{69}Ge was ~166 MBq after a typical 20 μAh irradiation.

Two large batches of ^{68}Ge were produced: the encapsulated gallium target generated 3.17 MBq after an

irradiation with 15 μA for 3.3 hours (49.6 μAh); and the 245.3 mg/cm^2 $NiGa_3$ target generated 11.15 MBq after 260.0 μAh with a maximum current of 40 μA. These ^{68}Ge activities were radiochemically separated, as it is explained in the next section, and then combined to prepare a small ^{68}Ge/^{68}Ga generator following the method published by Chakravarty et al [278].

5.3.2 *Radiochemical separation*

Looking at the extraction properties of DGA resin in HNO_3 solution published by Pourmand and Dauphas [192], a favorable separation of radioactive germanium from bulk gallium and nickel, as well as radioactive impurities of cobalt, copper and mercury, is expected when a solution at a concentration > 12 M HNO_3 is passed through a column filled with DGA resin. At 12 M HNO_3, germanium, gallium, nickel, cobalt, copper and mercury have distribution coefficients of the order of 10^3, 10^{-1}, 0, 10^0 and 0, respectively, which means that ^{6x}Ge is expected to be trapped in the resin while the rest of the elements are eluted with the mobile phase. Germanium is expected to release from the column in diluted acid mobile phase with a concentration < 3 M, at which the distribution coefficient towards the resin for this element is between 1 and 0.1. This separation method was successfully verified with our chromatographic setting having a ^{69}Ge trapping efficiency, after the loading and washing steps, of 85 ± 9% and an overall separation efficiency of 60 ± 10% (n = 6) of the ^{69}Ge produced, in 600 μL of deionized water. Figure 5.10 shows the ^{69}Ge elution profile in terms of the percentage of the total radioactivity produced at EoB eluted in each 200 μL fraction.

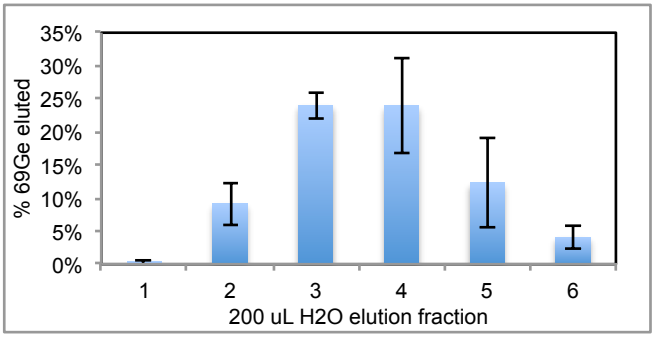

Figure 5.10 Elution profile of ^{69}Ge separated from gallium-based targets dissolved in HCl using a 200 mg DGA branched resin packed into a 0.5 cm ID column with a flow rate of 1.1 mL/min.

The complete elution profile of the main elements involved in the separation, except nickel, was obtained by collecting fractions from two separation runs with volumes of 1 mL in the loading (10 mL) and washing steps (5 mL), followed by fractions of 200 μL in the elution step. The fractions were then analyzed by gamma ray spectrometry using ^{69}Ge, ^{68}Ga (from ^{69}Ga(p,pn)), ^{65}Zn and ^{55}Co as tracers. Ge-69, ^{68}Ga and ^{65}Zn were quantified

after processing the encapsulated gallium target irradiated with 15.2 MeV; and ^{55}Co was quantified after processing one of the $NiGa_3$ targets irradiated with 11.0 MeV protons. Figure 5.11 shows the elution profiles in percentage per fraction and in cumulative percentage of the total radioactivity produced at EoB.

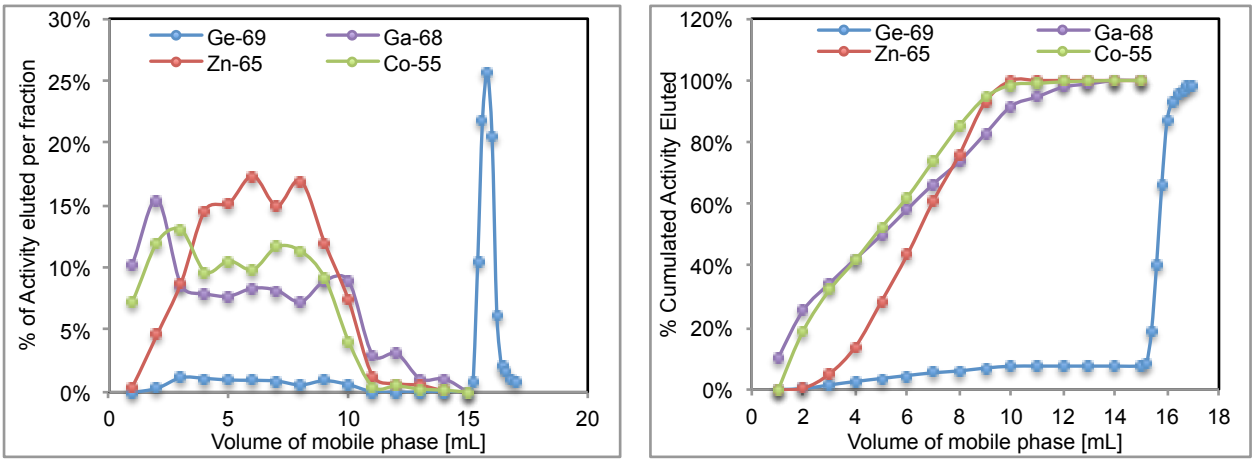

(a) (b)

Figure 5.11 Complete elution profile of the main elements involved in the separation of ^{69}Ge from gallium-based targets dissolved in HNO_3 in terms of percentage per volume (a) and cumulative percentage per total volume (b).

The γ-spectra of ^{69}Ge before and after the purification process are shown in Figure 5.12. The unpurified ^{69}Ge target sample contained significant levels of radionuclidic impurities, such as ^{197m}Hg (134 keV) and ^{55}Co (931 keV), which could be completely removed after the purification process (Figure 5.12(b)), resulting in ^{69}Ge with a radionuclidic purity > 99.99%.

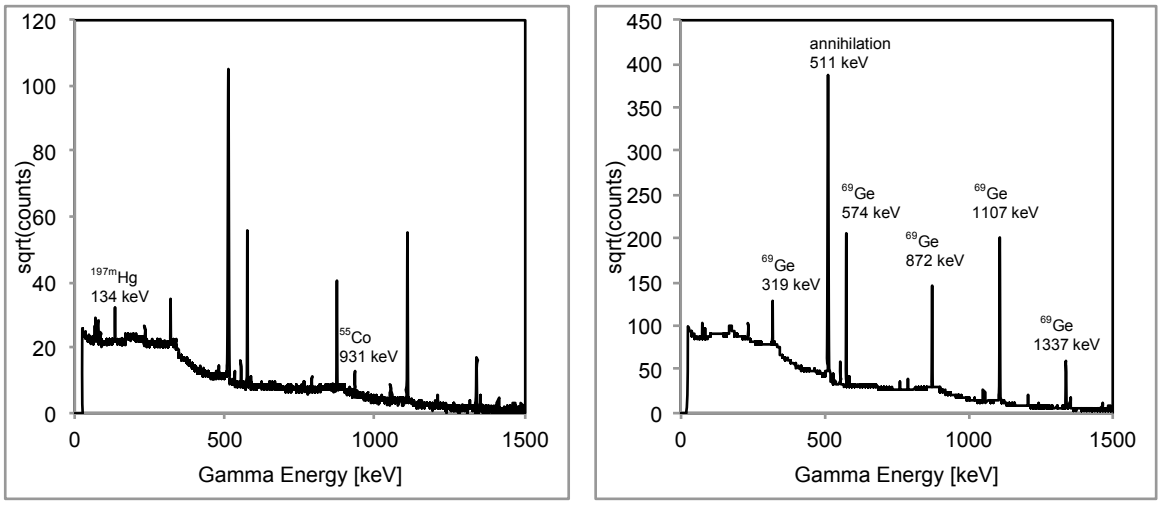

(a) (b)

Figure 5.12 Purification of ^{69}Ge. (a) γ-spectrum of ^{69}Ge sample before the purification process. The spectrum was recorded after allowing the samples to decay for 20 h after the end of irradiation. Significant levels of ^{197m}Hg and ^{55}Co were present as radionuclidic impurities. (b) γ-spectrum of ^{69}Ge sample after purification by extraction chromatography. The presence of radionuclidic impurities in the purified ^{69}Ge sample was negligible as evidenced from the absence of γ-peaks corresponding to the former impurities.

Figure 5.13 shows the decay logging from a sample of the separated stock of ^{69}Ge. The exponential fit to the logged activity reading from the dose calibrator indicates that the half-life of the separated product is 39.17 ± 0.04 h, or 0.3 ± 0.1% greater than the accepted value for ^{69}Ge: 39.05 h [300].

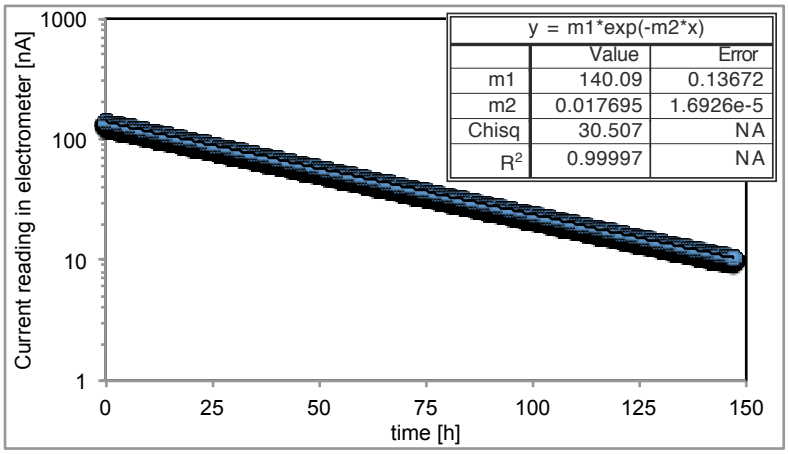

Figure 5.13 Data from logging the activity of a sample from the separated stock every 10 seconds for 9 hours and an exponential fit to the data which indicates that the half-life of the radioactivity in the sample is 39.17 ± 0.04 h, or 0.3 ± 0.1% greater than the value from accepted nuclear data: 39.05 h.

A 50 µL sample from the target solution and the combination of 200 µL fractions #3 to #5 that contain the germanium product (Figure 5.10) were analyzed for trace metal quantification with Agilent's 4200 MP-AES system. The main metal impurities found in the separated stock were: gallium (3.5 mM), iron (1.6 mM), zinc (494 µM), nickel (319 µM), cobalt (24 µM) and copper (2 µM). These results are summarized in Table 5.4, along with the corresponding separation factor for each element. No stable germanium was detected in any of the samples that were analyzed.

Table 5.4 Results form trace metal analysis on the germanium eluate used for labeling experiments.

Element	**Mass [µg]**	**Concentration [ppm]**	**Molarity [µM]**	**Separation Factor***
Gallium	24.5 ± 0.5	245.3 ± 5.5	3519 ± 78	2.6×10^3
Iron	9.2 ± 1.1	91.6 ± 11.2	1641 ± 201	8.0×10^3
Zinc	3.2 ± 0.1	32.3 ± 1.0	494 ± 15	< 1
Nickel	1.9 ± 0.1	18.7 ± 1.1	319 ± 19	9.7×10^3
Cobalt	0.14 ± 0.04	1.4 ± 0.4	24 ± 7	3.3×10^3
Copper	0.012 ± 0.001	0.12 ± 0.01	1.9 ± 0.2	3.9×10^3

* Calculated by dividing the mass in the target solution over the mass in the separated stock.

As it was mentioned in Section 5.3.1, a typical 20 µAh irradiation on a >35 mg/cm^2 thick $NiGa_3$ target generates ~166 MBq ^{69}Ge. 60% of this activity is separated, dried down and re-dissolved in 100 µL of 0.1 M HCl, which represents ~100 MBq ^{69}Ge with an activity concentration of 1000 GBq/L. Therefore, the effective specific activity (ESA) of the separated ^{69}Ge from such representative irradiation would be 1000 GBq/L divided by the total molar concentration of metal impurities shown in Table 5.4, that is, 6000 µM, which equals 0.17 GBq/µmol of metal

impurities. This ESA is one order of magnitude higher than the minimum required to radiolabel SPION under the protocol that was explained in Section 5.2.4, in which 37 MBq of ^{69}Ge are mixed with 1.55 μmol of SPION@PAA (500 μL from a 3.1 mM stock).

Following the methods of Chakravarty et al [278] with some variations, it was attempted to fabricate a small ^{68}Ge/^{68}Ga generator after loading the two separated batches of ^{68}Ge into a 0.5 cm diameter column filled with 245 mg of grinded zirconia (ZrO_2). Ge-68 in 0.01 M HNO_3 solution was quantitatively loaded into the ZrO_2 column with ~80% of the ^{68}Ga daughter and 100% of the ^{65}Zn impurity breaking through the column in this loading solution. However, upon build up of new ^{68}Ga generated by the ^{68}Ge trapped in the column, no significant elution of ^{68}Ga was achieved after several experiments involving many different kinds of eluents. Even when some elution of ^{68}Ga was detected, the activity was too diluted and accounted to only ~30% of the total generated ^{68}Ga. Figure 5.14 shows a PET/CT of the ^{68}Ge/^{68}Ga trapped in the ZrO_2 column. New eluents or elution protocols to make this small generator useful will be attempted in future work. Anyhow, following the reported methods in this chapter, we have shown that batches of tens of MBq of ^{68}Ge can be produced in a small biomedical cyclotron and that the activity can be efficiently separated with a high radionuclidic and chemical purity in a small volume, which is useful for the development of new designs of small generators or to prepare phantoms filled with ^{68}Ge in equilibrium with ^{68}Ga.

Figure 5.14 PET/CT image of ^{68}Ge/^{68}Ga trapped in a column filled with 245 mg ZrO_2 sorbent. The high density of ZrO_2 at the bottom of the column is manifested as a dark region due to low transmission of the x-rays from the CT scanner. The bright white spot inside the ZrO_2 material demonstrates how ^{68}Ge/^{68}Ga is mostly trapped in the upper part of the column.

5.3.3 *Image quality of ^{69}Ge*

The image quality of ^{69}Ge was assessed by visual inspection of the reconstructed microPET images from a Derenzo phantom. As seen in Figure 5.15(a), clear resolution was observed down to a rod diameter of 1.25 mm. Figures 5.15(b) and (c) show the gray intensity profile from 1.47 mm (7 pixels) and 2.10 mm (10 pixels) wide regions of interest that cover the top row of 1.25 mm diameter rods and the bottom row of 1.5 mm diameter rods on the image, respectively. Each peak from each profile was fitted with gaussian curves revealing full width at half

maximum (FWHM) values of 3.8 ± 1.0 and 4.0 ± 1.0 mm, respectively. The average peak to valley ratio in each of these profiles was 1.20 ± 0.04 and 1.23 ± 0.07, respectively. The measurements from the 1.5 mm region will be compared to those from Derenzo phantoms filled with the other radionuclides that are covered in this dissertation in Appendix A.

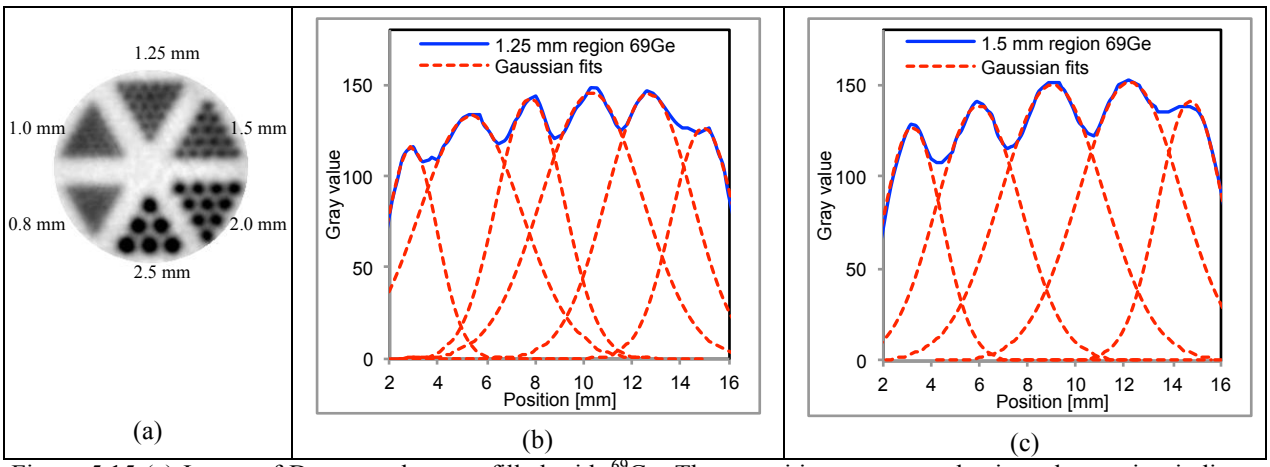

Figure 5.15 (a) Image of Derenzo phantom filled with ^{69}Ge. The quantities next to each triangular section indicate the diameter of each of the rods, which are separated from center to center by twice the diameter distance. As the figure shows, rods up to 1.25 mm can be easily resolved in PET images of ^{69}Ge. Profile distribution of ^{69}Ge from the 1.25 mm rods at the top of the triangular region (b) and the 1.5 mm rods at the bottom of their corresponding region.

5.3.4 *Synthesis of SPION, radiolabeling with ^{69}Ge, PEGylation and serum stability*

Transmission electron microscopy (TEM) images of SPION before and after PAA modification are shown in Figure 5.16 (a) and (b), respectively, which showed no obvious change in morphology. Dynamic light scattering (DLS) analysis of water soluble SPION@PAA in phosphate buffered saline (PBS, pH 7.4) solution indicated a diameter of ca. 23 nm (Figure 5.17), slightly larger than the core size (ca. 10 nm) observed by TEM, which is expected due to the PAA coating and hydration layer on SPION surface. Enhanced T_2* MR contrast imaging property of as-synthesized water soluble SPION@PAA has been demonstrated previously [304], which showed the decrease of T_2 time (from 484.4 ± 95.9 ms to 5.4 ± 0.4 ms) with the increase of Fe concentrations (from zero to 1.94 mM, as indicated in Table 5.5). The T_2 relaxivity (r_2) of SPION@PAA was estimated to be 93.8 $mM^{-1}s^{-1}$ in the 4.7 T microMRI scanner. As synthesized SPION@PAA was found to be highly stable in many different biological solutions (e.g., cell culture medium, saline) and mouse serum, with no visible aggregation even after storage for 6 months [304].

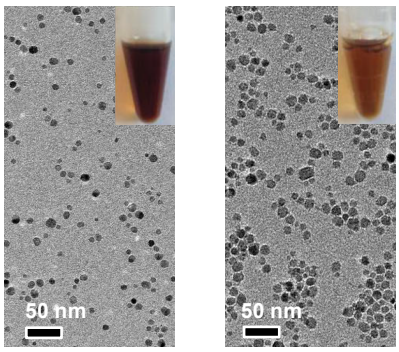

(a) (b)

Figure 5.16 (a) TEM image of SPION. The inset shows a digital photo of SPION in cyclohexane solution. (b) TEM image of SPION@PAA. Inset shows a digital photo of SPION@PAA in aqueous solution.

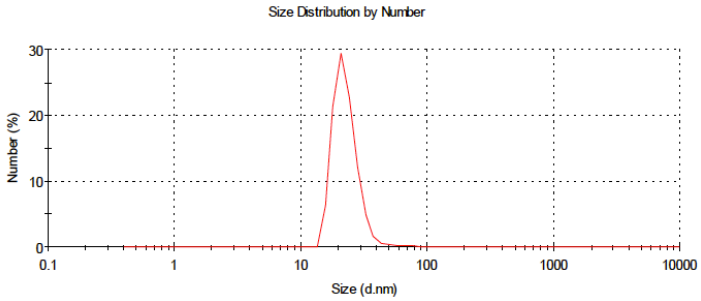

Figure 5.17 Particle size distribution of SPION@PAA measured by dynamic light scattering (DLS) analysis (peak size: ~23 nm).

Table 5.5 T_2 and R_2 values of SPION@PAA samples with varied Fe concentrations.

Fe concentration [mM]	0	0.24	0.49	0.97	1.94
T_2 time [ms]	484.4 ± 95.9	33.4 ± 1.6	17.7 ± 0.2	9.7 ± 0.1	5.4 ± 0.4
R_2 [1/s]	2.1 ± 0.2	30.0 ± 0.5	56.5 ± 0.3	103.0 ± 0.3	186.1 ± 4.3

The radiolabeling yield of ^{69}Ge-SPION@PAA was determined at different time intervals using radio-TLC), where ^{69}Ge-SPION (R_f = 0) could be easily distinguished from free ^{69}Ge ($R_f \approx 0.95$) (Figure 5.18 (a) and (b)). Radiolabeling yield of ^{69}Ge-SPION@PAA was found to be >75% after 3 h incubation at 37 °C, and gradually increased to ~90% after 24 h of incubation (specific radioactivity ca. 3.7 MBq/μmol of Fe) (Figure 5.18 (a), green line). Negative control experiment with the mixture of free ^{69}Ge and water showed nearly zero labeling yield, confirming the successful labeling of ^{69}Ge to SPION@PAA (Figure 5.18 (a), red line).

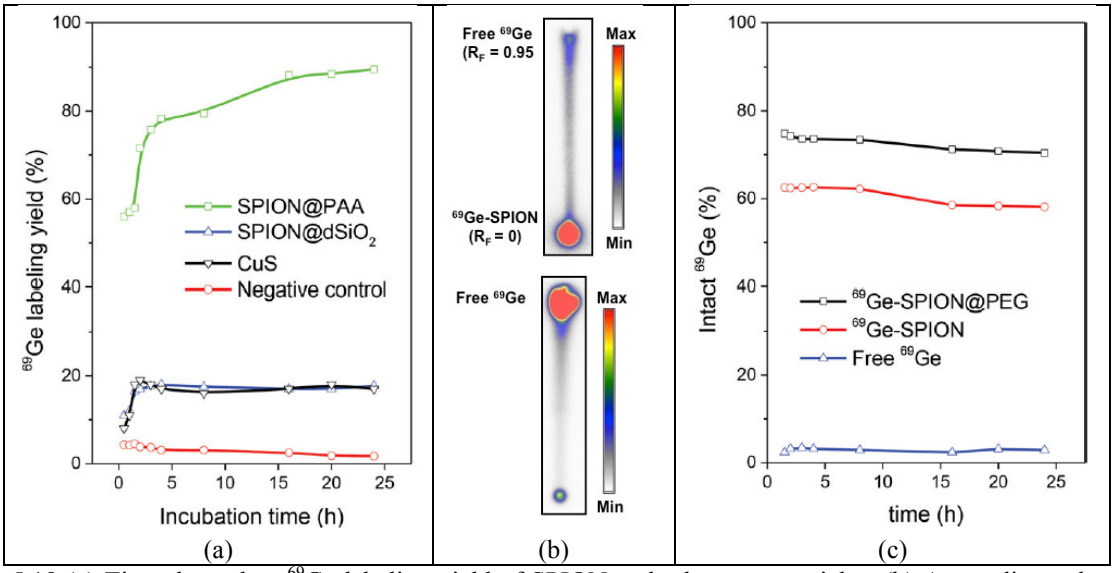

Figure 5.18 (a) Time-dependent ^{69}Ge labeling yield of SPION and other nanoparticles. (b) Autoradiograph of TLC plates of ^{69}Ge-SPION (top) and free ^{69}Ge (bottom). (c) Serum stability study of PEGylated (black line) and non-PEGylated ^{69}Ge-SPION (red line) in whole mouse serum at 37 °C.

The specific labeling of ^{69}Ge to SPION was further demonstrated by: i) blocking the SPION surface with a layer of dense silica ($dSiO_2$); and ii) using non-metal oxide nanoparticles (e.g., copper sulfide [CuS]) as nanoplatforms. The details on how these nanoparticles are synthesized are found in Appendix V. As expected, very low radiolabeling yield (i.e., <15%) was observed when mixing SPION@$dSiO_2$ or CuS with free ^{69}Ge under the same conditions (Figure 5.18 (a), blue and black lines, respectively). In order to rule out the possibility of ^{69}Ge uptake by the PAA, ^{69}Ge labeling of ligand-free SPION (bare SPION without any surface coating) and free PAA were carried out under similar conditions (Figure 5.19). The synthesis procedure of ligand-free SPION is also described in Appendix V. The results showed that the ^{69}Ge radiolabeling to ligand-free SPION (~2.0 mg/mL) was >95% at the end of 24 h, which was slightly higher than what was observed in the case of ^{69}Ge-SPION@PAA. Moreover, there was hardly any uptake of ^{69}Ge by PAA, clearly indicating the successful labeling of ^{69}Ge to SPION@PAA is due to the specific binding of ^{69}Ge with SPION, and nonspecific absorption of ^{69}Ge to PAA is negligible. All these systematic studies amply illustrate the specific affinity of ^{69}Ge to SPION.

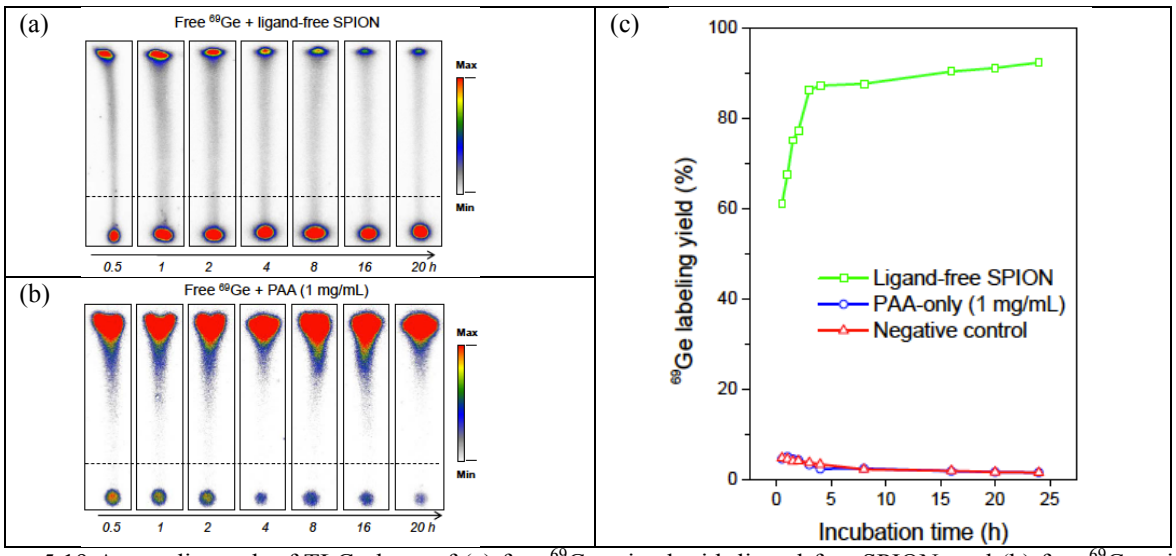

Figure 5.19 Autoradiograph of TLC plates of (a) free ^{69}Ge mixed with ligand-free SPION, and (b) free ^{69}Ge mixed with PAA (1 mg/mL) at different incubation times. (c) Time-dependent ^{69}Ge labeling yields of ligand-free SPION and PAA-only (1 mg/mL) samples.

In order to increase the in vivo stability of ^{69}Ge-SPION, PEGylation step was introduced for coating ^{69}Ge-SPION with a layer of poly(ethylene glycol) (PEG). Enhanced in vitro serum stability was also observed when comparing ^{69}Ge-SPION@PEG with non-PEGylated ^{69}Ge-SPION (Figure 5.18 (c)). ^{69}Ge-SPION@PEG was found to be highly stable (intact ^{69}Ge ca. 75%) even when incubated in excess volume of whole mouse serum at 37 °C (310 K) for 24 h (Figure 5.18 (c), black line). In contrast, non-PEGylated ^{69}Ge-SPION was significantly less stable in mouse serum with intact ^{69}Ge found to be <60% after 6 h of incubation. Before the in vivo PET imaging, ^{69}Ge-SPION@PEG was purified using PD-10 column with PBS as the mobile phase. The radioactivity fractions (which typically elute between 3.0 and 4.0 mL) of ^{69}Ge-SPION@PEG were collected. Free unlabeled ^{69}Ge was eluted out after 6 mL, which allowed complete and baseline separation of ^{69}Ge-SPION from ^{69}Ge.

5.3.5 *In Vivo PET Imaging, Biodistribution Studies and In Vivo MR Imaging*

PET scans were performed at 0.5, 3 and 6 hours post-injection (p.i.) of ^{69}Ge-PBS in three 4T1 tumor-bearing mice. Figure 5.20 shows the coronal and sagittal maximum intensity projection (MIP) images of mouse #3 with the scale bar set to a maximum of 10 %ID/g. Rapid urinary excretion is prominent within the first 30 minutes after injection as seen by the high intensity in signal in the kidneys and urinary bladder. Quantification of the VOIs covering the whole urinary bladder of each mouse reveals that 62.6 ± 3.8 %ID (obtained from 36.6 ± 13.1 %ID/g × 1.8 ± 0.5 cm^3) is about to be excreted within the first 30 min after injection. This observation agrees with that of

Ando et al [307], in which 61.8 %ID of ^{68}Ge was excreted at 3 h p.i. of $^{68}GeCl_4$ in rats. Moreover, tumor contrast in our study is absent as its uptake is comparable to that found in muscles.

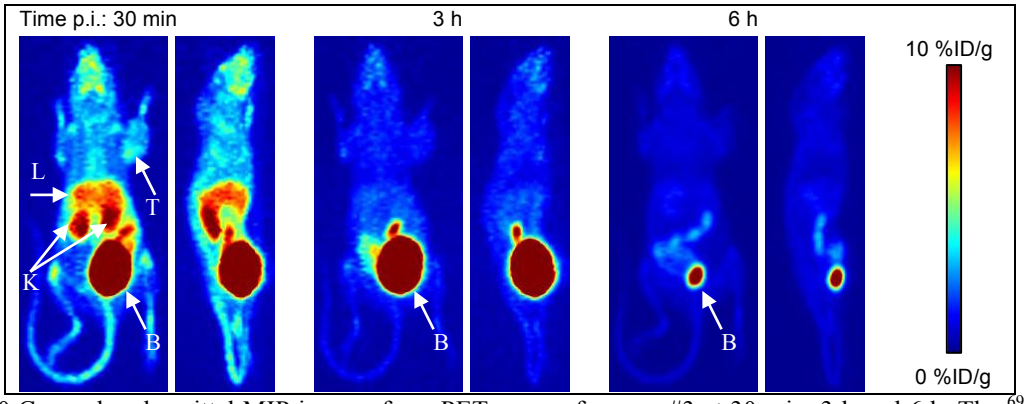

Figure 5.20 Coronal and sagittal MIP images from PET scans of mouse #3 at 30 min, 3 h and 6 h. The ^{69}Ge uptake level is color coded by the 0 to 10 %ID/g bar shown on the right. The PET scans for the other two mice show the same trend in biodistribution of ^{69}Ge-PBS. L: liver; K: kidneys; T: tumor; B: bladder.

Figure 5.21 shows the biodistribution over time and the time-activity curves in terms of %ID/g and %ID, respectively, from quantifications of VOIs covering the whole body, tumor, adductor and biceps femoris muscles and the delineable organs: liver, kidneys and bladder. The %ID plot also shows an exponential fits to the whole body, liver and kidney uptake curves from which a biological half-life was quantified as 1.6 h, 1.7 h and 1.5 h, respectively. The effective whole body half-life is 1.5 h, after taking into account the decay half-life of ^{69}Ge.

The organs with the highest %ID/g uptake are the kidneys followed by the liver. These results agree with those reported Mehard and Volcani after the intravenous (i.v.) administration of $^{68}Ge(OH)_4$ into Sprague-Dawley rats [308] and with those of Velikyan et al. after i.v. injection of $^{68}GeCl_4$ diluted in PBS also into Sprague-Dawley rats [309]. According to the latter publication, the elimination half-life within the first 6 h p.i. is 36 ± 5 min. The reason this value is shorter than the value in our study is because they obtained this half-life from the decay constant in the first exponential (α phase) of a bi-exponential fit. Although they do not explicitly show the other parameters in the fitted function, they report than only 1.8 ± 0.3% of the administered activity remains in the whole body of the animals at 168 h p.i. In our study, analysis of the whole body VOI in the last PET scan (6 h p.i.) indicates that only 9.8 ± 0.8 %ID remains in the animals.

From the biodistribution chart it can be seen that tumor uptake at 30 min p.i. is relatively high with a value of 2.2 ± 0.2 %ID/g if compared against the muscle uptake of 0.8 ± 0.1 %ID/g at this same time point. However, this tumor-to-muscle contrast is basically lost after 4 hours p.i. when the tumor and muscle uptake is 0.8 ± 0.1 %ID/g and 0.5 ± 0.1 %ID/g, respectively. These data demonstrate that weakly bound or "free" ^{69}Ge is not a good intrinsic

radiotracer for tumors as ^{44}Sc-citrate, ^{64}Cu-citrate and $^{64}CuCl_2$. Nevertheless, the fast whole body clearance of unlabeled ^{69}Ge is an advantage if we consider that ^{68}Ge breakthrough from ^{68}Ge/^{68}Ga generators is of concern due to its long physical half-live. For instance, from the biological half-life obtained from the fit to the whole body time-activity curve, the effective whole body half-life of ^{68}Ge-PBS is barely 1.6 h, which suggests that the effective dose caused by this longed-lived nuclide as an unlabeled species will be low, as it will be shown in section 5.3.7.

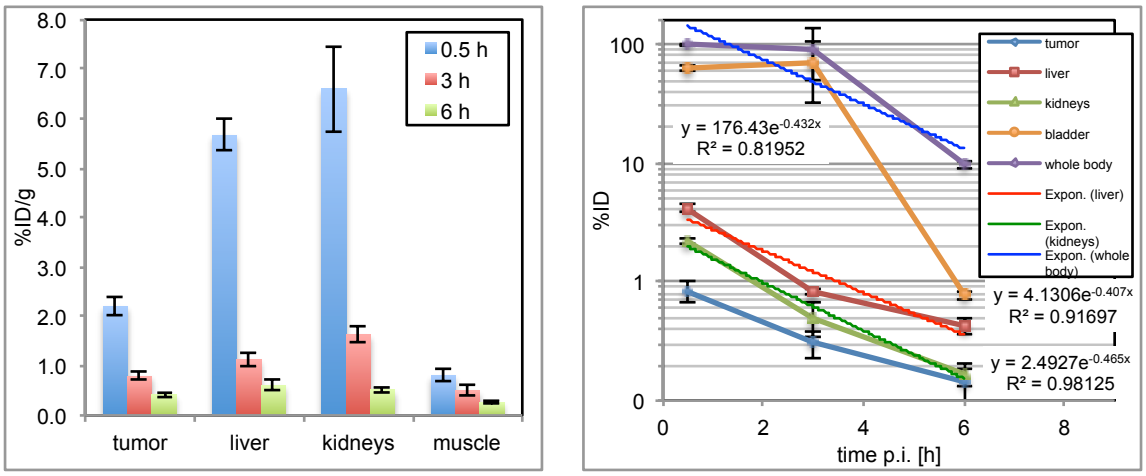

(a) (b)

Figure 5.21 Quantitative PET data presented as biodistribution charts in terms of %ID/g and time-activity curves in terms of %ID from: ^{69}Ge-PBS in mice bearing 4T1 tumors

The *in vivo* stability and biodistribution pattern of ^{69}Ge-SPION@PEG was assessed by PET imaging studies in normal BALB/c mice. Dominant liver uptake of ^{69}Ge-SPION@PEG was observed at different time points after intravenous (i.v.) injection (Figure 5.22 (a)), as expected for most nanoparticles. Mono-exponential fits to the time-activity curves in the liver and whole body reveal biological half-lives of 2.0 and 6.7 days, respectively. Quantitative data obtained from region-of-interest (ROI) analysis of the PET images are shown in Figure 5.23. In stark contrast, $^{69}GeCl_4$ in PBS (referred to as "free" ^{69}Ge) exhibited rapid renal clearance and nearly no accumulation in the liver (Figure 5.22 (a) at such late time points. This latter data is from a single mouse and hence it is not included in the pharmacokinetic analysis of ^{69}Ge-PBS. Such difference in biodistribution pattern is a direct evidence of the fact that ^{69}Ge-SPION@PEG could retain its integrity in vivo and thus demonstrates its suitability as a PET imaging probe. The liver uptake of ^{69}Ge-SPION@PEG was further confirmed by in vivo MRI, which clearly showed the darkening of the liver and no detectable signal change from the kidney (or bladder) after i.v. injection of Ge-SPION@PEG (Figure 5.22 (b)). It may be noted that non-radioactive Ge-SPION@PEG was prepared under the similar conditions for MRI since radioactive materials (e.g., ^{69}Ge-SPION@PEG) are not allowed in the microMRI facility of our

University. The biodistribution of ^{69}Ge-SPION@PEG was also investigated at 36 h post-injection (p.i.) after the final PET scan by measuring the tissue radioactivity. As shown in Figure 5.23 (b), dominant uptake of ^{69}Ge-SPION@PEG in the liver and spleen was observed, which validated that serial non-invasive PET imaging (Figure 5.22 (a)) accurately reflected the biodistribution pattern of ^{69}Ge-SPION@PEG in mice. All these studies demonstrate the feasibility of ^{69}Ge-SPION@PEG for dual-modality PET/MR imaging.

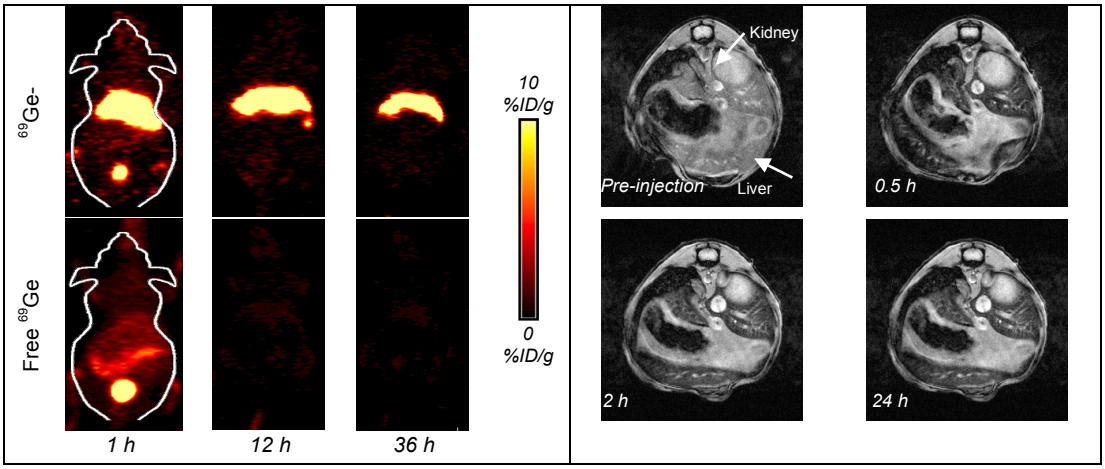

(a) (b)

Figure 5.22 (a) Serial in vivo PET images of ^{69}Ge-SPION@PEG (top) and ^{69}Ge-PBS (bottom) after i.v. injection into mice. (b) In vivo T_2*-weighted MR images of mice before and after i.v. of Ge-SPION@PEG (in PBS). Transaxial images are presented to show the liver uptake of Ge-SPION@PEG, as well as lack of accumulation or contrast enhancement in the kidneys.

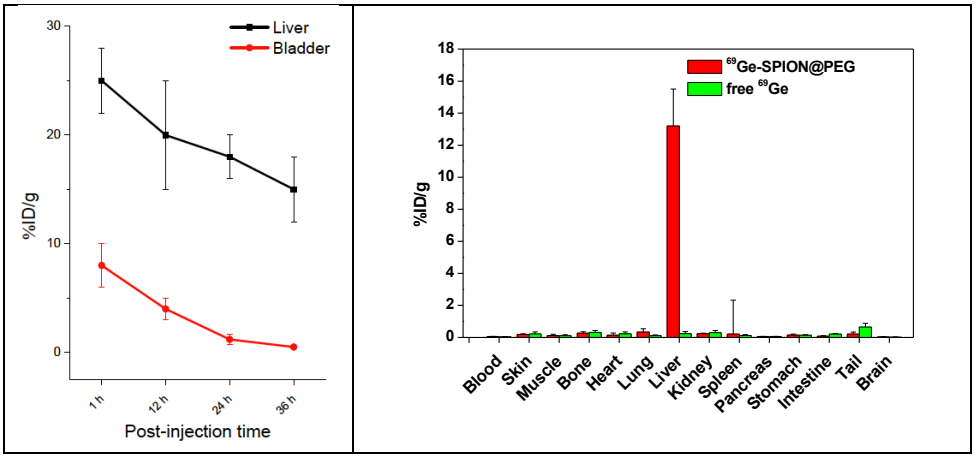

(a) (b)

Figure 5.23 (a) Quantitative data obtained from region-of-interest (ROI) analysis of PET images from mice injected with ^{69}Ge-SPION@PEG (n = 3). The error bar indicates the standard deviation. (b) Biodistribution pattern of ^{69}Ge-SPION@PEG and free ^{69}Ge in mice (n =3) at 36 h p.i. The error bar indicates standard deviation.

5.3.6 *Sentinel Lymph Node Mapping with ^{69}Ge-SPION@PEG*

PET scans upon subcutaneous injection of ^{69}Ge-SPION@PEG solution (40 µL, ca. 370 kBq) into the left footpad of normal BALB/c mice, showed accumulation of ^{69}Ge-SPION@PEG in the popliteal lymph node at 0.5 h,

2 h and 20 h p.i. (Figure 5.24 (a), as pointed by green arrows), with uptake values of 7.5 ± 2.5, 12.5 ± 3.1 and 28.0 ± 5.2 percentage injected dose per gram of tissue (%ID/g), respectively (n = 3; Figure 5.24 (b)). The accumulation of Ge-SPION@PEG in one of the lymph nodes (dashed green circle in Figure 5.24 (c)) could also be clearly visualized by MRI, which showed gradual and prominent darkening of the lymph node after injection of Ge-SPION@PEG (40 μL, 7.77 mM of Fe). As an internal control, the contralateral lymph node (dashed red circle in Figure 5.24 (c)) showed no contrast enhancement at all-time points examined. The accumulation of ^{69}Ge-SPION@PEG in lymph nodes after injection was primarily due to the small size (ca. 23 nm) of these nanoparticles, which is well suited to uptake by the lymphatics [310-312].

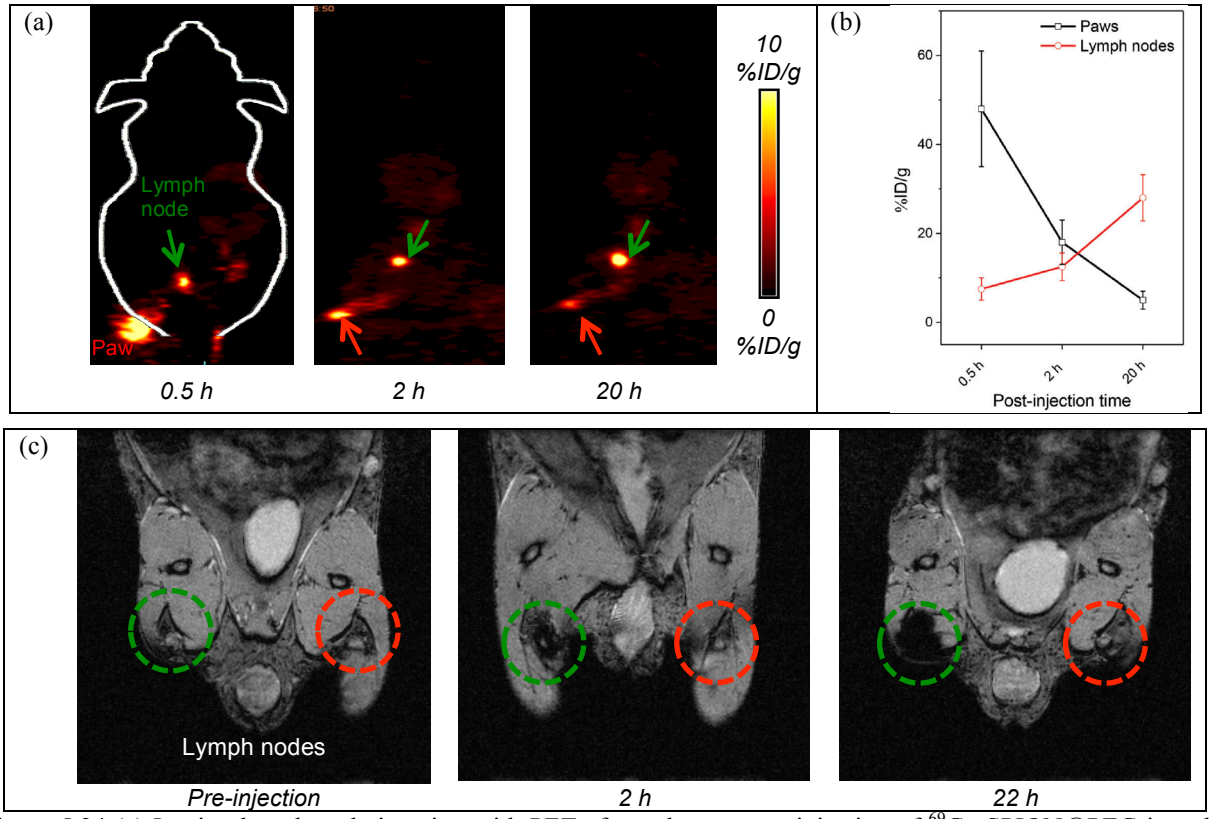

Figure 5.24 (a) In vivo lymph node imaging with PET after subcutaneous injection of ^{69}Ge-SPION@PEG into the left footpad of the mouse. Lymph nodes and paws were indicated by green and red arrows, respectively. (b) Quantification of the ^{69}Ge-SPION@PEGuptake by the lymph node and the mouse paw (n = 3). (c) In vivo lymph node mapping with MRI before and after injection of Ge-SPION@PEG into the left footpad of the mouse. Obvious darkening of the lymph node could be seen (dashed green circle), whereas no contrast enhancement was observed for the contralateral lymph node (dashed red circle).

Although dual-modality PET/MR imaging could only be achieved separately in our current work due to the lack of an integrated microPET/microMRI scanner, this work may serve as an important proof-of-concept to establish ^{69}Ge-SPION@PEG as a promising candidate for future simultaneous PET/MR imaging. With the growing interests in using clinical and preclinical PET/MR scanners for integrated and simultaneous whole-body PET/MR imaging

worldwide [313], further improvement of both the PET/MR scanners and the development of novel PET/MR imaging agents (e.g., ^{69}Ge-SPION@PEG) would benefit clinical cancer patient management in the future (e.g., diagnosis, staging, etc.). The chelator-free strategy reported here could also be effectively utilized for preparation of multifunctional theranostic agents for integrated imaging and therapy by incorporating therapeutically relevant isotopes (e.g., ^{77}Ge [$t_{1/2}$ = 11.3 h,

100% β^- , E_{max} = 2.2 MeV][273] or the Auger electron emitter ^{71}Ge) into SPION. With the presence of carboxyl groups at the surface of ^{69}Ge-SPION, further conjugation of specific targeting ligands, such as proteins, antibodies, or peptides, [314] could also be readily achieved, which would make this class of agents even more powerful for future cancer targeted imaging and therapy.

5.3.7 *Internal dosimetry of $^{69}GeCl_4$ in PBS, $^{68}GeCl_4$ in PBS and ^{69}Ge-SPION in humans*

Table 5.6 shows the ^{69}Ge-PBS and ^{69}Ge-SPION@PEG %ID uptake values extrapolated to a 73.7 kg standard adult male as defined by Cristy and Eckerman [49], using the mass extrapolation method by Kirschne [52], with the whole body mass per mouse set to the average value of 18.0 g in this study. The uptake in the urinary bladder was not extrapolated since the % excreted by the animal = % excreted by the human as suggested by Stabin [315].

Table 5.6 Extrapolation to %ID uptake of ^{69}Ge in standard adult male organs from studies in mice.

Organ	Organ mass in human male adult [g] [49]	Conversion factor %ID/g in mouse to %ID in human	%ID ^{69}Ge-PBS			%ID ^{69}Ge-SPION@PEG			
			30 min	3 h	6 h	1 h	12 h	24 h	36 h
Liver	1910	0.466	2.64	0.53	0.28	11.7	9.3	8.2	7.0
Kidneys	299	0.073	0.48	0.12	0.04	-	-	-	-
Urinary bladder	-	-	62.6	70.2	0.8	13.5	7.2	1.8	0.1
Remaining organs	Balance	Balance	34.3	21.0	8.8	74.8	77.2	78.3	79.5

After setting these %ID uptake values in the EXM portion of the OLINDA software and fitting them to mono-exponential functions (shown in Figure 5.25), the software automatically calculated the cumulative number of decays in each source organ and then the absorbed dose in every target organ considered by the software as well as the total body effective dose. Table 5.7 shows the biological half-lives, from the mono-exponential function fits, of Ge-PBS in the main organs in which it accumulates and the cumulative disintegrations that occur in each of these source organs, $\tilde{A}$, in units of Bq-h/Bq. Even though these values were obtained from the EXM portion of the OLINDA/EXM software, these can also be obtained "manually" using Equation 2.9, presented in Chapter 2.

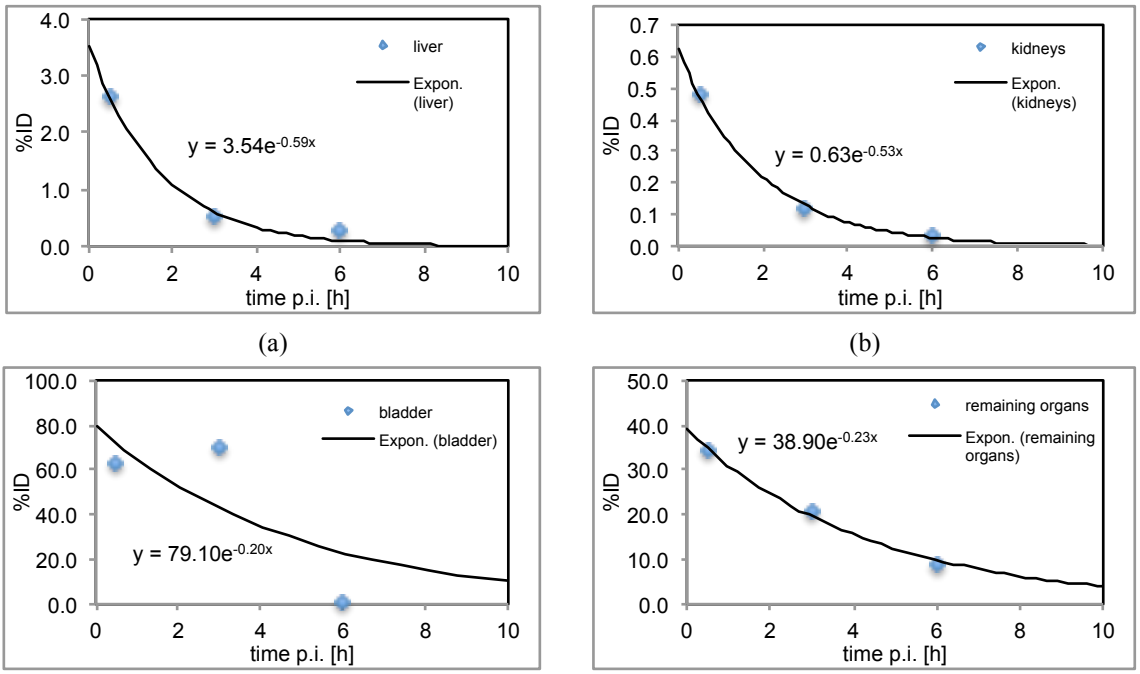

Figure 5.25 Fitted mono-exponential functions to the %ID uptake values of the main organs in which ^{69}Ge-PBS accumulates. The %ID values are extrapolated to a standard male human from %ID/g uptake values obtained from small animal studies.

Table 5.7 Biological half-lives of Ge-PBS in the main organs in which it accumulates and cumulative number of decays, $\tilde{A}$, of ^{68}Ge and ^{68}Ga in each of these source organs.

Source organ	λ_b [h^{-1}]	$t_{1/2,b}$ [h]	$\tilde{A}$ from ^{68}Ge [Bq-h/Bq]	$\tilde{A}$ from ^{68}Ga [Bq-h/Bq]	Ratio of $\tilde{A}$ values
Liver	0.59	1.2	0.060	0.029	2.0
Kidneys	0.53	1.3	0.012	0.005	2.2
Urinary bladder	0.20	3.4	3.90	0.97	4.0
Remaining organs	0.23	3.1	1.71	0.46	3.7

The effective dose was estimated as 73.2 μSv/MBq and 208 μSv/MBq of administered ^{69}Ge-PBS and ^{69}Ge-SPION@PEG, respectively. After substituting ^{69}Ge by ^{68}Ge, maintaining the original pharmacokinetic data, the effective dose from ^{68}Ge-PBS was estimated as 1.38 μSv/MBq. However, this value is highly underestimated since OLINDA does not take into account the emissions from the daughter of ^{68}Ge, i.e. ^{68}Ga, and ^{68}Ge by itself does not emit any penetrating radiation, i.e. high-energy gamma rays. If we substitute ^{69}Ge by ^{68}Ga in the original OLINDA file, the effective dose is estimated as 64.2 μSv/MBq ^{68}Ga, which is also underestimated because the half-life of ^{68}Ga is much shorter than the physical half-life of ^{68}Ge. Hence, in order to have a better estimate of the absorbed dose from the ^{68}Ga that is generated by ^{68}Ge, we will make two conservative assumptions: first, that ^{68}Ga is permanently in secular equilibrium with its parent; and second, that it follows exactly the same pharmacokinetics as ^{68}Ge. In other words, we need to estimate the absorbed dose from a fictitious nuclide that has the half-life of ^{68}Ge but that

emits the same radiation as ^{68}Ga. In order to do this with OLINDA and still be conservative, we need to multiply the effective dose that we have obtained using ^{68}Ga by the ratio of the cumulative decays in the source organ with the longest biological half-life ($t_{1/2,b}$) (i.e. the urinary bladder as shown in Figure 5.25) between ^{68}Ge and ^{68}Ga, using the pharmacokinetic data obtained with ^{69}Ge.

From Table 5.7, 4.0 is the largest ratio of cumulative decays between ^{68}Ge and ^{68}Ga, and therefore, a conservative estimate of the effective dose deposited by ^{68}Ge-PBS in equilibrium with its daughter ^{68}Ga is 4.0 * 64.2 μSv/MBq = 258 μSv/MBq ^{68}Ge.

The absorbed doses per target organ obtained from OLINDA are shown in Figure 5.26. As in the computation of the effective dose from ^{68}Ge-PBS in constant secular equilibrium with ^{68}Ga, the absorbed doses per organ for ^{68}Ge-PBS were obtained from OLINDA after feeding the software with the pharmacokinetics of ^{69}Ge-PBS and the emissions of ^{68}Ga; and multiplying the output results times 4.0, the highest ratio of cumulative decays in an organ between ^{68}Ge and ^{68}Ga. The critical tissue for both Ge-PBS tracers is the urinary bladder wall with absorbed doses of 1.05 mGy/MBq ^{69}Ge and 1.12 mGy/MBq ^{68}Ge. As shown in Figure 5.26, the administration of ^{69}Ge-SPION@PEG into a standard adult of 73.7 kg will cause absorbed doses > 0.1 mGy/MBq in every organ, but the two critical organs will be the urinary bladder wall and the liver with 0.64 and 0.37 mGy/MBq, respectively.

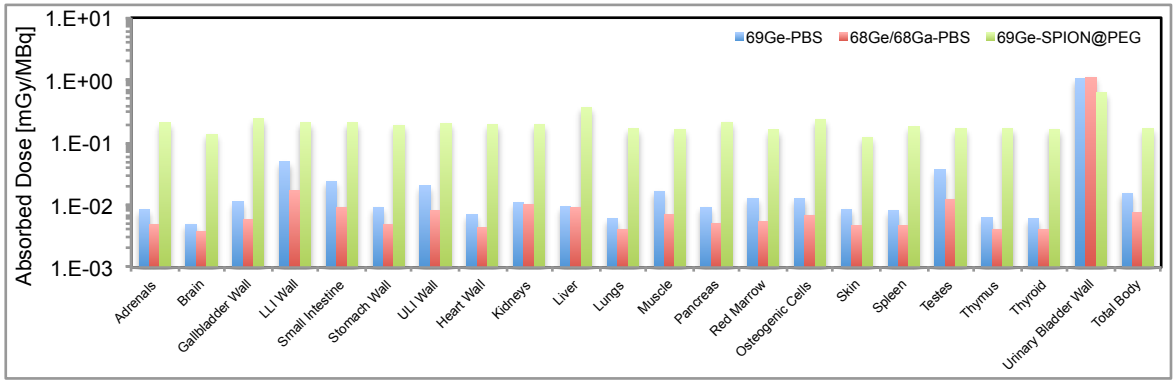

Figure 5.26 Absorbed dose to the organs of a standard adult male after administration of ^{69}Ge-PBS, ^{68}Ge-PBS (assuming that the ^{68}Ga daughter is in permanent equilibrium and that it follows the same pharmacokinetics as it's parent ^{68}Ge) and ^{69}Ge-SPION@PEG.

The implications of the estimated effective doses and absorbed doses per organ are as follows: up to 234 MBq of ^{69}Ge-SPION@PEG can be administered into a male patient within a year, considering that the FDA regulations have set either a maximum annual ED of 50 mSv or a maximum annual absorbed dose to any organ of 150 mGy in adult research subjects [75]. In this case, 234 MBq of ^{69}Ge-SPION@PEG will deposit an absorbed dose of 150 mGy to the urinary bladder wall and an effective dose of 48.7 mSv, coincidentally the annual dose limit for both a

particular organ and the whole body effective dose. Under the same constraints, the maximum activity of ^{68}Ge-PBS that can be injected into a male patient within a year is 134 MBq, which is also defined by the annual dose limit to the urinary bladder wall. This activity will result in an effective dose of 34.6 mSv. To put this in perspective, a clinical brand new 1850 MBq (50 mCi) ^{68}Ge/^{68}Ga generator could have a breakthrough of up to 7.2% of ^{68}Ge activity mixed with the eluted ^{68}Ga for administration into a male patient and still comply with the dose limits imposed by the FDA, although the absorbed dose caused by the ^{68}Ga-labeled tracer still needs to be taken into account and therefore the breakthrough must be < 7.2%. In any case, the order of magnitude of this breakthrough is three times larger than the current limits (< 0.001%) recommended by the European Pharmacopeia monograph [316, 317], and hence we can conclude that the regulations on ^{68}Ge generators are too conservative.

5.4 Conclusions

In this chapter two targetry methods for the production of ^{69}Ge and ^{68}Ge with a small biomedical cyclotron were developed, the best one being via high current (40 μA) proton irradiation on electroplated $NiGa_3$ on a gold substrate. A simple column-based "trap-and-release" isolation method based on the extraction resin DGA was also developed, which offers > 76% radioactive germanium separation yields.

Using SPION as a nanoplatform, we reported the synthesis and in vivo dual-modality PET/MR imaging of ^{69}Ge-SPION@PEG. To the best of our knowledge, this is the first example on the successful utilization of ^{69}Ge-based agent for PET/MR imaging. The key challenge involved in the preparation of ^{69}Ge-radiopharmaceuticals has been circumvented by incorporating ^{69}Ge onto SPION via a fast and highly specific chelator-free approach. The biodistribution pattern and the feasibility of ^{69}Ge-SPION@PEG for in vivo dual-modality imaging and lymph-node mapping have also been investigated.

Moreover, we have shown how ^{69}Ge could fill an important niche as a shorter-lived surrogate of ^{68}Ge to determine its biodistribution via PET and to calculate the internal dosimetry caused by it in situations in which it could represent an environmental hazard, such as when there is breakthrough from a ^{68}Ge/^{68}Ga generator, in the cyclotron facilities that produce ^{68}Ge or in the facilities that fabricate the ^{68}Ge/^{68}Ga generators. For instance, based on the high volatility of $GeCl_4$ in acidic environments, the internal dosimetry of inhaled $^{68}GeCl_4$ could be assessed with the analogue $^{69}GeCl_4$ in an experimental setting. In this chapter $^{69}GeCl_4$ diluted in PBS was used as a surrogate of $^{68}GeCl_4$ and it was shown that after intravenous administration, this compound rapidly clears from the whole

body, which surprisingly resulted in a relatively low effective dose considering that ^{68}Ge is a longed-lived nuclide and that it was assumed that it is constantly emitting the penetrating radiations of its daughter ^{68}Ga.

Chapter 6 Conclusions and Future Directions

In conclusion, we have described rapid and facile methods to recover ^{44}Sc, ^{55}Co, ^{58m}Co, ^{61}Cu, ^{64}Cu, ^{86}Y and ^{69}Ge, with yields > 76%, from proton or deuteron irradiated targets with excellent yield and high chemical and radiochemical purities. In most of the methods, the usage of a single column, minimal washing/elution steps and the elution of the radionuclide of interest in < 0.6 mL provides a convenient framework for the implementation of automatic separation modules. Furthermore, these separation methods also allowed to recover > 90% of the respective target materials, which is an essential requirement in the cases in which isotopically-erriched isotopes were implemented. This separation systems coupled to improved cyclotron production approaches might be the long waited answer to facilitate the translation of these radiometals into the clinic.

Moreover, novel targetry solutions were developed for the irradiation of isotopically-enrriched metallic iron targets for the production of radio-cobalt through deuteron irradiation. This technology can be easily translated to manganese production if the projectile particle is switched to protons. The theranostic pair, or perhaps it should be called trio, ^{55}Co and $^{58m/58g}$Co, was produced from ^{54}Fe and ^{57}Fe targets and then separated with high specific activity for radiolabeling chelator-conjugated biomolecules. As a proof of the high specific activity, the anti-CD105 antibody TRC105 was radiolabeled with radio-cobalt. To demonstrate the theranostic potential of the set of nuclides, this construct was injected into murine breast-cancer tumor bearing mice to demonstrate how treatment planning can be performed before therapy with ^{55}Co using conventional internal dosimetry approaches and how ^{58g}Co can be used to evaluate the effectiveness of the treatment post-therapy via quantitative PET imaging. Further work with this radiometal will focus in increasing the production capacity of ^{58m}Co by proton irradiation on ^{58}Fe and also on radiolabeling targeting vectors that accumulate in the tumor at a faster rate compared to a full antibody, such as peptides or antibody fragments.

Improvements on gallium targetry were also developed, which were mostly based on already published procedures from facilities that produce ^{68}Ge at a large-scale. Nevertheless, our methods were adapted to a small energy biomedical cyclotron, resulting in the production of the novel radio-metalloid ^{69}Ge. The significance of this nuclide hinges on the existence of a therapeutic analogue, the Auger electron emitter ^{71}Ge, which has a suitable half-life for targeted radionuclide therapy of 11.4 days. The therapeutic potential of this radionuclide will only be demonstrated as long as a novel radiolabeling method for this element is developed, which will enable to direct its highly ionizing radiation to cancer lesions. In this regard, we have demonstrated that ^{69}Ge incorporates and remains

stably bound into the structure of super paramagnetic iron oxide nanoparticles (SPION), which already have a niche as contrast agents in magnetic resonance imaging. As a proof of principle of how this construct could be used in dual PET/MRI imaging, we have demonstrated its application lymph node mapping using a small animal model. Moreover, we have shown how ^{69}Ge could fill an important niche as a shorter-lived surrogate of ^{68}Ge to determine its biodistribution via PET and to calculate the internal dosimetry caused by it in situations in which it could represent an environmental hazard, such as when there is breakthrough from a ^{68}Ge/^{68}Ga generator. Future work with ^{69}Ge, will focus in finding a chelator for this metalloid or a radiolabeling protocol that circumvents hydrolysis. For instance, chelation of this element with DTPA [318-320] and EDTA [321] has been reported, which indicates that this metalloid can potentially be radiolabeled like the more established transition radiometals.

Investigations on the biological fate of radiometals administered as simple salts in solution revealed that weakly-bound radio-copper ($CuCl_2$ and Cu-citrate) and radio-scandium (Sc-citrate) both have long biological half-lives in the body (> 33 h) and intrinsic tumor-targeting properties, with maximum uptakes that are > 4 %ID/g, in the murine breast cancer (4T1) and human glioblastoma (U87MG) tumor models that were employed in this thesis. On the contrary, weakly bound radio-cobalt and radio-germanium showed very low interaction in the body and low accumulation in the murine breast cancer xenografts, having whole body biological half-lives < 14 h and maximum uptakes in the tumor that are < 2.4 %ID/g. Future work with weakly bound radio-copper and radio-scandium will focus in quantifying tumor uptakes in other tumor cell lines implanted in rodents; and in the case of the theranostic ^{64}Cu, tumor models with high uptake will be employed in radiotherapy studies similar to the one that has been performed with ^{58m}Co-NOTA-TRC105. These studies would be based on internal dosimetry estimates and, if toxicity predictions allow it, several cycles of therapeutic quantities of ^{64}Cu would be administered. For instance, the results in Chapter 4, Table 4.13, indicated that ~4 GBq of weakly-bound ^{64}Cu injected into a mouse bearing a 0.5 g 4T1 tumor xenograft would deliver the ~230 Gy that we assumed would result in a therapeutic effect on the tumor. However, from the results in Table 4.19, such large activity would also deposit ~1200 Gy in the liver, which will definitely have a deleterious effect in the subject. Therefore, a fractionated regimen would have to be designed, for example by injecting doses of 150 MBq every other day to maintain the absorbed dose to the liver per fraction below the toxicity threshold for this organ (40 Gy). A more promising study could involve tumor xenografts that are ten times smaller than the ones employed in our studies, that is, with a mass of the order of tens of milligrams, which then would require ten times less ^{64}Cu activity resulting in lower normal organ toxicity. Other future work would be

the experimental demonstration of the therapeutic effects of ^{47}Sc-citrate in tumor-bearing mice that have been predicted in this dissertation using the ^{44}Sc analogue. Such project would involve the production of tens of MBq of ^{47}Sc in the PETtrace cyclotron by proton-bombardment on isotopically enriched ^{50}Ti. However, due to the low production yields and the high cost of ^{50}Ti, a better approach would be to obtain ^{47}Sc from collaborators such as Argonne National Lab, where they claim to be able to produce batches of tens or even hundreds of GBq.

Another important conclusion from the analysis of the PET data from ^{44}Sc-citrate in mice was that the effective dose from this agent, extrapolated to a human adult, using > 90% but < 100% radionuclidically pure, cyclotron-produced, ^{44}Sc from natural calcium targets is quite low: 72.9 μSv/MBq and comparable to that of mainstream tracers such as ^{68}Ga-DOTATATE or ^{68}Ga-HBED-CC-PSMA, which we believe justifies the clinical application of this economical supply of ^{44}Sc as an alternative to other more expensive options that result in 100% pure ^{44}Sc.

Future work regarding ^{86}Y will focus in improvements on the effective specific activity. From the trace metal analysis results, the metals that need to be removed, perhaps by adding an extra purification step to our current separation protocol, are zinc, cobalt and iron. Without changing our current separation method, another option to increase the ESA is to generate more activity in the target, which would be achievable by converting the $^{86}SrCO_3$ target to ^{86}SrO prior to irradiation. This would allow to increase the current on target by at least a factor of two from our current setting of 4 μA. Other future projects will involve the experimental verification of the therapeutic regimens of ^{90}Y-labeled vectors that are based on pharmacokinetic and internal dosimetry estimates obtained with the ^{86}Y-labeled analogues. For instance, from the work that was presented in this dissertation we have predicted that 40 MBq of ^{90}Y-DTPA-CHX-A”-TRC105 would deliver ~230 Gy to a 0.5 g 4T1 tumor xenograft in a mouse and that such activity would also deliver ~250 Gy to the spleen, the critical organ, which may or may not make such treatment toxic. Hence, these predictions require an experimental verification, which can be easily accomplished since ^{90}Y is relatively inexpensive and widely available.

Appendix A Derenzo phantoms

The following table shows the images of a miniature Derenzo phantom [47] filled with the positron emitters presented in this dissertation and others such as ^{18}F, ^{45}Ti, ^{68}Ga and ^{66}Ga. All were scanned with the Inveon microPET/CT scanner manufactured by Siemens Medical Solutions. One billion coincident counts were acquired per scan and the reconstructions were done with the Filtered Back Projection 2D (FBP2D) method with a matrix size of each slice of 512×512 pixels.

Nuclide	Derenzo image	$E_{\beta+max}$ [keV]	Mean range in water [mm]	Gray intensity profile from a 2.10 mm (10 pixels) wide region of interest that covers the bottom row of 1.5 mm Ø rods. All peaks are fitted to a gaussian curve	FWHM in middle rod of the 1.5 mm Ø region [mm]	Average peak to valley ratio in profile of 1.5 mm Ø rods
^{18}F	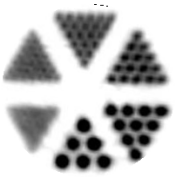	633	0.66	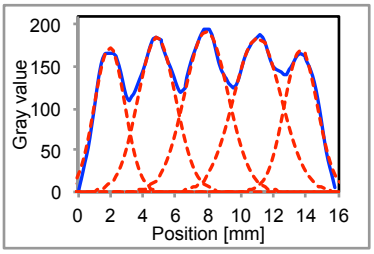	2.8 ± 0.5	1.50 ± 0.17
^{64}Cu	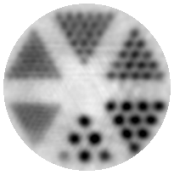	653	0.56	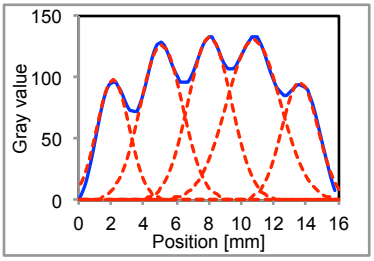	3.0 ± 0.6	1.38 ± 0.22
^{45}Ti	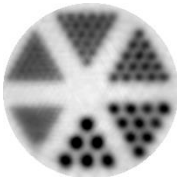	1040	1.47	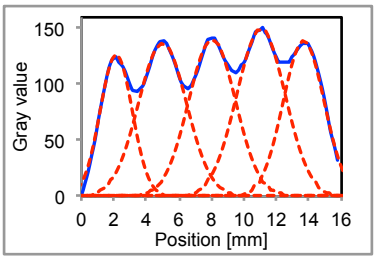	3.2 ± 0.5	1.35 ± 0.12
^{61}Cu	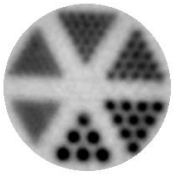	1216	1.80	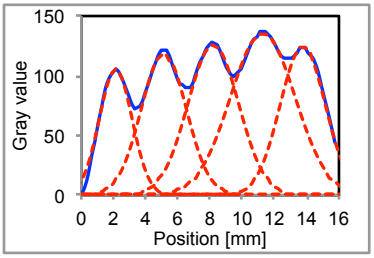	3.5 ± 0.8	1.35 ± 0.17

^{86}Y	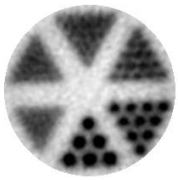	1221 main β^+ (12% BR)	2.51	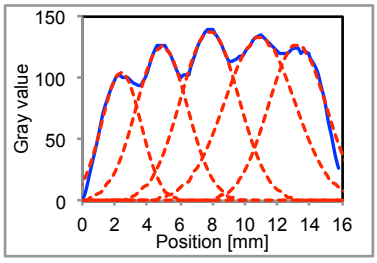	4.0 ± 0.8	1.21 ± 0.13
^{55}Co	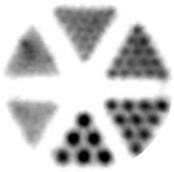	1499 main β^+ (46% BR)	2.15	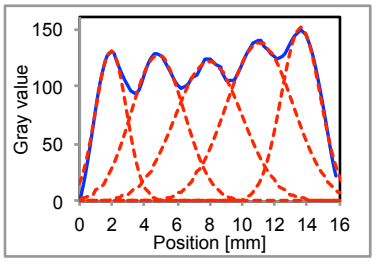	3.7 ± 1.2	1.28 ± 0.10
^{69}Ge	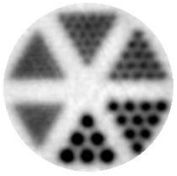	1205	1.85	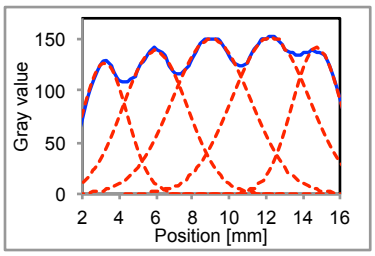	4.0 ± 1.0	1.23 ± 0.07
^{44}Sc	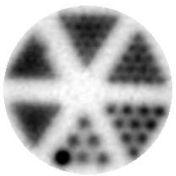	1474	2.46	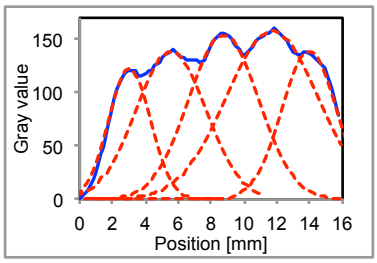	4.7 ± 1.3	1.14 ± 0.11
^{68}Ga	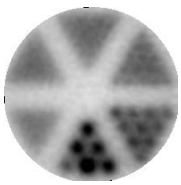	1899	3.56	-	-	-
^{66}Ga	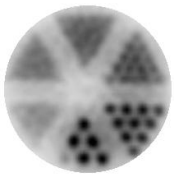	5175	8.69	-	-	-

Appendix B Measurement of the deuteron beam energy from the PETtrace cyclotron

The energy of the deuteron beam that is delivered at the beam port of the GE PETtrace cyclotron was measured from the activity ratio of ^{48}V($t_{1/2}$ = 16.0 d, E_γ = 983.5 keV, 99.98%) and ^{46}Sc ($t_{1/2}$ = 83.8 d, Eγ = 1120.5 keV, 99.987%) generated in a 0.025 mm thick titanium foil that was irradiated with 10 μA for 10 min. Both generated activities were measured with an efficiency calibrated high purity germanium detector (Canberra C1519). The activity ratio was then input on the fitted curve published by Gagnon et al. [322] that relates the natural logarithm of this ratio to the energy of the deuteron beam:

$$y = 0.98386\,x^3 - 6.6491\,x^2 + 16.0224\,x - 4.9685 \qquad \text{Equation B.1}$$

were y and x are the energy of the deuteron beam and the natural logarithm of the activity ratio of ^{48}V and ^{46}Sc, respectively. This relationship is based on the fact that the ratio of activities is uniquely related to the ratio of cross section values, $^{nat}Ti(d,xn)^{48}V$ and $^{nat}Ti(d,x\alpha)^{46}Sc$, and hence to the particular deuteron energy at which the cross-sections were accurately measured, as shown in the following equation:

$$\frac{A_{^{48}V}}{A_{^{46}Sc}} = \frac{\sigma_{^{48}V}\left(1-e^{-\lambda_{^{48}V}t_b}\right)}{\sigma_{^{46}Sc}\left(1-e^{-\lambda_{^{46}Sc}t_b}\right)} \qquad \text{Equation B.2}$$

where A, σ, λ and t_b represent the EoB activity, cross section, decay constant and bombardment time, respectively for ^{48}V and ^{46}Sc. The cross section data for both nuclides has been measured with high accuracy by Takacs et al [323] and therefore the unique value on the right side of the equation is related to a unique energy value at which the cross sections were measured.

The activities at EoB measured in the 0.025 mm titanium foil were 63.5 kBq ^{48}V and 9.4 kBq ^{46}Sc and the substitution of the natural logarithm of these values in Equation B.1 resulted in 8.2 MeV.

Appendix C Measurement of transverse size of the particle beams from the PETtrace cyclotron

The transverse extent of the proton and deuteron beams from the PETtrace cyclotron was measured via autoradiography on irradiated 0.05 mm thick nickel foils. For irradiation, the foils were mounted on a cold finger target support and held in place by four 4-40 bolts that screw to symmetric holes that are equidistant at 11.3 mm from the center of the target support. The aluminum ring clamp with a central hole of 12.5 mm diameter that is employed to hold the disks with electroplated material was not used to hold the nickel foils since it might collimate the beam and occult its true extent. Figure C.1 shows one of the nickel foils mounted in the solid target support before irradiation.

Figure C. 1 Foil setup in target holder

Irradiations with proton and deuteron beams were performed with 5 μA for 10 min after the beam was centered automatically by the PETtrace control system. The short-lived radio-copper products were allowed to decay for several hours, then the foils were dismounted from the target holder and placed on top of a sheet of paper, where four radioactive fiducial points were created applying ~1 μL with a few kBq of ^{89}Zr in solution in each of the four holes that are equidistant from the geometric center of the target holder (Figure C.2(a)). These fiducial points in the autoradiography image will be used to locate the center of the solid target holder. Afterwards, the foils were placed in contact with a phosphor plate for digital autoradiography with the Cyclone Phosphor Plate imaging system (Perkin Elmer).

As shown in Figure C.2(b), the proton and deuteron beams are centered on the target holder center, but both have elliptical shapes. Circular regions of interest (ROIs) centered in the center of the solid target holder were drawn in the autoradiography images to quantify the activity distribution in the foil in digital light units (DLU) (Figure C.2(c).

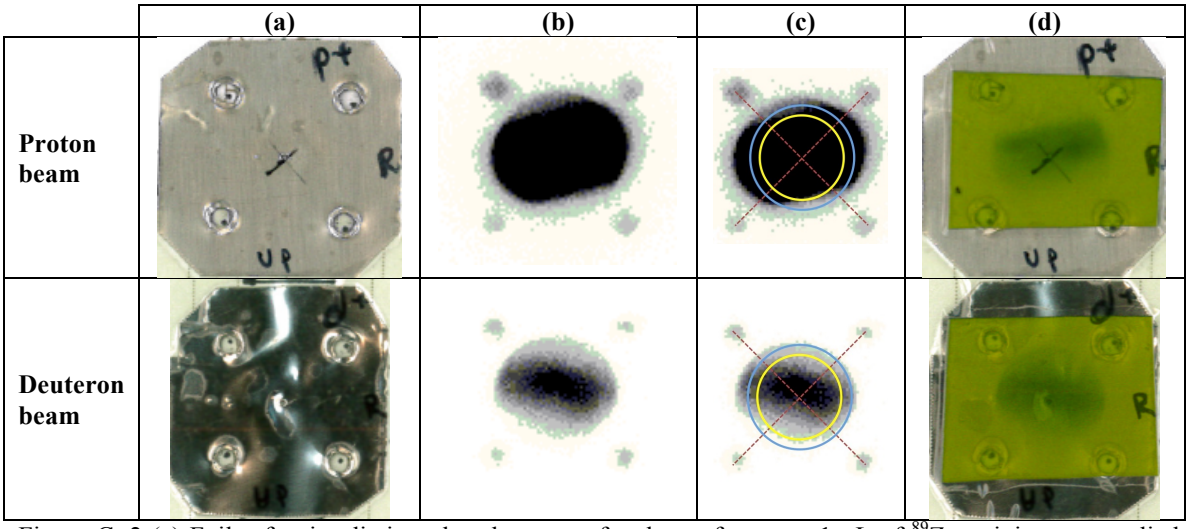

Figure C. 2 (a) Foils after irradiation placed on top of a sheet of paper. ~1 µL of ^{89}Zr activity was applied in each one of the holes that are equidistant from the geometric center of the target holder. (b) Digital autoradiography images that show the elliptical shape of the beam profile and the four fiducial points generated by ^{89}Zr. (c) Circular ROIs centered at the geometric center of the solid target holder. The diameter of the blue ROI corresponds to the diameter of the depression in the niobium crucible target and of the aluminum ring clamp: 12.3 mm. The yellow ROI has a diameter of 10.0 mm, which is the average diameter of the electroplated surface in the targets. ROIs of 9.0 mm and 11.0 mm diameters were also analyzed but are not shown in the figure. (d) Autoradiography in Gafchromic self-developing films taped on top of the irradiated foils.

The smallest diameter of the ROI that enclosed >99% of all the activity generated by the proton and deuteron beam was 15.5 mm for both, which defines the maximum extent of both beam's transverse size. Thus, circular targets that have smaller diameters that these dimensions, like the electroplated surface in the ^{64}Ni, ^{60}N, ^{58}Ni, ^{54}Fe, ^{57}Fe and $NiGa_4$ plated targets or the diameter of the depression in the niobium crucible that holds molten gallium or $^{86}SrCO_3$ powder, will not receive the whole beam intensity. Table III.1 presents the results of the DLU quantifications in ROIs that have the dimensions of our targets.

Table C. 1 Results of the ROI analysis of the digital autoradiography images of the irradiated foils.

		Proton beam		Deuteron beam	
ROI	**Diameter [mm]**	**DLU**	**% of whole beam**	**DLU**	**% of whole beam**
Whole beam strike	15.5	375,274,147.7		28,781,136.5	
Depression in Nb crucible / Al ring clamp	12.3	313,109,222.9	85%	23,770,214.6	84%
Electroplated surface	9.0	218,342,061.0	59%	16,286,560.4	58%
	10.0	250,041,489.1	68%	18,751,061.2	66%
	11.0	279,064,511.9	76%	21,063,441.9	74%

After the autoradiography analysis, a piece of Gafchromic self-developing radiographic film (Manufactured by Ashland) was taped on top of each one of the nickel foils to visually identify the extent of each beam profiles and to verify that it matched the autoradiography image (Figures C.2(d)).

Appendix D Electroplating cell description

The electroplating cell that was used for the preparartion of ^{64}Ni, ^{60}Ni, ^{54}Fe, ^{57}Fe and $NiGa_3$ targets consists of a glass tube (Ace Glass Inc.) (I.D. 1.56 cm) with a polytetrafluoroethylene (PTFE) plugin at one of its ends with a central perforation of 0.9 – 1.1 cm diameter and an O-ring grove to accommodate a viton O-ring at the bottom to seal the solution. The cathode is either a gold or silver disk (0.61 mm and 0.56 mm thick, respectively, 1.90 cm diameter), which is mounted on an aluminum plate. The exposed area of the cathode to the electrolytic solution (0.6 – 0.9 cm^2) is delimited by the central perforation of the PTFE plug. A platinum wire (0.25 mm diameter) is used as the anode, with the tip bent into a spiral shape of ~0.5 cm diameter in order to have a homogeneous electric field across the cathode. The platinum wire remains in a constant geometry throughout each electrodeposition procedure by fixing it inside a 13 cm long, 0.016" diameter, teflon tubing with the tip at 1 cm from the silver anode. An EXTECH power supply model 382200 provides the DC voltage. Figure D.1 shows a schematic and picture of the set up.

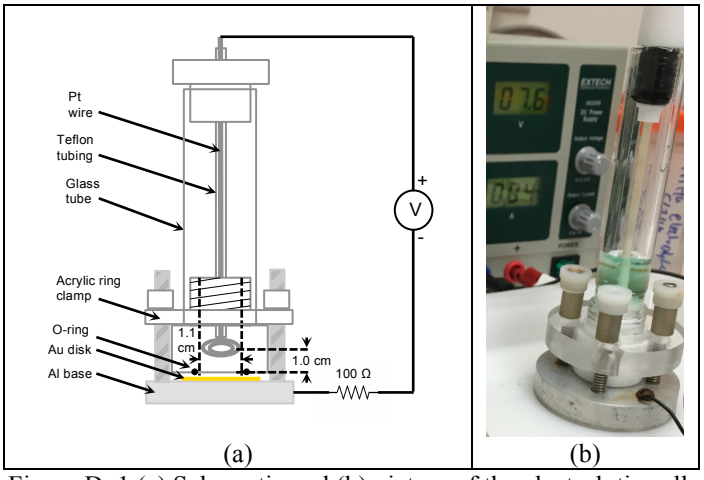

Figure D. 1 (a) Schematic and (b) picture of the electrolytic cell.

Appendix E Synthesis of nanoparticles used as negative controls to demonstrate the specific labeling of ^{69}Ge to SPION

Synthesis of SPION@dSiO$_2$

The synthesis of SPION@dSiO$_2$ was carried out by a base-catalyzed silica layer formation from tetraethylorthosilicate (TEOS) on as-prepared SPION in a water-in-oil reverse microemulsion [301]. Two mL of polyoxyethylene (5) nonylphenylether branched (Igepal CO-520 (NP-5)) were dispersed in cyclohexane (40 mL) in a 100 mL three-necked flask and stirred for 30 min. Subsequently, 0.5 mL of oleic acid capped SPION cyclohexane solution was injected into the cyclohexane/NP-5 mixture. The mixture was stirred at room temperature (22 ºC) for 2 h. Afterwards, ammonia (0.28 mL, 30%) was added, and the system was sealed and stirred for another 2 h. TEOS (250 μL) was delivered into the system at a precisely controlled rate of 200 μL/h using a syringe pump. The mixture was sealed and kept under magnetic stirring for 17 h at room temperature before addition of methanol to precipitate the nanoparticles. The as-synthesized SPION@dSiO$_2$ nanoparticles were washed with ethanol for more than 3 times to remove excess NP-5. The resulting SPION@dSiO$_2$ could be well-dispersed in water.

Synthesis of citrate capped CuS nanoparticles

The general procedures for the synthesis of citrate capped CuS nanoparticles were similar as that reported by Zhou et al. [324]. In a typical synthesis of CuS nanoparticles, 10 mL of $CuCl_2$ (0.8524 mg/mL) and 10 mL of sodium citrate (1 mg/mL) were added into 30 mL of HQ water. The mixture was stirred at room temperature for 30 min. Fifty μL of Na_2S (1 mmol/mL) was then added into the mixture and stirred for 5 min before reacting at 90 ºC in a water bath for 15 min. Citrate capped CuS with green color could be obtained and directly used for ^{69}Ge-labeling. Figure E.1 shows TEM images of SPION@dSiO$_2$ and CuS.

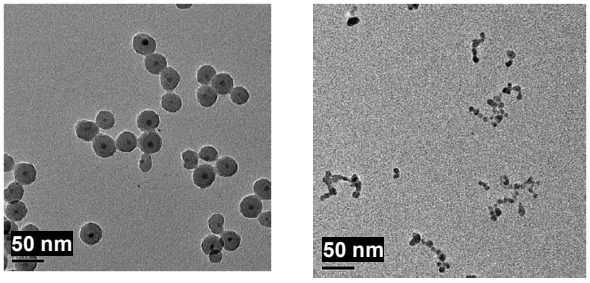

(a) (b)

Figure E. 1 TEM images of (a) SPION@dSiO$_2$ and (b) CuS nanoparticles.

Synthesis of ligand-free SPION

Ligand-free SPION was synthesized by following previously reported procedures with slight modifications [304], where the oleate-coated SPION nanoparticles were treated with hydrochloric acid (HCl) to protonate the oleate ligand, resulting in ligand-free SPION after the release of oleic acid from the surface. In a typical synthesis, deionized water (5 mL) was added in a 25 mL bottle, followed by addition of cyclohexane-dispersed oleate-coated SPION (5 mL). Subsequently, HCl (100 μL, 7.4 M) was added and the mixture was shaken for 10-20 min. Then, the water layer of the mixture was quickly collected using separating funnel and centrifuged (13000 rpm) for 10 min. The sample was then washed three times with acetone, resulting in ligand-free SPION (dispersed in water).

REFERENCES

[1] Vallabhajosula SR, Harwig JF, Siemsen JK, and Wolf W. Radiogallium localization in tumors - blood binding and transport and the role of transferrin. Journal of Nuclear Medicine 1980;21:650-6.

[2] Larson SM, Rasey JS, Allen DR, Nelson NJ, Grunbaum Z, Harp GD, et al. Common pathway for tumor-cell uptake of Ga-67 and Fe-59 via a transferrin receptor. Journal of the National Cancer Institute 1980;64:41-53.

[3] Weiner RE. The mechanism of Ga-67 localization in malignant disease. Nuclear Medicine and Biology 1996;23:745-51.

[4] Tsan MF and Scheffel U. Mechanism of Ga-67 accumulation in tumors. Journal of Nuclear Medicine 1986;27:1215-9.

[5] Tsan MF. Mechanism of Ga-67 accumulation in inflammatory lesions. Journal of Nuclear Medicine 1985;26:88-92.

[6] Hammersley PAG and Zivanovic MA. The relationship of Ga-67 uptake to citrate dose, compared with Ga-67-chloride and Ga-67-transferrin in rodent tissues and tumors. Nuklearmedizin 1980;19:25-8.

[7] Vavere AL and Welch MJ. Preparation, biodistribution, and small animal PET of Ti-45-Transferrin. Journal of Nuclear Medicine 2005;46:683-90.

[8] Peng F, Lu X, Janisse J, Muzik O, and Shields AF. PET of human prostate cancer xenografts in mice with increased uptake of ($CuCl_2$)-Cu-64. Journal of Nuclear Medicine 2006;47:1649-52.

[9] Jorgensen JT, Persson M, Madsen J, and Kjaer A. High tumor uptake of Cu-64: Implications for molecular imaging of tumor characteristics with copper-based PET tracers. Nuclear Medicine and Biology 2013;40:345-50.

[10] Qin CX, Liu HG, Chen K, Hu X, Ma XW, Lan XL, et al. Theranostics of Malignant Melanoma with (CuCl2)-Cu-64. Journal of Nuclear Medicine 2014;55:812-7.

[11] Chakravarty R, Chakraborty S, and Dash A. Cu-64(2+) Ions as PET Probe: An Emerging Paradigm in Molecular Imaging of Cancer. Molecular Pharmaceutics 2016;13:3601-12.

[12] Connett JM, Anderson CJ, Guo LW, Schwarz SW, Zinn KR, Rogers BE, et al. Radioimmunotherapy with a Cu-64-labeled monoclonal antibody: A comparison with Cu-67. Proceedings of the National Academy of Sciences of the United States of America 1996;93:6814-8.

[13] Kim KI, Jang SJ, Park JH, Lee YJ, Lee TS, Woo KS, et al. Detection of Increased Cu-64 Uptake by Human Copper Transporter 1 Gene Overexpression Using PET with ($CuCl_2$)-Cu-64 in Human Breast Cancer Xenograft Model. Journal of Nuclear Medicine 2014;55:1692-8.

[14] Cai HW, Wu JS, Muzik O, Hsieh JT, Lee RJ, and Peng FY. Reduced Cu-64 Uptake and Tumor Growth Inhibition by Knockdown of Human Copper Transporter 1 in Xenograft Mouse Model of Prostate Cancer. Journal of Nuclear Medicine 2014;55:622-8.

[15] Ferrari C, Asabella AN, Villano C, Giacobbi B, Coccetti D, Panichelli P, et al. Copper-64 Dichloride as Theranostic Agent for Glioblastoma Multiforme: A Preclinical Study. Biomed Research International 2015.

[16] Panichelli P, Villano C, Cistaro A, Bruno A, Barbato F, Piccardo A, et al. Imaging of Brain Tumors with Copper-64 Chloride: Early Experience and Results. Cancer Biotherapy and Radiopharmaceuticals 2016;31:159-67.

[17] Capasso E, Durzu S, Piras S, Zandieh S, Knoll P, Haug A, et al. Role of ($CuCl_2$)-Cu-64 PET/CT in staging of prostate cancer. Annals of Nuclear Medicine 2015;29:482-8.

[18] Lewis JS, Laforest R, Buettner TL, Song SK, Fujibayashi Y, Connett JM, et al. Copper-64-diacetyl-bis(N-4-methylthiosemicarbazone): An agent for radiotherapy. Proceedings of the National Academy of Sciences of the United States of America 2001;98:1206-+.

[19] Koumarianou E, Pawlak D, Korsak A, and Mikolajczak R. Comparison of receptor affinity of ^{nat}Sc-DOTA-TATE versus ^{nat}Ga-DOTA-TATE. Nucl Med Rev Cent East Eur 2011;14:85-9.

[20] Koumarianou E, Loktionova N, Fellner M, Roesch F, Thews O, Pawlak D, et al. Sc-44-DOTA-BN[2-14]NH2 in comparison to Ga-68-DOTA-BN[2-14]NH2 in pre-clinical investigation. Is Sc-44 a potential radionuclide for PET? Applied Radiation and Isotopes 2012;70:2669-76.

[21] Pruszynski M, Majkowska-Pilip A, Loktionova N, Eppard E, and Roesch F. Radiolabeling of DOTATOC with the long-lived positron emitter Sc-44. Applied Radiation and Isotopes 2012;70:974-9.

[22] Hernandez R, Valdovinos HF, Yang Y, Chakravarty R, Hong H, Barnhart TE, et al. Sc-44: An Attractive Isotope for Peptide-Based PET Imaging. Molecular Pharmaceutics 2014;11:2954-61.

[23] Muller C, Bunka M, Reber J, Fischer C, Zhernosekov K, Turler A, et al. Promises of Cyclotron-Produced Sc-44 as a Diagnostic Match for Trivalent beta(-)-Emitters: In Vitro and In Vivo Study of a Sc-44-DOTA-Folate Conjugate. Journal of Nuclear Medicine 2013;54:2168-74.

[24] Chakravarty R, Goel S, Valdovinos HF, Hernandez R, Hong H, Nickles RJ, et al. Matching the Decay Half-Life with the Biological Half-Life: ImmunoPET Imaging with Sc-44-Labeled Cetuximab Fab Fragment. Bioconjugate Chemistry 2014;25:2197-204.

[25] Filosofov D, Loktionova N, and Rosch F. A Ti-44/Sc-44 radionuclide generator for potential application of Sc-44-based PET-radiopharmaceuticals. Radiochimica Acta 2010;98:149-56.

[26] Hoehr C, Oehlke E, Benard F, Lee CJ, Hou X, Badesso B, et al. Sc-44g production using a water target on a 13 MeV cyclotron. Nuclear Medicine and Biology 2014;41:401-6.

[27] Krajewski S, Cydzik I, Abbas K, Bulgheroni A, Simonelli F, Holzwarth U, et al. Cyclotron production of Sc-44 for clinical application. Radiochimica Acta 2013;101:333-8.

[28] Severin G, Engle J, Valdovinos H, Barnhart T, and Nickles R. Cyclotron produced Sc-44g from natural calcium. Applied Radiation and Isotopes 2012;70:1526-30.

[29] Severin GW, Gagnon K, Engle JW, Valdovinos HF, Barnhart TE, and Nickles RJ. Sc-44g From Metal Calcium Targets For PET. In: MA AvilaRodriguez, JP Oneil, TE Barnhart, DW Dick, JM Koziorowski, SE Lapi, et al. editors. 14th International Workshop on Targetry and Target Chemistry; 2012, p. 125-8.

[30] Pruszynski M, Loktionova N, Filosofov D, and Rosch F. Post-elution processing of Ti-44/Sc-44 generator-derived Sc-44 for clinical application. Applied Radiation and Isotopes 2010;68:1636-41.

[31] Ford-Hutchinson AW and Perkins DJ. Binding of scandium ions to transferrin in-vivo and in-vitro. European Journal of Biochemistry 1971;21:55-&.

[32] Ford-Hutchinson AW and Perkins DJ. Scandium-46 metabolism - Binding to metalloproteins in-vivo and in-vitro. Radiation Research 1972;51:244-&.

[33] Li HY, Sadler PJ, and Sun HZ. Rationalization of the strength of metal binding to human serum transferrin. European Journal of Biochemistry 1996;242:387-93.

[34] Hayes RL, Byrd BL, Rafter JJ, and Carlton JE. The effect of scandium on the tissue distribution of Ga-67 in normal and tumor-bearing rodents. Journal of Nuclear Medicine 1980;21:361-5.

[35] Hayes RL, Rafter JJ, Byrd BL, and Carlton JE. Studies of the in vivo entry of Ga-67 into normal and malignant-tissue. Journal of Nuclear Medicine 1981;22:325-32.

[36] Hayes RL, Rafter JJ, Carlton JE, and Byrd BL. Studies of the in vivo uptake of Ga-67 by an experimental abscess - Concise communication. Journal of Nuclear Medicine 1982;23:8-14.

[37] Gasparini M, Bombardieri E, Castellani M, Tondini C, Maffioli L, Devizzi L, et al. Gallium-67 scintigraphy evaluation of therapy in non-Hodgkin's lymphoma. Journal of Nuclear Medicine 1998;39:1586-90.

[38] Nanni C, Errani C, Boriani L, Fantini L, Ambrosini V, Boschi S, et al. Ga-68-Citrate PET/CT for Evaluating Patients with Infections of the Bone: Preliminary Results. Journal of Nuclear Medicine 2010;51:1932-6.

[39] Braun T and Ghersini G. *Extraction chromatography*, Amsterdam ; New York: Elsevier Scientific Pub. Co, 1975.

[40] Burrows TW. Nuclear data sheets for A=47. Nuclear Data Sheets 2007;108:923-+.

[41] Attix FH. Appendixes. Introduction to Radiological Physics and Radiation Dosimetry: Wiley-VCH Verlag GmbH; 2007, p. 525-98.

[42] Levkovskij V. Activation cross section nuclides of average masses (A=40-100) by protons and alpha-particles with average energies (E=10-50 MeV). Activation cross-sections by protons and alphas. Moscow; 1991.

[43] Takacs S, Tarkanyi F, Sonck M, and Hermanne A. Investigation of the Mo-nat(p,x)Tc-96mg nuclear reaction to monitor proton beams: New measurements and consequences on the earlier reported data. Nuclear Instruments & Methods in Physics Research Section B-Beam Interactions with Materials and Atoms 2002;198:183-96.

[44] Ziegler JF, Ziegler MD, and Biersack JP. SRIM – The Stopping and Range of Ions in Matter. 2013. https://www.srim.org/

[45] Chen J, Singh B, and Cameron JA. Nuclear Data Sheets for A=44. Nuclear Data Sheets 2011;112:2357-495.

[46] Siikanen J, Peterson M, Tran TA, Roos P, Ohlsson T, and Sandell A. A Peristaltic Pump Driven Zr-89 Separation Module. 14th International Workshop on Targetry and Target Chemistry (WTTC). Mexico; AIP Conference Proceedings 2012;1509:206-10.

[47] Derenzo SE, Budinger TF, Huesman RH, Cahoon JL, and Vuletich T. Imaging properties of a positron tomograph with 280-BGO-crystals. IEEE Transactions on Nuclear Science 1981;28:81-9.

[48] Cox BL, Graves SA, Farhoud M, Barnhart TE, Jeffery JJ, Eliceiri KW, et al. Development of a novel linearly-filled Derenzo microPET phantom. Am J Nucl Med Mol Imaging 2016;6:199-204.

[49] Cristy M and Eckerman K. Specific Absorbed Fractions of Energy at Various Ages from Internal Photons Sources. Oak Ridge, TN: Oak Ridge National Laboratory; 1987.

[50] Stabin MG, Sparks RB, and Crowe E. OLINDA/EXM: The second-generation personal computer software for internal dose assessment in nuclear medicine. Journal of Nuclear Medicine 2005;46:1023-7.

[51] FDA. Section 510(k) clearance of OLINDA/EXM. 2004.
https://www.accessdata.fda.gov/cdrh_docs/pdf3/k033960.pdf
https://www.accessdata.fda.gov/scripts/cdrh/cfdocs/cfpmn/pmn.cfm?ID=K033960

[52] Kirschner AS, Ice RD, and Beierwaltes WH. Radiation-dosimetry of I-131-19-iodocholesterol. Journal of Nuclear Medicine 1973;14:713-7.

[53] Bolch WE, Eckerman KF, Sgouros G, and Thomas SR. MIRD Pamphlet No. 21: A Generalized Schema for Radiopharmaceutical Dosimetry-Standardization of Nomenclature. Journal of Nuclear Medicine 2009;50:477-84.

[54] ICRP. 1990 Recommendations of the International Commission on Radiological Protection. 1991;ICRP Publication 60.

[55] Stabin MG and Konijnenberg MW. Re-evaluation of absorbed fractions for photons and electrons in spheres of various sizes. Journal of Nuclear Medicine 2000;41:149-60.

[56] Stabin MG, Peterson TE, Holburn GE, and Emmons MA. Voxel-based mouse and rat models for internal dose calculations. Journal of Nuclear Medicine 2006;47:655-9.

[57] Takacs S, Tarkanyi F, Sonck M, and Hermanne A. Investigation of the $^{nat}Mo(p,x)^{96mg}Tc$ nuclear reaction to monitor proton beams: New measurements and consequences on the earlier reported data. Nuclear Instruments & Methods in Physics Research Section B-Beam Interactions with Materials and Atoms 2002;198:183-96.

[58] Alliot C, Kerdjoudj R, Michel N, Haddad F, and Huclier-Markai S. Cyclotron production of high purity Sc-44m,Sc-44 with deuterons from ($CaCO_3$)-Ca-44 targets. Nuclear Medicine and Biology 2015;42:524-9.

[59] van der Meulen NP, Bunka M, Domnanich KA, Muller C, Haller S, Vermeulen C, et al. Cyclotron production of Sc-44: From bench to bedside. Nuclear Medicine and Biology 2015;42:745-51.

[60] Duchemin C, Guertin A, Haddad F, Michel N, and Metivier V. Production of scandium-44m and scandium-44g with deuterons on calcium-44: cross section measurements and production yield calculations. Physics in Medicine and Biology 2015;60:6847-64.

[61] Wadas TJ, Wong EH, Weisman GR, and Anderson CJ. Coordinating radiometals of copper, gallium, indium, yttrium, and zirconium for PET and SPECT imaging of disease. Chem Rev 2010;110:2858-902.

[62] Anderegg G, Arnaud-Neu F, Delgado R, Felcman J, and Popov K. Critical evaluation of stability constants of metal complexes of complexones for biomedical and environmental applications (IUPAC Technical Report). Pure and Applied Chemistry 2005;77:1445-95.

[63] Martell A, Smith R, and Motekaitis R. NIST Critically Selected Stability Constants of Metal Complexes Database. https://www.nist.gov/srd/nist46

[64] Huclier-Markai S, Sabatie A, Ribet S, Kubicek V, Paris M, Vidaud C, et al. Chemical and biological evaluation of scandium(III)-polyaminopolycarboxylate complexes as potential PET agents and radiopharmaceuticals. Radiochimica Acta 2011;99:653-62.

[65] Severin GW, Gagnon K, Engle JW, Valdovinos HF, Barnhart TE, and Lewis JS. 44gSc from metal calcium targets for PET. AIP Conference Proceedings 2012;1509:125-8.

[66] Camera L, Kinuya S, Garmestani K, Wu C, Brechbiel MW, Pai LH, et al. Evaluation of the serum stability and in vivo biodistribution of CHX-DTPA and other ligands for yttrium labeling of monoclonal antibodies. J Nucl Med 1994;35:882-9.

[67] Le Loirec C and Champion C. Track structure simulation for positron emitters of medical interest. Part I: The case of the allowed decay isotopes. Nuclear Instruments & Methods in Physics Research Section A-Accelerators Spectrometers Detectors and Associated Equipment 2007;582:644-53.

[68] Sun HZ, Li HY, and Sadler PJ. Transferrin as a metal ion mediator. Chemical Reviews 1999;99:2817-42.

[69] Boswell CA, Sun XK, Niu WJ, Weisman GR, Wong EH, Rheingold AL, et al. Comparative in vivo stability of copper-64-labeled cross-bridged and conventional tetraazamacrocyclic complexes. Journal of Medicinal Chemistry 2004;47:1465-74.

[70] Gatter KC, Brown G, Trowbridge IS, Woolston RE, and Mason DY. Transferrin receptors in human-tissues - Their distribution and possible clinical relevance. Journal of Clinical Pathology 1983;36:539-45.

[71] Huebers HA and Finch CA. The physiology of transferrin and transferrin receptors. Physiological Reviews 1987;67:520-82.

[72] Burrows TW. Nuclear data sheets for A=48. Nuclear Data Sheets 2006;107:1747-+.

[73] Roesch F and Baum RP. Generator-based PET radiopharmaceuticals for molecular imaging of tumours: on the way to THERANOSTICS. Dalton Transactions 2011;40:6104-11.

[74] Roesch F. Scandium-44: benefits of a long-lived PET radionuclide available from the ^{44}Ti/^{44}Sc generator system. Current radiopharmaceuticals 2012;5:187-201.

[75] FDA. Title 21: Food and drugs. Chapter I: Food and Drug Administration Department of Health and Human Services. Subchapter D: Drugs for Human Use. Part 361: Prescription Drugs for Human Use Generally Recognized as Safe and Effective and Not Misbranded: Drugs Used in Research. Sec. 361.1 Radioactive drugs for certain research uses. https://www.accessdata.fda.gov/scripts/cdrh/cfdocs/cfcfr/CFRSearch.cfm?FR=361.1

[76] Walker RC, Smith GT, Liu E, Moore B, Clanton J, and Stabin M. Measured Human Dosimetry of Ga-68-DOTATATE. Journal of Nuclear Medicine 2013;54:855-60.

[77] Pfob CH, Ziegler S, Graner FP, Kohner M, Schachoff S, Blechert B, et al. Biodistribution and radiation dosimetry of Ga-68-PSMA HBED CC A PSMA specific probe for PET imaging of prostate cancer. European Journal of Nuclear Medicine and Molecular Imaging 2016;43:1962-70.

[78] Walczak R, Krajewski S, Szkliniarz K, Sitarz M, Abbas K, Choinski J, et al. Cyclotron production of Sc-43 for PET imaging. EJNMMI Physics 2015;2.

[79] Minegishi K, Nagatsu K, Fukada M, Suzuki H, Ohya T, and Zhang M-R. Production of scandium-43 and -47 from a powdery calcium oxide target via the $^{nat/44}$Ca(α,x)-channel. Applied Radiation and Isotopes 2016;116:8-12.

[80] Strigari L, Konijnenberg M, Chiesa C, Bardies M, Du Y, Gleisner KS, et al. The evidence base for the use of internal dosimetry in the clinical practice of molecular radiotherapy. European Journal of Nuclear Medicine and Molecular Imaging 2014;41:1976-88.

[81] Maxon HR, Thomas SR, Hertzberg VS, Kereiakes JG, Chen IW, Sperling MI, et al. Relation between effective radiation-dose and outcome of radioiodine therapy for thyroid-cancer. New England Journal of Medicine 1983;309:937-41.

[82] Flux GD, Haq M, Chittenden SJ, Buckley S, Hindorf C, Newbold K, et al. A dose-effect correlation for radioiodine ablation in differentiated thyroid cancer. European Journal of Nuclear Medicine and Molecular Imaging 2010;37:270-5.

[83] Matthay KK, Panina C, Huberty J, Price D, Glidden DV, Tang HR, et al. Correlation of tumor and whole-body dosimetry with tumor response and toxicity in refractory neuroblastoma. treated with I-131-MIBG. Journal of Nuclear Medicine 2001;42:1713-21.

[84] Pauwels S, Barone R, Walrand S, Borson-Chazot F, Valkema R, Kvols LK, et al. Practical dosimetry of peptide receptor radionuclide therapy with Y-90-labeled somatostatin analogs. Journal of Nuclear Medicine 2005;46:92S-8S.

[85] Dewaraja YK, Schipper MJ, Roberson PL, Wilderman SJ, Amro H, Regan DD, et al. I-131-Tositumomab Radioimmunotherapy: Initial Tumor Dose-Response Results Using 3-Dimensional Dosimetry Including Radiobiologic Modeling. Journal of Nuclear Medicine 2010;51:1155-62.

[86] Koral KF, Francis IR, Kroll S, Zasadny KR, Kaminski MS, and Wahl RL. Volume reduction versus radiation dose for tumors in previously untreated lymphoma patients who received iodine-131 tositumomab therapy - Conjugate views compared with a hybrid method. Cancer 2002;94:1258-63.

[87] Ho S, Lau WY, Leung TWT, Chan M, Johnson PJ, and Li AKC. Clinical evaluation of the partition model for estimating radiation doses from yttrium-90 microspheres in the treatment of hepatic cancer. European Journal of Nuclear Medicine 1997;24:293-8.

[88] Garin E, Lenoir L, Rolland Y, Edeline J, Mesbah H, Laffont S, et al. Dosimetry Based on Tc-99m-Macroaggregated Albumin SPECT/CT Accurately Predicts Tumor Response and Survival in Hepatocellular Carcinoma Patients Treated with Y-90-Loaded Glass Microspheres: Preliminary Results. Journal of Nuclear Medicine 2012;53:255-63.

[89] Strigari L, Sciuto R, Rea S, Carpanese L, Pizzi G, Soriani A, et al. Efficacy and Toxicity Related to Treatment of Hepatocellular Carcinoma with Y-90-SIR Spheres: Radiobiologic Considerations. Journal of Nuclear Medicine 2010;51:1377-85.

[90] Senthamizhchelvan S, Hobbs RF, Song H, Frey EC, Zhang Z, Armour E, et al. Tumor Dosimetry and Response for Sm-153-Ethylenediamine Tetramethylene Phosphonic Acid Therapy of High-Risk Osteosarcoma. Journal of Nuclear Medicine 2012;53:215-24.

[91] Sharkey RM, Pykett MJ, Siegel JA, Alger EA, Primus FJ, and Goldenberg DM. Radioimmunotherapy of the GW-39 human colonic tumor xenograft with I-131-labeled murine monoclonal-antibody to carcinoembryonic antigen. Cancer Research 1987;47:5672-7.

[92] Blumenthal RD, Sharkey RM, Kashi R, and Goldenberg DM. Comparison of therapeutic efficacy and host toxicity of 2 different I-131-labelled antibodies and their fragments in the GW-39 colonic-cancer xenograft model. International Journal of Cancer 1989;44:292-300.

[93] Sharkey RM, Kaltovich FA, Shih LB, Fand I, Govelitz G, and Goldenberg DM. Radioimmunotherapy of human colonic-cancer xenografts with Y-90-labeled monoclonal-antibodies to carcinoembryonic antigen. Cancer Research 1988;48:3270-5.

[94] Zalcberg JR, Thompson CH, Lichtenstein M, and McKenzie IFC. Tumor-immunotherapy in the mouse with the use of I-131-labeled monoclonal-antibodies. Journal of the National Cancer Institute 1984;72:697-704.

[95] Buchegger F, Vacca A, Carrel S, Schreyer M, and Mach JP. Radioimmunotherapy of human-colon carcinoma by I-131-labeled monoclonal anti-CEA antibodies in a nude-mouse model. International Journal of Cancer 1988;41:127-34.

[96] Buchsbaum DJ, Lawrence TS, Roberson PL, Heidorn DB, Tenhaken RK, and Steplewski Z. Comparison of I-131-labeled and Y-90 labeled monoclonal-antibody 17-1A for treatment of human colon cancer xenografts. International Journal of Radiation Oncology Biology Physics 1993;25:629-38.

[97] Buras RR, Beatty BG, Williams LE, Wanek PM, Harris JB, Hill LR, et al. Radioimmunotherapy of human colon cancer in nude-mice. Archives of Surgery 1990;125:660-4.

[98] Friberg S and Mattson S. On the growth rates of human malignant tumors: Implications for medical decision making. Journal of Surgical Oncology 1997;65:284-97.

[99] Edge S, Byrd DR, Compton CC, Fritz AG, Greene FL, and Trotti A (Editors). American Joint Committee on Cancer Staging Manual. 7th ed., New York, NY: Springer, 2010.

[100] Emami B, Lyman J, Brown A, Coia L, Goitein M, Munzenrider JE, et al. Tolerance of normal tissue to therapeutic irradiation. International Journal of Radiation Oncology Biology Physics 1991;21:109-22.

[101] Matthews DC, Appelbaum FR, Eary JF, Fisher DR, Durack LD, Hui TE, et al. Phase I study of I-131-anti-CD45 antibody plus cyclophosphamide and total body irradiation for advanced acute leukemia and myelodysplastic syndrome. Blood 1999;94:1237-47.

[102] Dawson NJ. Surface-area/body-weight relationship in mice. Australian Journal of Biological Sciences 1967;20:687-&.

[103] Stabin MG and Siegel JA. Physical models and dose factors for use in internal dose assessment. Health Physics 2003;85:294-310.

[104] Ilan E, Sandstrom M, Wassberg C, Sundin A, Garske-Roman U, Eriksson B, et al. Dose Response of Pancreatic Neuroendocrine Tumors Treated with Peptide Receptor Radionuclide Therapy Using Lu-177-DOTATATE. Journal of Nuclear Medicine 2015;56:177-82.

[105] van Vliet EI, Krenning EP, Teunissen JJ, Bergsma H, Kam BL, and Kwekkeboom DJ. Comparison of Response Evaluation in Patients with Gastroenteropancreatic and Thoracic Neuroendocrine Tumors After Treatment with Lu-177-DOTA(0),Tyr(3) Octreotate. Journal of Nuclear Medicine 2013;54:1689-96.

[106] van Vliet EI, van Eijck CH, de Krijger RR, van Dijkum EJN, Teunissen JJ, Kam BL, et al. Neoadjuvant Treatment of Nonfunctioning Pancreatic Neuroendocrine Tumors with Lu-177-DOTA(0),Tyr(3) Octreotate. Journal of Nuclear Medicine 2015;56:1647-53.

[107] Sansovini M, Severi S, Ambrosetti A, Monti M, Nanni O, Sarnelli A, et al. Treatment with the Radiolabelled Somatostatin Analog Lu-177-DOTATATE for Advanced Pancreatic Neuroendocrine Tumors. Neuroendocrinology 2013;97:347-54.

[108] Paganelli G, Sansovini M, Ambrosetti A, Severi S, Monti M, Scarpi E, et al. ^{177}Lu-DOTA-octreotate radionuclide therapy of advanced gastrointestinal neuroendocrine tumors: results from a phase II study. European Journal of Nuclear Medicine and Molecular Imaging 2014;41:1845-51.

[109] Severi S, Sansovini M, Ianniello A, Bodei L, Nicolini S, Ibrahim T, et al. Feasibility and utility of re-treatment with Lu-177-DOTATATE in GEP-NENs relapsed after treatment with Y-90-DOTATOC. European Journal of Nuclear Medicine and Molecular Imaging 2015;42:1955-63.

[110] Ianniello A, Sansovini M, Severi S, Nicolini S, Grana C, Massri K, et al. Peptide receptor radionuclide therapy with Lu-177-DOTATATE in advanced bronchial carcinoids: prognostic role of thyroid transcription factor 1 and F-18-FDG PET. European Journal of Nuclear Medicine and Molecular Imaging 2016;43:1040-6.

[111] Vaisman F, de Castro PHR, Lopes F, Kendler DB, Pessoa CHN, Bulzico DA, et al. Is There a Role for Peptide Receptor Radionuclide Therapy in Medullary Thyroid Cancer? Clinical Nuclear Medicine 2015;40:123-7.

[112] Baum RP, Kluge AW, Kulkarni H, Schorr-Neufing U, Niepsch K, Bitterlich N, et al. Lu-177-DOTA (0)-D-Phe(1)-Tyr(3)-Octreotide (Lu-177-DOTATOC) For Peptide Receptor Radiotherapy in Patients with Advanced Neuroendocrine Tumours: A Phase-II Study. Theranostics 2016;6:501-10.

[113] Baum RP, Kulkarni HR, Schuchardt C, Singh A, Wirtz M, Wiessalla S, et al. Lu-177-Labeled Prostate-Specific Membrane Antigen Radioligand Therapy of Metastatic Castration-Resistant Prostate Cancer: Safety and Efficacy. Journal of Nuclear Medicine 2016;57:1006-13.

[114] Kratochwil C, Giesel FL, Eder M, Afshar-Oromieh A, Benesova M, Mier W, et al. Lu-177 Lutetium-labelled PSMA ligand-induced remission in a patient with metastatic prostate cancer. European Journal of Nuclear Medicine and Molecular Imaging 2015;42:987-8.

[115] Kratochwil C, Giesel FL, Stefanova M, Benešová M, Bronzel M, Afshar-Oromieh A, et al. PSMA-Targeted Radionuclide Therapy of Metastatic Castration-Resistant Prostate Cancer with 177Lu-Labeled PSMA-617. Journal of Nuclear Medicine 2016;57:1170-6.

[116] Rahbar K, Schmidt M, Heinzel A, Eppard E, Bode A, Yordanova A, et al. Response and Tolerability of a Single Dose of 177Lu-PSMA-617 in Patients with Metastatic Castration-Resistant Prostate Cancer: A Multicenter Retrospective Analysis. Journal of Nuclear Medicine 2016;57:1334-8.

[117] Muselaers CHJ, Boers-Sonderen MJ, van Oostenbrugge TJ, Boerman OC, Desar IME, Stillebroer AB, et al. Phase 2 Study of Lutetium 177-Labeled Anti-Carbonic Anhydrase IX Monoclonal Antibody Girentuximab in Patients with Advanced Renal Cell Carcinoma. European Urology 2016;69:767-70.

[118] Herrmann K, Schottelius M, Lapa C, Osl T, Poschenrieder A, Hanscheid H, et al. First-in-Human Experience of CXCR4-Directed Endoradiotherapy with Lu-177- and Y-90-Labeled Pentixather in Advanced-Stage Multiple Myeloma with Extensive Intra- and Extramedullary Disease. Journal of Nuclear Medicine 2016;57:248-51.

[119] DuBois SG, Chesler L, Groshen S, Hawkins R, Goodarzian F, Shimada H, et al. Phase I Study of Vincristine, Irinotecan, and I-131-Metaiodobenzylguanidine for Patients with Relapsed or Refractory Neuroblastoma: A New Approaches to Neuroblastoma Therapy Trial. Clinical Cancer Research 2012;18:2679-86.

[120] DuBois SG, Groshen S, Park JR, Haas-Kogan DA, Yang XD, Geier E, et al. Phase I Study of Vorinostat as a Radiation Sensitizer with I-131-Metaiodobenzylguanidine (I-131-MIBG) for Patients with Relapsed or Refractory Neuroblastoma. Clinical Cancer Research 2015;21:2715-21.

[121] French S, DuBois SG, Horn B, Granger M, Hawkins R, Pass A, et al. I-131-MIBG followed by consolidation with busulfan, melphalan and autologous stem cell transplantation for refractory neuroblastoma. Pediatric Blood & Cancer 2013;60:879-84.

[122] Matthay KK, Weiss B, Villablanca JG, Maris JM, Yanik GA, DuBois SG, et al. Dose Escalation Study of No-Carrier-Added I-131-Metaiodobenzylguanidine for Relapsed or Refractory Neuroblastoma: New Approaches to Neuroblastoma Therapy Consortium Trial. Journal of Nuclear Medicine 2012;53:1155-63.

[123] Polishchuk AL, DuBois SG, Haas-Kogan D, Hawkins R, and Matthay KK. Response, Survival, and Toxicity After Iodine-131-Metaiodobenzylguanidine Therapy for Neuroblastoma in Preadolescents, Adolescents, and Adults. Cancer 2011;117:4286-93.

[124] Yanik GA, Villablanca JG, Mans JM, Weiss B, Groshen S, Marachelian A, et al. I-131-Metaiodobenzylguanidine with Intensive Chemotherapy and Autologous Stem Cell Transplantation for High-Risk Neuroblastoma. A New Approaches to Neuroblastoma Therapy (NANT) Phase II Study. Biology of Blood and Marrow Transplantation 2015;21:673-81.

[125] Bollen G. FRIB - Facility for Rare Isotope Beams. 5th International Symposium on Exotic Nuclei. Sochi, Russia; AIP Conference Proceedings 2010; 1224, 432-41.

[126] Ronningen R. Isotope Inventories in Cooling Loop. 2012. http://meetings.nscl.msu.edu/IsotopeWorkshop2012/Presentations/Ronningen/48Ca_560AMeV_water_1y_activities.txt

[127] Mamtimin M, Harmon F, and Starovoitova VN. Sc-47 production from titanium targets using electron linacs. Applied Radiation and Isotopes 2015;102:1-4.

[128] Rane S, Harris JT, and Starovoitova VN. Ca-47 production for Ca-47/Sc-47 generator system using electron linacs. Applied Radiation and Isotopes 2015;97:188-92.

[129] Starovoitova VN, Cole PL, and Grimm TL. Accelerator-based photoproduction of promising beta-emitters Cu-67 and Sc-47. Journal of Radioanalytical and Nuclear Chemistry 2015;305:127-32.

[130] Mausner LF, Kolsky KL, Joshi V, and Srivastava SC. Radionuclide development at BNL for nuclear medicine therapy. Applied Radiation and Isotopes 1998;49:285-94.

[131] Koning AJ and Rochman D. Modern Nuclear Data Evaluation with the TALYS Code System. Nuclear Data Sheets 2012;113:2841-934.

[132] Pietrelli L, Mausner LF, and Kolsky KL. Separation of carrier-free Sc-47 from titanium targets. Journal of Radioanalytical and Nuclear Chemistry-Articles 1992;157:335-45.

[133] Kolsky KL, Joshi V, Mausner LF, and Srivastava SC. Radiochemical purification of no-carrier-added scandium-47 for radioimmunotherapy. Applied Radiation and Isotopes 1998;49:1541-9.

[134] Rosch F, Qaim SM, and Stocklin G. Production of the positron emitting radioisotope Y-86 for nuclear medical application. Applied Radiation and Isotopes 1993;44:677-81.

[135] Stevens H, Jansen HML, De Reuck J, Lemmerling M, Strijckmans K, Goethals P, et al. ^{55}Co as a PET-tracer in stroke, compared with blood flow, oxygen metabolism, blood volume and gadolinium-MRI. Journal of the Neurological Sciences 1999;171:11-8.

[136] De Reuck J, Santens P, Keppens J, De Bleecker J, Strijckmans K, Goethals P, et al. Cobalt-55 positron emission tomography in recurrent ischaemic stroke. Clinical Neurology and Neurosurgery 1999;101:15-8.

[137] De Reuck J, Paemeleire K, Santens P, Strijckmans K, and Lemahieu I. Cobalt-55 positron emission tomography in symptomatic atherosclerotic carotid artery disease: borderzone versus territorial infarcts. Clinical Neurology and Neurosurgery 2004;106:77-81.

[138] Jansen HML, Pruim J, Vandervliet AM, Paans AMJ, Hew JM, Franssen EJF, et al. Visualization of damaged brain-tissue after ischemic stroke with cobalt-55 positron emission tomography. Journal of Nuclear Medicine 1994;35:456-60.

[139] Jansen HML, Willemsen ATM, Sinnige LGF, Paans AMJ, Hew JM, Franssen EJF, et al. Cobalt-55 positron emission tomography in relapsing-progressive multiple-sclerosis. Journal of the Neurological Sciences 1995;132:139-45.

[140] Jansen HML, vanderNaalt J, vanZomeren AH, Paans AMJ, VeenmavanderDuin L, Hew JM, et al. Cobalt-55 positron emission tomography in traumatic brain injury: A pilot study. Journal of Neurology Neurosurgery and Psychiatry 1996;60:221-4.

[141] Jansen HML, Paans AMJ, Vliet AMV, VeenmavanderDuin L, BolwijnMeijer CJW, Pruim J, et al. Cobalt-55 positron emission tomography in ischemic stroke. Clinical Neurology and Neurosurgery 1997;99:6-10.

[142] Jansen HM, Dierckx RA, Hew JM, Paans AM, Minderhoud JM, and Korf J. Positron emission tomography in primary brain tumours using cobalt-55. Nuclear Medicine Communications 1997;18:734-40.

[143] Korf J, Veenma-van der Duin L, Brinkman-Medema R, Niemarkt A, and de Leij L. Divalent cobalt as a label to study lymphocyte distribution using PET and SPECT. Journal of Nuclear Medicine 1998;39:836-41.

[144] Srivastava SC, Mausner LF, Kolsky KL, Mease RC, Joshi V, Meinken GE, et al. Production and use of cobalt-55 as an antibody label for PET imaging. Journal of Labelled Compounds and Radiopharmaceuticals 1994;35:389-91.

[145] Thisgaard H, Olesen ML, and Dam JH. Radiosynthesis of Co-55- and Co-58m-labelled DOTATOC for positron emission tomography imaging and targeted radionuclide therapy. Journal of Labelled Compounds & Radiopharmaceuticals 2011;54:758-62.

[146] Mastren T, Marquez BV, Sultan DE, Bollinger E, Eisenbeis P, Voller T, et al. Cyclotron Production of High-Specific Activity ^{55}Co and In Vivo Evaluation of the Stability of ^{55}Co Metal-Chelate-Peptide Complexes. Molecular imaging 2015;14:11-22.

[147] Dam JH, Olsen BB, Baun C, Hoilund-Carlsen PF, and Thisgaard H. In Vivo Evaluation of a Bombesin Analogue Labeled with Ga-68 and Co-55/57. Molecular Imaging and Biology 2016;18:368-76.

[148] Wallberg H, Ahlgren S, Widstrom C, and Orlova A. Evaluation of the Radiocobalt-Labeled MMA-DOTA-Cys(61) -Z(HER2:2395)-Cys Affibody Molecule for Targeting of HER2-Expressing Tumors. Molecular Imaging and Biology 2010;12:54-62.

[149] Regoeczi E, Bolyos M, and Nieboer E. Cobalt(III)-transferrin - Production and some of its properties. Analyst 1995;120:733-6.

[150] Wegner SV and Spatz JP. Cobalt(III) as a Stable and Inert Mediator Ion between NTA and His6-Tagged Proteins. Angewandte Chemie-International Edition 2013;52:7593-6.

[151] Duckworth OW, Bargar JR, Jarzecki AA, Oyerinde O, Spiro TG, and Sposito G. The exceptionally stable cobalt(III)-desferrioxamine B complex. Marine Chemistry 2009;113:114-22.

[152] Gramsbergen JBP, Veenmavanderduin L, Loopuijt L, Paans AMJ, Vaalburg W, and Korf J. Imaging of the degeneration of neurons and their processes in rat or cat brain by ($CaCl_2$)-Ca-45 autoradiography or ($CoCl_2$)-Co-55 positron emission tomography. Journal of Neurochemistry 1988;50:1798-807.

[153] Goethals P, Volkaert A, Vandewielle C, Dierckx R, and Lameire N. Co-55-EDTA for renal imaging using positron emission tomography (PET): A feasibility study. Nuclear Medicine and Biology 2000;27:77-81.

[154] Chantler C, Garnett ES, Parsons V, and Veall N. Glomerular filtration rate measurement in man by single injection method using ^{51}Cr-EDTA. Clinical Science 1969;37:169-&.

[155] Thisgaard H, Olesen ML, and Dam JH. Radiosynthesis of Co-55- and Co-58m-labelled DOTATOC for positron emission tomography imaging and targeted radionuclide therapy. Journal of Labelled Compounds & Radiopharmaceuticals 2011;54:758-62.

[156] Heppeler A, Andre JP, Buschmann I, Wang X, Reubi J-C, Hennig M, et al. Metal-ion-dependent biological properties of a chelator-derived somatostatin analogue for tumour targeting. Chemistry-a European Journal 2008;14:3026-34.

[157] Collins DA, Hogenkamp HPC, O'Connor MK, Naylor S, Benson LM, Hardyman TJ, et al. Biodistribution of radiolabeled adenosylcobalamin in patients diagnosed with various malignancies. Mayo Clinic Proceedings 2000;75:568-80.

[158] Waibel R, Treichler H, Schaefer NG, van Staveren DR, Mundwiler S, Kunze S, et al. New derivatives of vitamin B12 show preferential targeting of tumors. Cancer Research 2008;68:2904-11.

[159] Spellerberg S, Reimer P, Blessing G, Coenen HH, and Qaim SM. Production of ^{55}Co and ^{57}Co via proton induced reactions on highly enriched ^{58}Ni. Applied Radiation and Isotopes 1998;49:1519-22.

[160] Zaman MR and Qaim SM. Excitation functions of (d,n) and (d,alpha) reactions on Fe-54: Relevance to the production of high purity Co-55 at a small cyclotron. Radiochimica Acta 1996;75:59-63.

[161] Zaman MR, Spellerberg S, and Qaim SM. Production of Co-55 via the Fe-54(d, n)-process and excitation functions of Fe-54(d, t)Fe-53 and Fe-54(d, alpha)Mn-52m reactions from threshold up to 13.8 MeV. Radiochimica Acta 2003;91:105-8.

[162] Sharma H, Zweit J, Smith AM, and Downey S. Production of cobalt-55, a short-lived, positron emitting radiolabel for bleomycin. Applied Radiation and Isotopes 1986;37:105-9.

[163] Neirinckx RD. Cyclotron production of Ni-57 and Co-55 and synthesis of their bleomycin complexes. International Journal of Applied Radiation and Isotopes 1977;28:561-2.

[164] Lagunassolar MC and Jungerman JA. Cyclotron production of carrier-free cobalt-55, a new positron-emitting label for bleomycin. International Journal of Applied Radiation and Isotopes 1979;30:25-32.

[165] Avrigeanu M, Avrigeanu V, Bem P, Fischer U, Honusek M, Katovsky K, et al. Low energy deuteron-induced reactions on Fe isotopes. Physical Review C 2014;89.

[166] Khandaker MU, Kim K, Lee M, Kim KS, and Kim G. Excitation functions of (p,x) reactions on natural nickel up to 40 MeV. Nuclear Instruments & Methods in Physics Research Section B-Beam Interactions with Materials and Atoms 2011;269:1140-9.

[167] Holland JP, Sheh Y, and Lewis JS. Standardized methods for the production of high specific-activity zirconium-89. Nuclear Medicine and Biology 2009;36:729-39.

[168] Gagnon K, Severin GW, Barnhart TE, Engle JW, Valdovinos HF, and Nickles RJ. Ti-45 Extraction Using Hydroxamate Resin. 14th International Workshop on Targetry and Target Chemistry; Mexico; AIP Conference Proceedings 2012;1509:211-4.

[169] Valdovinos HF, Hernandez R, Barnhart TE, Graves S, Cai W, and Nickles RJ. Separation of cyclotron-produced Sc-44 from a natural calcium target using a dipentyl pentylphosphonate functionalized extraction resin. Applied Radiation and Isotopes 2015;95:23-9.

[170] Nesaraja CD, Geraedts SD, and Singh B. Nuclear Data Sheets for A=58. Nuclear Data Sheets 2010;111:897-1091.

[171] Chu SY, Ekström LP, and Firestone RB. The Lund/LBNL Nuclear Data Search. 1999. http://nucleardata.nuclear.lu.se/toi/xray.asp?act=list&el=Co

[172] Humm JL, Howell RW, and Rao DV. Dosimetry of Auger-electron-emitting radionuclides - Report No 3 of AAPM Nuclear-Medicine Task Group No 6. Medical Physics 1994;21:1901-15.

[173] Kassis AI, Sastry KSR, and Adelstein SJ. Kinetics of uptake, retention, and radiotoxicity of I-125 UdR in mammalian-cells - Implications of localized energy deposition by Auger processes. Radiation Research 1987;109:78-89.

[174] Pouget J-P, Santoro L, Raymond L, Chouin N, Bardies M, Bascoul-Mollevi C, et al. Cell membrane is a more sensitive target than cytoplasm to dense ionization produced by auger electrons. Radiation Research 2008;170:192-200.

[175] Kennel SJ, Boll R, Stabin M, Schuller HM, and Mirzadeh S. Radioimmunotherapy of micrometastases in lung with vascular targeted Bi-213. British Journal of Cancer 1999;80:175-84.

[176] Seon BK, Haba A, Matsuno F, Takahashi N, Tsujie M, She X, et al. Endoglin-Targeted Cancer Therapy. Current Drug Delivery 2011;8:135-43.

[177] Matsuno F, Haruta Y, Kondo M, Tsai H, Barcos M, and Seon BK. Induction of lasting complete regression of preformed distinct solid tumors by targeting the tumor vasculature using two new anti-endoglin monoclonal antibodies. Clinical Cancer Research 1999;5:371-82.

[178] Tabata M, Kondo M, Haruta Y, and Seon BK. Antiangiogenic radioimmunotherapy of human solid tumors in SCID mice using I-125-labeled anti-endoglin monoclonal antibodies. International Journal of Cancer 1999;82:737-42.

[179] Bernhardt P, Forssell-Aronsson E, Jacobsson L, and Skarnemark G. Low-energy electron emitters for targeted radiotherapy of small tumours. Acta Oncologica 2001;40:602-8.

[180] Uusijarvi H, Bernhardt P, Ericsson T, and Forssell-Aronsson E. Dosimetric characterization of radionuclides for systemic tumor therapy: Influence of particle range, photon emission, and subcellular distribution. Medical Physics 2006;33:3260-9.

[181] Thisgaard H, Elema DR, and Jensen M. Production and dosimetric aspects of the potent Auger emitter Co-58m for targeted radionuclide therapy of small tumors. Medical Physics 2011;38:4535-41.

[182] Thisgaard H, Olsen BB, Dam JH, Bollen P, Mollenhauer J, and Hoilund-Carlsen PF. Evaluation of Cobalt-Labeled Octreotide Analogs for Molecular Imaging and Auger Electron-Based Radionuclide Therapy. Journal of Nuclear Medicine 2014;55:1311-6.

[183] Sudar S and Qaim SM. Isomeric cross-section ratio for the formation of Co-58(m,g) in neutron, proton, deuteron, and alpha-particle induced reactions in the energy region up to 25 MeV. Physical Review C 1996;53:2885-92.

[184] Ziegler JF, Ziegler MD, and Biersack JP. SRIM - The stopping and range of ions in matter (2010). Nuclear Instruments & Methods in Physics Research Section B-Beam Interactions with Materials and Atoms 2010;268:1818-23.

[185] Sudar S and Qaim SM. Excitation-functions of proton and deuteron induced reactions on iron and alpha-particle induced reactions on manganese in the energy region up to 25-MeV. Physical Review C 1994;50:2408-19.

[186] Vosburgh GJ, Flexner LB, and Cowie DB. The determination of radioactive iron in biological material with particular reference to purification and separation of iron with isopropyl ether, ashing and electroplating technique, and accuracy of the method. J Biol Chem 1948;175:391-404.

[187] Piel H, Qaim SM, and Stocklin G. Excitation-functions of (p,xn)-reactions on Ni-nat and highly enriched Ni-62 - Possibility of production of medically important radioisotope Cu-62 at a small cyclotron. Radiochimica Acta 1992;57:1-5.

[188] McCarthy DW, Shefer RE, Klinkowstein RE, Bass LA, Margeneau WH, Cutler CS, et al. Efficient production of high specific activity Cu-64 using a biomedical cyclotron. Nuclear Medicine and Biology 1997;24:35-43.

[189] Avila-Rodriguez MA, Nye JA, and Nickles RJ. Simultaneous production of high specific activity Cu-64 and Co-61 with 11.4 MeV protons on enriched Ni-64 nuclei. Applied Radiation and Isotopes 2007;65:1115-20.

[190] Kraus KA and F. N. Anion Exchange Studies of the Fission Products. In: United Nations editor. International Conference on the Peaceful Uses of Atomic Energy. Geneva; 1955, p. 118.

[191] Pietrzyk DJ. Anion exchange separations of metal ions in partially nonaqueous solutions. Chemistry. Ames, Iowa: Iowa State University of Science and Technology; 1960, p. 117.

[192] Pourmand A and Dauphas N. Distribution coefficients of 60 elements on TODGA resin: Application to Ca, Lu, Hf, U and Th isotope geochemistry. Talanta 2010;81:741-53.

[193] Junde H. Nuclear data sheets for A=55. Nuclear Data Sheets 2008;109:787-+.

[194] Le Loirec C and Champion C. Track structure simulation for positron emitters of physical interest. Part II: The case of the radiometals. Nuclear Instruments & Methods in Physics Research Section A-Accelerators Spectrometers Detectors and Associated Equipment 2007;582:654-64.

[195] Sihver W, Pietzsch J, Krause M, Baumann M, Steinbach J, and Pietzsch H-J. Radiolabeled Cetuximab Conjugates for EGFR Targeted Cancer Diagnostics and Therapy. Pharmaceuticals (Basel, Switzerland) 2014;7:311-38.

[196] Hong H, Yang Y, Zhang Y, Engle JW, Barnhart TE, Nickles RJ, et al. Positron emission tomography imaging of CD105 expression during tumor angiogenesis. European Journal of Nuclear Medicine and Molecular Imaging 2011;38:1335-43.

[197] Zhang Y, Hong H, Engle JW, Bean J, Yang Y, Leigh BR, et al. Positron Emission Tomography Imaging of CD105 Expression with a Cu-64-Labeled Monoclonal Antibody: NOTA Is Superior to DOTA. Plos One 2011;6.

[198] Hong H, Severin G, Yang Y, Engle J, Zhang Y, Barnhart T, et al. Positron emission tomography imaging of CD105 expression with Zr-89-Df-TRC105. European Journal of Nuclear Medicine and Molecular Imaging 2012;39:138-48.

[199] Engle JW, Hong H, Zhang Y, Valdovinos HF, Myklejord DV, Barnhart TE, et al. Positron Emission Tomography Imaging of Tumor Angiogenesis with a Ga-66-Labeled Monoclonal Antibody. Molecular Pharmaceutics 2012;9:1441-8.

[200] Graves SA, Hernandez R, Fonslet J, England CG, Valdovinos HF, Ellison PA, et al. Novel Preparation Methods of Mn-52 for ImmunoPET Imaging. Bioconjugate Chemistry 2015;26:2118-24.

[201] Burrows FJ, Derbyshire EJ, Tazzari PL, Amlot P, Gazdar AF, King SW, et al. Up-regulation of endoglin on vascular endothelial cells in human solid tumors: Implications for diagnosis and therapy. Clinical Cancer Research 1995;1:1623-34.

[202] Fonsatti E, Nicolay HJM, Altomonte M, Covre A, and Maio M. Targeting cancer vasculature via endoglin/CD105: a novel antibody-based diagnostic and therapeutic strategy in solid tumours. Cardiovascular Research 2010;86:12-9.

[203] Jansen HML, Knollema S, vanderDuin LV, Willemsen ATM, Wiersma A, Franssen EJF, et al. Pharmacokinetics and dosimetry of cobalt-55 and cobalt-57. Journal of Nuclear Medicine 1996;37:2082-6.

[204] Stabin MG, Siegel JA, Sparks RB, Eckerman KF, and Breit HB. Contribution to red marrow absorbed dose from total body activity: A correction to the MIRD method. Journal of Nuclear Medicine 2001;42:492-8.

[205] Bouchet LG and Bolch WE. A three-dimensional transport model for determining absorbed fractions of energy for electrons within cortical bone. Journal of Nuclear Medicine 1999;40:2115-24.

[206] Bouchet LG, Jokisch DW, and Bolch WE. A three-dimensional transport model for determining absorbed fractions of energy for electrons within trabecular bone. Journal of Nuclear Medicine 1999;40:1947-66.

[207] Behr TM, Sgouros G, Vougioukas V, Memtsoudis S, Gratz S, Schmidberger H, et al. Therapeutic efficacy and dose-limiting toxicity of auger-electron vs. beta emitters in radioimmunotherapy with internalizing antibodies: Evaluation of I-125- vs I-131-labeled CO17-1A in a human colorectal cancer model. International Journal of Cancer 1998;76:738-48.

[208] Behr TM, Sgouros G, Stabin MG, Behe M, Angerstein C, Blumenthal RD, et al. Studies on the red marrow dosimetry in radioimmunotherapy: An experimental investigation of factors influencing the radiation-induced myelotoxicity in therapy with beta-, Auger/conversion electron-, or alpha-emitters. Clinical Cancer Research 1999;5:3031S-43S.

[209] Howell RW, Narra VR, Sastry KSR, and Rao DV. On the equivalent dose for Auger-electron emitters. Radiation Research 1993;134:71-8.

[210] Rosen LS, Gordon MS, Robert F, and Matei DE. Endoglin for Targeted Cancer Treatment. Current Oncology Reports 2014;16.

[211] Reddy S and Robinson MK. Immuno-Positron Emission Tomography in Cancer Models. Seminars in Nuclear Medicine 2010;40:182-9.

[212] Zhou Y, Baidoo KE, and Brechbiel MW. Mapping biological behaviors by application of longer-lived positron emitting radionuclides. Advanced Drug Delivery Reviews 2013;65:1098-111.

[213] Shih LB, Thorpe SR, Griffiths GL, Diril H, Ong GL, Hansen HJ, et al. The processing and fate of antibodies and their radiolabels bound to the surface of tumor-cells in-vitro - A comparison of 9 radiolabels. Journal of Nuclear Medicine 1994;35:899-908.

[214] Stabin MG, Kooij PPM, Bakker WH, Inoue T, Endo K, Coveney J, et al. Radiation dosimetry for indium-111-pentetreotide. Journal of Nuclear Medicine 1997;38:1919-22.

[215] Goldsmith SJ. Radioimmunotherapy of Lymphoma: Bexxar and Zevalin. Seminars in Nuclear Medicine 2010;40:122-35.

[216] Kratochwil C, Giesel FL, Stefanova M, Benesova M, Bronzel M, Afshar-Oromieh A, et al. PSMA-Targeted Radionuclide Therapy of Metastatic Castration-Resistant Prostate Cancer with Lu-177-Labeled PSMA-617. Journal of Nuclear Medicine 2016;57:1170-6.

[217] Wiseman GA, White CA, Sparks RB, Erwin WD, Podoloff DA, Lamonica D, et al. Biodistribution and dosimetry results from a phase III prospectively randomized controlled trial of Zevalin (TM) radioimmunotherapy for low-grade, follicular, or transformed B-cell non-Hodgkin's lymphoma. Critical Reviews in Oncology Hematology 2001;39:181-94.

[218] Afshar-Oromieh A, Avtzi E, Giesel FL, Holland-Letz T, Linhart HG, Eder M, et al. The diagnostic value of PET/CT imaging with the Ga-68-labelled PSMA ligand HBED-CC in the diagnosis of recurrent prostate cancer. European Journal of Nuclear Medicine and Molecular Imaging 2015;42:197-209.

[219] Martinho M and Münck E. 57Fe Mössbauer Spectroscopy in Chemistry and Biology. Physical Inorganic Chemistry: John Wiley & Sons, Inc.; 2010, p. 39-67.

[220] McCarthy DW, Bass LA, Cutler PD, Shefer RE, Klinkowstein RE, Herrero P, et al. High purity production and potential applications of copper-60 and copper-61. Nuclear Medicine and Biology 1999;26:351-8.

[221] Szajek LP, Meyer W, Plascjak P, and Eckelman WC. Semi-remote production of Cu-64 $CuCl_2$ and preparation of high specific activity Cu-64 Cu-ATSM for PET studies. Radiochimica Acta 2005;93:239-44.

[222] Alliot C, Michel N, Bonraisin AC, Bosse V, Laize J, Bourdeau C, et al. One step purification process for no-carrier-added Cu-64 produced using enriched nickel target. Radiochimica Acta 2011;99:627-30.

[223] Ohya T, Nagatsu K, Suzuki H, Fukada M, Minegishi K, Hanyu M, et al. Efficient preparation of high-quality 64Cu for routine use. Nuclear Medicine and Biology 2016;43:685-91.

[224] Garmestani K, Milenic DE, Plascjak PS, and Brechbiel MW. A new and convenient method for purification of ^{86}Y using a Sr(II) selective resin and comparison of biodistribution of ^{86}Y and ^{111}In labeled Herceptin (TM). Nuclear Medicine and Biology 2002;29:599-606.

[225] Park LS, Szajek LP, Wong KJ, Plascjak PS, Garmestani K, Googins S, et al. Semi-automated ^{86}Y purification using a three-column system. Nuclear Medicine and Biology 2004;31:297-301.

[226] Avila-Rodriguez MA, Nye JA, and Nickles RJ. Production and separation of non-carrier-added ^{86}Y from enriched ^{86}Sr targets. Applied Radiation and Isotopes 2008;66:9-13.

[227] Herzog H, Rosch F, Stocklin G, Lueders C, Qaim SM, and Feinendegen LE. Measurement of pharmacokinetics of yttrium-86 radiopharmaceuticals with PET and radiation-dose calculation of analogous Y-90 radiotherapeutics. Journal of Nuclear Medicine 1993;34:2222-6.

[228] Beyer GJ, Bergmann R, Kampf G, Mading P, and Rosch F. Simultaneous study of the biodistribution of radio-yttrium complexed with EDTMP and citrate ligands in tumor-bearing rats. Nuclear Medicine and Biology 1992;19:201-3.

[229] Rosch F, Herzog H, Plag C, Neumaier B, Braun U, MullerGartner HW, et al. Radiation doses of yttrium-90 citrate and yttrium-90 EDTMP as determined via analogous yttrium-86 complexes and positron emission tomography. European Journal of Nuclear Medicine 1996;23:958-66.

[230] Kutzner J, Hahn K, Grimm W, Rosler HP, Eckmann A, and Bender S. Y-90-citrate for pain-therapy by bone metastases. Nuc Compact-European-American Communications in Nuclear Medicine 1990;21:128-32.

[231] Davies AJ. Radioimmunotherapy for B-cell lymphoma: Y-90 ibritumomab tiuxetan and I-131 tositumomab. Oncogene 2007;26:3614-28.

[232] Rizzieri D. Zevalin (R) (ibritumomab tiuxetan): After more than a decade of treatment experience, what have we learned? Critical Reviews in Oncology Hematology 2016;105:5-17.

[233] Cremonesi M, Chiesa C, Strigari L, Ferrari M, Botta F, Guerriero F, et al. Radioembolization of Hepatic Lesions from a Radiobiology and Dosimetric Perspective. Frontiers in Oncology 2014;4:210.

[234] Adam Rebeles R, Van den Winkel P, Hermanne A, and Tárkányi F. New measurement and evaluation of the excitation function of ^{64}Ni(p,n) reaction for the production of ^{64}Cu. Nuclear Instruments and Methods in Physics Research Section B: Beam Interactions with Materials and Atoms 2009;267:457-61.

[235] Qaim SM, Uhl M, Rosch F, and Szelecsenyi F. Excitation-functions of (p,alpha)-reactions on Ni-64, Kr-78, and Sr-86. Physical Review C 1995;52:733-9.

[236] Takacs S, Sonck M, Azzam A, Hermanne A, and Tarkanyi F. Activation cross section measurements of deuteron induced reactions on Ni-nat with special reference to beam monitoring and production of Cu-61 for medical purpose. Radiochimica Acta 1997;76:15-24.

[237] Takacs S, Szelecsenyi F, Tarkanyi F, Sonck M, Hermanne A, Shubin Y, et al. New cross-sections and intercomparison of deuteron monitor reactions on Al, Ti, Fe, Ni and Cu. Nuclear Instruments & Methods in Physics Research Section B-Beam Interactions with Materials and Atoms 2001;174:235-58.

[238] Usman AR, Khandaker MU, Haba H, Murakami M, and Otuka N. Measurements of deuteron-induced reaction cross-sections on natural nickel up to 24 MeV. Nuclear Instruments & Methods in Physics Research Section B-Beam Interactions with Materials and Atoms 2016;368:112-9.

[239] Szelagowski H, Arvanitidis I, and Seetharaman S. Effective thermal conductivity of porous strontium oxide and strontium carbonate samples. Journal of Applied Physics 1999;85:193-8.

[240] Arvanitidis I, Du SC, Sohn HY, and Seetharaman S. The intrinsic thermal decomposition kinetics of $SrCO_3$ by a nonisothermal technique. Metallurgical and Materials Transactions B-Process Metallurgy and Materials Processing Science 1997;28:1063-8.

[241] Rosch F, Qaim SM, and Stocklin G. Nuclear-data relevant to the production of the positron emitting radioisotope Y-86 via the Sr-86(p,n)-processes and ^{nat}Rb(He-3,xn)-processes. Radiochimica Acta 1993;61:1-8.

[242] Avila-Rodriguez MA. Low energy cyclotron production of multivalent transition metals for PET imaging and therapy. University of Wisconsin-Madison PhD dissertation. 2007.

[243] Singh B. Nuclear data sheets for A=64. Nuclear Data Sheets 2007;108:197-+.

[244] Negret A and Singh B. Nuclear Data Sheets for A=86. Nuclear Data Sheets 2015;124:1-156.

[245] Yoo J, Tang L, Perkins TA, Rowland DJ, Laforest R, Lewis JS, et al. Preparation of high specific activity ^{86}Y using a small biomedical cyclotron. Nuclear Medicine and Biology 2005;32:891-7.

[246] Thieme S, Walther M, Pietzsch HJ, Henniger J, Preusche S, Mading P, et al. Module-assisted preparation of Cu-64 with high specific activity. Applied Radiation and Isotopes 2012;70:602-8.

[247] Bradshaw TJ, Bowen SR, Jallow N, Forrest LJ, and Jeraj R. Heterogeneity in Intratumor Correlations of F-18-FDG, F-18-FLT, and Cu-61-ATSM PET in Canine Sinonasal Tumors. Journal of Nuclear Medicine 2013;54:1931-7.

[248] Reischl G, Rosch F, and Machulla HJ. Electrochemical separation and purification of yttrium-86. Radiochimica Acta 2002;90:225-8.

[249] Wu AM and Senter PD. Arming antibodies: prospects and challenges for immunoconjugates. Nature Biotechnology 2005;23:1137-46.

[250] Philpott GW, Schwarz SW, Anderson CJ, Dehdashti F, Connett JM, Zinn KR, et al. RadioimmunoPET - Detection of colorectal-carcinoma with positron-emitting copper-64-labeled monoclonal-antibody. Journal of Nuclear Medicine 1995;36:1818-24.

[251] Cutler PD, Schwarz SW, Anderson CJ, Connett JM, Welch MJ, Philpott GW, et al. Dosimetry of copper-64-labeled monoclonal-antibody 1A3 as determined by PET imaging of the torso. Journal of Nuclear Medicine 1995;36:2363-71.

[252] Thakur ML, Zhang K, Berger A, Cavanaugh B, Kim S, Channappa C, et al. VPAC1 Receptors for Imaging Breast Cancer: A Feasibility Study. Journal of Nuclear Medicine 2013;54:1019-25.

[253] Tripathi S, Trabulsi EJ, Gomella L, Kim S, McCue P, Intenzo C, et al. VPAC1 Targeted Cu-64-TP3805 Positron Emission Tomography Imaging of Prostate Cancer: Preliminary Evaluation in Man. Urology 2016;88:111-8.

[254] Mortimer JE, Bading JR, Colcher DM, Conti PS, Frankel PH, Carroll MI, et al. Functional Imaging of Human Epidermal Growth Factor Receptor 2-Positive Metastatic Breast Cancer Using Cu-64-DOTA-Trastuzumab PET. Journal of Nuclear Medicine 2014;55:23-9.

[255] Lockhart AC, Liu YJ, Dehdashti F, Laforest R, Picus J, Frye J, et al. Phase 1 Evaluation of Cu-64 DOTA-Patritumab to Assess Dosimetry, Apparent Receptor Occupancy, and Safety in Subjects with Advanced Solid Tumors. Molecular Imaging and Biology 2016;18:446-53.

[256] Forster GJ, Engelbach M, Brockmann J, Reber H, Buchholz HG, Macke HR, et al. Preliminary data on biodistribution and dosimetry for therapy planning of somatostatin receptor positive tumours: comparison of Y-86-DOTATOC and In-111-DTPA-octreotide. European Journal of Nuclear Medicine 2001;28:1743-50.

[257] Jamar F, Barone R, Mathieu I, Walrand S, Labar D, Carlier P, et al. Y-86-DOTA(0)-D-Phe(1)-Tyr(3)-octreotide (SMT487) - a phase 1 clinical study: pharmacokinetics, biodistribution and renal protective effect of different regimens of amino acid co-infusion. European Journal of Nuclear Medicine and Molecular Imaging 2003;30:510-8.

[258] Kemp BJ, Hruska CB, McFarland AR, Lenox MW, and Lowe VJ. NEMA NU 2-2007 performance measurements of the Siemens Inveon (TM) preclinical small animal PET system. Physics in Medicine and Biology 2009;54:2359-76.

[259] Hueting R, Kersemans V, Cornelissen B, Tredwell M, Hussien K, Christlieb M, et al. A Comparison of the Behavior of Cu-64-Acetate and Cu-64-ATSM In Vitro and In Vivo. Journal of Nuclear Medicine 2014;55:128-34.

[260] Chakravarty R, Chakraborty S, Vimalnath KV, Shetty P, Sarma HD, Hassan PA, et al. ($CuCl_2$)-Cu-64 produced by direct neutron activation route as a cost-effective probe for cancer imaging: the journey has begun. RSC Advances 2015;5:91723-33.

[261] Henderson ES and Lister TA. Leukemia, Philadelphia: Saunders,1996.

[262] Loke KSH, Padhy AK, Ng DCE, Goh ASW, and Divgi C. Dosimetric considerations in radioimmunotherapy and systemic radionuclide therapies: a review. World journal of nuclear medicine 2011;10:122-38.

[263] Boerjesson PKE, Jauw YWS, de Bree R, Roos JC, Castelijns JA, Leemans CR, et al. Radiation Dosimetry of Zr-89-Labeled Chimeric Monoclonal Antibody U36 as Used for Immuno-PET in Head and Neck Cancer Patients. Journal of Nuclear Medicine 2009;50:1828-36.

[264] Obata A, Kasamatsu S, McCarthy DW, Welch MJ, Saji H, Yonekura Y, et al. Production of therapeutic quantities of Cu-64 using a 12 MeV cyclotron. Nuclear Medicine and Biology 2003;30:535-9.

[265] Lewis JS, Laforest R, Dehdashti F, Grigsby PW, Welch MJ, and Siegel BA. An imaging comparison of Cu-64-ATSM and Cu-60-ATSM in cancer of the uterine cervix. Journal of Nuclear Medicine 2008;49:1177-82.

[266] Pfeifer A, Knigge U, Mortensen J, Oturai P, Berthelsen AK, Loft A, et al. Clinical PET of Neuroendocrine Tumors Using Cu-64-DOTATATE: First-in-Humans Study. Journal of Nuclear Medicine 2012;53:1207-15.

[267] Pfeifer A, Knigge U, Binderup T, Mortensen J, Oturai P, Loft A, et al. Cu-64-DOTATATE PET for Neuroendocrine Tumors: A Prospective Head-to-Head Comparison with In-111-DTPA-Octreotide in 112 Patients. Journal of Nuclear Medicine 2015;56:847-54.

[268] Malmberg C, Ripa RS, Johnbeck CB, Knigge U, Langer SW, Mortensen J, et al. Cu-64-DOTATATE for Noninvasive Assessment of Atherosclerosis in Large Arteries and Its Correlation with Risk Factors: Head-to-Head Comparison with Ga-68-DOTATOC in 60 Patients. Journal of Nuclear Medicine 2015;56:1895-900.

[269] Helisch A, Forster GJ, Reber H, Buchholz HG, Arnold R, Goke B, et al. Pre-therapeutic dosimetry and biodistribution of Y-86-DOTA-Phe(1)-Tyr(3)-octreotide versus In-111-pentetreotide in patients with advanced neuroendocrine tumours. European Journal of Nuclear Medicine and Molecular Imaging 2004;31:1386-92.

[270] Walrand S, Flux GD, Konijnenberg MW, Valkema R, Krenning EP, Lhommel R, et al. Dosimetry of yttrium-labelled radiopharmaceuticals for internal therapy: Y-86 or Y-90 imaging? European Journal of Nuclear Medicine and Molecular Imaging 2011;38:57-68.

[271] Lewis JS, Herrero P, Sharp TL, Engelbach JA, Fujibayashi Y, Laforest R, et al. Delineation of hypoxia in canine myocardium using PET and copper(II)-diacetyl-bis(N-4-methylthiosemicarbazone). Journal of Nuclear Medicine 2002;43:1557-69.

[272] Zuber K and Singh B. Nuclear Data Sheets for A=61. Nuclear Data Sheets 2015;125:1-200.

[273] Mirzadeh S and Lambrecht RM. Radiochemistry of germanium. Journal of Radioanalytical and Nuclear Chemistry-Articles 1996;202:7-102.

[274] Kennel SJ and Mirzadeh S. Vascular targeting for radioimmunotherapy with Bi-213. Radiochimica Acta 1997;79:87-91.

[275] Park H-J and Tavlarides LL. Germanium(IV) Adsorption from Aqueous Solution Using a Kelex-100 Functional Adsorbent. Industrial & Engineering Chemistry Research 2009;48:4014-21.

[276] Neirinckx RD and Davis MA. Potential column chromatography generators for ionic Ga-68 .1. Inorganic substrates. Journal of Nuclear Medicine 1979;20:1075-9.

[277] Roesch F and Riss PJ. The Renaissance of the Ge-68/Ga-68 Radionuclide Generator Initiates New Developments in Ga-68 Radiopharmaceutical Chemistry. Current Topics in Medicinal Chemistry 2010;10:1633-68.

[278] Chakravarty R, Shukla R, Ram R, Tyagi AK, Dash A, and Venkatesh M. Development of a nano-zirconia based Ge-68/Ga-68 generator for biomedical applications. Nuclear Medicine and Biology 2011;38:575-83.

[279] Chakravarty R and Dash A. Role of Nanoporous Materials in Radiochemical Separations for Biomedical Applications. Journal of Nanoscience and Nanotechnology 2013;13:2431-50.

[280] Chakravarty R, Chakraborty S, Ram R, Dash A, and Pillai MRA. Long-Term Evaluation of 'BARC Ge-68/Ga-68 Generator' Based on the Nanoceria-Polyacrylonitrile Composite Sorbent. Cancer Biotherapy and Radiopharmaceuticals 2013;28:631-7.

[281] Guo J, Yang WL, and Wang CC. Magnetic Colloidal Supraparticles: Design, Fabrication and Biomedical Applications. Advanced Materials 2013;25:5196-214.

[282] Hao R, Xing R, Xu Z, Hou Y, Gao S, and Sun S. Synthesis, Functionalization, and Biomedical Applications of Multifunctional Magnetic Nanoparticles. Advanced Materials 2010;22:2729-42.

[283] Afaq A, Syed R, and Bomanji J. PET/MRI: a new technology in the field of molecular imaging. British Medical Bulletin 2013;108:159-71.

[284] Takacs S, Tarkanyi F, Hermanne A, and de Corcuera RP. Validation and upgrading of the recommended cross section data of charged particle reactions used for production of PET radioisotopes. Nuclear Instruments & Methods in Physics Research Section B-Beam Interactions with Materials and Atoms 2003;211:169-89.

[285] Johnson CH, Trail CC, and Galonsky A. Thresholds for (p, n) reactions on 26 intermediate-weight nuclei. Physical Review 1964;136:B1719-B29.

[286] National Nuclear Data Center. Q-value calculator. Brookhaven National Laboratory. http://www.nndc.bnl.gov/qcalc/

[287] Rostoker W. Embrittlement by liquid metals, New York: Reinhold Pub. Corp.,1960.

[288] Westwood AR, Preece CM, and Kamdar MH. Application of a crack propagation criterion to liquid-metal embrittlement - Cleavage of aluminum monocrystals in liquid gallium. ASM Transactions Quarterly 1967;60:723-&.

[289] Arzumanov AA, Alexandrenko VV, Borisenko AR, Ignatenko DN, Koptev VK, Lyssukhin SN, et al. Technique for irradiation of Nb-Ga targets at Kazakhstan isochronous cyclotron. Cyclotrons and their applications 2004 Proceedings of the seventeenth international conference. Japan; 2005, p. 707.

[290] Meinken GE, Kurczak S, Mausner LF, Kolsky KL, and Srivastava SC. Production of high specific activity 68Ge at Brookhaven National Laboratory. Journal of Radioanalytical and Nuclear Chemistry 2005;263:553-7.

[291] Fassbender M, Nortier FM, Phillips DR, Hamilton VT, Heaton RC, Jamriska DJ, et al. Some nuclear chemical aspects of medical generator nuclide production at the Los Alamos hot cell facility. Radiochimica Acta 2004;92:237-43.

[292] Roesch F and Filosofov DV. IAEA Radioisotopes and Radiopharmaceuticals Series, No. 2: Production of long lived parent nuclides for generators: ^{68}Ge, ^{82}Sr, ^{90}Sr and ^{188}W. Vienna: IAEA; 2010, p. 11-30.

[293] Naidoo C, van der Walt TN, and Raubenheimer HG. Cyclotron production of Ge-68 with a GaO_2 target. Journal of Radioanalytical and Nuclear Chemistry 2002;253:221-5.

[294] Loch C, Maziere B, Comar D, and Knipper R. A new preparation of Ge-68. International Journal of Applied Radiation and Isotopes 1982;33:267-70.

[295] van der Walt TN and Vermeulen C. Thick targets for the production of some radionuclides and the chemical processing of these targets at iThemba LABS. Nuclear Instruments & Methods in Physics Research Section A-Accelerators Spectrometers Detectors and Associated Equipment 2004;521:171-5.

[296] Gleason GI. A positron cow. The International journal of applied radiation and isotopes 1960;8:90-4.

[297] Mirzadeh S, Kahn M, Grant PM, and Obrien HA. Studies of the chemical behavior of carrier-free Ge-68 .1. Purification by distillation from acidic chloride solutions. Radiochimica Acta 1981;28:47-9.

[298] Hansen M. Constitution of Binary Alloys. Second Edition ed.: McGraw-Hill,1958.

[299] Adam-Rebeles R, Hermanne A, Van den Winkel P, De Vis L, Waegeneer R, Tarkanyi F, et al. Ge-68/Ga-68 production revisited: excitation curves, target preparation and chemical separation - purification. Radiochimica Acta 2013;101:481-9.

[300] Nesaraja CD. Nuclear Data Sheets for A=69. Nuclear Data Sheets 2014;115:1-134.

[301] Chen F, Bu WB, Chen Y, Fan YC, He QJ, Zhu M, et al. A Sub-50-nm Monosized Superparamagnetic Fe_3O_4@SiO_2 T-2-Weighted MRI Contrast Agent: Highly Reproducible Synthesis of Uniform Single-Loaded Core-Shell Nanostructures. Chemistry-an Asian Journal 2009;4:1809-16.

[302] Park J, An KJ, Hwang YS, Park JG, Noh HJ, Kim JY, et al. Ultra-large-scale syntheses of monodisperse nanocrystals. Nature Materials 2004;3:891-5.

[303] Zhang T, Ge J, Hu Y, and Yin Y. A general approach for transferring hydrophobic nanocrystals into water. Nano Letters 2007;7:3203-7.

[304] Chen F, Ellison PA, Lewis CM, Hong H, Zhang Y, Shi S, et al. Chelator-Free Synthesis of a Dual-Modality PET/MRI Agent. Angewandte Chemie-International Edition 2013;52:13319-23.

[305] Kopecky P and Mudrova B. Ge-68-Ga-68 generator for production of Ga-68 in an ionic form. International Journal of Applied Radiation and Isotopes 1974;25:263-8.

[306] Proulx ST and Detmar M. Molecular mechanisms and imaging of lymphatic metastasis. Experimental Cell Research 2013;319:1611-7.

[307] Ando A, Ando I, Hiraki T, and Hisada K. Relation between the location of elements in the periodic table and various organ-uptake rates. Nuclear Medicine and Biology 1989;16:57-80.

[308] Mehard CW and Volcani BE. Similarity in uptake and retention of trace amounts of silicon-31 and germanium-68 in rat tissues and cell organelles. Bioinorganic Chemistry 1975;5:107-24.

[309] Velikyan I, Antoni G, Sorensen J, and Estrada S. Organ biodistribution of Germanium-68 in rat in the presence and absence of ^{68}Ga Ga-DOTA-TOC for the extrapolation to the human organ and whole-body radiation dosimetry. American journal of nuclear medicine and molecular imaging 2013;3:154-65.

[310] Thorek DLJ, Ulmert D, Diop N-FM, Lupu ME, Doran MG, Huang R, et al. Non-invasive mapping of deep-tissue lymph nodes in live animals using a multimodal PET/MRI nanoparticle. Nature Communications 2014;5.

[311] Ravizzini G, Turkbey B, Barrett T, Kobayashi H, and Choyke PL. Nanoparticles in sentinel lymph node mapping. Wiley Interdisciplinary Reviews-Nanomedicine and Nanobiotechnology 2009;1:610-23.

[312] Moghimi SM, Hunter AC, and Murray JC. Nanomedicine: current status and future prospects. FASEB Journal 2005;19:311-30.

[313] Herzog H and Van Den Hoff J. Combined PET/MR systems: an overview and comparison of currently available options. Quarterly Journal of Nuclear Medicine and Molecular Imaging 2012;56:247-67.

[314] Yen SK, Padmanabhan P, and Selvan ST. Multifunctional Iron Oxide Nanoparticles for Diagnostics, Therapy and Macromolecule Delivery. Theranostics 2013;3:975-92.

[315] Stabin MG. Fundamentals of Nuclear Medicine Dosimetry: Springer New York,2008.

[316] Gallium (^{68}Ga) chloride solution for radiolabelling. In: EDftQoMH (EDQM) editor: European Pharmacopoeia 7.8; 2013, p. 2464: 5643-44.

[317] Gallium (^{68}Ga) edotreotide injection. In: EDftQoMH (EDQM) editor: European Pharmacopoeia 7.6; 2013, p. 2482: 4847–48.

[318] Seifullina II, Martsinko EE, Ilyukhin AB, and Sergienko VS. Synthesis, Properties, and the Structure of a Germanium(IV) Complex with Diethylenetriaminepentaacetic Acid: The Crystal Structure of Ge(OH)(H_2DTPA)-H_2O. Russian Journal of Inorganic Chemistry 1998;43:1509-12.

[319] Martsinko EE, Seifullina, II, and Verbetskaya TG. Heteronuclear complexes of germanium(IV) and of some other 3d metals with diethylenetriaminepentaacetic acid. Russian Journal of Coordination Chemistry 2005;31:541-4.

[320] Rusakova N, Smola S, Martsinko E, Seifullina I, Ermilov E, and Korovin Y. The first observation of 4f-luminescence in new heteronuclear lanthanide-germanium complexes. Journal of Fluorescence 2008;18:247-51.

[321] Langer HG. Solid complexes with tetravalent metal ions and ethylenediamime tetra- acetic acid (EDTA). Journal of Inorganic and Nuclear Chemistry (England) Merged with Inorg. Nucl. Chem. Lett. to form Polyhedron 1964:Medium: X; Size: Pages: 59-72.

[322] Gagnon K, Avila-Rodriguez MA, Wilson J, and McQuarrie SA. Experimental deuteron cross section measurements using single natural titanium foils from 3 to 9 MeV with special reference to the production of V-47 and Ti-51. Nuclear Instruments & Methods in Physics Research Section B-Beam Interactions with Materials and Atoms 2010;268:1392-8.

[323] Takacs S, Kiraly B, Tarkanyi F, and Hermanne A. Evaluated activation cross sections of longer-lived radionuclides produced by deuteron induced reactions on natural titanium. Nuclear Instruments & Methods in Physics Research Section B-Beam Interactions with Materials and Atoms 2007;262:7-12.

[324] Zhou M, Zhang R, Huang MA, Lu W, Song SL, Melancon MP, et al. A Chelator-Free Multifunctional Cu-64 CuS Nanoparticle Platform for Simultaneous Micro-PET/CT Imaging and Photothermal Ablation Therapy. Journal of the American Chemical Society 2010;132:15351-8.